Graphene and doped graphene elaborated by pulsed laser deposition

Yannick Bleu

Yannick Bleu. Graphene and doped graphene elaborated by pulsed laser deposition. Materials Science [cond-mat.mtrl-sci]. Université de Lyon, 2020. English. NNT : 2020LYSES033 . tel-03212304

HAL Id: tel-03212304
https://theses.hal.science/tel-03212304

Submitted on 29 Apr 2021

N° ordre NNT: **2020LYSES033**

THESE de DOCTORAT DE L'UNIVERSITE DE LYON

Opérée au sein du
Laboratoire Hubert-Curien

Ecole Doctorale N° 488
Sciences Ingénierie Santé SIS

Spécialité: Science des matériaux

Soutenue publiquement le 09/10/2020 par :

Yannick Mexon BLEU

Graphene and doped graphene elaborated by pulsed laser deposition

---

Devant le jury composé de :

Yann BATTIE	Professeur, Université de Lorraine	Rapporteur
Patrice MELINON	DR CNRS, ILM – Université Claude Bernard Lyon 1	Rapporteur
Anastasia TYURNINA	Research Fellow, Brunel University London, UK	Examinatrice
Florence GARRELIE	Professeur, Université Jean-Monnet Saint-Etienne	Présidente de Jury
Vincent BARNIER	Ingénieur de Recherche, Ecole des Mines Saint-Etienne	Invité
Florent BOURQUARD	Maître de Conférence, Université Jean-Monnet Saint-Etienne	Invité
José AVILA	Ingénieur de Recherche, Synchrotron SOLEIL, Paris	Co-directeur de thèse
Christophe DONNET	Professeur, Université Jean-Monnet Saint-Etienne	Directeur de thèse

Table of contents

Remerciements

Le travail présenté dans ce mémoire a été réalisé au sein du Laboratoire Hubert Curien (UMR 5516) de l'Université Jean Monnet de Saint-Etienne.

Cette thèse a été dirigée par M. Christophe Donnet et M. José Avila. Elle a été co-encadrée par Anne-Sophie Loir, Florent Bourquard et Vincent Barnier. Je les remercie vivement pour leur choix, leur aide et leur encadrement que j'ai beaucoup appréciés. J'exprime ici toute ma gratitude à l'ensemble de ce corps de direction et d'encadrement pour leurs compétences scientifiques, techniques, et leur dynamisme qui ont permis de mener à bien cette étude. Ils m'ont toujours soutenu tout en m'offrant beaucoup de liberté.

Je remercie Messieurs Yann Battie et Patrice Mélinon pour l'intérêt qu'ils ont accordé à mon travail en acceptant d'être rapporteurs, ainsi que Mme Anastasia Tyurnina et Mme Florence Garrelie qui m'ont fait l'honneur de faire partie de mon jury.

J'exprime toute ma gratitude au LABEX MANUTECH SISE qui a soutenu financièrement ma thèse. J'ai bénéficié de l'aide et des conseils de très nombreuses personnes au sein du Laboratoire Hubert Curien. Je tiens donc à remercier spécialement Jean-Yves Michalon qui m'a formé à l'utilisation de la machine de dépôts par évaporation ainsi qu'au spectromètre Raman. J'en profite pour remercier vivement Stéphanie Reynaud qui m'a formé à l'utilisation des microscopes MEB et AFM, sans oublier Yaya Lefkir pour les belles images HRTEM. Je voudrais également remercier Nicolas Faure pour son aide sur l'utilisation des lasers, le microscope optique et parfois au MEB. J'adresse également mes remerciements à Fred Celle pour sa disponibilité et sa formation à l'accès à la salle blanche ainsi qu'à l'utilisation du spin coater. Je remercie aussi Frédéric Christien (Mines St-Etienne) pour son modèle de diffusion qui a contribué largement au chapitre 3. Je tiens également à remercier Carole Chaix et Carole Farre de l'institut de sciences analytiques de Lyon pour les mesures d'électrochimie.

Ces 3 ans auraient été moins agréables sans la présence des autres doctorants du laboratoire. Je voudrais donc remercier Mathilde Prudent, Leïla Ben Mafhoud, Djaffar Iabbadden, Erieta Katerina Koussi, Yohan Bousset, et Maria Usuga. Je n'oublie pas non plus l'équipe informatique et le personnel administratif pour leur disponibilité.

Enfin, je remercie ma famille et à ma merveilleuse épouse pour son soutien.

Warning

Au cours de la $3^{\text{ème}}$ et dernière année de ce travail de recherche doctoral, est survenue la pandémie liée au COVID-19. Cette situation s'est traduite par une fermeture des laboratoires de recherche entre mars et mai 2020, suivie par une période pendant laquelle les moyens expérimentaux ont été très progressivement rendus accessibles, mais selon des règles sanitaires limitant leur utilisation.

Cette période a coïncidé avec les derniers mois de nos travaux, ce qui a empêché de conduire certaines expériences prévues, en particulier l'optimisation du protocole de transfert des couches de graphène qui aurait permis de réaliser des images de microscopies électroniques par transmission dans des conditions idéales, ainsi que des mesures de propriétés de conduction électronique de nos échantillons de graphène pur et dopé au bore.

During the third and last year of this research work, the COVID-19 pandemic occurred. This situation resulted in a closure of the research laboratories between March and May 2020, followed by a period during which the experimental tools were very gradually made available, but according to health rules limiting their use.

This period coincided with the last months of our work, which prevented certain planned experiments from being carried out, in particular the optimization of the graphene transfer protocol which would have made it possible to perform more and better transmission electron microscopy images under conditions ideal, as well as measurements of electronic properties of our obtained graphene and boron doped graphene.

List of abbreviations

a-C: Amorphous Carbon ... 40
a-C:B: Boron doped amorphous carbon ... 73
a-C:N: Nitrogen doped amorphous carbon ... 69
AFM: Atomic Force Microscope ... 24
ASE: Amplified Spontaneous Emission ... 70
BG: Boron doped graphene ... 170
BLG: Bilayer Graphene ... 30
BSE: Backscattered Electron ... 87
CMOS: Complementary Metal Oxide Semiconductor ... 37
CNT: Carbon Nanotubes ... 22
CPA: Chirped Pulse Amplification ... 69
CV: Cyclic voltammetry ... 78
CVD: Chemical Vapor Deposition ... 23
DLC: Diamond-Like Carbon ... 22
EBSD: Electron Backscatter Diffraction ... 78
EDS: Energy Dispersive Spectroscopy ... 88
EG: Epitaxial Graphene ... 36
FCVA: Filtered Cathodic Vacuum Arc ... 39
FeCl3: Iron (III) Chloride ... 142
FET: Field Effect Transistor ... 33
FHWM: Full Half-Width Maximum ... 81
FLG: Few-layer Graphene ... 30
FTO: Fluorine doped Tin Oxide ... 31
G: undoped graphene ... 179
GNPs: Graphene nanoplatelets ... 31
GRM: Graphene and related materials ... 22
HOPG: Highly Oriented Pyrolytic Graphite ... 27
HRTEM: High Resolution Transmission Electron Microscope ... 24
ISO: International Organization for Standardization ... 30
ITO: Indium Tin Oxide ... 31
KrF: Krypton Fluoride ... 69
LIBs: Lithium ion Batteries ... 33
LPE: Liquid Phase Exfoliation ... 38
MBE: Molecular Beam Epitaxy ... 39
MC: Mechanical exfoliation ... 34
NMP: N-methylpyrrolidone ... 38
ORR: Oxygen Reduction Reaction ... 51
PAPD: Pulse Arc Plasma Deposition ... 39
PECVD: Plasma Enhanced Chemical Vapor Deposition ... 36
PLD: Pulsed Laser Deposition ... 23
PVD: Physical Vapor Deposition ... 39
RT: Room Temperature ... 45

List of figures

List of Tables

Résumé de la thèse en français

Le graphène est, par définition, un matériau bidimensionnel, cristallin, constitué d'un réseau d'atomes de carbone en nid d'abeilles répartis sur une monocouche atomique. Le graphène est la « brique élémentaire » du graphite. Cependant, une évolution sémantique dans la communauté scientifique ne limite pas seulement le terme « graphène » à une monocouche de carbone, mais jusqu'à une dizaine de couches[1], ce qui représente une épaisseur de l'ordre de 3 à 4 nanomètres. En outre, de nos jours, la littérature scientifique utilise le terme « graphène et matériaux associés » (Graphene and Related Materials) pour dénommer toute variante de ce matériau élaboré par divers procédés de synthèse[2].

Le graphène a suscité un grand intérêt dans les communautés scientifiques au cours des 15 dernières années, en raison de propriétés remarquables, en particulier la conductivité électrique, la transparence optique, la résistance et la conductivité thermique, avec de nombreuses applications technologiques potentielles, comme les électrodes transparentes, l'émission de champs, les biocapteurs, les futures générations de batteries, les matériaux composites, etc.

Les recherches sur le graphène constituent l'exemple même des programmes les plus récents des travaux contemporains sur les matériaux à base de carbone, aux échelles micrométrique et nanométrique, si l'on considère les travaux antérieurs sur d'autres matériaux carbonés comme le Diamond-Like Carbon (DLC), les nanotubes de carbone (CNT) et les fullerènes.

La recherche sur le graphène a pris son essor avec les travaux pionniers de Geim et Novoselov en 2004, travaux qui ont conduit à l'attribution du prix Nobel de physique en 2010. Ce fut le point de départ d'une production scientifique colossale à l'échelle internationale, comme nous l'évoquerons dans notre bibliographie, production basée sur des programmes scientifiques et technologiques ambitieux dans de nombreux pays et continents, comme le Flagship Européen sur le graphène actuellement en cours. Aujourd'hui, après 15 ans de recherches intensives, les communautés scientifiques et industrielles cherchent à consolider et fiabiliser les méthodes de synthèse du graphène pour mieux comprendre les relations entre synthèse et propriétés, et produire des couches de graphène de qualité reproductible sur de grandes surfaces selon les standards de la microélectronique. Dans un article récent, Reiss et al.[2] ont observé que 124 ans séparent la découverte de silicium en 1824 et la première puce de silicium en 1958, et de nos jours la production de puces à base de silicium est une activité industrielle de masse. Le graphène nécessitera-t-il une période de gestation aussi longue? Probablement pas, si l'on considère les moyens scientifiques et techniques mobilisés actuellement sur ce sujet. Cependant, prêtons attention à une affirmation des auteurs de l'article de Reiss et al.[2] : « *Mettre un nouveau matériau sur le marché n'est pas sans défi et, de nos jours, les gens semblent penser que le développement de matériaux peut être aussi rapide que les développements de logiciels, ce qui n'est clairement pas le cas. Les innovations basées sur de nouveaux matériaux sont difficiles, longues et coûteuses, et souvent elles ne se concrétisent pas* » (De Réf.2, traduit de l'anglais). La « réussite » du graphène n'est donc pas encore un acquis !

En conséquence, le plus grand défi, avec le graphène, demeure le contrôle et la reproductibilité de la synthèse sur de grandes surfaces, ainsi que l'étude analytique, à l'échelle nanométrique, de films si particuliers à une échelle très réduite, films constitués de l'élément carbone formant une ou plusieurs couches déposées (ou transférées) sur des substrats adéquats en fonction des applications visées. Les scientifiques engagés dans la recherche sur les matériaux à base de graphène, soulignent à l'unanimité le besoin impérieux de valider la fiabilité et la reproductibilité des procédés, en explorant méticuleusement les relations nanostructure - propriétés macroscopiques non sans lien avec le procédé d'élaboration.

Ces recherches constituent un immense défi dans l'étude des matériaux en ce début du 21ème siècle. L'objectif de cette thèse est d'apporter une contribution à ces efforts déployés sur le long terme à l'échelle internationale. Nous avons choisi une approche particulière pour réaliser la synthèse du graphène, le dépôt par ablation laser pulsée (Pulsed Laser Deposition), qui permet en particulier le dopage des couches de graphène par des atomes choisis, de manière contrôlée et reproductible. En effet, par dopage, il est possible de modifier à la demande les propriétés intrinsèques du graphène. Ainsi, le graphène dopé peut présenter des propriétés intéressantes dans les domaines de l'électronique et du magnétisme, ou encore en chimie et électrochimie. Un large éventail d'applications utilisant des matériaux à base de graphène dopés est attendu. Différents types de dopants peuvent être introduits dans le graphène, tels que l'azote, le bore, le phosphore, le soufre, et bien d'autres encore, comme nous le détaillerons dans notre étude bibliographique.

À ce jour, le dépôt chimique en phase vapeur (Chemical Vapor Deposition) apparaît comme la méthode la plus étudiée et la plus prometteuse pour la synthèse du graphène. Cette méthode est déjà bien développée dans les laboratoires et commence à être utilisée dans l'industrie pour la production du graphène. Cependant, elle nécessite une étape à haute température (environ 1000°C), une source de carbone gazeux et un processus de transfert des couches de graphène sur le substrat choisi, ce qui reste souvent problématique. En matière de dopage, se posent des difficultés récurrentes de contrôler la concentration en dopants dans le graphène, à partir des phases gazeuses précurseurs.

Dans cette thèse, nous proposons une méthode de synthèse alternative basée sur un procédé physique (et non chimique), combinant le dépôt par laser pulsé (PLD) avec un recuit thermique rapide (Rapid Thermal Annealing). La PLD est bien connue pour réaliser le dépôt d'un précurseur de carbone solide, et cette méthode est maîtrisée par notre laboratoire depuis une vingtaine d'années, notamment pour la synthèse de DLC et de DLC dopés. Quant au RTA, il est utilisé pour un chauffage rapide qui permet d'obtenir du graphène à partir du précurseur élaboré par PLD, avec la possibilité d'éviter le processus de transfert. Les températures de chauffage peuvent être significativement inférieures à celles utilisées en CVD. La PLD consiste à vaporiser, grâce à la lumière focalisée d'un laser, une cible généralement constituée du matériau que l'on veut obtenir sous forme de film mince. Le matériau est ablaté sour la forme d'un panache constitué d'un plasma, et déposé sur le substrat choisi. Le procédé PLD permet souvent le dépôt d'un matériau de stœchiométrie quasi identique à celle de la cible, et la co-ablation ou l'ablation en présence d'un gaz réactif permet le contrôle de la composition d'un film multi-élémentaire, donc en particulier dopé.

Les objectifs scientifiques de la présente thèse sont donc d'étudier la croissance du graphène et du graphène dopé au bore en utilisant le procédé de synthèse par PLD combiné au traitement thermique par RTA. Nous étudierons l'effet de plusieurs paramètres sur la nature des films de graphène obtenus. L'incorporation de bore dans le graphène vise à apporter de nouvelles fonctionnalités au graphène. Nous chercherons à comprendre le mécanisme de croissance du graphène et du graphène dopé au bore, synthétisés en présence d'un catalyseur métallique. Nous caractériserons les films de graphène purs et dopés, pour mieux comprendre l'influence du procédé sur leurs nanostructures et leurs compositions. Enfin, nous explorerons les propriétés électrochimiques des films de graphène pur et de graphène dopé au bore, pour esquisser une perspective d'applications de ces films.

Même si cette thèse n'est pas le premier travail sur le graphène, elle ouvre une voie physique originale pour la synthèse et le dopage du graphène d'une manière contrôlable et probablement plus versatile que d'autres méthodes d'élaboration. Nos travaux cherchent à élargir les champs d'études de la PLD dans le domaine de la synthèse des couches minces. Ils contribuent à une avancée des connaissances fondamentales sur la synthèse du graphène et du graphène dopé au bore, au cœur des efforts actuels de la recherche pour intégrer ces matériaux dans des applications technologiques exigeants des performances toujours plus élevées.

Ce manuscrit de thèse se structure en cinq chapitres.

Le Chapitre 1 propose une synthèse bibliographique sur notre sujet. Cette synthèse se veut assez brève sur le graphène, déjà largement présenté dans des revues de synthèse. Nous insisterons davantage sur l'élaboration du graphène par le procédé PLD.

Le Chapitre 2 présente la méthodologie expérimentale que nous avons mise en œuvre dans nos recherches. Cette méthodologie concerne d'une part le procédé d'ablation laser pulsé couplé au traitement thermique RTA pour la synthèse du graphène et du graphène dopé, d'autre part les méthodes de caractérisation complémentaires afin de sonder, selon une approche multi-échelle, la nanoarchitecture, la composition et les propriétés électrochimiques des films élaborés.

Le Chapitre 3 présente les mécanismes de croissance du graphène à partir d'une couche mince amorphe à base de carbone, élaborée par PLD. La méthode originale que nous avons utilisée est une analyse chimique par spectroscopie de photoélectrons X (XPS) mise en œuvre in situ pendant le chauffage sous vide, et donc pendant la croissance du graphène. Nous avons mis en évidence un mécanisme de diffusion – ségrégation du carbone dans le catalyseur métallique à base de nickel. Nous avons montré que la croissance du graphène débute à des températures relativement basses (300°C) et se poursuite au moins jusqu'à 500°C. Un modèle de diffusion – ségrégation a été mis en œuvre pour mieux comprendre les mécanismes observés expérimentalement.

Le Chapitre 4 explore l'effet des paramètres de synthèse a priori les plus influents sur la nature et la nanoarchitecture des couches de graphène obtenus, en termes de nombre de couches, de défauts, de tailles des amas de carbone graphéniques et d'homogénéité en surface. Nous démontrons plus particulièrement les effets de la nature des substrats à base de silicium, de l'épaisseur initiale de la couche de carbone et de la couche du catalyseur métallique, et des paramètres du traitement thermique RTA, notamment la température. Aux températures les plus élevées, nous mettons en évidence un phénomène, déjà connu, de démouillage du catalyseur métallique, bien en-deçà de son point de fusion. Nous avons cherché à mettre en évidence quels pouvaient être les liens entre ce démouillage (qui dépend de la température et de l'épaisseur du film catalytique) sur la qualité du graphène obtenu. Ces travaux nous ont permis de cerner une gamme de paramètres (épaisseur de la couche carbonée précurseure, épaisseur du catalyseur, température RTA) permettant d'optimiser les couches de graphène. Une perspective de production de graphène sans procédé de transfert ultérieur est ainsi ouverte.

Le chapitre 5 propose, sans doute pour la première fois à notre connaissance dans la littérature scientifique, la synthèse de graphène dopé au bore, par couplage de la PLD avec le RTA. Nous mettons en évidence qu'il est envisageable de contrôler la teneur en bore dans le graphène, en contrôlant cette teneur dans la couche précurseure réalisée par co-ablation de carbone et de bore, et ce même si cette concentration est affectée par le traitement RTA. Enfin, nous avons exploré le comportement électrochimique des couches de graphène dopé au bore, comparées aux couches de graphène non dopé. Ces travaux, très préliminaires et conduits en fin de thèse, mettent en évidence un effet significatif du dopage au bore sur la cinétique électrochimique observée.

La conclusion permet une synthèse de l'ensemble, et dessine quelques perspectives scientifiques pour la suite de ces travaux de recherche.

Références

1. Ye, R. & Tour, J. M. Graphene at Fifteen. *ACS Nano* (2019) doi:10.1021/acsnano.9b06778.
2. Reiss, T., Hjelt, K. & Ferrari, A. C. Graphene is on track to deliver on its promises. *Nat. Nanotechnol.* **14**, 907–910 (2019).

General Introduction

Graphene is, by definition, a one-atom-thick pure carbon crystal with a honeycomb-like structure. However, a semantic evolution in the scientific community does not only limit the term "graphene" to a carbon monolayer but up to 10 layers[1]. Besides, nowadays, the literature uses the term "Graphene and related materials (GRM)" to name any variant of this wonder material[2]. Graphene has become of great interest in both scientific and engineering communities from the past 15 years, owing to its range of unique properties including high conductivity, transparency, strength, and thermal conductivity, with many potential applications in research and industry, as transparent electrodes, field emitters, biosensors, batteries, composites, and so on. The research on graphene constitutes one of the most recent and contemporary stages of investigation in the scientific community of carbon-based at the micrometer and nanometer scales if one considers the literature dealing typically on Diamond-Like Carbon (DLC) films, carbon nanotubes (CNT), fullerenes.

Research on graphene has emerged with the pioneering work of Geim and Novoselov in 2004 and their Nobel Prize in Physics in 2010. This was the "starting point" of a huge worldwide scientific production, as mentioned later in our first chapter, based on ambitious scientific and technological programs in many countries and continents, as the European Flagship on Graphene presently in progress. Nowadays, about 15 years after the "graphene take-off", the scientific and industrial communities are looking to consolidate the synthesis methods of graphene to better understand and control the correlation between synthesis and properties.

In a recent paper, Reiss et al.[2] observed that 124 years separate the discovery of silicon in 1824, and the first silicon chip in 1958, and now Si chip production is a mass-market activity. Does graphene require such a similarly long period? Probably not, if one considers the scientific and technical means mobilized today. However, let us mention an assertion written by the already mentioned authors:

> "*Bringing a new material to market is not without its challenge and, in this day and age, people seem to assume that materials development can be as quick as software developments, which is clearly not the case. Innovations based on new materials are hard, long, and expensive, and often it does not come to final fruition" (From Ref.*[2]*).*

As a consequence, the highest challenge, with graphene, remains the control and reproducibility of the synthesis over wide surfaces, as well as the analytical investigation at (ultra) low scales, of films constituted by a light element (carbon) forming one or few-layer deposited (or transferred) on adequate substrates depending on the targeted applications. Therefore, scientists committed in graphene-based material research, emphasize unanimously the strong need to provide trusted validation on graphene related-materials, meaning to explore meticulously the nanostructure – macroscopic property relationships, in connection with the synthesis route. This is a great challenge, and the objective of this Ph.D. project is to contribute to this long-term work in progress, by considering a particular approach to achieve the graphene synthesis, including doping of graphene layers in a controlled and reproducible way. Indeed, by doping, it is possible to modify on demand the intrinsic properties of graphene. Thus, doped graphene presents interesting properties such as superconductivity, ferromagnetism, and enhanced chemical and electrochemical activity, which promote a wide range of applications using graphene-based materials. Various types of dopants have been introduced in graphene material such as N, B, P, or S, as mentioned later in our bibliography.

To date, chemical vapor deposition (CVD) appears the most promising route of graphene synthesis, and this method is already well developed in both the laboratory and industry environments. However, it requires high-temperature treatment, gas carbon source, and a transfer process, which is still problematic. In this Ph.D. project, we propose an alternative synthesis method, combining pulsed laser deposition (PLD) with rapid thermal annealing (RTA). On one side, PLD allows the deposition of the solid carbon precursor, and on the other side, RTA is used for rapid heating which makes it possible to obtain graphene without the need for transfer. PLD consists of vaporizing, thanks to the focused light of a laser, a target generally made up of the material that one wants to obtain in the form of a thin film. The material is ejected into a plasma ablation plume and is deposited on a substrate. The PLD process generally allows the deposition of a material of the same stoichiometry as the target, and co-ablation or ablation in the presence of a reactive gas allows control of the film composition. The scope of the present thesis is therefore to study the growth of graphene and boron-doped graphene by using the PLD method combined with the RTA process. Indeed, the incorporation of boron aims to bring new graphene functionality.

Firstly, we aim to understand the mechanism of PLD graphene growth. Secondly, the goal is to synthesize and characterize pure and doped graphene films to better understand the influence of the process on their structures and properties. Lastly, we started to explore the electrochemical performance of pure graphene and boron-doped graphene films, to provide a perspective of applications of such films. Even though this thesis is not the first work on graphene, it paves a new physical route for graphene synthesis and doping in a controllable manner, which appears to be much easier compared to the other methods. It widens the investigation fields of PLD in the field of thin-film synthesis. It also pushes a little further scientific knowledge to consolidate the graphene topic, which is at a critical time in its existence compared to the expected applications.

This Ph.D. project was performed in Laboratoire Hubert Curien of University Jean Monnet (Saint-Etienne, France), in the frame of GRAPHENE project, labeled by LABEX MANUTECH SISE (Surface and Interfaces Science and Engineering) of Université de Lyon, a consortium of academic laboratories and industries supported by the French "Plan d'Investissements d'Avenir". Our investigations were supported by the research theme "Laser-matter interaction" of Laboratoire Hubert Curien, focused on laser irradiation effects in condensed matter for material processing, functionalization, and fabrication. We also relied on the experimental tools and skills of four platforms of Laboratoire Hubert Curien: "Ultra-short laser", "Planar Technology and Instrumentation", "Characterization" and "Electron microscopy". Indeed, this work enabled access to different characterization spectroscopy and microscopy techniques: Raman spectroscopy, Scanning Electronic Microscopy, Atomic Force Microscopy, and Transmission Electron Microscopy were performed at Laboratoire Hubert-Curien. Transmission electron microscopy was carried out by Yaya Lefkir and Stéphanie Reynaud. X-Ray Photoelectron spectroscopies were performed either at Ecole Nationale Supérieure des Mines de Saint-Etienne (Vincent Barnier), at Synchrotron SOLEIL (José Avila) and Ecole Centrale de Lyon (Jules Galipaud), depending on the availability of the apparatus. We also worked on a model of carbon diffusion developed by Frédéric Christien at Ecole Nationale supérieure des Mines de Saint-Etienne. For electrochemical analysis, a collaboration was made with Institut des Sciences Analytiques (ISA) of Lyon (Carole Farre and Carole Chaix) for cyclic voltammetry measurements on our undoped and boron-doped graphene.

This manuscript is organized in five chapters as illustrated in **Figure 0.1** and outlined below.

In Chapter 1, we discuss the graphene generalities and review the state of the art about the growth of graphene using the pulsed laser deposition method. By doing so, we realized that PLD has been less extensively used for graphene and doped graphene synthesis, which had encouraged our work.

In Chapter 2, we describe the experimental protocols related to the synthesis method and the characterization techniques including microscopies (SEM, AFM, and HRTEM), spectroscopies (Raman, XPS, UV-Visible absorption) and cyclic voltammetry for electrochemical property measurement.

Chapter 3 is devoted to the study of the PLD graphene growth mechanism by carbon diffusion-segregation through the nickel catalyst. Herein, we demonstrated, using thermal heating performed with in situ XPS, how carbon starts to diffuse through nickel at relatively low temperatures, and segregates into graphene sheets on the top surface, at a temperature well below temperatures required in CVD processes to achieve graphene. Thanks to a model of diffusion-segregation, we were able to discuss the graphene synthesis mechanism from a solid carbon source obtained by PLD.

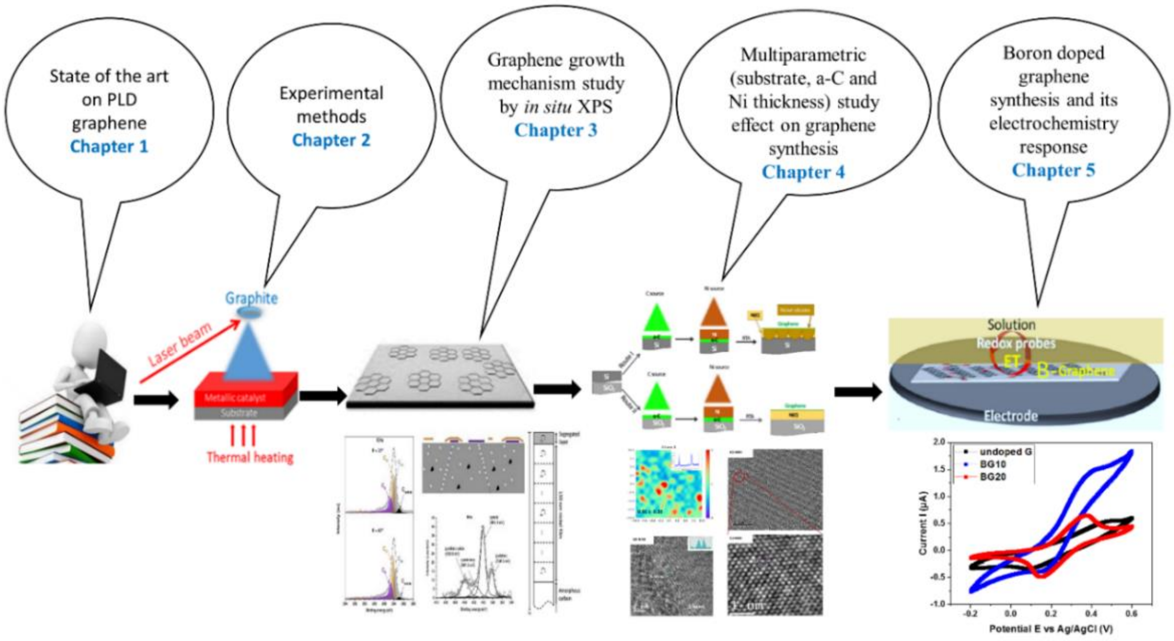

Figure 0. 1 Illustration of the organization of the contents of this Ph.D. manuscript.

Chapter 4 reports the multi-parametric studies for the optimization of PLD graphene synthesis. With this study, we observed that silicon-based substrates used for graphene growth highly influence the quality and layer number of the resulting graphene, whether it is silicon or fused silica. Moreover, the starting thicknesses of the amorphous carbon and the nickel catalyst, as well as annealing temperature, affect considerably the synthesized graphene.

Chapter 5 concerns the boron doping effects in terms of structural, chemical, and electrochemical properties of graphene. Here, we successfully demonstrated for the first time the use of the PLD method for synthesis of boron-doped graphene exhibiting an electrochemical performance much higher than the one of undoped graphene. All these results position the pulsed laser deposition method as an alternative route for graphene and doped graphene synthesis.

Finally, we summarized our main results in the general conclusions, paving the way towards future research suggestions.

References

1. Ye, R. & Tour, J. M. Graphene at Fifteen. *ACS Nano* (2019) doi:10.1021/acsnano.9b06778.
2. Reiss, T., Hjelt, K. & Ferrari, A. C. Graphene is on track to deliver on its promises. *Nat. Nanotechnol.* **14**, 907–910 (2019).

Chapter 1: Graphene synthesis using pulsed laser deposition: State of art

I. Background on graphene

Graphene is an exceptional two-dimensional (2D) material that has a significant interest in both academia and industry research. The first study on graphene, or 2D graphite, can be dated to as early as 1947 when Wallace examined the electronic energy bands in crystalline graphite using the 'tight binding' approximation[1]. Since it was shown that the semi-metallic phase is unstable in two dimensions (2D)[2], single-layer graphene has long been regarded as 'academic' material. Even so, many experimental efforts were made to obtain single-layer graphene. For example, in 1992, the single-layer graphite structure produced by hydrocarbon decomposition was observed on the Pt(111) surface under a scanning tunneling microscope (STM)[3]. In 1997, Ohashi and co-workers[4] cleaved graphite material to evaluate the thickness impact of graphite crystals on electrical properties. They reduced with success the thickness of graphite films to 30 nm. In 2004, Novoselov and Geim[5] inspired by the previous works presented a reliable approach for making single-layer graphene by repeatedly peeling highly oriented pyrolytic graphite (HOPG). This demonstration of the mechanical exfoliation technique, known as the scotch tape method, caused a good sensation and excited several research groups to analyze the structure and properties of graphene. Consequently, Geim and Novoselov awarded the Nobel Prize in Physics 2010 for their innovative experiments on graphene material. Graphene structure presents a 2D honeycomb lattice, with a compact single layer of carbon atoms. Being the basic block for all graphitic materials, the graphene plane can be wrapped into 0D fullerenes, rolled into 1D nanotubes, or stacked into 3D graphite[6,7] as shown in **Figure 1.1**.

1. Graphene crystalline structure

The word "graphene" is made up of the prefix "graph" from graphite and the suffix "ene" from the carbon/carbon double bonds[8]. Graphene is a two-dimension (2D) form of graphite, in other words, graphene can be called 2D graphite. The electronic structure of carbon is composed of 6 electrons including 4 of valence: $1s^2\ 2s^2\ 2p^2$, which gives rise to an s orbital and three p (p_x, p_y, p_z) orbitals presenting sp^2 or sp^3 hybridizations depending on the structure. Sp^3 hybridization gives rise to four covalent bonds (this is the case of diamond or Diamond-Like Carbon (DLC)). In the case of graphene, but also fullerenes (C60), carbon nanotubes, and graphite, sp^2

hybridization between the s orbital and two p (p_x and p_y) orbitals lead to a trigonal planar structure with the formation of three covalent in-plane σ-bonds (**Figure 1.2**). These covalent σ bonds between carbon atoms form the hexagonal structure of graphene with an interatomic length of ~ 0.142 nm and are responsible for its good mechanical strength. The additional p_z orbital perpendicular to the planar structure of graphene occupies the out-of-plane π bond. The overlap of the p_z between neighboring carbon atoms gives rise to the formation of the π half-filled bond, responsible for the electronic conductivity of graphene.

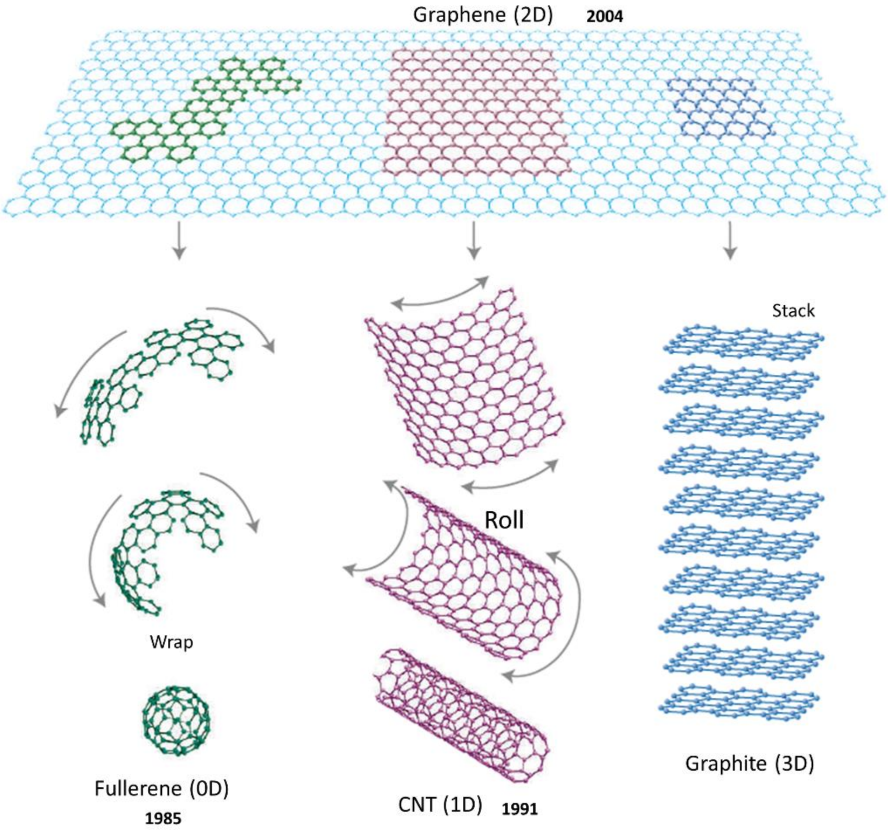

Figure 1. 1 Illustration of graphene as a mother of carbon allotropes and can be converted to fullerenes, carbon nanotubes, and graphite. Adapted from reference[7].

The structure of graphene is composed of a unit cell of two carbon atoms. It consists of two triangular sublattices with two non-equivalent atoms illustrated by the blue and orange atoms in **Figure 1.3a**. The interatomic distance of two atoms is a_0 = 0.142 nm and the lattice vectors can be described as:

$$a_1 = \frac{a}{2}\left(1, \sqrt{3}\right), \ a_2 = \frac{a}{2}\left(1, -\sqrt{3}\right)$$

Where a = 0.246 nm is the lattice constant in the plane.

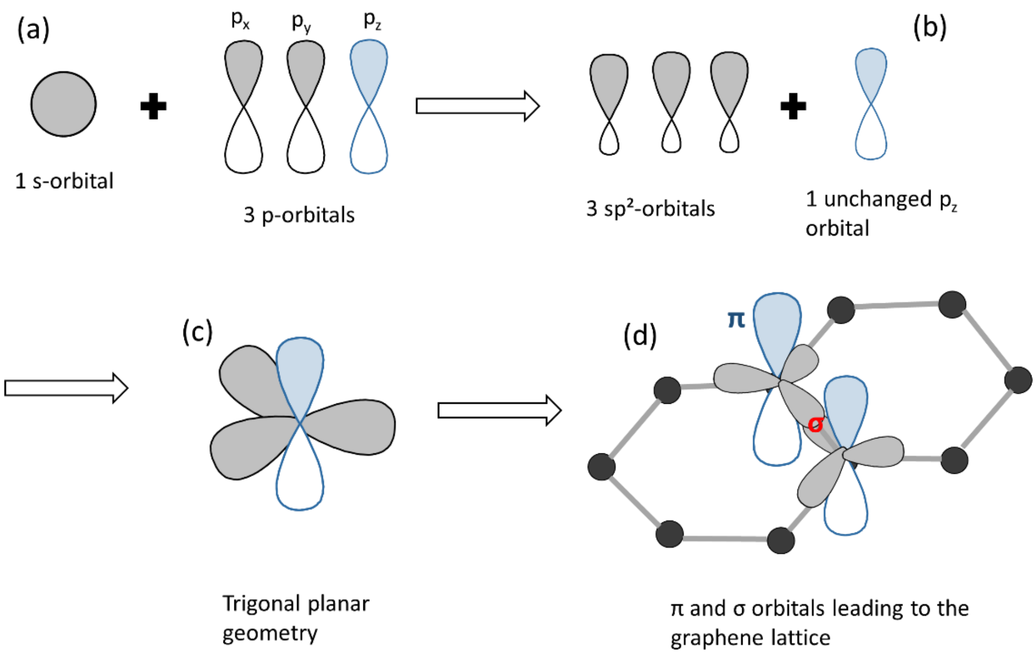

Figure 1. 2 Illustration of the carbon sp^2 hybridization: (a) its electronic structure comprises an s orbital and three p orbitals. (b) The sp^2 hybridization consists of three sp^2 orbitals and one p_z orbital perpendicular to the other three, (c) triangular planar geometry, (d) π, and σ orbitals leading to the graphene lattice.

The velocity of delocalized electrons in graphene is constant and independent of momentum, which leads to the conclusion that the charge carriers (electrons and holes) can be described by the Dirac equation for the massless particles with an effective speed of light $v_F = 10^6$m/s. The band structure of graphene presented in **Figure 1.3b** is different from metal and is different from the semiconductor band structure because there is no energy gap. For this reason, graphene can be considered a zero bandgap material. The band structure of graphene is positioned somewhere around these two extremes, which make graphene to act like a semimetal. In a closer look at **Figure 1.3b**, it can be observed that the valence and conduction bands meet at the Fermi energy, forming conical bands, which touch at the K and K' high-symmetry points in the Brillouin zone. The absence of an electronic bandgap in graphene limits its applicability in various areas such as transistors technology where a bandgap is needed for on-off switching operations. However, the bandgap of graphene can be tuned by electrical or chemical doping. This is why graphene doping has emerged as a hot topic in the past few years. The discussion about the chemical graphene doping with nitrogen and boron will be detailed further in this chapter.

The term "graphene" is often prefixed by "monolayer or single layer," "bilayer," "trilayer," "few-layer" or "multilayer." To address the discrepancy in definitions, the International

Organization for Standardization (ISO) released its chosen terminologies for graphene and graphene derivatives in 2017. It defines the layer numbers of graphene as the following: single-layer graphene (SLG), bilayer graphene (BLG), and few-layer graphene (FLG) to be 1, 2, and 3−10, respectively[9]. This definition was based on the finding that SLG is a semimetal with zero bandgap[5], and its stacking changes the physical and electronic properties[8,10].

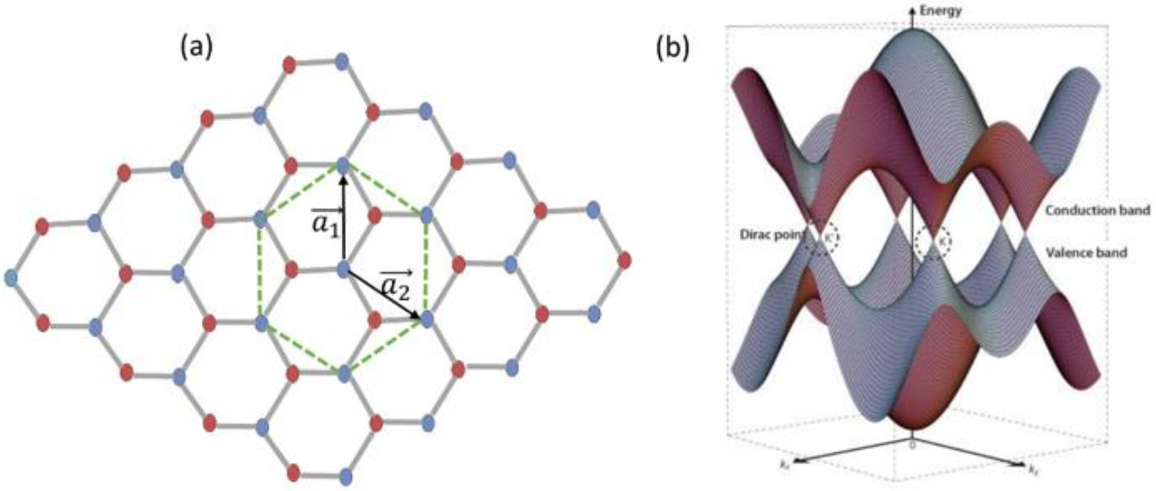

Figure 1. 3 (a) Graphene lattice representation: the two inequivalent atoms of the unit cell are highlighted with blue and red colors. (b) Graphene energy bands close to the Fermi level: the conduction and valence bands touch at K and K' points. Adapted from[11].

In terms of the stacking order, single-layer graphene (SLG) does not have stacking but can exist in a rippled form. The bilayer (BLG) and few-layer (FLG) graphene can display different stacking arrangements, as illustrated in **Figure 1.4**. These stacking orders include mainly the Bernal stacking (AB)[12], the rhombohedral stacking (ABC)[13], and turbostratic stacking with an interlayer spacing > 0.342 nm larger than that of crystalline graphene (0.335 nm)[14].

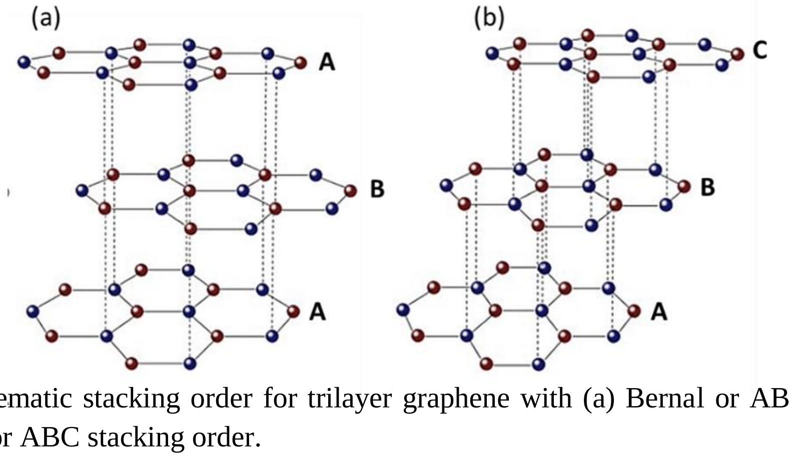

Figure 1. 4 Schematic stacking order for trilayer graphene with (a) Bernal or ABA stacking and (b) Rhombohedral or ABC stacking order.

The turbostratic stacking is a specific lattice arrangement with no discernible stacking order and exhibits relative rotational angles that cannot be described by the classic atomic plane families' graphene. Furthermore, when the graphene with AB stacking go beyond 10 layers at room temperature, the nanosized assembly becomes graphite-like and is called graphene nanoplatelets (GNPs). Another structural parameter that may affect the graphene properties is its edges. Graphene edges can exhibit armchair or zigzag configurations with different electronic and magnetic properties[14–16].

2. Properties and potential applications

Graphene has exceptional properties, it is described as the thinnest, most flexible and strongest material known[17], and it is impermeable to gases[18]. Graphene has a C-C bond length of about 0.142 nm, with a weak Van der Waals interaction between layers. **Table 1.1** lists some of the outstanding properties of single-layer graphene. One of the most useful properties of graphene is that it is a zero bandgap semimetal with very high electrical conductivity. Indeed, at the Dirac point in graphene, the electrons and holes behave like the particles with zero effective mass. Due to these physical properties, the carriers' mobility is about 200, 000cm^2/Vs. However, because of the presence of charge scattering by the underlying substrate and impurities or wrinkles in graphene, all these properties could be strongly affected[19,20].

Properties	Values	Comparison with other materials	References
Optical transparency	97.7%	An alternative to ITO and FTO films	Nair et al., Science 320, 2008[20]
Electron mobility	200 000 cm^2 v^{-1} s^{-1}	140 × higher than Si	Bolotin et al., Sol. Stat. Com. 146, 2008[21]
RT Thermal conductivity	5000 W m^{-1} K^{-1}	10 × higher than Cu	Balandin et al., Nano Lett. 8, 2008[22]
Theoretical specific surface area	2630 m^{2}g^{-1}	2 × larger than CNTs	Züttel, et al., Appl. Phys. A 78, 2004[23]
Tensile strength	125 GPa	100 × greater than steel	Lee et al., Science 321, 2008[24]
Elastic modulus	1 TPa	…	
Fermi velocity	1×10^6 m s^{-1}	…	Du et al., Nat. Nanotechn. 3, 2008[25]

Table 1. 1 The most exceptional properties of single-layer graphene compared to other materials such as ITO (Indium-Tin Oxide), FTO (Fluorine-doped Tin Oxide), Silicon, Copper, carbon nanotubes, and steel.

Graphene absorbs 2.3% of incident white light[20]. Besides, its transmittance linearly decreases with its number of layers. Thanks to the low density of states near the Dirac point in graphene, a shift of the Fermi level due to the gate causes a considerable variation of charge density, leading to a striking change in transmission[26]. Due to the strength of the C-C bonds, graphene is the strongest material as the monolayer, with Young's modulus of 1.0 TPa and stiffness of

130 GPa[27]. Besides, graphene has a very high current carrying capacity and high thermal conductivity (up to 5000 W/mK)[22].

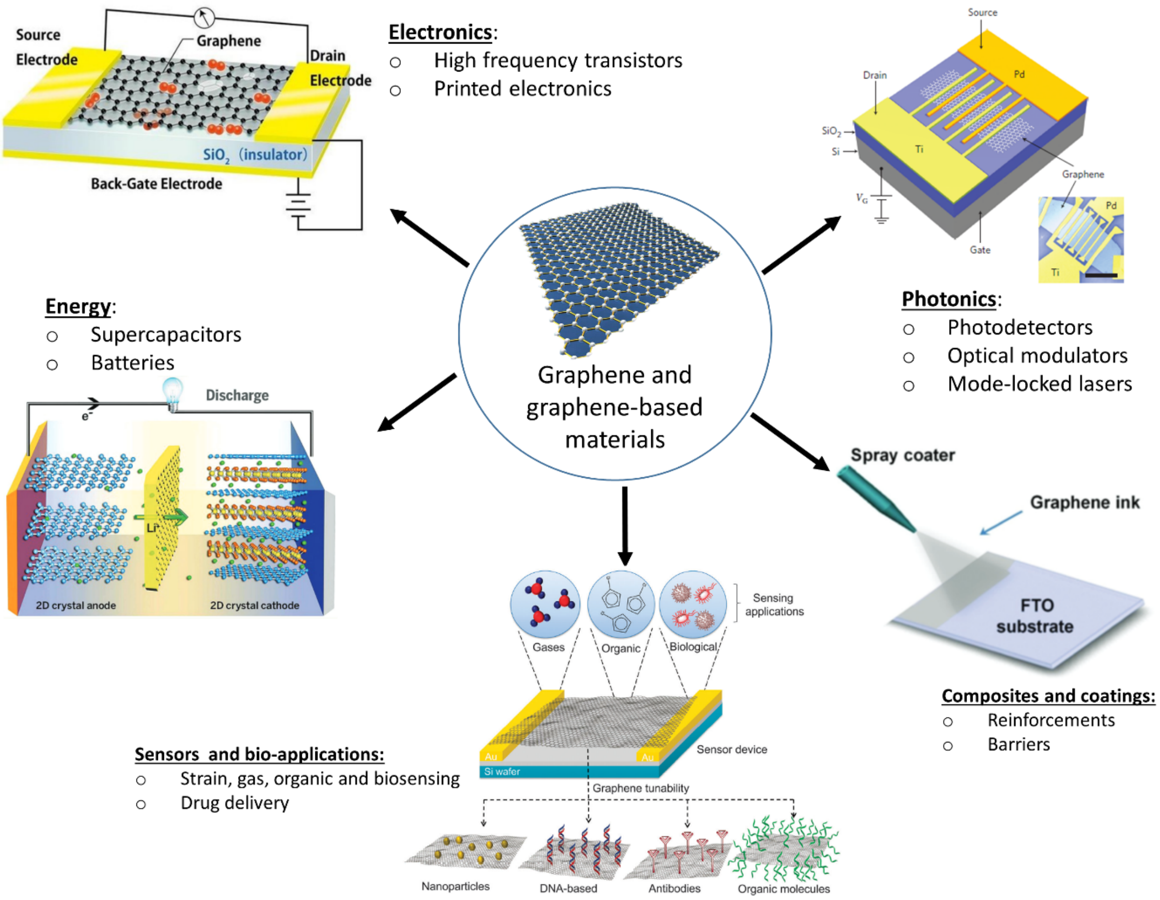

Figure 1. 5 Applications of graphene and graphene-based materials in various industrial sectors. Adapted from[28–31].

It is worth noting that most properties are recorded on high-quality monolayer graphene and are not anymore the same when using bilayer or few-layer graphene. Moreover, it has been shown that the physical properties of graphene are sensitive to the thickness or number of layers. For instance, the transmittance of graphene decreases from monolayer to a few-layer graphene[32]. A gradual change in its electronic properties has been observed when increasing numbers of layers[33]. The measured thermal conductivity is highly influenced by the graphene thickness: the value for four-layer graphene is almost the same as that of bulk graphite[34]. Hardness and elastic modulus are also substantially dependent on the number of graphene layers, and a linear decrease in both properties has been observed when the number of layers increases up to four[35]. All the exceptional properties of graphene have led to many promising applications for electronic devices (High-frequency transistors, printed electronics), photonics devices (photodetectors, optical modulators), composites and coatings (as reinforcements, barriers), energy devices (supercapacitors, batteries), sensors, and bio-applications (strain, gas, organic and biosensing, drug delivery). **Figure 1.5** shows some applications of graphene in numerous industrial sectors. In electronics, the first graphene field-effect transistor (FET) was reported in 2004, which shows a strong ambipolar electric field-effect, but could not be used for the fabrication of effective FET due to the zero bandgap[5]. Later graphene field-effect transistors (FET) on various substrates were fabricated to show high carrier carrying[36–38]. To improve the on-off ratio for effective transistors, graphene nanoribbons fabricated by chemical and lithographic methods have been studied theoretically and experimentally[39–41]. For future optoelectronic devices, graphene has a potential application as transparent electrodes for solar cells and liquid crystal displays to replace ITO due to its high cost, limited supply, and brittle nature of indium[42–44]. Due to the unique 2D structure and high mobility, graphene has been used as an electron acceptor in photovoltaic devices, such as a layered graphene-quantum dot hybrid[42]. The tunable bandgap and large optical absorptivity of graphene are appealing for photodetectors, optical modulators, and mode-locked lasers[46–48]. In the energy area, graphene has a great potential to be implemented as electrodes/absorber in solar cells[49–51], electrochemical/thermal energy harvester[52–54], supercapacitors[55–57], electrodes in LIBs (Li-Ion Batteries)[58–60], hydrogen and bio-energy storage[61–63]. In composites and coatings applications, graphene has raised considerable concern about the applications in many industrial fields because of its excellent anti-corrosion properties. Therefore, graphene coatings can isolate corrosive media from the base and provide effective protection for metals. However, defects in graphene may accelerate the corrosion of substrate metals in the long term[64,65]. In the domain of sensor and bio applications, chemical and biological sensors based on graphene FET are keeping continuous interest because of its low noise, high sensitivity, chemical stability, and biocompatible nature[66–68]. The operational principle is based on the change of graphene electronic conductivity due to the absorption of molecules on the graphene surface. Numerous reports have shown evidence of the graphene sensor to O_2, H_2, NO_2, H_2O_2, SO_2, NH_3, DNA, and dinitrotoluene[67,69–73]. Besides, a variety of graphene-derivative (graphene, graphene oxide, and reduced graphene oxide with metal-hybrid) are actively under investigation. In addition to gas sensors, several graphene-based electrochemical sensors[74,75], mechanical (pressure[76], strain[77], bio (DNA, glucose, peptide, bacteria, enzyme)[78–81] have been reported.

3. Graphene synthesis methods

Graphene was first produced by micromechanical exfoliation of graphite[82]. This method still provides high-quality graphene in terms of purity, defects, and mobility and optoelectronic properties. However, large-scale assembly is required for the widespread application of this material. Numerous approaches are developed to produce a stable supply of graphene in large areas and quantities, exploitable for mass applications. These include growth by chemical vapor deposition (CVD), thermal decomposition of silicon carbide (SiC), and liquid phase exfoliation as shown in **Figure 1.6**. Since the graphene quality and performance are strongly dependent on the process carried out for synthesis, here we briefly review the state-of-art of these most used synthesis methods.

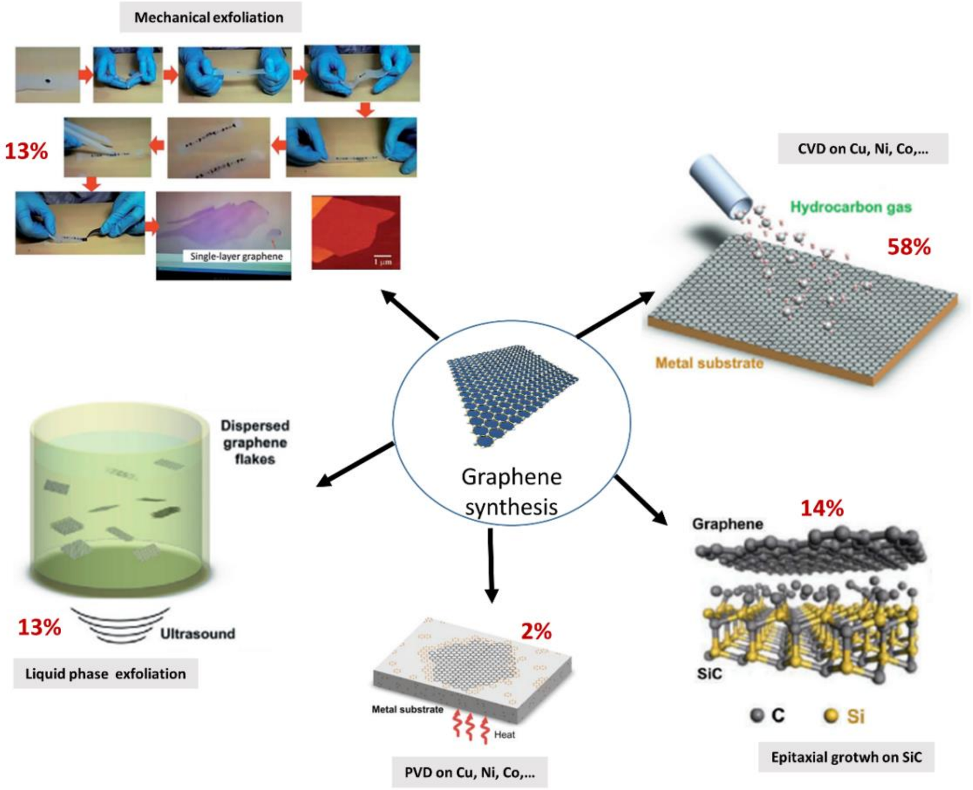

Figure 1. 6 A schematic illustration of the most used graphene synthesis methods and the less used PVD technique, Adapted from[83–85]. The percentage represents the rate of published papers on the different synthesis methods among 15 000 representative selected articles taken from Web of Science (accessed 31/01/2020).

a. *Mechanical exfoliation (MC)*

The mechanical exfoliation (MC) method is considered as a fundamental and groundbreaking work reported by Novoselov and co-workers in 2004[5,83]. This method illustrated in **Figure 1.7**, involves peeling off a piece of natural graphite or highly oriented pyrolytic graphite (HOPG) employing adhesive tape**[83]**. It has been optimized to produce SLG of up to millimetres**[86]** in size, and with high structural and electronic quality. Although MC is a method of choice for fundamental research, with most key results on individual SLG being obtained on such layers, its disadvantages are the low yield, and non-exploitable for large-scale applications. Nevertheless, the obtained graphene films are useful for fundamental studies as well as proof of concept waiting for large-scale manufacturing. Thus, although MC is impractical for large-scale applications, it is still the method of choice for fundamental studies. Indeed, the vast majority of basic results and prototype devices were obtained using the graphene sheets from the MC method.

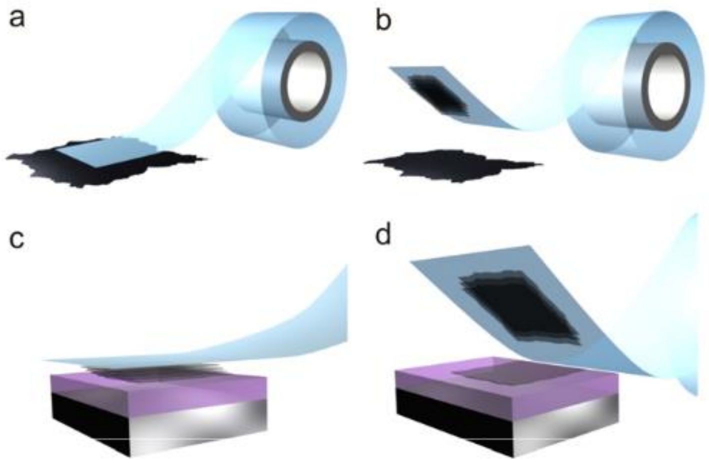

Figure 1. 7 Micromechanical exfoliation of 2D crystals. (a) Adhesive tape is pressed against a 2D crystal so that the top few layers are attached to the tape (b). (c) The tape with crystals of layered material is pressed against a surface of choice. (d) Upon peeling off, the bottom layer is left on the substrate**[87]**.

b. Chemical vapor deposition (CVD)

The chemical vapor deposition (CVD) growth of graphene has proved to be one of the most efficient methods to fabricate wafer-scale graphene layers. Graphene has been elaborated on a variety of transition metals surfaces, such as copper (Cu)**[88]**, nickel (Ni)**[89]**, ruthenium (Ru)**[90]**, iridium (Ir)**[91]**, and so on, acting as a catalyst to promote graphene generally at high temperature. In general, the growth process involves the thermal decomposition of the hydrocarbon sources on a heated substrate, as illustrated in **Figure 1.8**. During the process, the precursor gas serving as carbon supply, e.g. methane, ethylene, or propanol, is sent into the furnace chamber with the optimized pressure and flow rate. The precursor reacts with the metal catalyst at elevated temperature (up to 1200°C) and forms a graphene sheet on the catalyst surface. The metal substrates not only act as a catalyst to lower the energy barrier of the reaction but also determines the graphene deposition mechanism as shown in **Figure 1.8** In the case of metal possessing high carbon solubility (such as polycrystalline Ni, Co, and Fe), the carbon will dissolve into the metal bulk according to the solubility of carbon and segregate to the surface to form graphene films. On the other hand, for metal having low carbon solubility (such as Cu), carbon atoms will nucleus to form graphene domains and expand laterally with the decomposition of hydrocarbon at high temperatures.

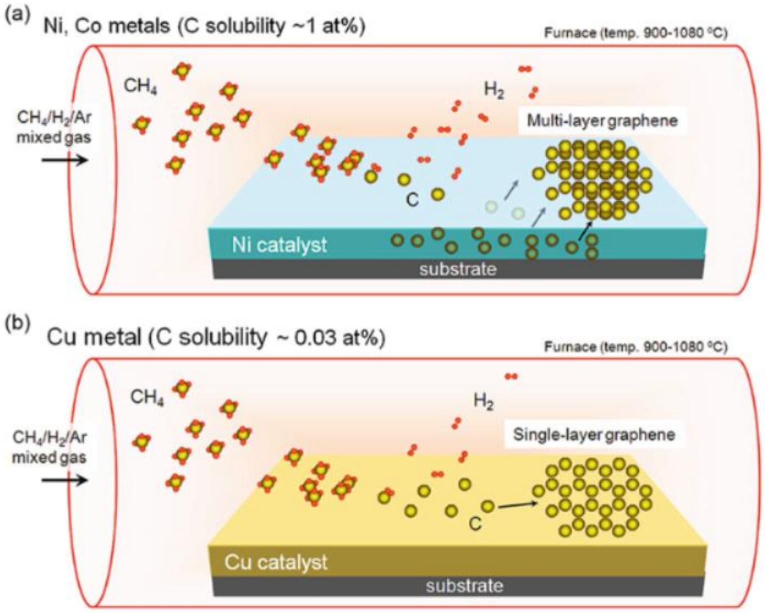

Figure 1. 8 Growth mechanism of graphene sheets on different types of metal catalysts. (a) Inhomogeneous multilayer graphene tends to grow on Ni and Co, which has high C solubility. (b) Uniform single-layer graphene can be grown on low C solubility metal, like Cu[92].

Since Li *et al.*[88] have firstly produced the uniform monolayer graphene sheet on Cu foils at low pressure in 2009, Cu has been considered as an ideal substrate. In the meantime, Reina *et al.*[89] have demonstrated one or two layers of graphene can be grown on Ni surface during atmospheric pressure CVD. They found that the non-uniformity of graphene layers was formed along the boundaries of Ni grain. Indeed, Cu and Ni are the most commonly used catalysts due to their low cost, etchability, and large grain size. There are many different variants of CVD processes: thermal, plasma enhanced (PECVD), cold wall, hot wall, reactive, and many more.

c. *Epitaxial graphene (EG) on silicon carbide (SiC)*

The graphene growth on SiC by the sublimation method, illustrated in **Figure 1.9**, is usually known as epitaxial graphene (EG). As early as 1975, graphite layers were first obtained by annealing the SiC substrate (> 800°C) under ultra-high vacuum (UHV)[93]. However, EG has not attracted much attention until 2004 when Berger and co-workers[94] have detected the 2D electron gas behavior by processing a field-effect transistor with ultra-thin graphite layers grown on 6H-SiC (0001). Since then, the EG grown on SiC has been largely investigated and considered as one of the most viable candidates for the graphene-based nanoelectronic devices fabrication.

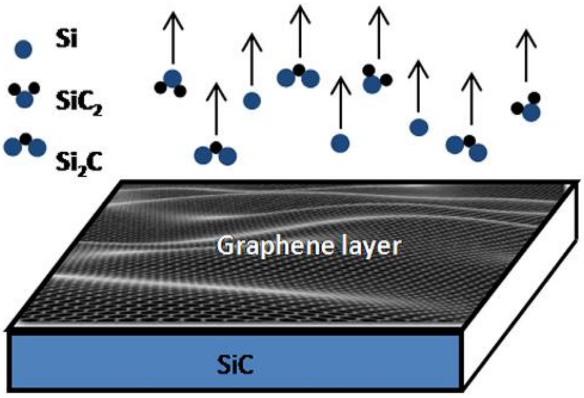

Figure 1. 9 Growth of epitaxial graphene on silicon carbide wafer via sublimation of silicon atoms[95].

Starke et al.[96] have studied the structural and electronic properties of graphene growth on both SiC (0001) and SiC $(000\overline{1})$. They showed the different surface reconstruction of SiC during the graphene synthesis on two faces. For instance, when during graphene synthesis on SiC (0001), they noticed the presence of the interfacial reconstructed carbon layer (known as buffer layer) between graphene and SiC (0001), whereas it is absent in the case of graphene growth on SiC $(000\overline{1})$. However, the uniform graphene films were always difficult to obtain under the UHV synthesis condition which was consistent with the results of theoretical calculations[97]. The prominent work concerning the improvement of the uniformity of EG happened later with the works of Virojanadara *et al.*[98] and Emtsev *et al.*[99]. They synthesized large-scale homogeneous graphene films using the sublimation of SiC (0001) using an argon (Ar) pressure. Besides, they suggested that the growth kinetics under the argon pressure close to the atmospheric one (1 atm Ar pressure) is under thermodynamic stability because of the higher growth temperature (> 1650°C) and the reduced Si sublimation rate. A higher growth temperature can enhance the mobility of C and Si atoms, leading to easier surface reconstruction. These growth dynamics have been later supported by theoretical calculations[100]. Most importantly, this method has been largely repeated by other research groups and similar results have been achieved which confirm the reproducibility and controllability of this growth process. Indeed, the accessibility of wafer-scale and high-quality films, which is also compatible with the CMOS-based electronic devices, is the major advantage of the sublimation growth of EG under Ar pressure.

d. Liquid-phase-exfoliation (LPE)

Liquid-phase exfoliation (LPE) of graphite was used for the first time in 2008 by Hernandez et al.[101] through the sonication of graphite powder in N-methylpyrrolidone (NMP). **Figure 1.10** describes schematically the liquid phase exfoliation method. Indeed, there have been several techniques of LPE reported, such as sonication assisted LPE[102,103], high-shear mixing[104], microfluidization[105], etc. Historically, LPE includes mostly two exfoliation techniques of graphite: cavitation in sonication and shear forces in a high-shear mixer. Lately, microfluidizer has been proven effective for graphite exfoliation in suitable aqueous under high shear rate. Sonication assisted LPE is an effective exfoliation method and has been widely used to prepare graphene, but suffers from high energy-extensive consumption and low efficiency[103]. Generally, the sonication power is used to induce a physical or chemical modification in certain systems through the generation of cavitation bubbles.

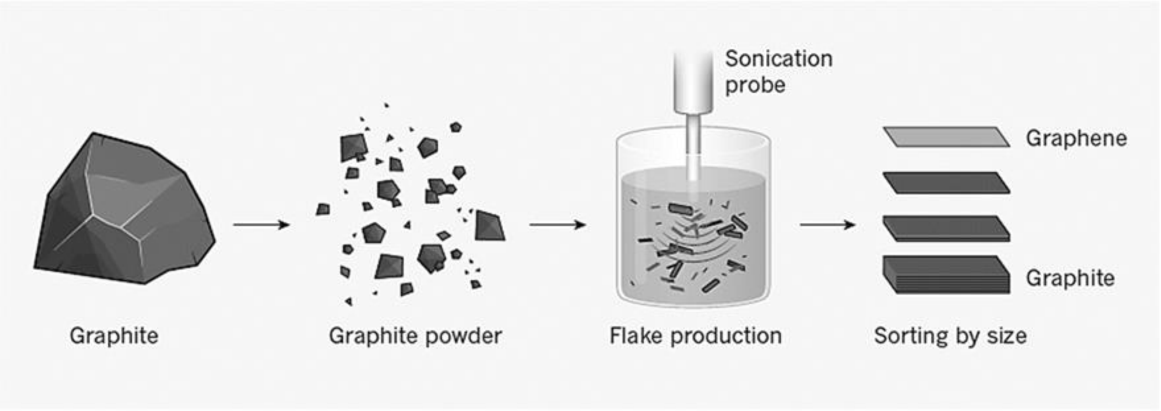

Figure 1. 10 A Liquid-phase exfoliation of graphene adapted from[106].

High-shear mixing assisted LPE has been shown that graphene can be exfoliated in the suitable liquid under shear force. Moreover, the application of high shear forces by using high-shear mixers has been examined as scalable routes of graphite exfoliation[104]. In 2014, Paton and co-workers[104] made important progress within the graphene production using shear exfoliation, which promoted the tremendous development of shear exfoliation technique. They demonstrated that the high-shear mixing of graphite in suitable solvents could lead to the high-concentrated dispersions of graphene films. Microfluidization is a high-pressure homogenization route[105]. It provides moderate exfoliation conditions, which can facilitate to decrease the formation of defects. It is a recent technique, which has been used to produce graphene-based materials such as graphene quantum dots[107,108] and graphene-based conductive inks[109].

e. Physical Vapor Deposition (PVD)

Apart from the above-mentioned most used techniques for graphene synthesis, various PVD methods have been reported such as molecular beam epitaxy (MBE)[110], pulsed laser deposition (PLD)[111], filtered cathodic vacuum arc (FCVA)[112], pulse arc plasma deposition (PAPD)[113] and magnetron sputtering[114]. One of the common points of these PVD techniques for graphene synthesis is that the carbon precursor is in solid form, compared to CVD with precursors in a gaseous state (**Figure 1.11**). However, a clear consensus about the growth mechanism of graphene on a metal surface by PVD based methods has not been established yet, in particular in the presence of a metal catalyst. Chapter 3 of this work will contribute in this way. Indeed, PVD is a mature technology for thin film deposition with specified functions by condensing vaporized atoms, molecules, or ions onto a target substrate. PVD can also provide an easy way to deposit pure carbon species onto desired substrates. Considering the compatibility with the modern silicon-based manufacturing process, PVD may play an important role in future graphene synthesis. Furthermore, for graphene synthesis, the most used PVD technique apart from PLD method are magnetron sputtering, MBE and FCVA.

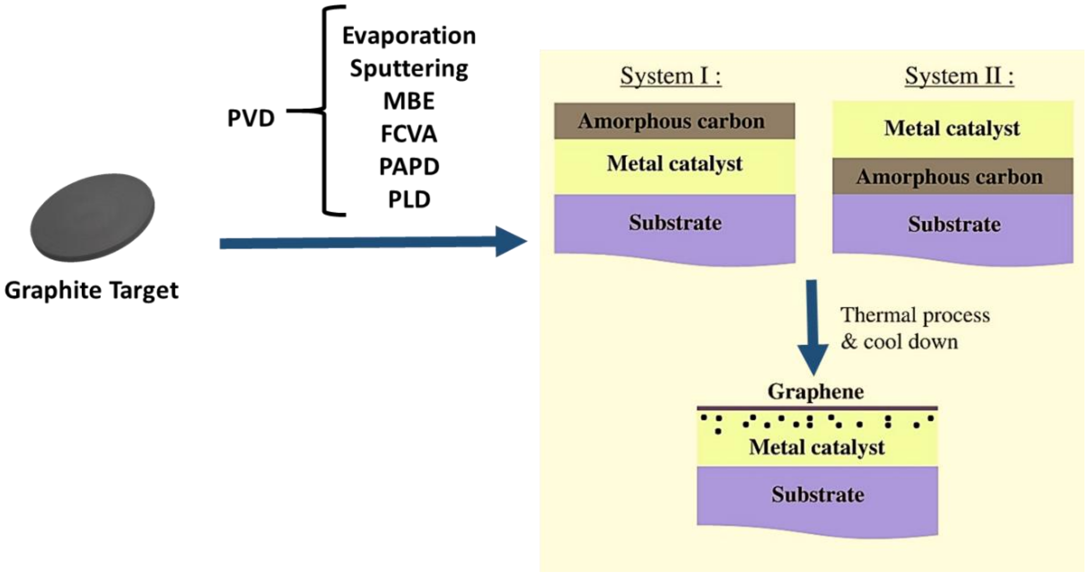

Figure 1. 11 Synthesis of graphene using various PVD methods: deposition of amorphous carbon using PVD and transformation into graphene by thermal annealing.

Among these techniques, magnetron sputtering provides a constant flow of carbon atoms in a given direction. Consequently, amorphous carbon can be deposited on various substrates in this manner. In this method, two fields are used: electrical and magnetic. The interaction between both fields causes the electrons to spiral near the target surface (graphite for carbon deposition), thereby increasing the probability that electrons will strike the argon gas (inert gas) to generate ions. The generated ions collide with the target surface under the action of an electric field to sputter the target, producing in this way the deposit on the substrate. Orofeo et al.[115] used this method to deposit amorphous carbon on SiO_2/Si substrate coated with nickel or cobalt catalyst. After thermal annealing in vacuum, they found out that large area, homogenous, single-layer graphene films were grown on the substrate. Another technique related to PVD is molecular beam epitaxy (MBE) which has been widely used for epitaxial growth of high-quality semiconductor thin films. Recently, it has also been used to deposit carbon films for graphene growth on various substrates, including metal, semiconductors, and insulators. In MBE, the growth occurs when the atoms and molecules from the starting materials are evaporated and interact chemically on a heated substrate. The UHV nature of the MBE process produces extremely high-purity thin films. For the growth of graphene using MBE, the carbon atoms are directly evaporated from the heated graphite filament and reach the substrate surfaces in the atomic form. For instance, with this MBE method, Lin et al.[116] demonstrated the synthesis of high-quality few-layer graphene on 100 μm Cu foils at low substrate temperature 300 °C. The FCVA technique has some distinct advantages over the conventional sputtering technique to prepare the a-C film coating in the terms of the relatively high energy of the depositing particle flux and the degree of ionization present[112]. FCVA is a variety of arc deposition processes used to deposit thin films for a wide range of applications. Originally, arc cathodic deposition was used to deposit low-grade hard coatings. The deposition process uses a plasma created by forming an electric arc between a carbon electrode and a graphite cathode. The beam produced is small (1 to 10 μm) and has a very high current density (from 106 to 108 $A.cm^{-2}$). This process leads to the production of unwanted particles such as macroparticles that degrade the coating performance. To address these problems, FCVA was developed to eliminate the macroparticles using a magnetic filter. Indeed, the ejected particles from the process are fed into a curved duct that has a focusing magnetic field and a steering field that separates the particles by mass, thus "filtering" them. Oldfield et al.[117] reported the use of this FCVA method for synthesis of multilayer graphene on SiO_2 substrate, at a moderate temperature of 750°C using the copper catalyst. They concluded that FCVA can produce multilayer graphene.

Besides, when depositing the amorphous carbon (a-C) using PVD, two systems can be used as shown in **Figure 1.11**: metal catalyst/a-C/substrate (the system I) and a-C/metal catalyst/substrate (the system II) stacking configuration. Both configurations lead to graphene growth after thermal heating and cooling. However, one of the main differences between the two stacking orders is that with the first configuration (metal catalyst/a-C), technically, the metal catalyst can be heated before or during the a-C deposition. This procedure can increase the metal catalyst grain size and consequently enlarge the grain size of the resulting graphene. Furthermore, it is worth noting that using PVD methods for graphene growth, the thermal heating is necessary to transform the deposited amorphous carbon (a-C) into graphene. Indeed, combining PVD methods with thermal annealing to synthesize graphene is advantageous for four main reasons. First, PVD deposition and annealing can be performed with a wide range of substrate materials (e.g., Si, SiC, and SiO_2) and transition metals or alloys[118–120]. Second, the annealing temperature range is lower than that of traditional CVD methods. Third, these methods are highly repeatable, straightforward, and controllable. Fourth, the growth process can be adjusted to synthesize single-layer to multilayer graphene. The main disadvantages of PVD-thermal annealing methods are the non-uniform thickness of graphene resulting from the preferential growth of graphene from defects and the need for vacuum, inert, or reduced environments. Since the scope of this thesis is to explore the potentialities of the PLD method for graphene and boron-doped graphene synthesis, the next section shall describe this PLD technique for graphene growth.

II. Focus on Pulsed Laser Deposition (PLD) for graphene synthesis

1. General considerations

PLD technique was first used in 1965 by Smith and Turner[121] to fabricate semiconductors and dielectric thin films using a ruby laser, which is considered as a very versatile thin-film growth process. The basic principle of PLD consists of focusing a pulsed laser beam towards a target material that is ablated, forming a plasma plume containing species ejected towards a substrate on which thin film growth. Since the laser source is located outside the deposition chamber, PLD deposition can be performed either in an ultra-high vacuum or in ambient gas[122]. In 1987, Dijkkamp et al.[123] used the PLD method for the deposition of high-temperature superconductors. Since that work, this deposition technique has been extensively used for all kinds of oxides, nitrides, carbides, and for preparing metallic systems and even polymers[122]. It has been also used to deposit all kinds of carbon-based materials, including fullerenes, carbon nanotubes, graphite, and diamond-like carbon[124–127]. Using this PLD method, the ablated species have high kinetic energy up to a few keV[128], which allows the deposition of adherent thin films at relatively low temperatures.

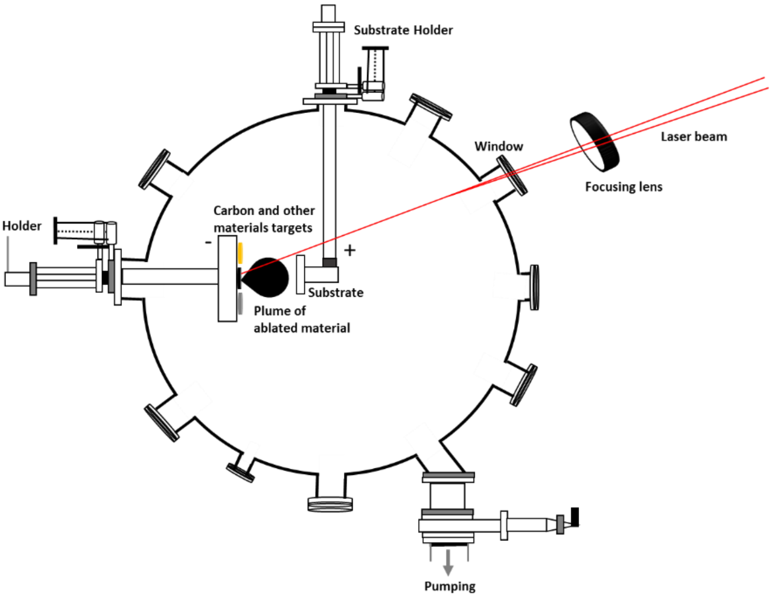

Figure 1. 12 Schematic of the illustration of the pulsed laser deposition technique.

Figure 1.12 is a scheme of the PLD working principle. Inside the vacuum chamber (ultrahigh vacuum, UHV), targets of elementary or alloy elements are struck at an angle of 45° by high energy focused pulsed laser beam (nanosecond or femtosecond). The ablated species from the target(s) are deposited directly onto the substrate. The principle behind the PLD mechanisms can be briefly described as the following. The focused laser beam is absorbed in the surface of a solid target, induces an energetic plasma plume containing ions and atoms, impinging the substrate in front of the target. Depending on various process parameters, including the characteristics of the laser used, the ambient pressure, as well as the substrate temperature, a single-crystal, a polycrystalline or amorphous film, can be obtained[129,130]. The quality of the deposited materials is often controlled by adjusting the following experimental parameters: the laser parameters (fluence, wavelength, pulse duration, and repetition rate), and the deposition conditions (target to - substrate distance, temperature, nature, and pressure of the chamber, etc.)[131,132]. With respect to CVD, the PLD method is conceptually simple, versatile, rapid, and cost-effective. It allows good control of thickness and morphology, and usable with temperature-sensitive materials, especially those with an active chemical surface. Indeed, by CVD, the control of the stoichiometry of multicomponent materials (such as doped graphene) is strongly dependent on the nature, pressure, and flow of the various gas precursor, whereas PLD, is known to achieve better control of the stoichiometry of various complex materials, as already succeeded for superconductors oxides[123,133]. Indeed, composite thin films with complex composition can be deposited by using several targets to perform co-ablation in a controlled and reproducible way. The main drawback of PLD compared to CVD is the smaller deposited areas due to the size of the plasma plume. This may be considered as a severe limitation for industrial large-scale manufacturing. However, engineering developments have shown their ability to cover large deposition areas, as made by Solmates Company from Netherlands[134]. Moreover, PLD is considered as one of the most versatile methods for thin film deposition, in particular, to explore a wide area of film compositions and nanostructures, before further transfer and developments achieved with other deposition techniques in an industrial perspective. Lastly, the energetic laser source used for PLD allows ablated species from graphite target to have high kinetic energies and to further penetrate the substrate surface, rather than remaining stacked on the film surface[132]. In comparison with other PVD methods, PLD has two main specificities. Firstly, synthesis is carried out by a pulsed mode, meaning that a small amount of matter can be ejected in a few microseconds. Secondly, due to the rapid intense heating and high non- equilibrium bond breaking of the target material, stoichiometric growth can be readily achieved using PLD[135]. In the context of graphene synthesis, PLD provides an alternative way to control the thickness and composition of the graphene precursor, using laser wavelength, power, and temperature and gas pressure. For graphene synthesis, PLD was used for the first time by Cappelli et al.[136] in 2005. The authors reported the synthesis of nanosized graphene clusters on Si <100> substrates, at temperatures ranging from room temperature (RT) to 900◦C using Nd: YAG laser operating in the near IR (λ= 532 nm, repetition rate τ = 10Hz, pulse width τ = 7 ns, fluence $\varphi \sim 7$ J/cm^2, deposition time = 15min). Since then, many other groups have used PLD to synthesize graphene. **Tables 1.2** and 1.**3** give an overview of graphene synthesis using this versatile PLD method up to now. **Table 1.2** lists the graphene synthesis work using PLD without metal catalysts and **Table 1.3** shows the graphene growth studies using PLD with metal catalysts. Some groups certainly synthesize graphene by PLD without metals catalysts to avoid the transfer process. However, there are some disparities in the results in terms of graphene formation. For example, Kumar and Khare[137] reported the growth of multi-layer and few-layer graphene on SiO_2 substrate without a metal catalyst using Nd:YAG laser ablation of a graphite target under temperatures ranging from room temperature to 300, 500, and 700◦C. By Raman spectroscopy, they found out that the intensity ratio of the 2D and G bands for growth at RT was about $I_{2D}/I_G \sim 0.33$ corresponding to the formation of multilayer graphene. In the same work, the synthesis at a high temperature of 700°C gives $I_{2D}/I_G \sim 0.47$ indicating the formation of few-layer graphene. Furthermore, Kumar et al.[138] showed that without using a nickel catalyst, there is no graphene formation, while with using nickel catalyst at 750°C, the observed graphene formation by Raman analysis with $I_{2D}/I_G \sim 0.57$. Considering these disparities, which can be due to the numerous parameters that may play a role during the PLD graphene synthesis, other groups preferred using metal catalysts to improve the quality of the graphene. Recently, we have published an extensive review paper[111] gathering most of the articles on the graphene growth using PLD, from which this chapter is largely inspired. In the following section, we shall discuss the PLD graphene synthesis using a metallic catalyst.

2. PLD graphene synthesis using a metal catalyst

Using a metallic catalyst is one of the most widely used methods of producing graphene by both CVD and PLD. That accelerates the graphene synthesis process and the resulting graphene depends on the used metal catalyst. **Figure 1.13** illustrates the PLD graphene synthesis using a metal catalyst. It is worth recalling that as in all PVD techniques; PLD for graphene growth can be performed using two stacking configurations: metal catalyst /a-C and a-C/metal catalyst. **Figure 1.13** shows only the one with the amorphous carbon on top, which is the most used configuration in this work. Besides, after graphene growth, the metal catalyst is etched with acid and then transferred onto another substrate of choice to obtain freestanding graphene. Like in CVD, common metals have been used as catalysts for the synthesis of graphene with the PLD technique. These include nickel (Ni), copper (Cu), cobalt (Co), and iron (Fe) that have lattice constants of about 0.352, 0.361, 0.251 and 0.287 nm, respectively[139] as shown in **Table 1.3**. Among them, Ni and Cu have the smallest lattice mismatches with graphene lattice (0.357 nm). Co has the highest solubility for carbon and Fe is cheaper than Ni and Co. Other metals and alloys including tin (Sn)[140] and nickel-copper (Ni-Cu) alloy[141] have been used for graphene synthesis.

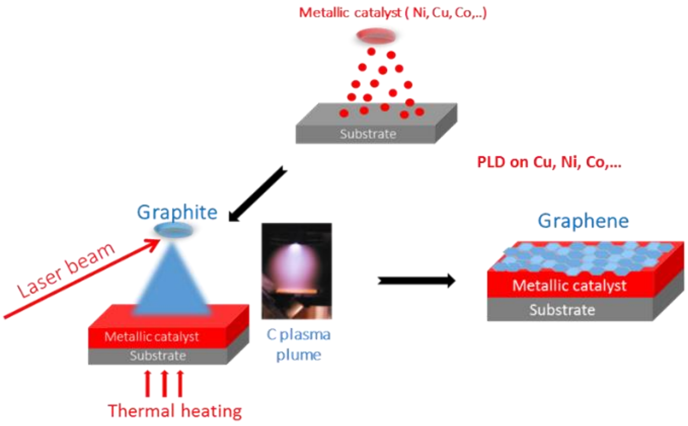

Figure 1. 13 A schematic description of the different steps for PLD graphene synthesis using a metallic catalyst thin film.

	Laser parameters	Atmosphere	Deposition conditions	Targets	Distance Target/Substrate	Graphene Types	References
Graphene/Si<100>	Nd:YAG, λ = 532 nm, τ = 7 ns, ν = 10 Hz, fluence = 7 J/cm^2	10^{-5} Pa	RT and 900 °C /15min	HOPG	5 cm	Nano sized graphene clusters	Capelli et al., Diam. Relat. Mater. 14, 959–964 (**2005**)[136]
Graphene/Si<100>	Nd:YAG, λ= 1064 nm, τ= 7 ns, ν = 10 Hz, fluences = 7.8, 11 and 14 J/cm^2	10^{-4} Pa	RT to 800 °C	Graphite	N/A	well-ordered nanographene	Capelli et al., Appl. Surf.Sci. 254, 1273–1278 (**2007**)[142]
Graphene/Si	Nd:YAG, λ= 532 nm, τ = 7 ns, ν = 1 Hz, fluences = 0.8 -20 J/cm^2	10^{-5} Torr - grown in 1 Torr argon gas	RT	HOPG	15 - 60 mm	freestanding 2D few-layer	Qian et al., Appl. Phys. Lett. 98:173108 (**2011**)[131]
Graphene/SiO$_2$/Si, **Graphene/SiNx/Si** **Graphene/p-Si**	KrF, λ= 248 nm, τ = 20 ns, ν= 10 H, fluences = 3, 5, and 6 J/cm^2	10^{-8} mbar - grown in 20 mTorr Ar/O$_2$ gas	300, 593, and 973 K	HOPG	15 - 60 mm	nanostructured graphene	Sarath Kumar and Alshareef, Appl. Phys. Lett. 102:012110 (**2013**)[143]
Graphene/SiNx/Si **NGraphene/SiNx/Si**	KrF laser, l = 248 nm, t = 20 ns, ν = 10 Hz, fluence= 6,1 J/cm^2	Gr: 20 mTorr Ar; N-Gr : 20, 100, 250 and 500 mTorr N$_2$ gas	973 K	HOPG	N/A	Graphene thin films of both p and n-types	Sarath Kumar et al., Appl. Phys. Lett. 103:192109 (**2013**)[144]
Graphene/SiO$_2$	Nd:YAG, fluence = 5 J/cm^2	10^{-6} mbar + ambient oxygen during carbon deposition	RT to 800 °C /15 min	Graphite	3 cm	Multi-few layer graphene	Kumar and Khare, Appl. Surf. Sci. 317, 1004–1009 (**2014**)[137]
Graphene/Quartz **Graphene/Sapphire** **Graphene/n-Si**	KrF, λ = 248 nm, τ = 25 ns, ν = 5 Hz, fluence = 4 J/cm^2	10^{-5} Pa - grown in 10 Pa Ar gas	750 °C/ 90s	HOPG	5 mm	few-layer graphene	Xu et al., Laser Phys. Lett. 11:096001 (**2014**)[145]
Graphene/Sapphire	Nd:YAG, λ= 266 nm, τ = 20 ns, ν = 10 Hz, fluence = 1,2 J/cm^2	10^{-5} Torr	400, 500, and 600 °C/ 90s	HOPG	40 mm	few-layer graphene	Na et al., Trans. Electr. Electron. Mater. 16, 70–73 (**2015**)[146]
Graphene/n-Si(100)	Ti:sapphire fs laser, λ = 800 nm, τ = 80 fs, ν = 1 Hz, fluences = 0.1, 0.3, and 0.5 J/cm^2	10^{-6} Torr	300 and 473 K	HOPG	50 mm	few-layer graphene	Xiangming Dong et al., Chin. Opt. Lett. 13, 021601–021604 (**2015**)[147]
N-Graphene/SiO$_2$/Si	KrF laser, λ = 248 nm, τ = 20 ns, ν = 10 Hz, laser energy = 100 mJ	Gr is grown in 10^{-5} Pa N-Gr is grown in 9, 50, 100, 240 Pa of nitrogen gas	1053K	Graphite	5 cm	N-doped graphene	Ren et al., Mater. Lett. 204, 65–68(**2017**)[148]

Table 1. 2 Summary of graphene grown on different substrates using PLD method without a metallic catalyst layer

	Laser parameters	**Atmosphere**	**Deposition Conditions**	**Targets**	**Distance Target/ Substrate**	**Metallic Catalyst**	**Annealing Conditions**	**Type of graphene**	**References**
Graphene/Si	ArF laser, λ= 193 nm, τ = 20–30 ns, ν = 10 Hz, laser energy = 300 mJ	10^{-6} Torr	1100, 1200, 1300 °C	Pyrolytic carbon	X	Ni (500 nm)	1100, 1200, 1300 °C before C deposition	Transparent Few-layer	Zhang and Feng, Carbon 48, 359–364 (**2010**)[149]
Graphene/n-Si	KrF, λ = 248 nm, τ = 25 ns, ν = 10 Hz, laser energy = 50 mJ	5.10^{-6} Torr	750 ° C - 1.5 min	Graphite	X	Ni (600 nm)	750 ° C - 1.5 min during C deposition	few-layer	Koh et al., Appl. Phys. Lett. 97:114102 (**2010**)[132]
Graphene/SiO_2/Si	KrF, λ = 248 nm, fluence (Ni)= 5.43 J/cm^2, fluence 4.40 J/cm^2, ν = 4 Hz	2.10^{-6} Torr	RT (Ni deposition), 650°C - (C deposition)	Nickel, Graphite	35 mm	Ni (25-75nm)	650 °C-1 h before C deposition	few-layer	Wang et al., AIP Adv.1:022141 (**2011**)[150]
Graphene/n-Si	KrF, λ= 248 nm, τ = 25 ns, ν= 10 Hz, laser energy = 50 mJ	5.10^{-4} Pa	750° C - 1.5 min	Carbon	X	Ni, Cu, Co, Fe	750 ° C - 1.5 min during C deposition	few-layer	Koh et al., Diam. Relat. Mater. 25, 98–102 (**2012**)[139]
Graphene/SiO_2/Si	KrF, λ= 248 nm, τ = 20 ns, ν = 10 Hz, laser energy = 75 mJ	$5\text{-}6.10^{-6}$ Torr	1010 °C	Carbon	X	Ni (300 nm)	1010°C during C deposition	Monolayer/Bilayer, Few-layer	Hemani et al., Appl. Phys. Lett. 103:134102 (**2013**)[151]
Graphene/Cu foil	CO_2 laser, λ= 10.6 µm	4.10^{-6} Torr	RT	Pyrolytic Graphite	50 mm	Cu foil	RT to 700 °C, 15 min	Sharp folded, Wrinkled graphene	Kaushik et al., Vacuum 110, 1–6. (**2014**)[152]
Graphene/n-Si	KrF laser, λ= 248 nm, τ = 20 ns, ν = 10 Hz, fluence = 15 J/cm^2	10^{-4} Pa	RT- 10 min	Graphite	3.6 cm	Ni (150 nm)	780 ° C – 45 min	Textured few-layer	Tite et al., Thin Solid Films 604, 74–80 (**2014**)[153]
Graphene/n-Si	KrF laser, λ = 248 nm, τ = 20 ns, ν = 10 Hz, fluence = 15 J/cm^2	10^{-4} Pa	RT- 150 s	Graphite	3.6 cm	Ni (150 nm)	780 ° C - 45 min, after C deposition	Few- layer	Tite et al., Appl. Phys. Lett. 104:041912 (**2016**)[154]

Graphene/n-Si	KrF, λ= 248 nm, τ = 20 ns, ν = 10 Hz, fluence = 40 J/cm^2	10^{-4} Pa	RT	Graphite	3.6 cm	Ni (300 nm)	780 ° C - 45 min, after C deposition	Self-organized multilayer	Fortgang et al., ACS Appl.Mater. Interfaces 8, 1424–1433 (**2016**)[155]
Graphene/Si(111) **Graphene/Si(100)**	Nd: YAG, λ= 355 nm, τ = 8 ns, ν = 10 Hz, fluence= 3.18 J/cm^2	10^{-5} Torr	700, 750, 800°C , 100 s	HOPG	50 mm	Ni (150-250 nm), Cu (150-250 nm)	700, 750, 800 °C - 100 s during C deposition	Few- and multilayer	Kumar et al., J. Mater. Sci. 52, 12295–12306 (**2017**)[156]
Graphene/Si(100)	Ti:sapphire, λ= 800 nm, τ = 35 ns, ν = 1 kHz, laser energy = 3.5 mJ/pulse	10^{-5} Torr	500°C	HOPG	60 mm	double Ni (100 nm)	500 °C during C deposition	Large-area few-layer	Dong et al., J. Mater. Sci. 52, 2060–2065 (**2017**)[157]
Graphene/SiO$_2$/Si	ν = 10 Hz, laser energy = 30mJ	5.10^{-5} Pa	RT	Carbon	5 cm	Sn (500nm)	250 °C, after C, Sn deposition	multilayer	Vishwakarma et al., Sci. Rep. 7:43756 (**2017**)[140]
Graphene/Cu foil	Nd: YAG, λ= 1064 nm, τ = 6 ns, ν = 5 Hz, laser energy = 50 mJ/pulse	10^{-5} Torr	300, 400, 500 °C - 2 and 30 min	Graphite	5 cm	Cu foil	300, 400, 500 °C - 2 and 30 min during C deposition	few-layer	Abd Elhamid A. E.M. et al., J. Appl. Phys. 121:025303 (**2017**)[158]
Graphene/Ni-Cu alloy	Nd:YAG, λ= 1064 nm, τ = 6 ns, ν = 10 Hz, laser energy = 150 mJ for (Ni) ν = 5 Hz, laser energy = 100 mJ for (C)	4.10^{-6} Torr	RT or 600 °C for Ni deposition, RT for C deposition	HOPG	5 cm	Ni-Cu alloy	600 °C - 30 min before C deposition	few-layer	Abd Elhamid A. E.M. et al., J. Appl. Phys. 121:025303 (**2017**)[141]
N-Graphene/SiO$_2$	femtosecond laser, λ= 800 nm, τ = 60 fs, ν = 1 kHz, fluence= 5 J/cm^2	N$_2$ pressure: 0.5, 1 and 10 Pa	RT	Graphite	36 mm	Ni (150 nm)	780 °C - 30 min after Ni deposition	Tri-layer bernal ABA	Maddi et al., Sci. Rep. 8:3247 (**2018**)[159]
Graphene/Cu(111)	KrF, λ= 248 nm, ν = 1 Hz, fluence = 4 J/cm^2	$4.5.10^{-5}$ Pa	X	HOPG	10 cm	Cu(111)	1000°C	Bilayer	Jin Wang et al., Nanomaterials, 8, 885 (**2018**)[160]
Graphene/Cu foil	Nd:YAG, λ= 1064 nm, τ = 6 ns, ν = 10 Hz, laser energy = 150 mJ, ν = 10 Hz for (Ni),	$5.3.10^{-5}$ Pa	600°C	HOPG	10 cm	Ni-Cu composite film	600 ° C - 2 min during C deposition	Few-layer	Abd Elhamid A. E.M. et al., Thin Solid Films 653 93–100(**2018**)[161]

	laser energy = 100 mJ , ν = 10 Hz for (C)								
Graphene/SiO_2/Si	KrF, λ= 248 nm, τ = 20 ns, laser energy = 230 mJ, ν = 10 Hz for (Ni), laser energy = 100 mJ , ν = 4 Hz for (C)	2.10^{-6} Torr	RT (Ni deposition), RT and under magnetic field (C deposition)	HOPG	35 mm	Ni (300 nm)	C deposition under Magnetic field B=350 mT	Few-layer	F. Larki, et al. Diam. Relat. Mater. 93, 233–240 (**2019**)[162]
Graphene/Glass	λ = 532 nm, τ = 8 ns, ν = 10 Hz, fluence = 3.18 J/cm^2	1.10^{-5} Torr	RT	HOPG	5 cm	Ni (250 nm)	750 ° C - 100 s during C deposition	Few-layer	P. Kumar, et al. Results in Physics 14, 102350 (**2019**)[138]
Graphene/Cu(111)	KrF, λ= 248 nm, ν = 1 Hz, fluence = 4.25-8.49 J/cm^2	$4.5.10^{-5}$ Pa	1000°C	HOPG	10 cm	Cu(111)	1000°C- 40 min after C deposition	Monolayer, bilayer	J. Wang, et al.Applied Surface Science 494, 651–658 (**2019**)[163]
N-Graphene/Si	femtosecond laser, λ= 800 nm, τ = 60 fs, ν = 1 kHz, fluence= 5 J/cm^2	N_2 pressure: 1.10^{-1} mbar	780°C	Graphite	36 mm	Ni (150 nm)	780 ° C -during C deposition	Textured few-layer graphene	Bourquard et al. Materials 12, 666 (**2019**)[164]
Graphene/Si **Graphene/SiO_2**	KrF, λ= 248 nm, τ = 20 ns, ν = 10 Hz, fluence = 4.5 J/cm^2	1.10^{-4} Pa	RT	Graphite	36 mm	Ni (60 nm)	600- 1000°C after C – 10 min deposition	Bilayer to multilayer	Bleu et al., Journal Raman Spectrosc. 112 (**2019**)[165], ***Work of this thesis***
Graphene/SiO_2	KrF, λ= 248 nm, τ = 20 ns, ν = 10 Hz, fluence = 5 J/cm^2	1.10^{-6} mbar	RT	Graphite	36 mm	Ni (50 nm)	800- 1000°C - 420 s after C deposition	Bilayer predominance	Y. Bleu et al. Mat. Chem. and Phy. 238, 121905 (**2019**)[166], ***Work of this thesis***
N-Graphene/SiO_2	femtosecond laser, λ= 800 nm, τ = 60 fs, ν = 1 kHz, fluence= 5 J/cm^2	N_2 pressure: 10 Pa	RT	Graphite	40 mm	Ni (150 nm)	200-500°C in 1.10^{-7} Pa after C deposition	Few-layer	Y. Bleu et al. Carbon 155, 410-420 **(2019)**[167]**,** ***Work of this thesis***

Table 1. 3 Summary of graphene grown on different substrates using the PLD method with a metallic catalyst layer

PLD graphene was first produced using a metal catalytic layer in 2010 by Zhang and Feng[149] using deposition temperatures ranging from 1000 to 1300°C and 500 nm of nickel thin film. Since that time, many studies have been reported for PLD graphene synthesis using nickel thin film catalyst. **Table 1.3** shows an overview of various works on graphene synthesis using the PLD technique with a metal catalytic layer. Nickel is the most widely used catalyst for graphene synthesis using the PLD method. Nickel thin film has high carbon solubility, low cost, and ease of fabrication in electronic devices. However, its high carbon solubility makes it difficult to control the number of graphene layers. Thus, in most cases, instead of single-layer graphene, either a few-layer/multilayer graphene or a mixture of single-layer, bilayer, and few-layer/multi-layer graphene are formed[139,150,151]. It appears that using polycrystalline nickel leads to a higher percentage of few-layer graphene due to the presence of grain boundaries. According to the studies summarized in **Table 1.3**, the quality of the synthesized graphene can depend on the thickness of the nickel catalytic layer, the thickness of the carbon layer, the deposition temperature and duration, the annealing time and temperature, and the cooling rate. All these parameters, in addition to those of the PLD technique, e.g., fluence, laser wavelength, and the repetition rate, influence the quality of the resulting graphene. Moreover, due to the high solubility of carbon in nickel, it remains challenging to control the number of layers of the obtained graphene using polycrystalline nickel as a catalyst.

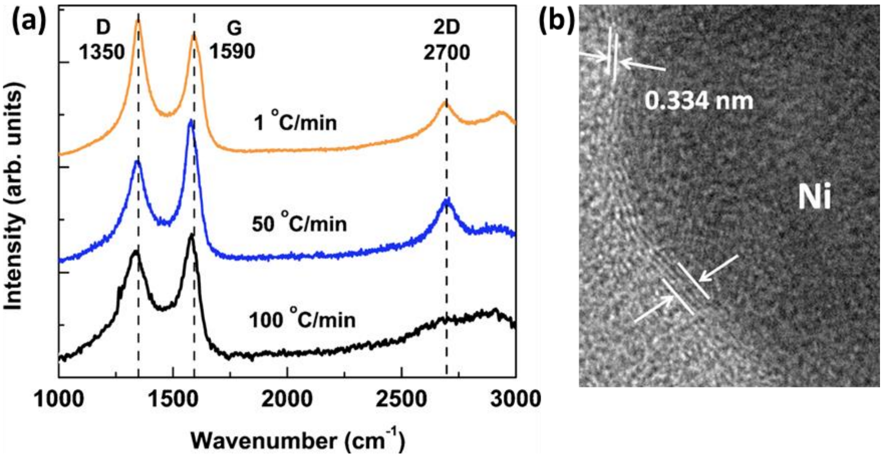

Figure 1. 14 (a) Raman spectra of samples cooled at different rates (b) Cross-section TEM showing at the graphene layers above Ni adapted from ref[132].

Apart from nickel, other metals catalysts have been used for graphene synthesis with the PLD method. The graphene growth using copper (Cu), cobalt (Co), tin (Sn), iron (Fe), and Cu-Ni alloys as catalysts have also been reported. Koh et al.[132,139] reported the comparison of PLD graphene synthesis with Ni, Co, Cu, and Fe metal catalysts and the cooling effect on the graphene synthesis. Indeed, they obtained few-layer graphene formation on nickel under controlled cooling conditions such as initial cooling rate of 1°C/min to 550°C, followed by a faster cooling rate of 20°C/min to room temperature as shown in **Figure 1.14**. Whereas using the same conditions, graphene was formed only with the nickel catalyst and not observed on the other metal catalysts. In addition, when increasing the cooling rate, graphene was formed on Co and was much more homogeneous than on Ni. They, therefore, concluded that the cooling rate is an important parameter that can affect graphene growth. Using CO_2 laser ablation of pyrolytic graphite target placed in a vacuum chamber at a pressure of 10^{-6} Torr, Kaushik et al.[152] observed graphene ribbons synthesis. Nanostructures of graphene on Cu foil were observed at a low temperature of about 400°C. On the same Cu foil substrate, it was demonstrated by Abd Elhamid and co-workers[158] the possibility of growing graphene using the PLD technique at the relatively low temperature of 500°C and an optimal cooling rate. Recently, Wang et al.[163] demonstrated the formation of the bilayer and single-layer graphene on a single crystal of copper Cu (111) at high-temperature growth of 1000°C. It is worth mentioning that, with Cu, no study has been reported using copper film as the catalyst, rather copper foil or copper single crystal are used directly as the substrate and catalyst at the same time. Vishwakarma et al.[140] reported an attempt to grow by PLD multilayer graphene at a low temperature (250°C) using another metal catalyst, namely tin (Sn). Another attempt was made by Elhamid et al.[141] on metal Ni-Cu composite substrates. They reported that graphene synthesis could be achieved through graphite ablation using the PLD technique on catalyst Ni-Cu composite substrates at low temperatures. The intensity ratio of the 2D and G Raman bands was 0.66, indicating the formation of trilayer graphene. This close look at the literature, confirms that few studies have been done on graphene synthesis with catalytic metals other than nickel using the PLD technique.

3. Doped graphene synthesis using the PLD method

As discussed above, graphene is one of the most attractive carbon nanostructures exhibiting remarkable properties. Many of them are promising in the context of technological applications, but it is often necessary to be able to modify and control them according to the specific needs of each application. For instance, from the electronic point of view, based on the band structure, the conduction and valence bands in pristine graphene touch at one single point, i.e. Dirac point (**Figure 1.15a**).

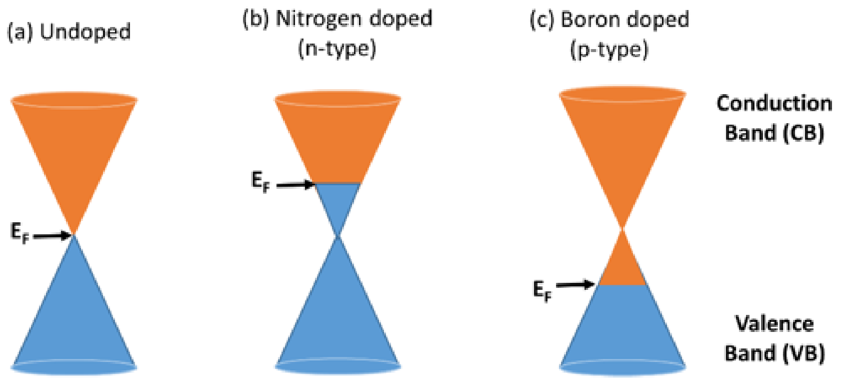

Figure 1. 15 Energy dispersion of graphene around the Dirac point, indicating a change in the Fermi level. Blue indicates levels filled with electrons while orange indicates empty levels. (a) Undoped graphene. (b) Nitrogen-doped graphene (n-type). (c) Boron-doped graphene (p-type).

The Fermi level lays at Dirac point with a fully occupied valence band and empty conduction band, which means that there are no states to occupy and hence no carriers. Consequently, no free carriers could contribute to electrical transport. However, by introducing heteroatoms, known as doping, one can shift the Fermi level up to conduction band or down to valence band, changing the electrical property of the material. Therefore, the possibility of adjusting the graphene chemistry by doping emerged as a powerful tool to endow this material with useful new properties or to modify on demand its intrinsic capabilities[168]. Indeed, doped graphene presents quite appealing properties such as superconductivity, ferromagnetism, and enhanced chemical and electrochemical activity, which promote a widespread application of graphene-based materials in different technologies. Various types of dopants have been introduced in graphene such as N, B, P, or S. However, boron and nitrogen have attracted much more attention because their atomic radii are close to that of carbon. The incorporation of nitrogen in graphene has been widely exploited for inducing n-type conductivity, representing, therefore, an important element for the development of microelectronic devices. In fact, in nitrogen-doped graphene, as shown in **Figure 1.15b**, the doping will induce carriers in the system, moving the Fermi level away from Dirac point and lies within the conduction band, leading to n-type conductivity. In addition, it has been demonstrated that its incorporation in the graphene lattice can efficiently boost the catalytic performances in several electrochemical processes, and especially for the oxygen reduction reaction (ORR)[169]. Boron doping, shown schematically in **Figure 1.15c**, moves the Fermi level away from Dirac point and lies within valance band inducing p-type conductivity in graphene. Besides, the incorporation of boron can trigger a quite appealing chemical and electrochemical activity in the graphene basal plane. Moreover, compared to the nitrogen doping, the in-plane incorporation of boron in graphene is easier.

Furthermore, due to the longer and strong BC bonding, the lattice stress in the boron-doped graphene structure is reduced and the mechanical properties are preserved while changing the thermal conductivity[170].

In the literature, several studies have been reported on boron and nitrogen-doped graphene using CVD and other methods. In 2013, Kumar and co-workers[144] demonstrated for the first time the synthesis of doped graphene by using the PLD method. They showed that using argon gas during the carbon ablation, it is possible to obtain p-doped graphene, whereas using nitrogen gas, and they obtained n-doped graphene. Following this work, Ren et al.[148] synthesized nitrogen-doped graphene (NG) *in situ* using ultraviolet-pulsed laser deposition in the presence of nitrogen on Si/SiO_2 substrates without the need for a metal catalytic layer. Different nitrogen-doped graphene was grown with various nitrogen concentrations, up to 3.3 at%. They also claimed that the nitrogen-doped graphene chemically enhanced the Raman signal with respect to the pristine graphene. Recently, work from our group[159] reported the synthesis of trilayer nitrogen-doped graphene with ABA (Bernal) configuration with the pyrrolic nitrogen predominance using the PLD method using femtosecond laser ablation of graphite under nitrogen atmosphere. The amount of nitrogen in graphene was within 2-3 at.%, with the proof that this amount could be controlled by monitoring the nitrogen pressure. In short, few studies have been done on the synthesis of substitutional-doped graphene using the PLD method. For nitrogen-doped graphene, only four papers[144,148,159,164] have been reported, and for boron-doped graphene, no work has yet been published using the PLD method. However, using PLD for nitrogen and boron-doped graphene synthesis can pave an alternative route for this material. Therefore, more studies on doped graphene synthesis using the PLD method are needed. The scope of this thesis is to study in deep the synthesis and characterization of graphene and boron-doped graphene using the PLD method as detailed in the following final section.

III. Conclusions

In this chapter, we have discussed the fascinating properties of graphene due to its honeycomb lattice structure and unique cone-like band structure. We have also presented on one hand the most commonly used elaboration techniques of graphene films, i.e. mechanical exfoliation, Chemical Vapor Deposition (CVD), thermal decomposition of SiC, liquid-phase exfoliation (LPE). On the other hand, the less used Physical Vapor Deposition (PVD) method was reported. Among various PVD techniques, PLD has been discussed as an alternative route for making graphene and doped graphene. The PLD method can be used for graphene growth without a metallic catalyst, but there are some disparities in the reported results. Some groups report the formation of few-layer graphene, while other groups reported that without a catalytic layer, there is no graphene formation. Therefore, the PLD using a metal catalyst has been mostly used for graphene growth. Based on the results reported here, PLD graphene of different quality, from high to low, from single to multilayer can be produced, depending on the specific growth conditions, including the substrate temperature, the energy density of the laser, the background pressure, annealing rate and time invested. Moreover, PLD graphene can be synthesized at relatively low temperatures. However, it is sometimes a mixture of single, bilayer, trilayer, few-layer, and multi-layer graphene with a small area. The growth conditions consequently need to be optimized to produce high quality with continuous and large-area graphene. Until now, Ni metal has been the most used catalyst for graphene synthesis by the PLD technique. Only, few studies have been reported for the other metal catalysts. Furthermore, doped graphene can be produced using PLD. Nevertheless, up to now, only four studies have reported on nitrogen-doped graphene (n doping) and none on boron-doped graphene (p doping) using PLD.

In the past, PLD has proven to be a powerful tool for thin film deposition. Today, it is believed that PLD will play an important role in making graphene and doped graphene materials for various applications in the future. Therefore, the main objectives of this research work are the following:

- To explore the capabilities of the PLD technique of making graphene (G) and boron-doped graphene (BG).
- To understand the mechanism of the graphene growth using PLD versus the process parameters.
- To characterize the synthesized G and BG thin films through the combination of Raman, XPS, SEM, AFM, and HRTEM.
- To explore some properties of the graphene and boron-doped graphene films such as optical and electrochemistry properties.

References

1. Wallace, P. R. The Band Theory of Graphite. *Phys. Rev.* **71**, 622–634 (1947).
2. Fradkin, E. Critical behavior of disordered degenerate semiconductors. II. Spectrum and transport properties in mean-field theory. *Phys. Rev. B* **33**, 3263–3268 (1986).
3. Land, T. A., Michely, T., Behm, R. J., Hemminger, J. C. & Comsa, G. STM investigation of single layer graphite structures produced on Pt(111) by hydrocarbon decomposition. *Surface Science* **264**, 261–270 (1992).
4. Ohashi, Y., Koizumi, T., Yoshikawa, T., Hironaka, T. & Shiiki, K. Size Effect inthe In-plane Electrical Resistivity of Very Thin Graphite Crystals. *TANSO* **1997**, 235–238 (1997).
5. Novoselov, K. S. *et al.* Electric Field Effect in Atomically Thin Carbon Films. *Science* **306**, 666–669 (2004).
6. Geim, A. K. Graphene prehistory. *Phys. Scr.* **2012**, 014003 (2012).
7. Geim, A. K. & Novoselov, K. S. The rise of graphene. *Nat Mater* **6**, 183–191 (2007).
8. Bianco, A. *et al.* All in the graphene family – A recommended nomenclature for two-dimensional carbon materials. *Carbon* **65**, 1–6 (2013).
9. ISO/TS 80004-13:2017(en), Nanotechnologies — Vocabulary — Part 13: Graphene and related two-dimensional (2D) materials. https://www.iso.org/obp/ui/#iso:std:iso:ts:80004:-13:ed-1:v1:en.
10. Castro Neto, A. H., Guinea, F., Peres, N. M. R., Novoselov, K. S. & Geim, A. K. The electronic properties of graphene. *Rev. Mod. Phys.* **81**, 109–162 (2009).
11. Ando, T. The electronic properties of graphene and carbon nanotubes. *NPG Asia Materials* **1**, 17–21 (2009).
12. Partoens, B. & Peeters, F. M. From graphene to graphite: Electronic structure around the K point. *Phys. Rev. B* **74**, 075404 (2006).
13. Mak, K. F., Shan, J. & Heinz, T. F. Electronic Structure of Few-Layer Graphene: Experimental Demonstration of Strong Dependence on Stacking Sequence. *Phys. Rev. Lett.* **104**, 176404 (2010).
14. Malard, L. M., Pimenta, M. A., Dresselhaus, G. & Dresselhaus, M. S. Raman spectroscopy in graphene. *Physics Reports* **473**, 51–87 (2009).
15. Jia, X., Campos-Delgado, J., Terrones, M., Meunier, V. & S. Dresselhaus, M. Graphene edges: a review of their fabrication and characterization. *Nanoscale* **3**, 86–95 (2011).
16. Acik, M. & Chabal, Y. J. Erratum: “Nature of Graphene Edges: A Review”. *Jpn. J. Appl. Phys.* **51**, 039201 (2012).

17. Edwards, R. S. & Coleman, K. S. Graphene Film Growth on Polycrystalline Metals. *Accounts of Chemical Research* **46**, 23–30 (2013).
18. Bunch, J. S. *et al.* Impermeable Atomic Membranes from Graphene Sheets. *Nano Lett.* **8**, 2458–2462 (2008).
19. Ju, L. *et al.* Photoinduced doping in heterostructures of graphene and boron nitride. *Nature Nanotechnology* **9**, 348–352 (2014).
20. Nair, R. R. *et al.* Fine Structure Constant Defines Visual Transparency of Graphene. *Science* **320**, 1308–1308 (2008).
21. Bolotin, K. I. *et al.* Ultrahigh electron mobility in suspended graphene. *Solid State Communications* **146**, 351–355 (2008).
22. Balandin, A. A. *et al.* Superior Thermal Conductivity of Single-Layer Graphene. *Nano Lett.* **8**, 902–907 (2008).
23. Züttel, A., Sudan, P., Mauron, P. & Wenger, P. Model for the hydrogen adsorption on carbon nanostructures. *Appl. Phys. A* **78**, 941–946 (2004).
24. Lee, C., Wei, X., Kysar, J. W. & Hone, J. Measurement of the Elastic Properties and Intrinsic Strength of Monolayer Graphene. *Science* **321**, 385–388 (2008).
25. Du, X., Skachko, I., Barker, A. & Andrei, E. Y. Approaching ballistic transport in suspended graphene. *Nature Nanotechnology* **3**, 491–495 (2008).
26. Mak, K. F. *et al.* Measurement of the Optical Conductivity of Graphene. *Phys. Rev. Lett.* **101**, 196405 (2008).
27. Zhu, Y. *et al.* Graphene and Graphene Oxide: Synthesis, Properties, and Applications. *Advanced Materials* **22**, 3906–3924 (2010).
28. Perreault, F., Faria, A. F. de & Elimelech, M. Environmental applications of graphene-based nanomaterials. *Chem. Soc. Rev.* **44**, 5861–5896 (2015).
29. Casaluci, S., Gemmi, M., Pellegrini, V., Di Carlo, A. & Bonaccorso, F. Graphene-based large area dye-sensitized solar cell modules. *Nanoscale* **8**, 5368–5378 (2016).
30. Ji, L., Meduri, P., Agubra, V., Xiao, X. & Alcoutlabi, M. Graphene-Based Nanocomposites for Energy Storage. *Advanced Energy Materials* **6**, 1502159 (2016).
31. Mueller, T., Xia, F. & Avouris, P. Graphene photodetectors for high-speed optical communications. *Nature Photon* **4**, 297–301 (2010).
32. Zhu, S.-E., Yuan, S. & Janssen, G. C. A. M. Optical transmittance of multilayer graphene. *EPL* **108**, 17007 (2014).

33. AlZahrani, A. Z. & Srivastava, G. P. Gradual changes in electronic properties from graphene to graphite: first-principles calculations. *J. Phys.: Condens. Matter* **21**, 495503 (2009).
34. Klintenberg, M. *et al.* Evolving properties of two-dimensional materials: from graphene to graphite. *J. Phys.: Condens. Matter* **21**, 335502 (2009).
35. Zhang, Y. & Pan, C. Measurements of mechanical properties and number of layers of graphene from nano-indentation. *Diamond and Related Materials* **24**, 1–5 (2012).
36. Meric, I., Baklitskaya, N., Kim, P. & Shepard, K. L. RF performance of top-gated, zero-bandgap graphene field-effect transistors. in *2008 IEEE International Electron Devices Meeting* 1–4 (2008). doi:10.1109/IEDM.2008.4796738.
37. Wu, Y. *et al.* High-frequency, scaled graphene transistors on diamond-like carbon. *Nature* **472**, 74–78 (2011).
38. Wang, Z. *et al.* Free radical sensors based on inner-cutting graphene field-effect transistors. *Nat Commun* **10**, 1–10 (2019).
39. Fiori, G. & Iannaccone, G. Simulation of Graphene Nanoribbon Field-Effect Transistors. *IEEE Electron Device Lett.* **28**, 760–762 (2007).
40. Hwang, W. S. *et al.* Room-Temperature Graphene-Nanoribbon Tunneling Field-Effect Transistors. *npj 2D Mater Appl* **3**, 1–7 (2019).
41. Hammam, A. M. M., Schmidt, M. E., Muruganathan, M., Suzuki, S. & Mizuta, H. Sub-10 nm graphene nano-ribbon tunnel field-effect transistor. *Carbon* **126**, 588–593 (2018).
42. Mahmoudi, T., Wang, Y. & Hahn, Y.-B. Graphene and its derivatives for solar cells application. *Nano Energy* **47**, 51–65 (2018).
43. Zhang, W. *et al.* Graphene:silver nanowire composite transparent electrode based flexible organic solar cells with 13.4% efficiency. *J. Mater. Chem. A* **7**, 22021–22028 (2019).
44. Guo, C. X. *et al.* Layered graphene/quantum dots for photovoltaic devices. *Angew. Chem. Int. Ed. Engl.* **49**, 3014–3017 (2010).
45. Yin, Z. *et al.* Real-time DNA detection using Pt nanoparticle-decorated reduced graphene oxide field-effect transistors. *Nanoscale* **4**, 293–297 (2012).
46. Hu, X. & Wang, J. Design of graphene-based polarization-insensitive optical modulator. *Nanophotonics* **7**, 651–658 (2018).
47. Mu, H. *et al.* Graphene and Mo2C vertical heterostructure for femtosecond mode-locked lasers [Invited]. *Opt. Mater. Express, OME* **9**, 3268–3276 (2019).

48. Murali, K., Abraham, N., Das, S., Kallatt, S. & Majumdar, K. Highly Sensitive, Fast Graphene Photodetector with Responsivity >10 ^{6} A/W Using a Floating Quantum Well Gate. *ACS Appl. Mater. Interfaces* **11**, 30010–30018 (2019).
49. Das, S., Pandey, D., Thomas, J. & Roy, T. The Role of Graphene and Other 2D Materials in Solar Photovoltaics. *Advanced Materials* **31**, 1802722 (2019).
50. Song, L., Yu, X. & Yang, D. A review on graphene-silicon Schottky junction interface. *Journal of Alloys and Compounds* **806**, 63–70 (2019).
51. Kalita, G., Kayastha, M. S., Uchida, H., Wakita, K. & Umeno, M. Direct growth of nanographene films by surface wave plasma chemical vapor deposition and their application in photovoltaic devices. *RSC Adv.* **2**, 3225–3230 (2012).
52. Yin, J., Zhang, Z., Li, X., Zhou, J. & Guo, W. Harvesting Energy from Water Flow over Graphene? *Nano Lett.* **12**, 1736–1741 (2012).
53. Yang, Z. *et al.* Harvesting Low-Grade Heat via Thermal-Induced Electric Double Layer Redistribution of Nanoporous Graphene Films. *Langmuir* **35**, 7713–7719 (2019).
54. Kang, T. J. *et al.* Electrical Power From Nanotube and Graphene Electrochemical Thermal Energy Harvesters. *Advanced Functional Materials* **22**, 477–489 (2012).
55. Liu, C., Yu, Z., Neff, D., Zhamu, A. & Jang, B. Z. Graphene-based supercapacitor with an ultrahigh energy density. *Nano Lett.* **10**, 4863–4868 (2010).
56. Yang, Z. *et al.* Carbon nanotube- and graphene-based nanomaterials and applications in high-voltage supercapacitor: A review. *Carbon* **141**, 467–480 (2019).
57. Huang, L., Santiago, D., Loyselle, P. & Dai, L. Graphene-Based Nanomaterials for Flexible and Wearable Supercapacitors. *Small* **14**, 1800879 (2018).
58. Wu, Z.-S., Ren, W., Xu, L., Li, F. & Cheng, H.-M. Doped graphene sheets as anode materials with superhigh rate and large capacity for lithium ion batteries. *ACS Nano* **5**, 5463–5471 (2011).
59. Li, C. *et al.* Recent progress of graphene-based materials in lithium-ion capacitors. *J. Phys. D: Appl. Phys.* **52**, 143001 (2019).
60. Cho, S., Jung, I., Jang, H.-J., Liu, L. & Park, S. Bimetallic junction mediated synthesis of multilayer graphene edges towards ultrahigh capacity for lithium ion batteries. *Nanoscale* **10**, 5214–5220 (2018).
61. Tozzini, V. & Pellegrini, V. Reversible Hydrogen Storage by Controlled Buckling of Graphene Layers. *J. Phys. Chem. C* **115**, 25523–25528 (2011).

62. Gangu, K. K., Maddila, S., Mukkamala, S. B. & Jonnalagadda, S. B. Characteristics of MOF, MWCNT and graphene containing materials for hydrogen storage: A review. *Journal of Energy Chemistry* **30**, 132–144 (2019).
63. Byun, K.-E. *et al.* Graphene-polymer hybrid nanostructure-based bioenergy storage device for real-time control of biological motor activity. *ACS Nano* **5**, 8656–8664 (2011).
64. Ding, R. *et al.* A brief review of corrosion protective films and coatings based on graphene and graphene oxide. *Journal of Alloys and Compounds* **764**, 1039–1055 (2018).
65. Cui, G. *et al.* A comprehensive review on graphene-based anti-corrosive coatings. *Chemical Engineering Journal* **373**, 104–121 (2019).
66. Fowler, J. D. *et al.* Practical Chemical Sensors from Chemically Derived Graphene. *ACS Nano* **3**, 301–306 (2009).
67. Raval, B. & Banerjee, I. Functionalized Graphene Nanocomposite in Gas Sensing. in *Functionalized Graphene Nanocomposites and their Derivatives* 295–322 (Elsevier, 2019). doi:10.1016/B978-0-12-814548-7.00015-5.
68. Fan, X. *et al.* Humidity and CO2 gas sensing properties of double-layer graphene. *Carbon* **127**, 576–587 (2018).
69. Wu, W. *et al.* Wafer-scale synthesis of graphene by chemical vapor deposition and its application in hydrogen sensing. *Sensors and Actuators B: Chemical* **150**, 296–300 (2010).
70. Yavari, F., Castillo, E., Gullapalli, H., Ajayan, P. M. & Koratkar, N. High sensitivity detection of NO2 and NH3 in air using chemical vapor deposition grown graphene. *Appl. Phys. Lett.* **100**, 203120 (2012).
71. Zhang, B. *et al.* A New Electrochemical Biosensor for Determination of Hydrogen Peroxide in Food Based on Well-Dispersive Gold Nanoparticles on Graphene Oxide. *Electroanalysis* **23**, 1821–1829 (2011).
72. Ren, Y. *et al.* Detection of sulfur dioxide gas with graphene field effect transistor. *Appl. Phys. Lett.* **100**, 163114 (2012).
73. Chen, C. W. *et al.* Oxygen sensors made by monolayer graphene under room temperature. *Appl. Phys. Lett.* **99**, 243502 (2011).
74. Taniselass, S., Arshad, M. K. M. & Gopinath, S. C. B. Graphene-based electrochemical biosensors for monitoring noncommunicable disease biomarkers. *Biosensors and Bioelectronics* **130**, 276–292 (2019).
75. Nag, A., Mitra, A. & Mukhopadhyay, S. C. Graphene and its sensor-based applications: A review. *Sensors and Actuators A: Physical* **270**, 177–194 (2018).

76. Yue, Z. *et al.* Towards ultra-wide operation range and high sensitivity: Graphene film based pressure sensors for fingertips. *Biosensors and Bioelectronics* **139**, 111296 (2019).
77. Yang, T., Zhao, X., He, Y. & Zhu, H. Graphene-Based Sensors. in *Graphene* 157–174 (Elsevier, 2018). doi:10.1016/B978-0-12-812651-6.00006-9.
78. Szunerits, S. & Boukherroub, R. Graphene-based biosensors. *Interface Focus* **8**, 20160132 (2018).
79. Yao, Y. & Ping, J. Recent advances in graphene-based freestanding paper-like materials for sensing applications. *TrAC Trends in Analytical Chemistry* **105**, 75–88 (2018).
80. Zhang, C., Zhang, Z., Yang, Q. & Chen, W. Graphene-based Electrochemical Glucose Sensors: Fabrication and Sensing Properties. *Electroanalysis* **30**, 2504–2524 (2018).
81. Wasfi, A., Awwad, F. & Ayesh, A. I. Graphene-based nanopore approaches for DNA sequencing: A literature review. *Biosensors and Bioelectronics* **119**, 191–203 (2018).
82. Novoselov, K. S. *et al.* Two-dimensional atomic crystals. *PNAS* **102**, 10451–10453 (2005).
83. Bonaccorso, F. *et al.* Production and processing of graphene and 2d crystals. *Materials Today* **15**, 564–589 (2012).
84. Yang, G., Li, L., Lee, W. B. & Ng, M. C. Structure of graphene and its disorders: a review. *Science and Technology of Advanced Materials* **19**, 613–648 (2018).
85. Yi, M. & Shen, Z. A review on mechanical exfoliation for the scalable production of graphene. *J. Mater. Chem. A* **3**, 11700–11715 (2015).
86. Geim, A. K. Graphene: Status and Prospects. *Science* **324**, 1530–1534 (2009).
87. Novoselov, K. S. & Neto, A. H. C. Two-dimensional crystals-based heterostructures: materials with tailored properties. *Phys. Scr.* **T146**, 014006 (2012).
88. Li, X. *et al.* Large-Area Synthesis of High-Quality and Uniform Graphene Films on Copper Foils. *Science* **324**, 1312–1314 (2009).
89. Reina, A. *et al.* Layer Area, Few-Layer Graphene Films on Arbitrary Substrates by Chemical Vapor Deposition. *Nano Lett.* **9**, 3087–3087 (2009).
90. Sutter, P. W., Flege, J.-I. & Sutter, E. A. Epitaxial graphene on ruthenium. *Nature Mater* **7**, 406–411 (2008).
91. N'Diaye, A. T. *et al.* Growth of graphene on Ir(111). *New J. Phys.* **11**, 023006 (2009).
92. Ago, H. CVD Growth of High-Quality Single-Layer Graphene. in *Frontiers of Graphene and Carbon Nanotubes: Devices and Applications* (ed. Matsumoto, K.) 3–20 (Springer Japan, 2015). doi:10.1007/978-4-431-55372-4_1.
93. Van Bommel, A. J., Crombeen, J. E. & Van Tooren, A. LEED and Auger electron observations of the SiC(0001) surface. *Surface Science* **48**, 463–472 (1975).

94. Berger, C. *et al.* Ultrathin Epitaxial Graphite: 2D Electron Gas Properties and a Route toward Graphene-based Nanoelectronics. *J. Phys. Chem. B* **108**, 19912–19916 (2004).

95. Mishra, N., Boeckl, J., Motta, N. & Iacopi, F. Graphene growth on silicon carbide: A review (Phys. Status Solidi A 9⁄2016). *physica status solidi (a)* **213**, 2269–2269 (2016).

96. Starke, U. & Riedl, C. Epitaxial graphene on SiC(0001) and and SiC(000¯1): from surface reconstructions to carbon electronics. *J. Phys.: Condens. Matter* **21**, 134016 (2009).

97. Kageshima, H., Hibino, H., Yamaguchi, H. & Nagase, M. Stability and reactivity of steps in the initial stage of graphene growth on the SiC(0001) surface. *Phys. Rev. B* **88**, 235405 (2013).

98. Virojanadara, C. *et al.* Homogeneous large-area graphene layer growth on 6H-SiC(0001). *Phys. Rev. B* **78**, 245403 (2008).

99. Emtsev, K. V. *et al.* Towards wafer-size graphene layers by atmospheric pressure graphitization of silicon carbide. *Nature Mater* **8**, 203–207 (2009).

100. Sun, G. F. *et al.* Si diffusion path for pit-free graphene growth on SiC(0001). *Phys. Rev. B* **84**, 195455 (2011).

101. Hernandez, Y. *et al.* High-yield production of graphene by liquid-phase exfoliation of graphite. *Nature Nanotech* **3**, 563–568 (2008).

102. Shen, Z., Li, J., Yi, M., Zhang, X. & Ma, S. Preparation of graphene by jet cavitation. *Nanotechnology* **22**, 365306 (2011).

103. Phiri, J., Gane, P. & Maloney, T. C. High-concentration shear-exfoliated colloidal dispersion of surfactant–polymer-stabilized few-layer graphene sheets. *J Mater Sci* **52**, 8321–8337 (2017).

104. Paton, K. R. *et al.* Scalable production of large quantities of defect-free few-layer graphene by shear exfoliation in liquids. *Nature Materials* **13**, 624–630 (2014).

105. Wang, Y.-Z., Chen, T., Gao, X.-F., Liu, H.-H. & Zhang, X.-X. Liquid phase exfoliation of graphite into few-layer graphene by sonication and microfluidization. *mat express* **7**, 491–499 (2017).

106. Kauling, A. P. *et al.* The Worldwide Graphene Flake Production. *Advanced Materials* **30**, 1803784 (2018).

107. Qian, J. *et al.* Graphene quantum dots-assisted exfoliation of graphitic carbon nitride to prepare metal-free zero-dimensional/two-dimensional composite photocatalysts. *J Mater Sci* **53**, 12103–12114 (2018).

108. Buzaglo, M., Shtein, M. & Regev, O. Graphene Quantum Dots Produced by Microfluidization. *Chem. Mater.* **28**, 21–24 (2016).

109. Karagiannidis, P. G. *et al.* Microfluidization of Graphite and Formulation of Graphene-Based Conductive Inks. *ACS Nano* **11**, 2742–2755 (2017).

110. Lopes, J. M. J. & Vignaud, D. Molecular Beam Epitaxy of Graphene and Hexagonal Boron Nitride. in *Molecular Beam Epitaxy* 487–513 (Elsevier, 2018). doi:10.1016/B978-0-12-812136-8.00023-2.

111. Bleu, Y. *et al.* Review of Graphene Growth From a Solid Carbon Source by Pulsed Laser Deposition (PLD). *Front Chem* **6**, (2018).

112. Seo, J. H. *et al.* Few layer graphene synthesized by filtered vacuum arc system using solid carbon source. *Current Applied Physics* **12**, S131–S133 (2012).

113. Miyoshi, M., Arima, Y., Kubo, T. & Egawa, T. Self-forming graphene/Ni patterns on sapphire utilizing the pattern-controlled catalyst metal agglomeration technique. *Applied Physics Letters* **110**, 013103 (2017).

114. An, S. *et al.* A facile method for the synthesis of transfer-free graphene from co-deposited nickel–carbon layers. *Carbon* **109**, 154–162 (2016).

115. Orofeo, C. M., Ago, H., Hu, B. & Tsuji, M. Synthesis of large area, homogeneous, single layer graphene films by annealing amorphous carbon on Co and Ni. *Nano Research* **4**, 531–540 (2011).

116. Lin, M.-Y. *et al.* Low-temperature grown graphene films by using molecular beam epitaxy. *Appl. Phys. Lett.* **101**, 221911 (2012).

117. Oldfield, D. T., McCulloch, D. G., Huynh, C. P., Sears, K. & Hawkins, S. C. Multilayered graphene films prepared at moderate temperatures using energetic physical vapour deposition. *Carbon* **94**, 378–385 (2015).

118. Wintterlin, J. & Bocquet, M.-L. Graphene on metal surfaces. *Surface Science* **603**, 1841–1852 (2009).

119. Xiong, W. *et al.* Single-Step Formation of Graphene on Dielectric Surfaces. *Advanced Materials* **25**, 630–634 (2013).

120. Kesarwani, A. K. *et al.* Determining the number of layers in graphene films synthesized by filtered cathodic vacuum arc technique. *Fullerenes, Nanotubes and Carbon Nanostructures* **24**, 725–731 (2016).

121. Smith, H. M. & Turner, A. F. Vacuum deposited thin films using a ruby laser. *Applied Optics* **4**, 147–148 (1965).

122. Krebs, H.-U. *et al.* Pulsed Laser Deposition (PLD) -- A Versatile Thin Film Technique. in *Advances in Solid State Physics* 505–518 (Springer, Berlin, Heidelberg). doi:10.1007/978-3-540-44838-9_36.

123. Dijkkamp, D. *et al.* Preparation of Y-Ba-Cu oxide superconductor thin films using pulsed laser evaporation from high Tc bulk material. *Appl. Phys. Lett.* **51**, 619–621 (1987).

124. Ying, Z. C., Hettich, R. L., Compton, R. N. & Haufler, R. E. Synthesis of nitrogen-doped fullerenes by laser ablation. *J. Phys. B: At. Mol. Opt. Phys.* **29**, 4935 (1996).

125. Radhakrishnan, G., Adams, P. M. & Bernstein, L. S. Plasma characterization and room temperature growth of carbon nanotubes and nano-onions by excimer laser ablation. *Applied Surface Science* **253**, 7651–7655 (2007).

126. Sikora, A. *et al.* Structure of diamondlike carbon films deposited by femtosecond and nanosecond pulsed laser ablation. *Journal of Applied Physics* **108**, 113516 (2010).

127. Acharya, K. P. *et al.* Pulsed laser deposition of graphite counter electrodes for dye-sensitized solar cells. *Applied Physics Letters* **97**, 201108 (2010).

128. Katsuno, T. *et al.* Optical properties of high-density amorphous carbon films grown by nanosecond and femtosecond pulsed laser ablation. *Appl. Phys. A* **81**, 471–476 (2005).

129. Nomura, K. *et al.* Room-temperature fabrication of transparent flexible thin-film transistors using amorphous oxide semiconductors. *Nature* **432**, 488–492 (2004).

130. Maddi, C. *et al.* Structure, electrochemical properties and functionalization of amorphous CN films deposited by femtosecond pulsed laser ablation. *Diamond and Related Materials* **65**, 17–25 (2016).

131. Qian, M. *et al.* Formation of graphene sheets through laser exfoliation of highly ordered pyrolytic graphite. *Applied Physics Letters* **98**, 173108 (2011).

132. Koh, A. T. T., Foong, Y. M. & Chua, D. H. C. Cooling rate and energy dependence of pulsed laser fabricated graphene on nickel at reduced temperature. *Appl. Phys. Lett.* **97**, 114102 (2010).

133. Vitug, J. *et al.* Nanosecond and femtosecond laser deposition of BiSrCaCuO on MgO. in *ICPS 2013: International Conference on Photonics Solutions* vol. 8883 888308 (International Society for Optics and Photonics, 2013).

134. Solmates - Home. https://www.solmates.nl/.

135. Yang, Z. & Hao, J. Progress in pulsed laser deposited two-dimensional layered materials for device applications. *Journal of Materials Chemistry C* **4**, 8859–8878 (2016).

136. Cappelli, E. *et al.* Orientation tendency of PLD carbon films as a function of substrate temperature: A NEXAFS study. *Diamond and Related Materials* **14**, 959–964 (2005).

137. Kumar, I. & Khare, A. Multi- and few-layer graphene on insulating substrate via pulsed laser deposition technique. *Applied Surface Science* **317**, 1004–1009 (2014).

138. Kumar, P., Lahiri, I. & Mitra, A. Nickel mediated few-layer graphene growth on glass substrates by pulsed laser deposition. *Results in Physics* **14**, 102350 (2019).

139. Koh, A. T. T., Foong, Y. M. & Chua, D. H. C. Comparison of the mechanism of low defect few-layer graphene fabricated on different metals by pulsed laser deposition. *Diamond and Related Materials* **25**, 98–102 (2012).

140. Vishwakarma, R. *et al.* Transfer free graphene growth on SiO2 substrate at 250 °C. *Sci Rep* **7**, (2017).

141. Abd Elhamid, A. M., Aboulfotouh, A. M., Hafez, M. A. & Azzouz, I. M. Room temperature graphene growth on complex metal matrix by PLD. *Diamond and Related Materials* **80**, 162–167 (2017).

142. Cappelli, E., Orlando, S., Servidori, M. & Scilletta, C. Nano-graphene structures deposited by N-IR pulsed laser ablation of graphite on Si. *Applied Surface Science* **254**, 1273–1278 (2007).

143. Sarath Kumar, S. R. & Alshareef, H. N. Ultraviolet laser deposition of graphene thin films without catalytic layers. *Applied Physics Letters* **102**, 012110 (2013).

144. Sarath Kumar, S. R., Nayak, P. K., Hedhili, M. N., Khan, M. A. & Alshareef, H. N. In situ growth of p and n-type graphene thin films and diodes by pulsed laser deposition. *Applied Physics Letters* **103**, 192109 (2013).

145. Xu, S. C. *et al.* Direct synthesis of graphene on any nonmetallic substrate based on KrF laser ablation of ordered pyrolytic graphite. *Laser Phys. Lett.* **11**, 096001 (2014).

146. Na, B. J., Kim, T. H., Lee, C. & Lee, S.-H. Study on Graphene Thin Films Grown on Single Crystal Sapphire Substrates Without a Catalytic Metal Using Pulsed Laser Deposition. *Transactions on Electrical and Electronic Materials* **16**, 70–73 (2015).

147. Xiangming Dong, X. D., Shibing Liu, S. L., Haiying Song, H. S., Peng Gu, P. G. & Xiaoli Li, X. L. Few-layer graphene film fabricated by femtosecond pulse laser deposition without catalytic layers. *Chinese Optics Letters* **13**, 021601–021604 (2015).

148. Ren, P. *et al.* Fabrication of nitrogen-doped graphenes by pulsed laser deposition and improved chemical enhancement for Raman spectroscopy. *Materials Letters* **204**, 65–68 (2017).

149. Zhang, H. & Feng, P. X. Fabrication and characterization of few-layer graphene. *Carbon* **48**, 359–364 (2010).

150. Wang, K., Tai, G., Wong, K. H., Lau, S. P. & Guo, W. Ni induced few-layer graphene growth at low temperature by pulsed laser deposition. *AIP Advances* **1**, 022141 (2011).

151. Hemani, G. K. *et al.* Interfacial graphene growth in the Ni/SiO system using pulsed laser deposition. *Applied Physics Letters* **103**, 134102 (2013).

152. Kaushik, V., Sharma, H., Shukla, A. K. & Vankar, V. D. Sharp folded graphene ribbons formed by CO2 laser ablation for electron field emission studies. *Vacuum* **110**, 1–6 (2014).

153. Tite, T. *et al.* Graphene-based textured surface by pulsed laser deposition as a robust platform for surface enhanced Raman scattering applications. *Applied Physics Letters* **104**, 041912 (2014).

154. Tite, T. *et al.* Surface enhanced Raman spectroscopy platform based on graphene with one-year stability. *Thin Solid Films* **604**, 74–80 (2016).

155. Fortgang, P. *et al.* Robust Electrografting on Self-Organized 3D Graphene Electrodes. *ACS Applied Materials & Interfaces* **8**, 1424–1433 (2016).

156. Kumar, P. *et al.* Growth of few- and multilayer graphene on different substrates using pulsed nanosecond Q-switched Nd:YAG laser. *J Mater Sci* **52**, 12295–12306 (2017).

157. Dong, X., Liu, S., Song, H. & Gu, P. Growth of large-area, few-layer graphene by femtosecond pulsed laser deposition with double-layer Ni catalyst. *J Mater Sci* **52**, 2060–2065 (2017).

158. Abd Elhamid, A. E. M., Hafez, M. A., Aboulfotouh, A. M. & Azzouz, I. M. Study of graphene growth on copper foil by pulsed laser deposition at reduced temperature. *Journal of Applied Physics* **121**, 025303 (2017).

159. Maddi, C. *et al.* Nano-Architecture of nitrogen-doped graphene films synthesized from a solid CN source. *Scientific Reports* **8**, (2018).

160. Wang, J. *et al.* Tailoring the Grain Size of Bi-Layer Graphene by Pulsed Laser Deposition. *Nanomaterials* **8**, 885 (2018).

161. Abd Elhamid, A. M., Aboulfotouh, A. M., Hafez, M. A. & Azzouz, I. M. Structural effect of Ni-Cu catalysts for graphene growth by pulsed laser deposition. *Thin Solid Films* **653**, 93–100 (2018).

162. Larki, F., Kameli, P., Nikmanesh, H., Jafari, M. & Salamati, H. The influence of external magnetic field on the pulsed laser deposition growth of graphene on nickel substrate at room temperature. *Diamond and Related Materials* **93**, 233–240 (2019).

163. Wang, J. *et al.* Pulsed laser deposition of monolayer and bilayer graphene. *Applied Surface Science* **494**, 651–658 (2019).

164. Bourquard, F. *et al.* Electroanalytical Performance of Nitrogen-Doped Graphene Films Processed in One Step by Pulsed Laser Deposition Directly Coupled with Thermal Annealing. *Materials* **12**, 666 (2019).

165. Bleu, Y. *et al.* Raman study of the substrate influence on graphene synthesis using a solid carbon source via rapid thermal annealing. *J Raman Spectrosc* **50**, 1630–1641 (2019).

166. Bleu, Y. *et al.* Graphene synthesis on SiO2 using pulsed laser deposition with bilayer predominance. *Materials Chemistry and Physics* **238**, 121905 (2019).

167. Bleu, Y. *et al.* Dynamics of carbon diffusion and segregation through nickel catalyst, investigated by in-situ XPS, during the growth of nitrogen-doped graphene. *Carbon* **155**, 410–420 (2019).

168. Kuila, T. *et al.* Chemical functionalization of graphene and its applications. *Progress in Materials Science* **57**, 1061–1105 (2012).

169. Wang, H., Maiyalagan, T. & Wang, X. Review on Recent Progress in Nitrogen-Doped Graphene: Synthesis, Characterization, and Its Potential Applications. *ACS Catal.* **2**, 781–794 (2012).

170. Agnoli, S. & Favaro, M. Doping graphene with boron: a review of synthesis methods, physicochemical characterization, and emerging applications. *J. Mater. Chem. A* **4**, 5002–5025 (2016).

Chapter 2: Experimental methodology for graphene synthesis & characterization

This chapter will present the experimental methods for graphene growth by pulsed laser deposition and annealing as well as the characterization techniques that have been used. During the optimization of the graphene growth processes, more than 200 samples have been synthesized and analyzed. Firstly, the nickel thin film catalyst deposition by thermal evaporation and the two lasers used for amorphous carbon and doped amorphous carbon deposition will be presented. Then, we will describe the ex-situ rapid thermal annealing (RTA) process. Afterward, the main techniques and methodologies to characterize graphene-based material including Raman spectroscopy, X-rays photoelectron spectroscopy (XPS), scanning electron microscope (SEM), atomic force microscopy (AFM), transmission electron microscope (TEM), and UV-Vis for transmittance measurement, will be introduced. These measurements allow us to investigate the structure, chemical composition, and morphology of the synthesized films. Lastly, the voltammetry technique used for the investigation of the electrochemical properties of some of our samples will be briefly presented. It should be noted that this chapter focuses on the fundamentals of these techniques and the information that can be obtained from them. If needed, in the next chapters, we will give some more details.

I. Nickel catalyst and carbon precursor deposition process

1. Nickel thin film deposition by thermal evaporation

When using the Thermal Evaporation deposition technique, a solid material is vaporized in a high vacuum environment onto any substrate. This produces thin film coatings of the material with a controlled thickness ranging from microns to a few nanometers[1]. It mostly relies on two methods: electron beam evaporation or resistive evaporation. In this work resistive thermal evaporation was used for nickel thin film deposition on desired substrates.

Resistive evaporation is a process in which the material is heated to its evaporation point by using electrical energy. The vaporized atoms then travel to the substrate where they condense and nucleate together to form the thin film coating. For resistive evaporation coating, a high level of vacuum is required to improve the film purity.

Moreover, during this process, two crucial factors need to be taken into account, the measurement of the film thickness and the control of the film deposition rate. For these purposes, a quartz oscillator crystal measures the oscillation frequency of the substrate holder during the deposition. Then, by measuring the variation of this frequency, the quartz balance gives in its screen the deposited thickness as well as the deposition rate.

The procedure of resistive evaporation involves the placement of pellets of the material to be deposited into thin films on a metal nacelle between two metal electrodes at the bottom of the chamber. The substrates facing down are held by screws to a substrate-holder placed above the nacelle inside the chamber. A high vacuum is created within the chamber. Then, the material is heated to its melting temperature by passing an optimum current through the electrodes and further increase of the current, consequently increase the temperature, leading to evaporation of the material onto the desired substrate for thin film deposition.

During every evaporation process, a vacuum of about 10^{-6} mbar was created within the chamber by pumping for at least 2 hours. The density, impedance, and tooling factors for nickel material were set to 8.91 g/cm^2, 26.68 Ω, and 200% respectively. Once vacuum was achieved, the evaporation and consequently, the thin-film deposition process was done by passing a current of 135−140 A with deposition rate no more than 2 nm/s, within the chamber. Nickel pallets with 99.99% purity were used as the source material for the deposition. In this work, four different nickel film thicknesses were used: 25 nm, 50 nm, 60 nm, and 150 nm.

2. Amorphous carbon thin film deposition by laser ablation

a. The amorphous carbon deposition chamber

The amorphous carbon and doped (B, N) amorphous carbon thin film depositions were carried out in a MECA 2000 stainless steel chamber. The vacuum chamber is illustrated in **Figure 2.1a,** and its picture is shown in **Figure 2.1b**. A Varian micro leak valve allows gas to be introduced with the controlled flow. The pressure in the chamber is measured using a Sky ™ Leybold Inficon IR090 gauge. Combining a Pirani system and a hot cathode system, the gauge operates from 10^{-10} to 10^{-3} mbar. The vacuum chamber is linked to two pumps: primary and secondary pumps. The primary pump is for the primary vacuum (10^{-3} mbar) achieved by the use of the Varian Triscroll vacuum pump. Once the primary vacuum is reached, the secondary pump is used to achieve a high vacuum of 10^{-7} mbar.

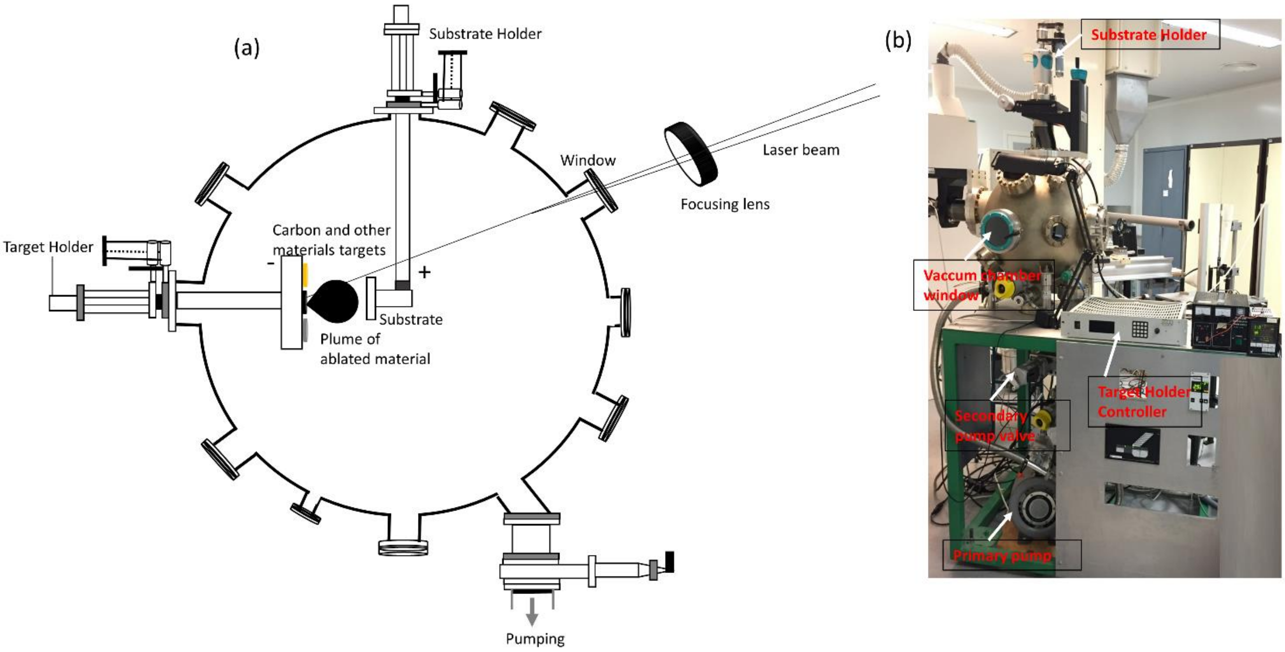

Figure 2. 1 (a) Schematic illustration of pulsed laser deposition vacuum chamber, (b) Photo of the used vacuum chamber machine.

A quartz window allows the laser beams to enter the chamber and be focused on solid-state deposition targets at a 45° angle. The window absorbs approximately 10 % of the laser beam energy. Two manipulators are used for positioning the deposition targets and substrate. The substrate holder allows for translation in every direction and a 360° rotation around the vertical axis. The target holder only allows for two degrees of freedom: translation towards the substrate and rotation around this translation axis. The translational degree of freedom allows us to vary the distance between the target and the substrate, and the other permits to rotate the motor to 360° and the motor allows us to work with different targets. The target holder has eight rotatory targets that can change the choice of different target position during the deposition. The distance between the target and the substrate can vary by rotating the substrate and target holders. The targets are also rotatable to homogeneously ablate the surface by forming concentric paths. The distance between the target and the substrate is set at 4 cm for all depositions. In the context of this work, two lasers were used to perform the deposition by laser ablation: one with femtosecond pulse duration and another one with nanosecond pulse duration. However, it is worth noting that most of the amorphous carbon depositions were carried out using the laser with nanosecond pulse duration because of its availability.

b. *Femtosecond laser system*

A femtosecond Titanium: Sapphire laser (Coherent Legend Elite) system was used for the deposition of some of the thin films. The system with a 60 fs fundamental pulse duration, a central wavelength of 800 nm, and a repetition rate of 1 kHz was employed for the deposition of a-C and a-C:N. It consists of an oscillator and amplifier as illustrated in **Figure 2.2**. The oscillator produces the femtosecond laser pulses with low energy, which is amplified by an amplifier with the principle of chirped pulse amplification (CPA).

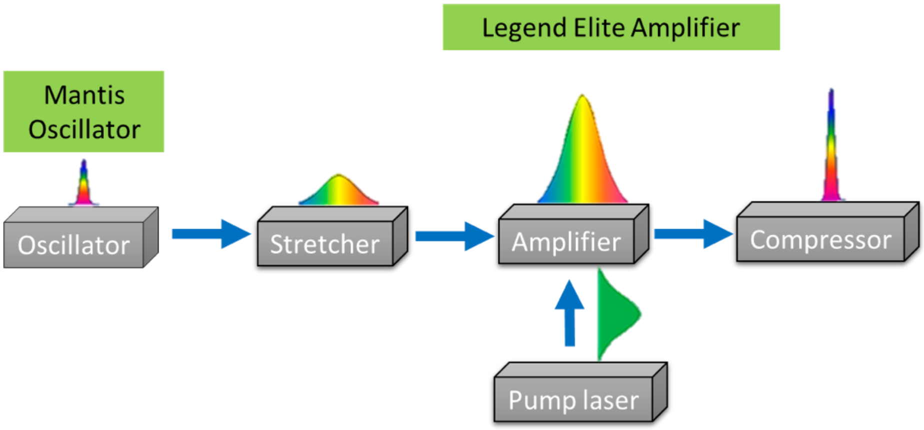

Figure 2. 2 Schematic of chirped pulse amplification (CPA) of the femtosecond laser system.

c. *Nanosecond laser system*

Most of the samples produced during this work were made using a KrF (Krypton Fluoride) excimer from the Lamba Physiks.

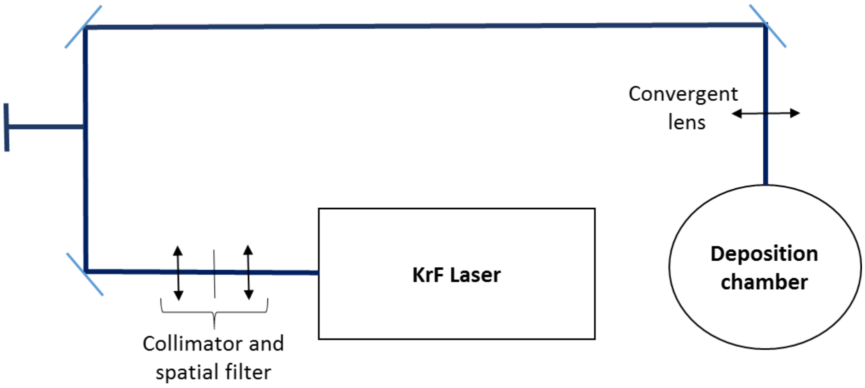

Figure 2. 3 The optical assembly of the KrF excimer laser

The system has a 20 ns pulse duration at a wavelength of 248 nm and a repetition rate of 10 Hz. The laser is directed by a series of 3 mirrors to the deposition chamber. To correct the divergence of the beam, a collimator is added to the output of the laser. A self-formed filter is also added to the focal point of the first lens to improve the quality of the beam by cutting the ASE (Amplified Spontaneous Emission). The optical assembly is illustrated in **Figure 2.3**.

d. Determination of laser fluence

The laser fluence, denoted F, is one of the most important parameters for thin film deposition using a laser ablation process. It is defined by the following formula:

$$F = \frac{E}{\Sigma} \qquad \text{(Eq.2.1)}$$

where E is the energy per pulse in joule and Σ is the surface of the laser spot in cm^2.

The laser fluence of both lasers was calculated according to the procedure proposed by Liu and co-workers[2]. In this method, the Gaussian radial distribution of the beam energy on the target is considered. Then, we define F_{crete} the fluence at the center of the beam (peak fluence) and r the distance to the center of the beam. For a Gaussian beam, the beam width ω is the distance from the center of the beam for which the intensity is divided by e^2 (with “e” the Euler constant). Finally, we define “F_{th}” the fluence ablation threshold of the material and “r_{th}” the radius threshold above which there is no longer any ablation. These different parameters are illustrated in **Figure 2.4**.

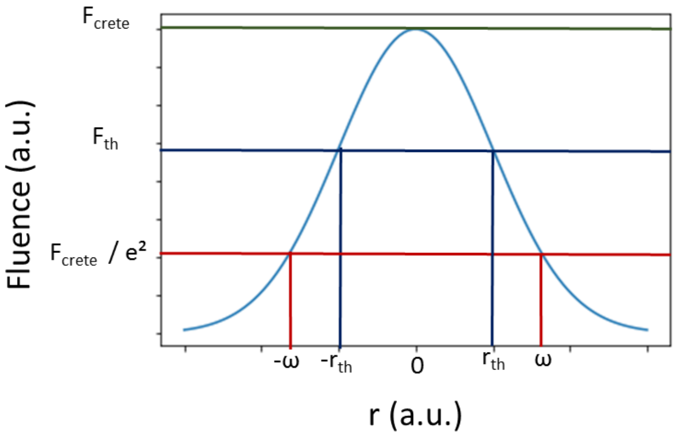

Figure 2. 4 Radial distribution of the laser fluence

The spatial distribution of the laser fluence is therefore given by:

$$F(r) = F_{crete} e^{-2\frac{r^2}{\omega^2}} = F_{crete} e^{-2\frac{\pi r^2}{\pi \omega^2}} \qquad \text{(Eq.2.2)}$$

πr^2 and $\pi\omega^2$ being respectively the surfaces of the studied area and the laser beam.

We can define the ablated threshold surface (corresponding to r_{th}), which gives:

$$\frac{F_{th}}{F_{crete}} = e^{-2\frac{\Sigma_{th}}{\Sigma}} \qquad \text{(Eq.2.3)}$$

That is to say: $$\Sigma_{th} = \frac{\Sigma}{2}\left(ln(F_{crete}) - ln(F_{th})\right) \qquad \text{(Eq.2.4)}$$

However, in the case of a Gaussian distribution, the peak value is twice the average value of the distribution. We, therefore, have $F_{crete} = 2 \times F_{mean}$ the average fluence. Either for an energy pulse E:

$$F_{crete} = 2 \times \frac{E}{\Sigma} \qquad \text{(Eq.2.5)}$$

In the same way, one can consider the laser pulse of minimum energy making it possible to damage the material E_{th}, whose peak value of the fluence distribution will be F_{th}. So

$$F_{th} = 2 \times \frac{E_{th}}{\Sigma} \qquad \text{(Eq.2.6)}$$

It comes immediately:

$$\Sigma_{th} = \frac{\Sigma}{2}\left(ln(E) - ln(E_{th})\right) \qquad \text{(Eq.2.7)}$$

The measurement of the laser energy is done using a calorimeter to measure the average power delivered at a given frequency. Then a set of impacts is performed by changing the laser energy without affecting the position of the focusing lens. Afterward, we measure the ablated area (where the fluence was above the ablation threshold) and represent this area as a function of the logarithm of the energy (E).

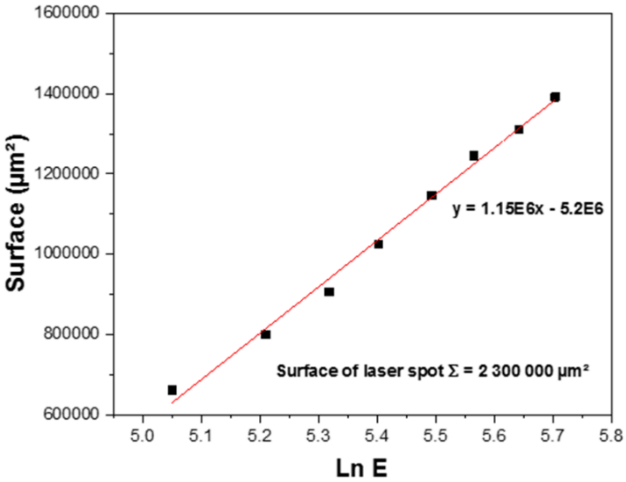

Figure 2. 5 Linear regression performed on the surfaces of ablation craters. The target is made of silicon and each crater is obtained from 10 shots.

Finally, we exploit the affine relation between these two values (Eq.2.7) to obtain, via a linear fit, the surface of the laser beam. One example of such a measurement made on a silicon target using the KrF laser is shown in **Figure 2.5**. Therefore, with the linear relation between the ablated surface and the logarithm of the energy, the surface of the beam was estimated at 2 300 000 μm^2. Also, using Eq.2.1, the laser fluence was calculated to be around 5.2 J/cm^2. This fluence was used in most of the experiments done using a KrF laser.

e. Amorphous carbon, nitrogen-doped amorphous and boron-doped carbon deposition

Knowing the deposition rate for each material is important because it allows controlling the quantity of the doping element inserted into the carbon matrix. The principle is simple: we deposited for a given time (long enough to be as precise as possible) the amorphous carbon (a-C) from a graphitic target, the nitrogen-doped amorphous carbon (a-C:N) from a graphitic target in the presence of a nitrogen gas pressure, and boron (B) from the boron target, as described in details later. By measuring the thickness of the layer and dividing it by the ablation time, we deduced the deposition rate. The film thicknesses are measured with a Veeco Dektak3 ST mechanical profilometer. The thickness is evaluated by measuring the step height of the films. The step is created by masking the substrate during deposition with the adhesive tape. The carbon and boron deposition rates under the various production conditions are shown in **Table 2.1**. It is worth mentioning that the deposition rate is recording after the cleaning of the window in which the laser passes through for ablation. Therefore, it is necessary to clean this window from time to time to stay in the same deposition conditions. Otherwise, when this window gets dirty, the deposition of all materials collapse.

Fluence Materials	5 $J.cm^{-2}$ (fs)	5 $J.cm^{-2}$ (ns)	6 $J.cm^{-2}$ (ns)
a-C	10 $nm.min^{-1}$	18 $nm.min^{-1}$	26 $nm.min^{-1}$
a-C: N(16%)	2.5 $nm.min^{-1}$	-	-
B	-	0.5 $nm.min^{-1}$	1 $nm.min^{-1}$

Table 2. 1 Carbon, nitrogenated amorphous carbon, boron deposition rate as a function of the used fluences.

- Nitrogen-doped amorphous carbon (a-C:N) deposition

We prepared our a-C: N thin films using femtosecond pulsed laser deposition (fs-PLD) by ablating a high purity graphite target (99.9995% purity) onto silicon (Si), and SiO_2 substrates.

A femtosecond laser system working at 800 nm wavelength, with a pulse duration of 60 fs and a repetition rate of 1 kHz was used.

The substrates were mounted on sample holder at a distance of 40 mm from the target. High purity (99.9995%) N_2 gas was used as the reactant gas. Before the deposition, the chamber was pumped until a base pressure of 10^{-6} mbar. A mass flow controller regulates the static pressure of N_2 flux between 0-0.5 mbar pressures.

For all the deposition conditions, the laser fluence is kept constant at 5 $J.cm^{-2}$. The deposition rate of amorphous carbon without nitrogen content was 10 nm/min, whereas the one of a-C:N was around 2.5 nm/min for 0.1 mbar partial pressure corresponding to 16 at% of the nitrogen in a-C:N as reported in the previous studies of our group[3,4]. The ablation time was adjusted to keep an a-C:N film thickness of 10 nm. The transformation of nitrogen-doped amorphous carbon into nitrogen-doped graphene occurs when heating *in situ* the sample during the deposition or after the deposition. **Figure 2.6** illustrates the different steps of the synthesis of nitrogen-doped graphene.

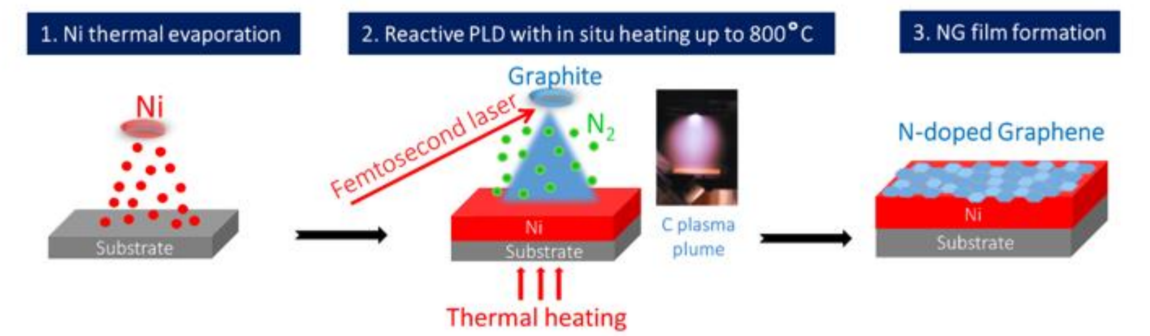

Figure 2. 6 A schematic illustration of the synthesis of nitrogen-doped graphene film from amorphous carbon nitride (a-C: N).

- Boron doped amorphous carbon (a-C:B) deposition

We prepared our a-C:B thin films using nanosecond pulsed laser deposition (ns-PLD) by ablating alternatively a graphite and boron targets onto SiO_2 and SiO_2/Si substrates. Ablation was operated at room temperature by an excimer laser KrF with 248 nm wavelength, a pulse duration of 20 ns, a repetition rate of 10 Hz with different fluence, and therefore deposition rate. Again, here, the conversion of boron-doped amorphous carbon into boron-doped graphene can occur when heating the sample after the deposition. The synthesis process of pulsed laser co-deposition is illustrated in **Figure 2.7**.

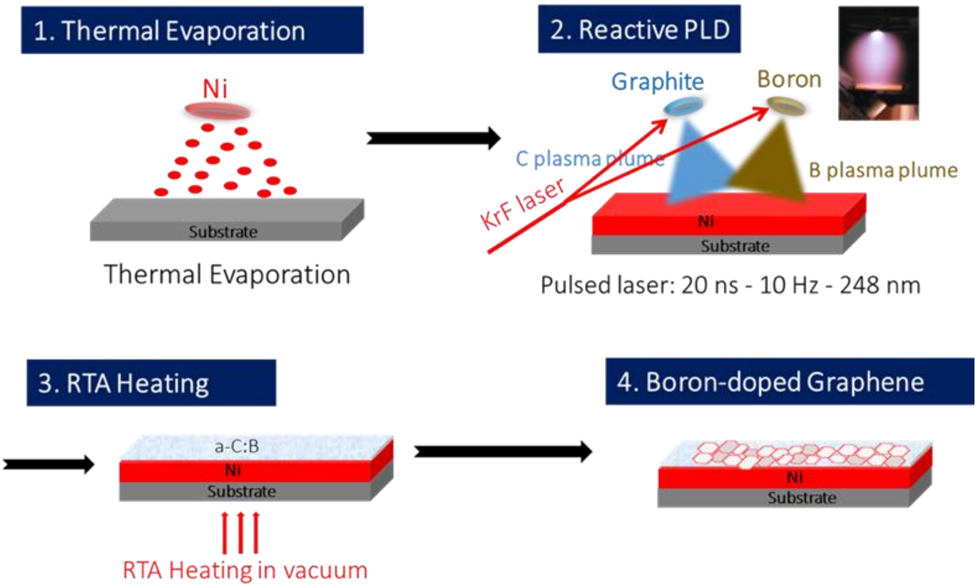

Figure 2. 7 A schematic illustration of pulsed laser co-deposition (PLD) of carbon and boron (a-C:B), and its conversion into boron-doped graphene via thermal treatment.

Before the deposition of a-C:B, one has to calculate the number of shots and sequences on each target according to the boron content in a-C:B and to the a-C:B thickness. For this, we firstly ablated the graphite target to obtain the ablation rate of carbon. Secondly, we did the same with the boron target to get the ablation rate of boron. **Figure 2.8** shows the cross-section SEM image of the deposited boron film with a thickness of around 60 nm. The boron film is continuous and homogeneous, and its thickness has been considered to calculate the ablation rate of boron. The below paragraph gives detail of all these calculations.

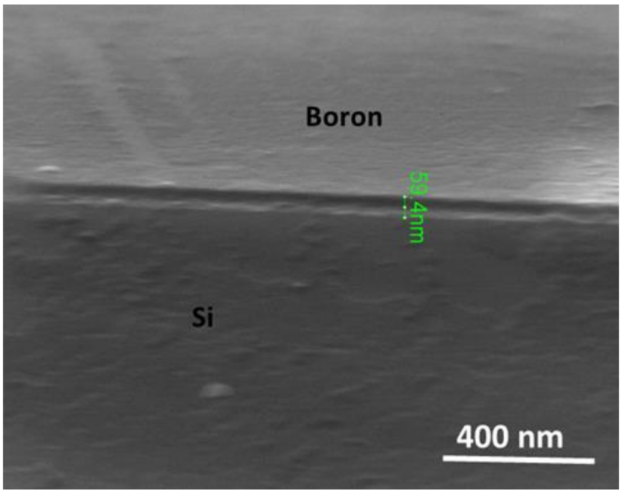

Figure 2. 8 SEM image of the cross-section of boron film used to calibrate the ablation rate on Si substrate.

Considering [B] the atomic fraction of boron B into the boron doped amorphous carbon a-C:B, ρ_C, and ρ_B are the densities of a-C (DLC) and boron B, respectively 3 and 2.3 g.cm^{-3}, being characteristic of typical DLC and crystalline boron. M_C = 12 g.mol^{-1} and M_B = 11 g.mol^{-1} are the corresponding the atomic masses of carbon and boron respectively· The deposited volume of C and B are respectively V_C and V_B, and are proportional to their thicknesses e_C and e_B for a given deposited surface S:

$$V_C = S \times e_C \qquad\qquad V_B = S \times e_B \qquad \text{(Eq.2.8)}$$

v_C and v_B are the ablation speed for carbon and boron targets at 160 mJ (6.2 J.cm^{-2}) with the KrF laser: v_C = 26 nm.mn^{-1} et v_B = 1 nm.mn^{-1} (here the ablation speed correspond to the deposition rate). Therefore, for a pulse frequency f = 10 Hz: v_C = 0.04333 nm/shot et v_B = 0.00167 nm/shot.

It is necessary to link the desired atomic concentration of boron [B] with its fraction of thickness e_B in the layer of thickness $e_B + e_C$, controlled by the times and the ablation rates of C and B.

N: Avogadro number (at.mol^{-1}), N_C and N_B: the number of C and B atoms respectively:

$$[B] = \frac{N_B}{N_C + N_B} \qquad \text{with} \quad N_X = \frac{\rho_X V_X N}{M_X} \qquad \text{(Eq.2.9)}$$

$$[B] = \frac{\frac{\rho_B V_B N}{M_B}}{\frac{\rho_B V_B N}{M_B} + \frac{\rho_C V_C N}{M_C}} = \frac{1}{1 + \frac{(100 - e_B) M_B \rho_C}{e_B M_C \rho_B}} \qquad \text{(Eq.2.10)} \quad \text{Due to} \quad \frac{V_C}{V_B} = \frac{e_C}{e_B} \quad \text{(cf. Eq.2.8)}$$

In this equation (Eq.2.10), for better clarity, we set $e_C + e_B$ = 100 nm (the "e" are therefore % in thickness).

We need to reverse this formula, that is to say, calculating e_B to make the deposition, having fixed [B] (= 0.16 to have 16 at% of boron in a-C:B). We chose the value of 16 at.% as a reference value based on the previous work on a-C:B film deposition of our group[5]. The reverse formula is the following:

$$e_B = \frac{100}{1 + \left(\frac{1}{[B]} - 1\right)\frac{M_C \rho_B}{M_B \rho_C}} \qquad \text{(Eq.2.11)}$$

Applying the formula of the Eq.2.11 for [B] = 0.16 (16 at. %), one obtains e_B = 18.55 nm of boron for a total of 100 nm of a-C:B. We obtain then e_B = 18.55 nm and e_C = 81.45 nm.

Now to optimize the sequence of shots and the number of sequences, to make an a-C: B as "mixed" as possible at the atomic level. We propose, as an elementary sequence, a combination of shots to make a monolayer of a-C:B, of thickness x = 0.3 nm distance between graphene planes.

For 100 nm of a-C:B; 18.55 nm of B is required, and for 0.3 nm of a-C:B: 0.05565 nm of B and 0.24435 nm of C are therefore required. To deposit 0.05565 nm of B at the speed of 0.00167 $nm.shot^{-1}$, it takes 33 shots. Moreover, to deposit 0.24435 nm of C at the speed of 0.043 $nm.shoot^{-1}$, it takes 5.7 shots rounded to 6 shots.

Finally, to make a 4 nm layer of a-C: B, we should repeat this sequence (33 shots on boron and 6 shots on carbon targets) 6.67 times, rounded up to 14 times. Altogether, these 14 successive sequences of 6 shots on C followed by 33 shots on B lead to a-C: B layer (16% at.) with a thickness of around 4 nm.

In addition to 16 at. % of boron in a-C:B, we chose two other doping levels (25 and 50%) based on the previous calculations, to have additional points for comparison. These doping levels were chosen higher based on our previous experience on nitrogen-doped graphene. Indeed, the nitrogen content on the a-C:N precursor is generally lower than its content on the synthesis nitrogen-doped graphene. Thus, we considered the same reasoning for the boron case. It is worth mentioning that after deposition and checking the boron doping level using XPS spectroscopy, we did not find the expected calculated doping level, as depicted in Table 2.2 gathering different parameters for the elaboration of a-C:B 4 nm thick, with the three doping contents. The difference between the calculated boron content and experimental one deduced from XPS may be due to a sur-estimation of the densities of the film, in particular the boron film. Indeed, the exact determination of the density of the deposited boron film (as well as the deposited carbon film) remains a challenge. More details on the composition and chemical bonds of the a-C:B will be developed in Chapter 5 when we will study the transformation of the a-C:B film precursors into boron-doped graphene by RTA process.

Calculated doping level (at. %)	Number of laser shots per sequence	Number of sequences	Measured doping level by XPS (at. %)
a-C:B (4 nm) (16 %)	C : 6 B : 33	14	2 %
a-C:B (4 nm) (25 %)	C : 5 B : 52		4.5 %
a-C:B (4 nm) (50 %)	C : 3 B : 96		9 %

Table 2. 2 Parameters of the elaboration of boron-doped amorphous carbon using the co-ablation of carbon and boron.

II. Post deposition annealing: Rapid Thermal Annealing (RTA)

The annealing of most of the studied samples was performed in our high-temperature furnace, AS-One 100 Standard version (**Figure 2.9a**) which was fabricated by the company Annealsys[6], in Montpellier - France. A schematic illustration of the RTA system is shown in **Figure 2.9b**. The heating is performed by halogen lamps irradiation, which allows fast heating (~ 20°C s^{-1}) thanks to high supply power of about 30 kW. In our experiment, we used a silicon carbide susceptor containing the samples placed at the center of the chamber close to the heating lamps, which permits an enhanced temperature uniformity. This reactor can sustain a wide range of temperatures from room temperature up to 1300°C. A pyrometer (calibrated by a thermocouple in contact with the substrate) measured the heating temperature on the backside of the sample holder. Then the temperature control takes command with a defined temperature ramp and precisely surveillance by the pyrometer. Later, the target temperature upholds at desired one for a specific annealing time.

This furnace is equipped with a standard primary pump for reaching a rough vacuum (10^{-2} mbar) at room temperature. An additional pure gas line is connected to the furnace to allow purging and cleaning of the chamber with nitrogen (N_2) when the whole process is completed. Computer software developed by Annealsys can control all components of the furnace and records the full data logging and process history. We note that our samples are stored in plastic sample boxes without additional precautions.

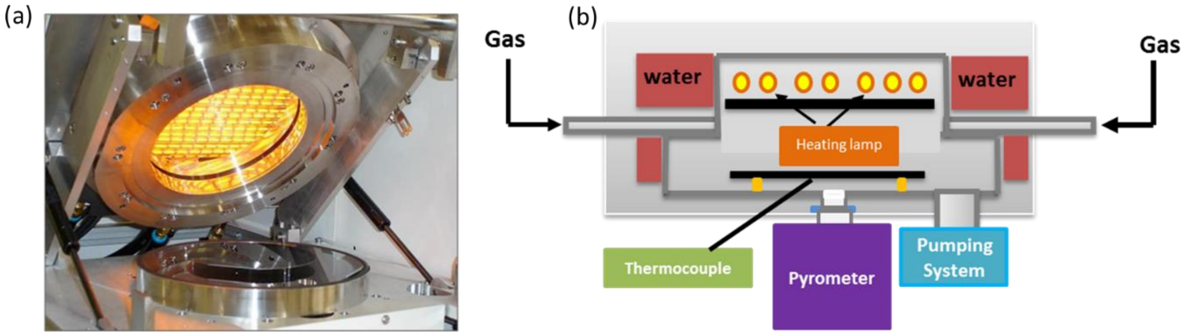

Figure 2. 9 (a) Photograph of AS-One 100 furnace, fabricated by Annealsys; (b) Schematic illustration of Rapid Thermal Annealing RTA system.

III. Physico-chemical and structural characterization methodologies

In this section, we present the different characterization techniques which have been used to characterize the amorphous carbon (a-C), doped amorphous carbon (a-C:N or a-C:B), as well as pristine and doped graphene thin films. Before the film deposition, the calibration of the film thickness is performed using a profilometer as mentioned above. Here, we start by describing briefly the profilometer technique. Then, we describe a wide variety of techniques used to study the Physico-chemical properties of the synthesized graphene films. These techniques are mainly:

- Scanning electron microscopy (SEM), and atomic force microscopy (AFM) for surface morphology information.
- Raman spectroscopy, transmission electron microscopy (TEM), and electron backscatter diffraction (EBSD) in SEM for the microstructural characteristics.
- X-ray photoelectron spectroscopy (XPS) for chemical composition and bonds analysis.
- Cyclic voltammetry (CV) used to investigate the electrochemical properties.

It is worth noting that for analyzing such an ultrathin film as graphene, much care needs to be taken because, in addition to its difficulties arise not only because of the material thinness but also because it is composed of light elements(C (Z=6), B (Z=5), N (Z=7)), which make for a very challenging characterization of the synthesized materials, which are sensitive to irradiation damages during analysis. In **Table 2.3**, we gather all the techniques employed and the corresponding accessible information.

Techniques	**Information**
Profilometer	Calibration of thin film deposition
Raman spectroscopy	Carbon structure, crystallinity, number of graphene layers, uniformity of the grown graphene by mapping
Transmission electron microscope (TEM)	Carbon structure, crystallinity, number of graphene layers
Scanning electron microscope (SEM & EBSD)	Surface morphology and crystalline surface structure of nickel catalyst
Atomic force microscope (AFM)	Surface topography
X-rays photoelectron spectroscopy (XPS)	Surface chemical composition, chemical bonding, doping element detection
UV-Vis spectroscopy	Transmittance analysis
Cyclic Voltammetry	Electrochemical property

Table 2. 3 Summary of all the investigation techniques used in this thesis and relating accessible results.

1. Profilometer

Thickness, as well as surface profile, is one of the key characterization parameters of our deposited amorphous carbon thin films. A profilometer is one of the instruments that are used for this purpose and there are mainly two types: stylus and optical profilometer. In this work, we have used a stylus profilometer Veeco Dektak3 ST (**Figure 2.10b**) to measure the thickness of the deposited amorphous carbon films.

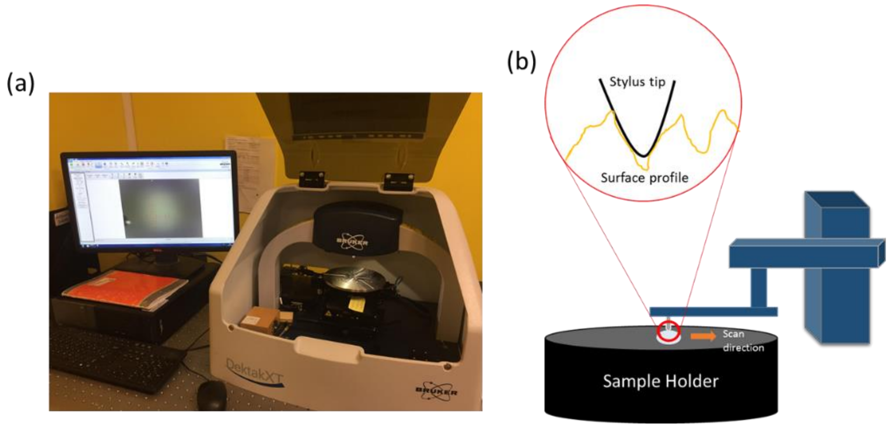

Figure 2. 10 (a) Photograph of DektakXT stylus profilometer from our lab (b) Schematic of a stylus profilometer.

A stylus profilometer comprises mostly two parts namely, the detector probe and the sample stage. For measurements, the probe physically moves along the surface to obtain the surface height. The probe determines the surface undulations concerning a prior set reference. It is a highly sensitive device and its resolution depends on the diameter of the needle tip[7]. Thus, as a result, the stylus provides not so accurate results in the case of very thin films in the order of a few nanometers (typically, less than 50 nm).

2. Raman spectroscopy

Raman spectroscopy is a widely used tool for graphene-based material characterization[8–13].

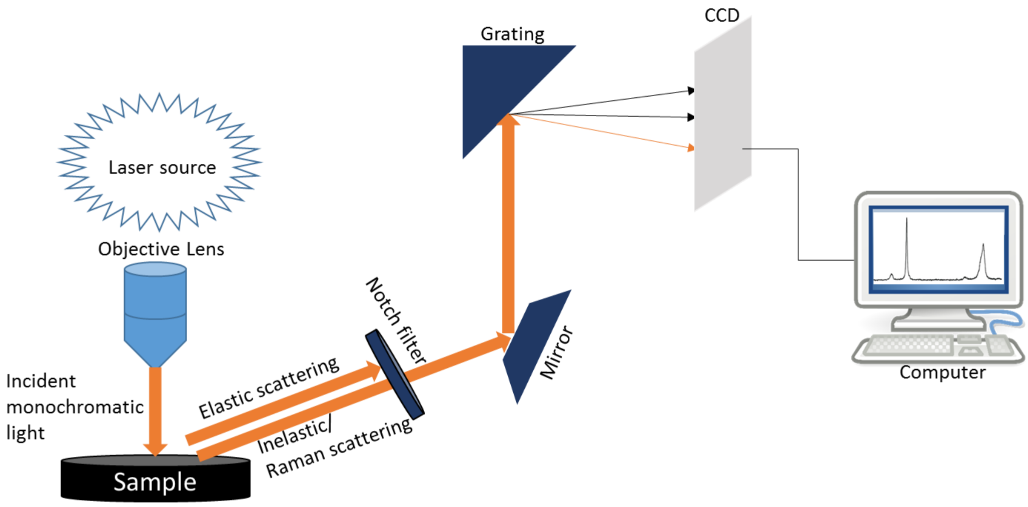

Figure 2. 11 Schematic of a Raman spectrometer

In Raman experiments, a monochromatic light illuminates the sample and the diffused light is detected after it interacts with the vibrational levels in the sample. Besides the elastic process known as Rayleigh scattering, only a small fraction of the photons undergo inelastic scattering and are diffused with a different energy than incident photons. The origin of this scattering is the Raman-active optical phonons in the material. Thus, a lattice vibration (a phonon) can be excited (Stokes scattering) or annihilated (anti-Stokes scattering) when interacting with incident photons, which are reemitted with the corresponding added or subtracted energies. The difference between the emitted photon frequency and the incident light frequency is called the Raman shift and is expressed in cm^{-1}. Raman spectrum is generally presented in the form of scattered intensity as a function of the Raman shift. Since the vibrational states are unique signatures of both the material and its structure, Raman spectra are different from one material to another, which makes Raman spectroscopy a powerful technique for identification and analysis of material characteristics. For instance, when studying the various forms of the carbon allotropes, this technique can reveal the geometric structure and bonding which differs from one form to another. Especially for the study of graphene, Raman spectroscopy provides various information such as the defects, crystallinity, strain and the number of layers. The schematic of a Raman spectrometer is shown in **Figure 2.11**.

a. Raman spectrum of graphene

In graphene material, three main peaks dominate the Raman spectrum: D, G, and 2D peaks located at about 1350, 1580, and 2700 cm^{-1} respectively, for freestanding graphene measured with an excitation wavelength of 514.5 nm**[10,12]**.

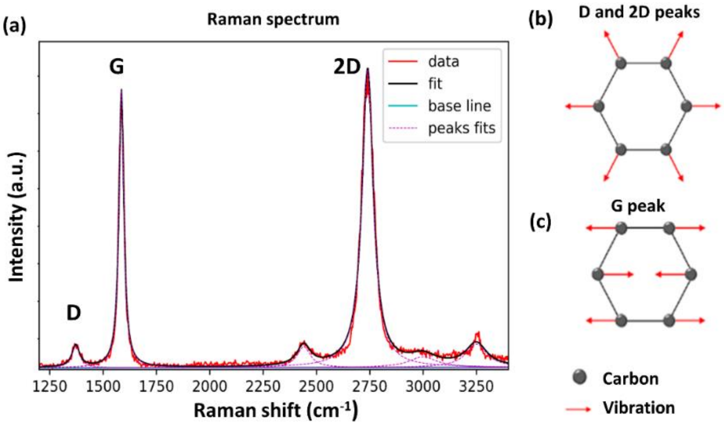

Figure 2. 12 (a) Raman spectrum from our synthesized graphene with the three major characteristic peaks. (b) Representation of the vibrational mode related to D and 2D peak. (c) Representation of the vibrational mode associated with the G peak.

Figure 2.12 shows a Raman spectrum of graphene. The D peak located around 1350 cm^{-1} is a breathing mode of the carbon rings (see in **Figure 2.12b**). This mode only becomes active in the presence of structural defects (wrinkles, folding, edges, etc.) and depends on photon excitation energy. It is attributed to a double resonant process, which involves a scattering, by a defect in the graphene lattice. There is only one phonon involved in the D peak scattering process. The G peak originates from the in-plane stretching vibrations of the sp^2 carbon atoms (see in **Figure 2.12c**). The 2D band originates from a two phonon double resonance Raman process that is a second-order Raman process originating from the in-plane breathing-like mode of the carbon hexagonal rings (see in **Figure 2.12b**)[7–10,12]. Because two phonons are involved for the 2D peak, the energy shift for the 2D band is twice that of the D band, hence its name. Therefore, Raman spectroscopy can provide useful information on the defects (D peak), the degree of graphitization by in-plane vibration of sp^2-bond carbon atoms (G peak), the stacking order (2D peak) as well as the number of graphene layers via the relative intensity ratio of each peak as will be described next.

b. Number of Graphene Layers

Raman spectroscopy has been considered an ideal tool to estimate the number of graphene layers. Many methods including the G band intensity and position, the 2D band position, and full half-width maximum (FHWM), and the ratio of intensity between the 2D and G (I_{2D}/I_G) peaks have been used for graphene number of layers estimation. However, the most commonly used in the literature to distinguish single-layer graphene (SLG) with few-layer graphene (FLG)[10,12,14] are the FWHM of 2D peak and the intensity ratio between 2D and G peak. It has been reported that the FWHM of 2D peak increases and the I_{2D}/I_G decreases when the number of graphene layers increases. For instance, the 2D peak of monolayer graphene can usually be fitted by a single Lorentzian peak with an FHWM of about 35 cm^{-1}, while four Lorentzian peaks are needed to fit the 2D-peak of bilayer graphene due to their distinct electronic band structure[10,12]. In the literature, there is a huge amount of results on the estimation of the graphene layer number using I_{2D}/I_G and FWHM (2D) data. Additionally, the 2D peak position upshifts to 50 cm^{-1} when the number of layers increases from 1 to 5. For more than four and five layers, the FWHM (2D) cannot be used to quantify the number of layers, and the 2D signature becomes similar to that of graphite. Moreover, Bayle et al.[15] have questioned the reliability of using the FWHM of 2D peak due to its sensibility to the stacking order between consecutive graphene layers. Furthermore, several factors such as strain, doping, and stacking order have a great chance to alter the shape of the 2D peak. Therefore, in most of our estimation of the graphene layer number in this work, we have used the intensity ratio between 2D and G peaks with the following criterion in **Table 2.4** based on several references[16–21] on the graphene growth using a solid carbon source with a nickel catalyst.

Layer number	I_{2D}/I_G
1 Layer	> 1.4
2 Layers	0.7 – 1.4
3 Layers and more	< 0.7

Table 2. 4 Summary of I_{2D}/I_G ratio used for the estimation of the graphene layer number in this thesis.

Despite this, some possible limitations still force us to combine other techniques as a complementary criterion to further confirm the results. In the current work, the Raman analysis was combined with TEM images to evidence the number of graphene layers.

c. Crystallite Size

Tuinstra and Koenig have shown that the D to G peak intensity ratio (I_D/I_G) is directly related to the crystallite size (L_a) in the 3D graphite by the following equation[22,23]:

$$L_a(nm) = (2.4 \times 10^{-10})\lambda^4 (\frac{I_D}{I_G})^{-1} \qquad \text{(Eq.2.12)}$$

where $\boldsymbol{\lambda}$ is the laser wavelength in nanometers and $\boldsymbol{L_a}$ is the average size of the crystallites. Since graphene is also a graphitic material, therefore, its crystallite size can be estimated using this Tuinstra– Koenig relation[24].

d. Uniformity and stacking order

To get an idea about the uniformity of our samples, Raman mapping is one of the best ways. Such an investigation can give insights into the uniformity of the graphene layer number, the defect density, and crystallite size as well. In this work, we performed Raman mapping not only for the ratio intensity of I_{2D}/I_G, I_D/I_G but also for the D, G, 2D peaks positions, and widths.

Bilayer and few or multilayer graphene can exhibit various stacking orders such as ABA (Bernal), ABC (rhombohedral), and twist or rotated stacking, as it has been mentioned in Chapter 1. Generally, the line shape of the Raman 2D band is used to determine the stacking orders[25]. When the 2D band shape is symmetric, it corresponds to the ABA stacking whereas it is an asymmetric shape for ABC stacking[10,25,26]. The width of the 2D band plays also a role in determining the stacking sequence. However, the width of the 2D band may be affected, becoming broad by the presence of a defect, chemical doping, and so on. **Figure 2.13** reported[25] the difference between the spectra of ABA trilayer (in green) and ABC trilayer (in red). A spatial Raman mapping of FWHM (2D) shows effectively the identification of Bernal (ABA stacking order) and rhombohedral (ABC order) trilayer graphene. Therefore, the distribution of the stacking sequence can be determined using the shape and width of the 2D band. In this work, when needed, we using the shape of the 2D peak for the stacking sequence identification.

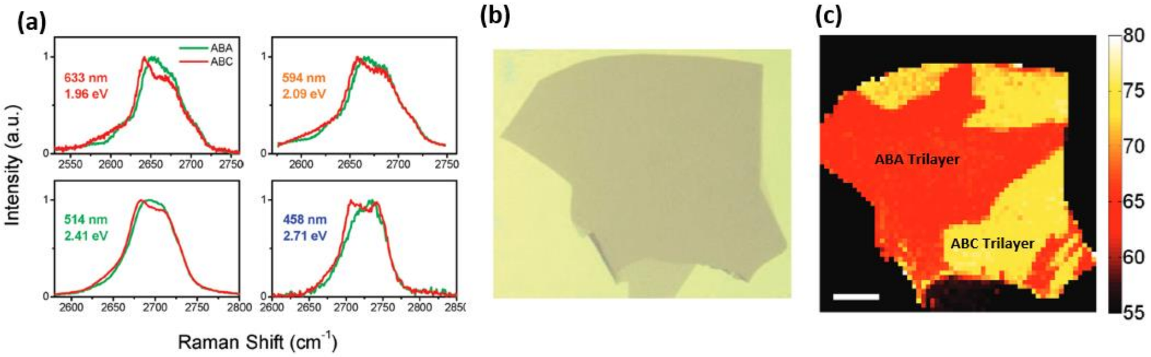

Figure 2. 13 (a) Raman spectra of ABA and ABC trilayer graphene; (b) Optical image and (c) corresponding spatial map of the spectral width of the Raman 2D-mode feature for trilayer graphene samples[25].

e. *Doping effect*

Besides defects such as point defects or edges that can be found in graphene, chemical doping can be performed to tune its electronic and optical properties. When incorporating dopants in graphene, its Raman spectrum still presents the three mains peaks discussed earlier: the G, 2D, and D peaks. Since the D band is Raman active in the presence of defects, it is generally not used to characterize doping. The G and 2D bands are both strongly influenced by the carrier concentration and they have been extensively studied for doping characterization[28–31]. The G peak width decreases symmetrically as the concentration of electrons or holes increases. The doping dependence of the G peak width is also caused by the electron-phonon coupling, which is expected since the G peak width is predominately determined by electron-phonon scattering[32]. Besides, there is a lack of consensus concerning the G peak position. Some works reported a shift of the G peak position toward lower wavenumbers for n-type doping and a shift toward higher wavenumbers for p-type doping[33–35], while some other studies reported that the

G peak upshifts for both holes and electron doping[28,36]. Concerning the 2D peak, its position increases as the holes concentration increases and decreases as the electron concentration increases[31,37]. Furthermore, the G and 2D peaks are sensitive to the strain due to its influence on band structure[38]. It is known that these two peaks will redshift for tensile strain and up-shift for compressive strain. Therefore, the identification of the doping effect using Raman measurement has to be done with much care because several effects are involved at the same time. In this thesis, we have preferred using X-rays photoelectron spectroscopy (XPS) to confirm the doping levels and chemical bonding of dopants.

f. *Instrumentation for Raman spectroscopy*

Raman spectroscopy has been performed using an Aramis Jobin Yvon spectrometer using four different laser excitation wavelengths, namely, 325, 442, 488, and 633 nm, and equipped with a charge-coupled device (CCD) camera. Only two of these wavelengths (442 and 633 nm) were used here. The laser beam was focused on the sample with a confocal 100 × objective. A custom-made SciPy python code allows us to automatize the extraction of parameters such as the intensity, width, and position of the Raman peaks. Most peaks are fitted using Lorentzian functions, except for the G peak which is fitted with a Breit-Wigner-Fano function accounting for its asymmetry compared to a classical Lorentzian profile. Various data processing tools involved in this thesis are background subtraction, intensity normalization, peak fitting, and the correlation between the studied coefficients (intensity ratio, width, position).

3. X-Rays photoelectron spectroscopy (XPS)

X-ray photoelectron spectroscopy (XPS) is a surface-sensitive technique that provides information about the chemical structure and the composition of a material[39,40]. With this technique, the sample is placed in an ultrahigh vacuum chamber to remove the absorbed gasses, contamination, and increase the mean free path of photoelectrons. The sample is then irradiated by a monochromatic X-ray beam of energy hν, with “h” is the Planck constant and “ν” is the photon's frequency. The photon energy (hν) is transferred to a core electron, a photoelectron is emitted as a result and its kinetic energy (KE) is measured as illustrated in **Figure 2.14**. This kinetic energy of photoelectron depends on the potential barrier. The energy barrier consists of two components, the binding energy (BE) of the core electrons and the work function (φ) of spectrometer[41,42].

$$BE = h\nu - KE - \varphi \qquad \text{(Eq.2.13)}$$

The binding energy does not only depend on the specific element but it depends on the chemical environment of the source atom (chemical structure). The valence band density changes as chemical bonds are formed, resulting in a binding energy shift. If the electrons are withdrawn from the atom by bond formation, then the binding energy of core electrons is increased. The XPS spectrum is a plot of the number of detected electrons versus the binding energy of emitted electrons. Each chemical element produces a specific set of peaks at characteristics binding energy making it possible to measure a sample's stoichiometry.

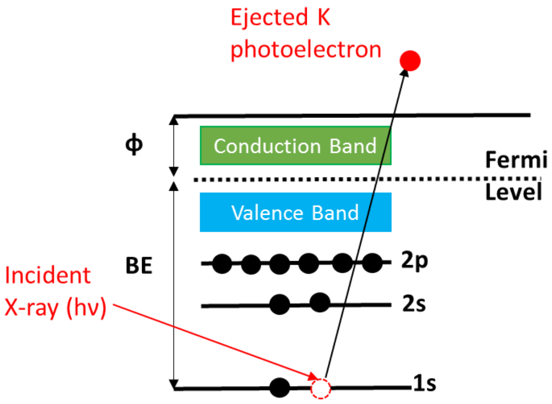

Figure 2. 14 (a) Scheme of the XPS process, showing photoionization of an atom by the ejection of a 1s electron.

Besides, the depth analysis is very small, usually around 2-10 nm, depends on the mean free path of the emitted electrons, which is in an order of few nanometers (5-10 nm). Therefore, this technique only allows probing the extreme surface of the material, determining the chemical states of the elements that are present within the material. However, depending on the emission angle, the depth analyzed is not the same. Indeed, the intensity depends on the depth according to Beer-Lambert law**41**:

$$I_z = I_0 \,.\, e^{-z/\lambda \sin\theta} \qquad \text{(Eq.2.14)}$$

I_z (I_0 respectively) is the intensity of the photoelectrons emitted by the atoms at depth z (the atoms of the surface), θ the angle of emission relative to the surface, and λ the electron mean free path. Therefore, to be able to overcome angular dependence, the spectrum can be measured at different analysis angles (35 ° and 65 ° relative to the surface). At 35 °, the electrons emitted come mainly from the surface, while at 65 °, they emerge from a greater depth. This angle-resolved XPS was used in the study presented in chapter 3.

In this thesis, the XPS measurement was performed in three locations depending on the availability of the instrument. In the case of XPS performed at École des Mines de Saint-Étienne, the spectra were acquired by Vincent Barnier. The XPS apparatus is equipped with a heating furnace allowing to heat the sample to 600°C. The samples were characterized with a Thermo VG Theta probe spectrometer instrument with a focused monochromatic AlKα source (hν = 1486.68 eV, 400 μm spot size). The photoelectrons were analyzed using a concentric hemispherical analyzer operating in the constant ΔE mode. The energy scale calibrated with sputter cleaned pure reference samples of Au, Ag, and Cu so that Au4f7/2, Ag3d5/2, and Cu3p3/2 were positioned at binding energies of respectively 83.98, 386.26 and 932.67 eV. In the case of XPS performed at École Centrale de Lyon, the spectra were acquired by Jules Galipaud. The samples were characterized with a ULVAC-PHI Versaprobe II spectrometer instrument with a focused monochromatic AlKα source (hν = 1486.68 eV, 200 μm spot size). The data treatment for both is performed by using Avantage, Casa XPS, and Origin software tools. The XPS experiment carried out at Synchrotron SOLEIL (Saclay, France), ANTARES beamline, the spectra were acquired by José Avila. The ring operating conditions were 2.5 GeV electron energy, with injection currents of 500 mA and "Top-up" mode. Radiation was monochromatized using a plane-grating monochromator (PGM), which is characterized by a slitless entrance and the use of two varied linear spacing (VLS) gratings with variable groove depth (VGD) along the grating lines. The diameter of the X-ray spot impinging the surface is 140 μm and the X-ray energy was fixed at 700 eV for analysis of the graphene film. The photoemission spectra were taken with incident photon energies of 700 eV), with 190 meV energy resolution. The data treatment is performed by using other software, namely Igor. In the context of this work, this XPS technique is mainly used to determine whether our graphene films are doped or not, to get access to the doping concentration in terms of atomic percent and the type of bonding of carbon with nitrogen or boron.

4. Ultraviolet-Visible spectrophotometry

Ultraviolet-visible (UV-Vis) spectrophotometry is typically used in determining the optical transmittance of a thin film on a transparent support (e.g., fused Silica). Monolayer graphene (SLG) absorbs only $\pi\alpha \approx 2.3$ % of white light, where $\alpha = e^2/\hbar c$ is the fine-structure constant[43,44]. Therefore, the numbers of graphene layers can be estimated from the optical transmittance of the synthesized graphene. The PLD-grown graphene film is first dipped into 4M $FeCl_3$ solution to remove the nickel catalyst particles, then rinsed with deionized water several times, and finally passed through the transmittance measurement. In this study, the optical transmittance of graphene film is carried out using a spectrophotometer Cary50 Probe (Varian) within the spectral range 200–800 nm. The pristine fused silica is used as a reference.

5. Scanning Electron Microscopy (SEM)

Scanning electron microscopy (SEM) was used to analyze the surface morphology of our thin films. The SEM technique is very simple and is frequently used in micro-scale material characterization because of its ease of operation, large depth of focus, wide range of magnification, and good image resolution, and there is no need for special sample preparation. Briefly, inside the SEM, electrons are emitted from an electron gun and accelerated by cascaded anodes. The beam of electrons is converged by electromagnetic condenser lenses to a specific spot. When the electron beam passes through scanning coils, it interacts with the sample surface. **Figure 2.15** shows a schematic illustration of the electrons and X-rays that are generated from the electron-beam sample interaction and their related excitation volumes. These are produced following the interaction between the incident electrons and the sample surface. The interaction of an electron beam with the sample surface generates secondary electrons (SE), which are commonly used for imaging the surface morphology of a sample. The detector of electrons can collect the SE signal and the program translates into greyscale images after a full scan. Analysis of secondary electrons provides a topographic image. Indeed, for a constant acceleration voltage, their intensity depends only on the angle between the surface and the beam. The lower the incidence, the greater the number of secondary electrons emitted.

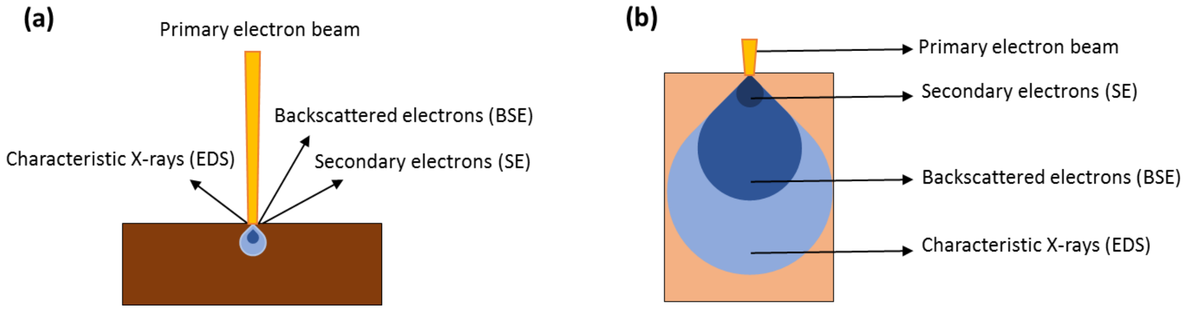

Figure 2. 15 (a) Schematic of the signals resulting from the interaction of the electrons with the sample in SEM analysis. (b) The excitation volume for the generation of each signal.

Backscattered electrons can be generated by the electron beam-sample interaction. They are emitted by elastic scattering of electrons at the sample surface. The BSE signal is dependent on the atomic number of the elements that constitute the sample. Their analysis provides information on the chemical composition of the material. It supplies a contrast between two regions that are enriched in different elements. Therefore, the backscatter rate depends on the atomic number of the atoms in the area scanned. The higher the atomic number, the brighter the area analyzed. With the BSE signal, another detector can be attached to the SEM to provide microstructural information about the crystallographic nature of the material. This technique is known as electron backscattered diffraction (EBSD). Indeed, this technique can reveal useful information about the crystalline grain of the materials such as the size, the crystallographic orientation, and the boundary of the grains as well as the texture. Characteristic X-rays are also produced from the sample when the electron from the inner shell of an atom is removed by the excitation of an electron from the primary electron beam. These X-rays are related to the energy dispersive spectroscopy (EDS) and are used to determine the type of elements that constitute the sample. By analyzing the spectrum of X photons, it is, therefore, possible to establish an elementary mapping of the sample. In this thesis, we used the microscope Nova NanoSEM 200 (MEB-FEG) and the resolution is 1 μm operates up to 30 kV, and sometimes its EDS option.

6. Atomic Force Microscope (AFM)

As the scanning electron microscope, atomic force microscopy (AFM) is one of the main tools for surface topography information. AFM provides a three-dimensional surface profile. Due to its high resolution, it is usually used for the determination of surface roughness. This technique is based on measuring the force between the probe and the sample surface such as Van der Waals force, mechanical contact, etc. It uses a sharp tip to scan the surface of a sample. The tip is mounted at the end of a cantilever, which bends in response to the forces exerted on the tip by the sample. As the tip is brought close to the surface, the forces lead to the deflection of the cantilever. The deflection is measured by detecting the change in the position of a laser beam from the end of the cantilever[45]. Different modes are possible depending on the type of interaction forces between the tip and the sample surfaces.

In contact mode, there is physical contact between the tip and the sample surface. The sample surface creates the deflection of the cantilever, which allows the measurement of the film topography. In non-contact mode, the cantilever vibrates and the amplitudes are measured between the sample and the tip[46].

Applied to graphene material, AFM is one of the tools to get access to the surface features and thickness of graphene. Monolayer graphene has a thickness of about 0.34 nm and this value adds up accordingly for multilayer graphene. AFM can measure height variations down to 0.1 nm, it is therefore very suitable for graphene thickness determination. Nevertheless, it is very difficult in practice to get very precise values for graphene film height, as it can depend on changing cohesive forces between graphene and supporting substrates. Besides, some contaminations on the graphene surface can increase the difficulty of determining the real graphene thickness. Frequently, the thickness of monolayer graphene is found in between 0.4 nm and 1.0 nm, instead of 0.34 nm[47,48]. Therefore, AFM is not the most accurate technique to determine the number of layers in graphene. In this thesis, an Agilent technologies 5500 AFM was used to mainly obtain the surface topography and roughness of our samples. The data treatment was done by using Gwyddion software.

7. Transmission Electron Microscopy (TEM)

The transmission electron microscope is one of the highest resolution characterization tools available for the study of nanomaterials at the atomic level such as graphene. The TEM equipment requires a high set of equipment to achieve a high resolution in a range of 0.1 nm. The electron microscope has three main parts. The first is the electron beam gun and the illumination system, where the electrons are thermionically emitted and focused onto a thin sample, which should be thin enough to transmit the electrons by the electromagnetic lens system. The electrons are generated by a thermionic or field emission gun and injected into the column with accelerating voltages between 30 kV and 300 kV. The second is the sample stage and the objective lens, which is the heart of the microscope. To form a signal in the transmission electron microscope an electron transparent sample (usually having a thickness below 50 nm) is subject to the accelerated and focused beam of electrons and placed in front of the electromagnetic objective lenses. The electron beam transmits the sample and the electrons undergo the scattering process, which affects the provided information. The third part is the imaging system. The image of the sample is projected onto a fluorescent screen, which converts the optical image into an electronic image. It is also possible to observe diffraction patterns. The High-Resolution Transmission Electron Microscope (HRTEM) is powerful enough to visualize the crystal structure and the resolution down to the atomic scale.

Pristine crystalline graphene is sensitive to knock-on damage at voltages above 86 kV[49]. Thus, it requires an acceleration voltage lower than 86 kV for non-destructive electron beam exposure. The low-acceleration voltage, such as 60 kV, coupled with spherical aberration (Cs) corrector, one can obtain atomic resolution imaging in graphene, with other analytical techniques, such as energy dispersion X-ray spectroscopy (EDS) and electron energy loss spectroscopy (EELS). In this thesis, our graphene samples were characterized using the recently installed HRTEM. The instrument is a JEOL NEOARM microscope, equipped with a spherical aberration corrector, operating under UHV to increase the mean free path of the electrons at an acceleration voltage of 60 - 200 kV. The NeoARM features a unique cold field emission gun (Cold-FEG).

New generation STEM detectors (such as bright field, dark field, and secondary electron detector) are designed for HR-STEM state of the art imaging. It benefits instrumental development of GIF Quantum ER to provide energy-filtered TEM, and electron energy loss spectroscopic measurements allowing quantitative information on the elemental composition and the local chemical environment.

8. Electrochemical measurements

The measurement of electrochemical properties of graphene-based materials is necessary for their future use in environmental analytical microsystems, and reactivity of graphene electrodes in the electrochemical sensors. An oxidation-reduction reaction is any chemical reaction in which the oxidation number of molecules, atoms, or ion changes by gaining or losing an electron. Applying a potential difference between two electrodes that are immersed in an electrolyte solution can cause electron transfer between atomic and molecular species, within the electrolyte. Then, the electrons move towards the positive electrode, while the ionized molecules (positively charged) are accelerating towards the negative electrode. As a result, it is observed the dependence of current between the electrodes with the applied potential.

Cyclic voltammetry (CV) is an electrochemical technique, which measures the developed current in an electrochemical cell. Using the three-electrode system, which consists of a reference electrode, a counter electrode, and a working electrode, the CV is carried out by cycling the potential of a working electrode and measuring the resulting current. The potential step varies linearly with time; this ramping is known as a scan rate. The potential is applied between the reference and the working electrodes, and then the response is measured between the working and the counter electrodes.

As shown in **Figure 2.16a**, a typical reduction occurs from A to D, and oxidation occurs from D to G. In the forward sweep, from a higher potential A to a lower potential D, the potential is scanned negatively. The potential D namely the switching potential is the point where the voltage is sufficient to give rise to oxidation or reduction of an analyte. In the reverse backward sweep, the potential scans positively from D to G. This cycle can be repeated several times during a single scan, and the scan rate can vary[50,51]. **Figure 2.16b** shows the voltammogram of the reversible reduction of a 1 mM Fc^+ (Fc means “ferrocene”) solution to Fc. The reduction process occurs from the initial potential to D the switching potential. In this region, the potential is scanned negatively to induce a reduction. At point C, where the peak cathodic current (i_{pc})

and potential (E_{pc}) is observed, the current is dictated by the delivery of additional Fc^+ via diffusion from the bulk solution. When the switching potential (D) is attained, the sweep direction is reversed, and the potential is scanned positively from D to G, resulting in the anodic current (I_{pa}) and oxidation reaction. Besides, the concentrations of Fc^+ and Fc at the electrode surface are equal at points B and E, following the Nernst equation, $E = E_{1/2}$[50]. The peak potential at F is called the anodic peak potential (E_{pa}) and is reached when all the Fc present at the electrode surface is oxidized back to Fc^+.

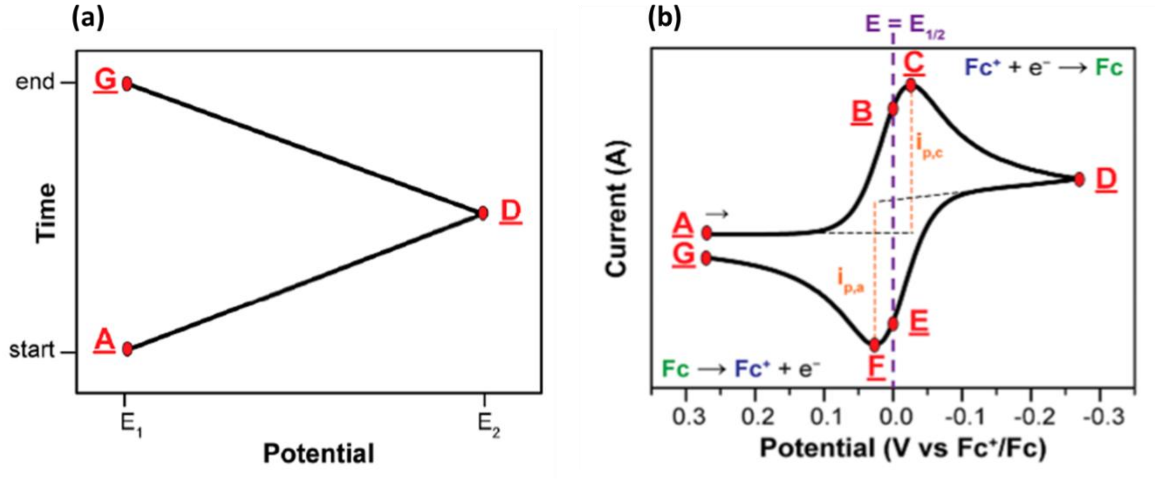

Figure 2. 16 (a) A typical cyclic voltammetry potential. (b) Voltammogram of the reversible reduction of a 1 mM Fc^+ solution to Fc, at a scan rate of 100 mV s^{-1}[50].

The separation between the two peaks potentials $\Delta Ep = E_{pa} - E_{pc}$ is used to determine the electrochemical reversibility for a redox couple with the following equation[51]:

$$\Delta E_p = 59/n\ [\mathrm{mV}]\ (\text{at } 25°\mathrm{C}) \qquad \text{(Eq.2.15)}$$

This value is independent of the scan rate for fast electron transfer, in other words for electrochemically reversible processes referred to as “Nernstian” processes. Indeed, if the reduction process is chemically and electrochemically reversible, the difference between the anodic and cathodic peak potentials, called peak-to-peak separation (ΔEp), is 57 mV at 25°C, and the width at half max on the forward scan of the peak is 59 mV[51]. By contrast, the presence of electrochemical irreversibility is indicated by the increase of ΔEp values when the scan rate increases.

Here, in this work, the electrochemical measurements were performed with our collaborative laboratory ISA (Lyon, France) in a conventional one compartment-three electrodes cell. The electrochemical cell is hermetically closed on one side with graphene and boron-doped graphene electrodes, and on the other side, a planar platinum electrode was used as the counter electrode. Ag/AgCl electrode was used as a reference. A multichannel potentiostat VMP3 was used for measurements and the results were recorded and analyzed using EC-Lab software from BioLogic Science Instruments. The electrochemical characterization of graphene and boron-doped graphene films were studied by CV starting from -0.2 V vs SCE to 0.6 V vs SCE repeated 3 times in a solution containing 5 mL of Fc-bismethanol 0.5mM and $NaClO_4$ 0.1M as support electrolyte and the scan rate was 50 mV/s.

IV. Conclusions

In this chapter, we presented the graphene and doped graphene synthesis method used in this work. It describes in one hand the resistive evaporator used for nickel catalyst thin film, the pulsed laser deposition (PLD) to obtain a carbon-based solid precursor, the rapid thermal annealing (RTA) system utilize to convert the amorphous carbon into graphene-based material. On the other hand, this chapter covers the different characterization methodologies and techniques carried out to measure, at various scales, the physico-chemical and structural characteristics of the films.

Indeed, the studied materials (carbon precursor and more particularly graphene) require careful and precise characterization given the sensitivity of the information to small variations. We have to take into consideration the specificities of graphene characterization which is often considered “at the frontier” between material and surface science, taking into account, in particular, the ultra-low film thicknesses (from one monolayer to a few ones) and surface homogeneity, the constituting light elements (including N and B dopants, in addition to the carbon skeleton), and the film sensitivity to irradiation damages during analysis.

In the following Chapter 3, we will present and discuss the study of the graphene growth mechanism by carbon diffusion and segregation into the nickel catalyst through XPS analysis and modeling.

References

1. What is Thin Film Deposition By Thermal Evaporation? http://www.semicore.com/news/71-thin-film-deposition-thermal-evaporation.
2. Liu, J. M. Simple technique for measurements of pulsed Gaussian-beam spot sizes. *Opt. Lett., OL* **7**, 196–198 (1982).
3. Maddi, C. *et al.* Structure, electrochemical properties and functionalization of amorphous CN films deposited by femtosecond pulsed laser ablation. *Diamond and Related Materials* **65**, 17–25 (2016).
4. Maddi, C. *et al.* Nano-Architecture of nitrogen-doped graphene films synthesized from a solid CN source. *Scientific Reports* **8**, (2018).
5. Sikora, A. Incorporation de bore dans des films minces de '"Diamond-Like Carbon"': élaboration par ablation laser pulsée et caractérisation. 188.
6. ©annealsys.com 2020. RTP system for rapid thermal annealing and rapid thermal CVD. https://www.annealsys.com/products/rtp-and-rtcvd/as-one.html.
7. O'Donnell, K. A. Effects of finite stylus width in surface contact profilometry. *Appl. Opt., AO* **32**, 4922–4928 (1993).
8. Casiraghi, C. Raman intensity of graphene. *physica status solidi (b)* **248**, 2593–2597 (2011).
9. Ferrari, A. C. Raman spectroscopy of graphene and graphite: Disorder, electron–phonon coupling, doping and nonadiabatic effects. *Solid State Communications* **143**, 47–57 (2007).
10. Malard, L. M., Pimenta, M. A., Dresselhaus, G. & Dresselhaus, M. S. Raman spectroscopy in graphene. *Physics Reports* **473**, 51–87 (2009).
11. Cançado, L. G. *et al.* Quantifying Defects in Graphene via Raman Spectroscopy at Different Excitation Energies. *Nano Lett.* **11**, 3190–3196 (2011).
12. Ferrari, A. C. *et al.* Raman Spectrum of Graphene and Graphene Layers. *Phys. Rev. Lett.* **97**, 187401 (2006).
13. Ferrari, A. C. & Robertson, J. Interpretation of Raman spectra of disordered amorphous carbon. *Physical Review B* **61**, 14095–14107 (2000).
14. Martins Ferreira, E. H. *et al.* Evolution of the Raman spectra from single-, few-, and many-layer graphene with increasing disorder. *Phys. Rev. B* **82**, 125429 (2010).

15. Bayle, M. *et al.* Dependence of the Raman spectrum characteristics on the number of layers and stacking orientation in few-layer graphene. *physica status solidi (b)* **252**, 2375–2379 (2015).
16. Peng, Z., Yan, Z., Sun, Z. & Tour, J. M. Direct Growth of Bilayer Graphene on SiO2 Substrates by Carbon Diffusion through Nickel. *ACS Nano* **5**, 8241–8247 (2011).
17. Xiong, W. *et al.* Single-Step Formation of Graphene on Dielectric Surfaces. *Advanced Materials* **25**, 630–634 (2013).
18. Pan, G. *et al.* Transfer-free growth of graphene on SiO2 insulator substrate from sputtered carbon and nickel films. *Carbon* **65**, 349–358 (2013).
19. Orofeo, C. M., Ago, H., Hu, B. & Tsuji, M. Synthesis of large area, homogeneous, single layer graphene films by annealing amorphous carbon on Co and Ni. *Nano Res.* **4**, 531–540 (2011).
20. Hemani, G. K. *et al.* Interfacial graphene growth in the Ni/SiO2 system using pulsed laser deposition. *Appl. Phys. Lett.* **103**, 134102 (2013).
21. An, S. *et al.* A facile method for the synthesis of transfer-free graphene from co-deposited nickel–carbon layers. *Carbon* **109**, 154–162 (2016).
22. Tuinstra, F. & Koenig, J. L. Raman Spectrum of Graphite. *J. Chem. Phys.* **53**, 1126–1130 (1970).
23. Matthews, M. J., Pimenta, M. A., Dresselhaus, G., Dresselhaus, M. S. & Endo, M. Origin of dispersive effects of the Raman D band in carbon materials. *Phys. Rev. B* **59**, R6585–R6588 (1999).
24. Cançado, L. G. *et al.* General equation for the determination of the crystallite size La of nanographite by Raman spectroscopy. *Appl. Phys. Lett.* **88**, 163106 (2006).
25. Lui, C. H. *et al.* Imaging Stacking Order in Few-Layer Graphene. *Nano Lett.* **11**, 164–169 (2011).
26. Fang, W. *et al.* Rapid Identification of Stacking Orientation in Isotopically Labeled Chemical-Vapor Grown Bilayer Graphene by Raman Spectroscopy. *Nano Lett.* **13**, 1541–1548 (2013).
27. Jhang, S. H. *et al.* Stacking-order dependent transport properties of trilayer graphene. *Phys. Rev. B* **84**, 161408 (2011).
28. Pisana, S. *et al.* Breakdown of the adiabatic Born–Oppenheimer approximation in graphene. *Nature Mater* **6**, 198–201 (2007).
29. Stampfer, C. *et al.* Raman imaging of doping domains in graphene on SiO2. *Appl. Phys. Lett.* **91**, 241907 (2007).

30. Casiraghi, C. Doping dependence of the Raman peaks intensity of graphene close to the Dirac point. *Phys. Rev. B* **80**, 233407 (2009).
31. Das, A. *et al.* Monitoring dopants by Raman scattering in an electrochemically top-gated graphene transistor. *Nature Nanotechnology* **3**, 210–215 (2008).
32. Beams, R., Gustavo Cançado, L. & Novotny, L. Raman characterization of defects and dopants in graphene. *J. Phys.: Condens. Matter* **27**, 083002 (2015).
33. Iqbal, M. Z., Kelekci, O., Iqbal, M. W. & Eom, J. The structural and electrical evolution of chemical vapor deposition grown graphene by electron beam irradiation induced disorder. *Carbon* **59**, 366–371 (2013).
34. Singh, A. K. *et al.* Tailoring the Electrical Properties of Graphene Layers by Molecular Doping. *ACS Appl. Mater. Interfaces* **5**, 5276–5281 (2013).
35. Iqbal, M. Z., Siddique, S., Iqbal, M. W. & Eom, J. Formation of p–n junction with stable p-doping in graphene field effect transistors using deep UV irradiation. *J. Mater. Chem. C* **1**, 3078–3083 (2013).
36. Yan, J., Zhang, Y., Kim, P. & Pinczuk, A. Electric Field Effect Tuning of Electron-Phonon Coupling in Graphene. *Phys. Rev. Lett.* **98**, 166802 (2007).
37. Tongay, S. *et al.* Stable hole doping of graphene for low electrical resistance and high optical transparency. *Nanotechnology* **22**, 425701 (2011).
38. Ferralis, N., Maboudian, R. & Carraro, C. Evidence of Structural Strain in Epitaxial Graphene Layers on 6H-SiC(0001). *Phys. Rev. Lett.* **101**, 156801 (2008).
39. Brundle, C. R., PhD, L. W., Evans, C. A., Wilson, S. & Wilson, G. *Encyclopedia of Materials Characterization: Surfaces, Interfaces, Thin Films*. (Gulf Professional Publishing, 1992).
40. Barr, T. L. *Modern ESCAThe Principles and Practice of X-Ray Photoelectron Spectroscopy*. (CRC Press, 1994).
41. Watts, J. F. & Wolstenholme, J. *An Introduction to Surface Analysis by XPS and AES*. (John Wiley & Sons, 2019).
42. Heide, P. van der. *X-ray Photoelectron Spectroscopy: An introduction to Principles and Practices*. (John Wiley & Sons, 2011).
43. Kuzmenko, A. B., van Heumen, E., Carbone, F. & van der Marel, D. Universal Optical Conductance of Graphite. *Phys. Rev. Lett.* **100**, 117401 (2008).
44. Nair, R. R. *et al.* Fine Structure Constant Defines Visual Transparency of Graphene. *Science* **320**, 1308–1308 (2008).

45. Binnig, G., Quate, C. F. & Gerber, Ch. Atomic Force Microscope. *Phys. Rev. Lett.* **56**, 930–933 (1986).
46. Saint Jean, M., Hudlet, S., Guthmann, C. & Berger, J. Van der Waals and capacitive forces in atomic force microscopies. *Journal of Applied Physics* **86**, 5245–5248 (1999).
47. Obraztsova, E. A., Osadchy, A. V., Obraztsova, E. D., Lefrant, S. & Yaminsky, I. V. Statistical analysis of atomic force microscopy and Raman spectroscopy data for estimation of graphene layer numbers. *physica status solidi (b)* **245**, 2055–2059 (2008).
48. Yao, Y., Ren, L., Gao, S. & Li, S. Histogram method for reliable thickness measurements of graphene films using atomic force microscopy (AFM). *Journal of Materials Science & Technology* **33**, 815–820 (2017).
49. Bachmatiuk, A. *et al.* Low Voltage Transmission Electron Microscopy of Graphene. *Small* **11**, 515–542 (2015).
50. Elgrishi, N. *et al.* A Practical Beginner's Guide to Cyclic Voltammetry. *J. Chem. Educ.* **95**, 197–206 (2018).
51. Mabbott, G. A. An introduction to cyclic voltammetry. https://pubs.acs.org/doi/pdf/10.1021/ed060p697 (1983) doi:10.1021/ed060p697.
52. Savéant, J.-M. *Elements of Molecular and Biomolecular Electrochemistry: An Electrochemical Approach to Electron Transfer Chemistry*. (John Wiley & Sons, 2006).

Chapter 3: Mechanism of graphene growth by carbon diffusion-segregation through nickel catalyst: an in situ XPS study

Using pulsed laser deposition for graphene growth, the carbon source is in the solid form as when using the other PVD methods. However, despite several reports on graphene synthesis using a solid carbon source and a metal catalyst, more investigations are needed to understand the atomic-scale mechanism responsible for graphene synthesis.

In this chapter, we studied the growth mechanism of nitrogen-doped graphene obtained by thermal heating of a typical a-C:N film deposited by PLD coupled with X-ray photoelectron spectroscopy (XPS) experiments during the vacuum thermal heating process at different temperatures and times. The results are obtained not only using the XPS and angle resolved-XPS (AR-XPS) but also some ex-situ techniques such as Raman spectroscopy for graphene identification, scanning electron microscopy (SEM) and electron backscattering diffraction (EBSD) for the surface morphology and grains orientation. After analysis and interpretations, our results are compared to the reported studies on the graphene growth mechanism using either CVD or PVD methods.

This chapter is organized in four parts consecutive to the description of the experimental protocol. In the first section, we analyzed the results of the surface morphology and grain orientations of the annealed samples, which is after graphene synthesis. The discussion is focused in particular on the nickel grain size and the nickel grain orientation consecutive to the thermal treatment. In the second part, we examined in situ the chemical forms of carbon and nitrogen, at the end of the annealing process responsible for the nitrogen-doped graphene growth, and before cooling. In the third section, the kinetics of diffusion of the different chemical forms of carbon deduced from in situ XPS snapshots, through the nickel catalyst during thermal annealing at the investigated temperatures and times, are presented. In the last part, we focused on the modeling of carbon diffusion-segregation through nickel thin film, as a function of the same annealing conditions as for the XPS experiments.

I. Experimental protocol

Graphene growth. This stage involves three main steps, as depicted in **Figure 3.1**: the deposition of a-C:N film on the cleaned SiO_2 substrates using pulsed laser deposition (PLD), the deposition of nickel thin film catalyst by thermal evaporation, and the thermal annealing process responsible for the diffusion-segregation of carbon through nickel. Firstly, after ultrasonically cleaned in acetone, ethanol and deionized water baths, the SiO_2 substrate is introduced in a vacuum chamber pumped at a base pressure of 10^{-7} mbar. Then, amorphous carbon films are deposited by femtosecond pulsed laser ablation of high purity graphite target (99.9995% purity) at room temperature with a nitrogen dose of about 16% (nitrogen gas pressure of 0.1 mbar during the ablation process). The ablation time is about 3 min to obtain 10 nm of a-C:N film.

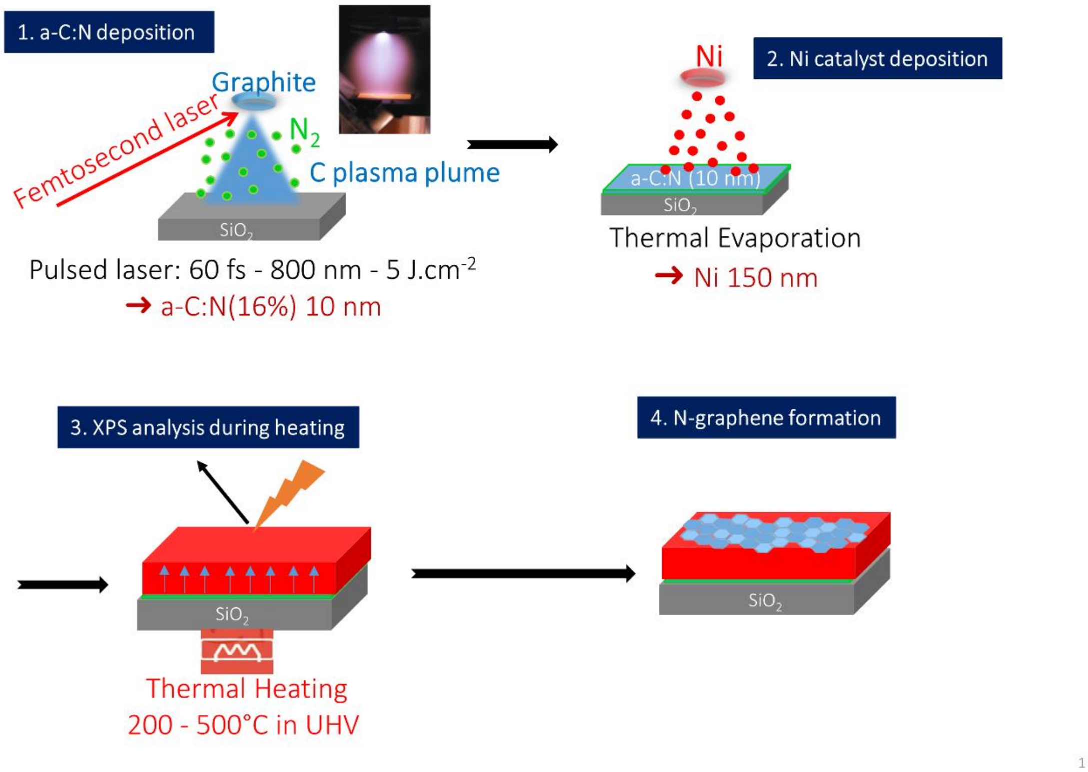

Figure 3. 1 The synthesis process of N-doped graphene films, by thermal heating of a Ni/a-C:N/SiO_2 with in situ XPS analysis.

Secondly, the a-C:N/SiO_2 substrate is placed in another vacuum chamber for 150 nm of nickel thin film deposition using the resistive thermal vacuum evaporator described in chapter 2. Lastly, the key point of this study is the thermal annealing coupled with the in-situ XPS analysis. The Ni(150 nm) /a-C:N (10 nm)/ SiO_2 samples were heated at 200, 300 and 500 °C with a heating ramp rate of 1 °C/s, in an ultrahigh vacuum pressure of 10^{-9} mbar, inside the XPS chamber, as summarized in **Table 3.1**. Before the annealing, a slight argon sputtering was performed followed by a survey spectrum (0-1400 eV) to check that only nickel was detected at the surface of the samples. For each thermal treatment, no other elements were detected at this step. After that, the samples were annealed using a resistive heater incorporated in the sample holder to obtain time-resolved recordings of C1s and $Ni2p_{3/2}$ core levels. The temperature was controlled using a combination of a thermocouple in contact with the surface of the sample, and a pyrometer. For time-resolved analysis, fast acquisition of C1s and $Ni2p_{3/2}$ was performed in snapshot mode using the 128 channels of the energy-dispersive 2D detector axis. Other details on XPS analysis have been described in chapter 2. Angle-resolved XPS measurements were performed at the end of each treatment just before cooling, with an analyzer pass energy of 50 eV. This pass energy gives a width of the $Ag3d_{5/2}$ peak measured on a sputter clean pure Ag sample of 0.55 eV. It is worth noting that these measurements were acquired thanks to the ability of the spectrometer to simultaneously collect several photoelectron emission angles in the acceptance range of 60° without tilting the sample. Components of the C1s peak were adjusted using line shapes consisting of a convolution product of a Gaussian function (75%) and Lorentzian function (25%) for C_{dis} and $C_{carbides}$ and asymmetric lines shapes for C_{Gr} and C_B components for which parameters (tail percentage, height, and exponent) were adjusted on analyzed pure HOPG reference sample.

Heating Temperature	Heating time from room temperature Ramp: +1°C/s	In situ analysis during annealing	Ex-situ analysis
200 °C	6 h 34 min	XPS	None
300 °C	6 h 24 min	XPS	Raman, SEM, EBSD
500 °C	1 h 31 min	XPS	Raman, SEM, EBSD

Table 3. 1 Experimental conditions for thermal heating of $Ni/a\text{-}C:N/SiO_2$ films, with in situ XPS during heating and ex-situ complementary experiments.

Characterizations. The three samples obtained after thermal annealing at 200, 300 and 500°C were also analyzed using other complementary ex-situ techniques. For the graphene structure identification, Raman spectroscopy was performed at a wavelength of 442 nm. The scanning electron microscope and electron-backscattered diffraction (EBSD) were used to obtain the morphological and microstructural information in our samples.

II. Morphology and microstructure analysis of the film after annealing

We investigated the morphology and microstructure analysis using a scanning electron microscope and electron backscattering diffraction measurements on the following samples: the as-deposited Ni on a-C:N/SiO_2 substrate, the deposited film Ni/a-C:N/SiO_2 annealed at 300°C and 500°C in the ultra-high vacuum XPS chamber.

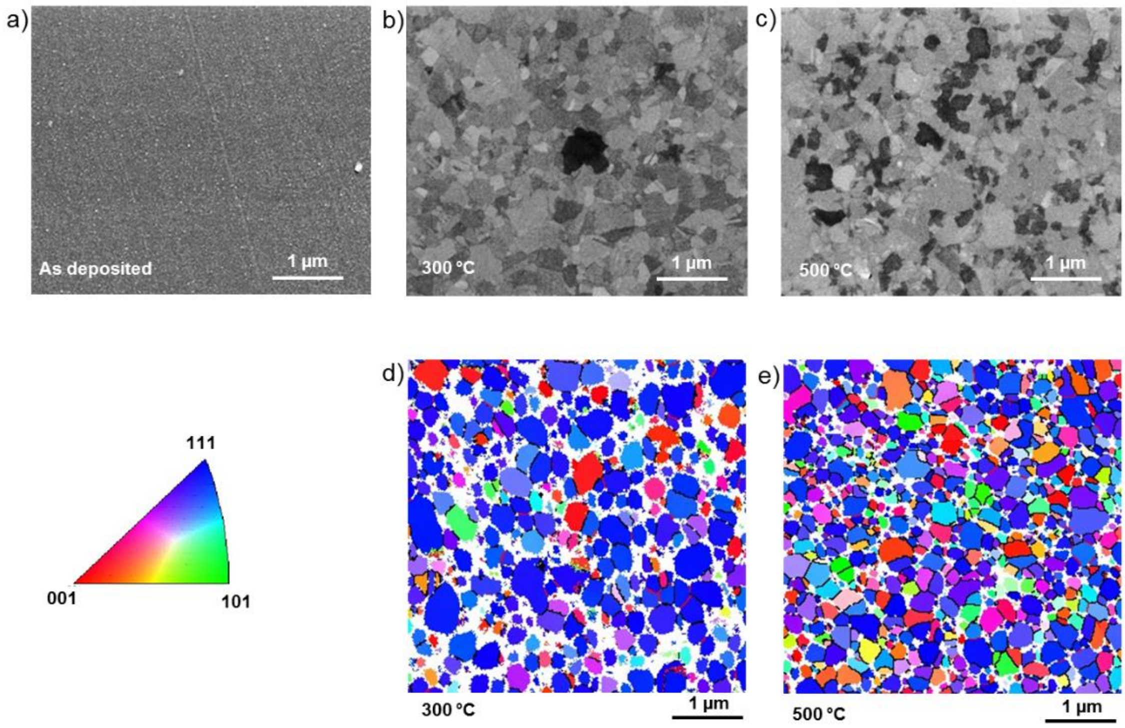

Figure 3. 2 SEM images of a) the as-deposited Ni/a-C:N/SiO_2 before annealing b) after annealing at 300 °C and c) after annealing at 500 °C performed in the ultrahigh vacuum in the XPS chamber. Electron backscattering diffraction (EBSD) orientation map along the sample's Z-direction of d) sample annealed at 300°C and e) 500°C[2].

We observe on the SEM images (**Figure 3.2.a**) that the as-deposited Ni on a-C:N/SiO_2 substrate is very smooth without any revealed grains. After annealing at 300 and 500°C, we can observe that the nickel grain structure was revealed in both images giving an average grain size of about 200 nm (**Figure 3.2.b-e**). Besides, the electron backscattering diffraction orientation maps along the sample's Z-direction of the annealed samples at 300°C and 500°C, presented in **Figures 3.2.d-e**, indicate a (111) texture for both thermal treatments. It was reported that Ni

(111) is ideal for epitaxial graphene due to its weak lattice mismatch of 1.3%[1]. Therefore, this (111) texture observed in the samples annealed at 300 and 500°C could be favorable for epitaxial graphene formation.

III. Carbon and nitrogen chemistry after diffusing across the nickel layer

We performed the XPS measurements on the annealed samples at 200, 300 and 500°C. The carbon chemistry was examined by assigning four components within the C1s spectrum based on preceding interpretations related to graphene films obtained by using metallic catalyst[3,4]. In their work, Weatherup and al.[5] considered that the graphene-catalyst interaction is based on the binding energy shift of the graphitic (Csp^2) component. Taking into account this interaction, we also considered two components for graphene: a component C_{Gr} centered at 284.4 +/-0.1 eV for weakly interacting graphene layers and a component C_B located at 284.8 +/- 0.1 eV for graphene that strongly interacts with the nickel catalyst. The function and parameters (binding energy, full width at half maximum, peak asymmetry) for the C_{Gr} and C_B components were determined using C1s spectrum measured on a pure HOPG reference sample. The two other contributions in the C1s peak were a component C_{dis} at 283.8 +/-0.1 eV corresponding to carbon in solid solution Ni(C) interstitially dissolved in the metal catalyst and a component $C_{carbide}$ at 282.9 +/-0.1 eV associated with the precipitation of nickel carbides. In addition, the N1s spectrum at the end of thermal annealing at 500 °C (i.e. before cooling) was fitted with four components as shown in **Figure 3.3.** The N/(N+C) ratio deduced from XPS analysis is about 4 at.%. and the four components observed on this N1s spectrum are interpreted based on previous reported works[4,6–8]. There were detected at 398.2, 400.1, and 401.5 eV for pyridinic, pyrrolic, and quaternary (or graphitic) nitrogen configuration respectively, in the N-doped graphene films, with a predominance of the pyrrolic configuration. An additional pyridinic oxide configuration was detected at a higher binding energy of 403.9 eV. The C_B and C_{Gr} components certainly include the carbon-nitrogen bonds, but the low nitrogen concentration of 4 at.% did not enable the identification of their contribution. Besides, the amount of nitrogen decreased during the transformation of a-C:N to nitrogen-doped graphene, from 16 to 4 at. %. This may be probably due to the diffusion of nitrogen through the nickel catalyst during the process. It is also worth mentioning that nickel nitride which was evidenced by an N1s peak at binding energy at 395.8 eV[9] were not detected which involves that no or few amounts of nitrides (< 0.1 %at) were formed during thermal annealing. Our nitrogen content is comparable with what was found using the hydrothermal method[8] and thermal exfoliation of graphite oxide for graphene doping with nitrogen[7].

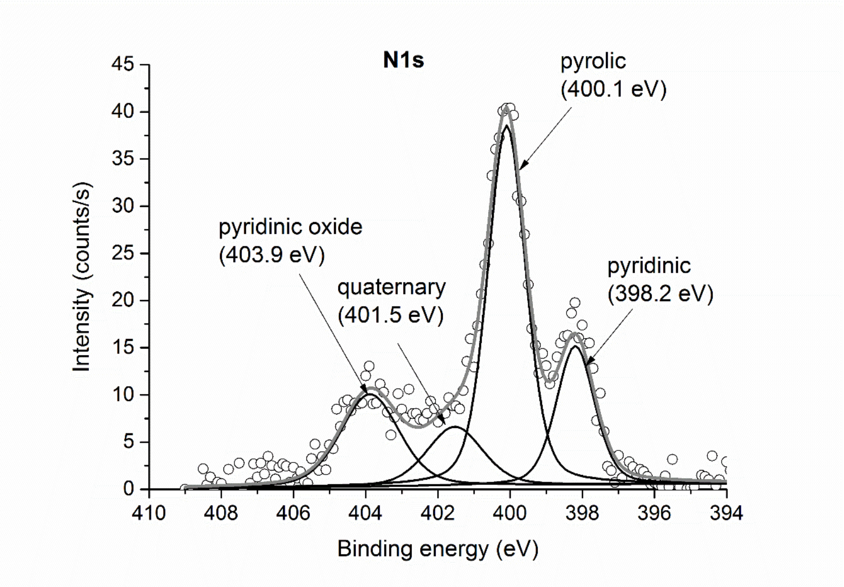

Figure 3. 3 The N1s spectrum recorded at the end of the annealing treatment at 500 °C before cooling[2].

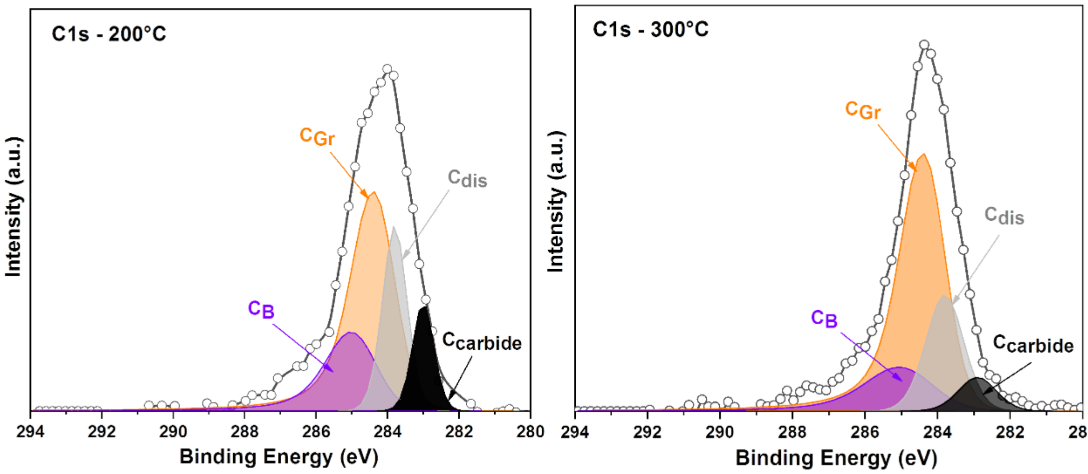

Figure 3. 4 XPS analysis of C1s at the end of annealing treatments with adjustments of C1 peaks using the four components: a) at 200 °C; b) at 300 °C

Concerning the XPS spectra of C1s, **Figure 3.4** shows typical adjustment using the four previously described components of C1s spectra recorded in XPS at the end of thermal annealing at 200 and 300°C (i.e. before cooling). The four carbon components are well defined, and the components related to graphene (C_{Gr} and C_B) are already present at a temperature as low as 200°C. For the annealed sample at 500°C, C1s spectra were recorded in XPS angle-resolved mode for a photoelectron take-off angle of 35° and take-off angle of 65° (**Figure 3.5a).** Indeed, the measurement at 35° is more bulk sensitive while the one at 65° is more surface sensitive. A comparison of the C1s peak fitting was done for the depth analysis, to obtain the difference in the proportions of the component and the rules out the inhomogeneous distribution. **Figure 3.5b** shows the logarithm of the ratio of 35° "bulk sensitive" and 65° "surface-sensitive" emission angle intensities for each C1s components. Considering that, the signal from a species arises from a layer buried beneath a layer of depth d; this value can be expressed as follows:

$$-\ln\left(\frac{I_{35°}}{I_{65°}}\right) = d\left[\left(1/\lambda\cos(35)\right) - \left(1/\lambda\cos(65)\right)\right] \qquad \text{(Eq.3.1)}$$

Assuming the same electron inelastic mean free path λ for the different components, the logarithm of the intensity ratio gives a direct measurement of the relative value of d.

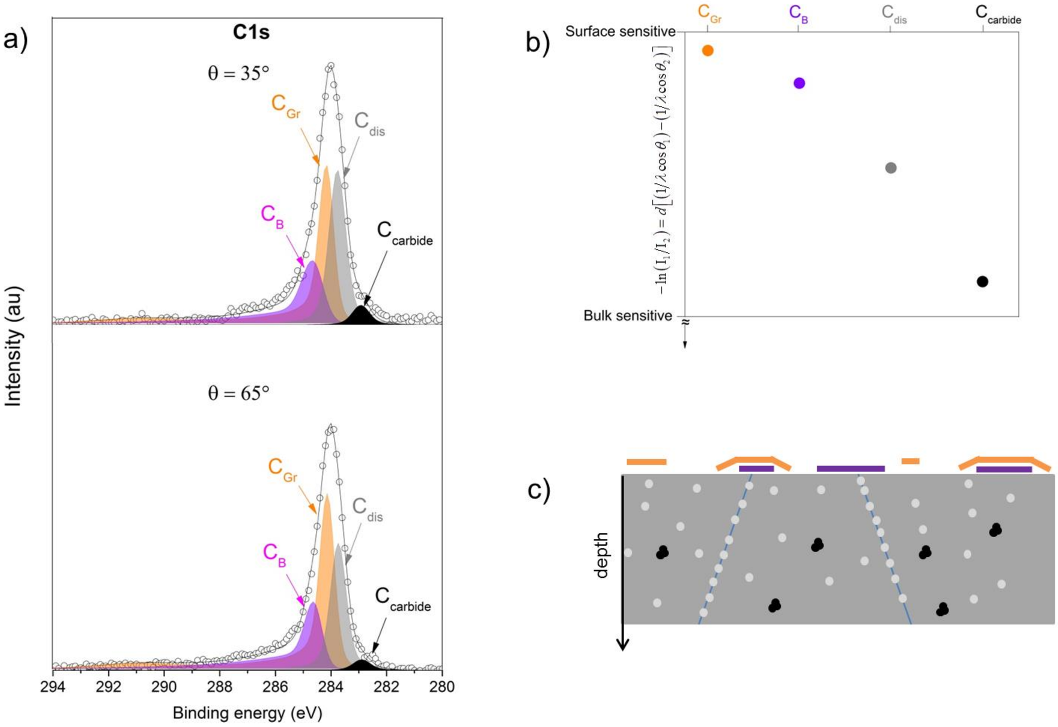

Figure 3. 5 Angle-resolved XPS analysis of C1s at the end of annealing treatment at 500 °C before cooling: a) adjustments of C1 peaks at two photoelectron escape angles using the four components, b) relative depth plot based on the logarithm of the ratio of intensities at ϴ=35° and ϴ=65°, and indicating the relative sensitivity to the surface of each component used to adjust C1s, c) Schematic in-depth distribution based on the relative depth plot results of the carbon species: graphene weakly interacting with Ni "component C_{Gr}", graphene strongly interacting with Ni "component C_B", carbide "component $C_{carbide}$" and carbon dissolved "component C_{dis}"[2].

Figure 3.5b shows the relative depth plot of the four C1s components and demonstrates that C_{Gr} and C_B components are surface-sensitive, while $C_{carbide}$ and C_{dis} components are bulk sensitive (the $C_{carbide}$ component is more bulk sensitive with respect to the C_{dis} component). Based on these observations, a schematic distribution of the different carbon species is proposed in **Figure 3.5c**. The C_{Gr} and C_B surface-sensitive components are associated with the segregation of carbon and the growth of graphene layers at the surface of the sample. The weakly interacting graphene layers tied to the C_{Gr} component is considered as additional graphene layers or rotated graphene, while C_B is considered as strongly interacting epitaxial graphene**[5,10]**. This difference in interaction is confirmed on the relative depth plot of **Figure 3.5b**, with a component C_{Gr} slightly more sensitive to the surface than C_B. On the other hand, the $C_{carbide}$ component is bulk sensitive and may arise from the formation of nickel carbides**[11]**. It is worth noting that at the binding energy of the $C_{carbide}$ component, i.e. close to 283 eV, these carbides are generally assigned to metastable Ni_3C**[12]** from which graphene growth mechanism can be involved in solid state**[11,13]**.

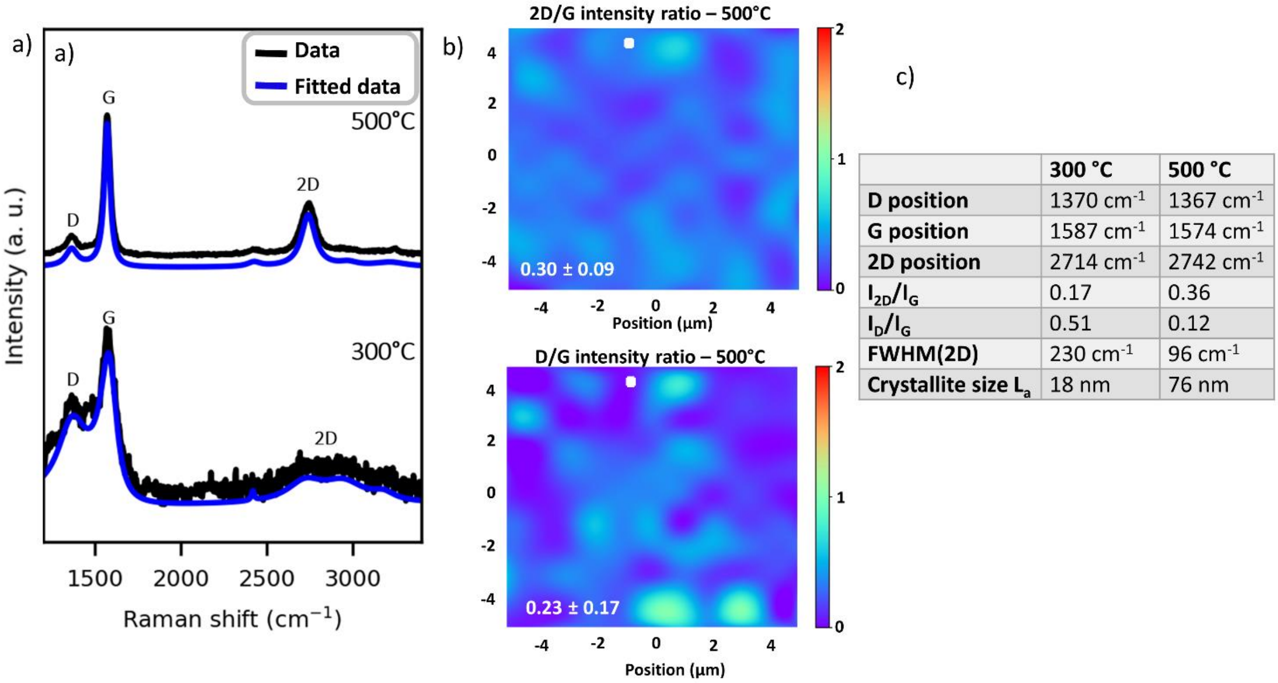

	300 °C	**500 °C**
D position	1370 cm^{-1}	1367 cm^{-1}
G position	1587 cm^{-1}	1574 cm^{-1}
2D position	2714 cm^{-1}	2742 cm^{-1}
I_{2D}/I_G	0.17	0.36
I_D/I_G	0.51	0.12
FWHM(2D)	230 cm^{-1}	96 cm^{-1}
Crystallite size L_a	18 nm	76 nm

Figure 3. 6 a) Raman spectra of the N-doped graphene films after heat treatments at 300 °C and 500 °C in an ultrahigh vacuum; b) Raman mappings (10 x 10 µm²) of the I_{2D}/I_G and I_D/I_G intensity ratios related to the N-doped graphene film synthesized at 500°C. The white mark corresponds to the location of the spectrum depicted in (a). The values 0.30 and 0.23 correspond to the mean values of the I_{2D}/I_G and I_D/I_G intensity ratios respectively over the mapped area; c) Raman characteristics deduced from the spectra depicted in Figure a and b.

For the graphene structure identification, we performed the Raman measurement on the annealed samples at 300 and 500°C, and the interpretation of the Raman D (1350 cm^{-1}), G (1580 cm^{-1}) and 2D (2700 cm^{-1}) bands was based on the literature**[14,15]**. **Figure 3.6a-c** shows the Raman spectra and the corresponding D, 2D, and G band positions and ratios, as well as the FWHM of the 2D band and the crystallite size L_a, deduced from the Tuinstra-Koenig relation**[16]**.

For the annealed sample at 300 °C (after 6 h 24 min of thermal annealing), a wide low 2D band was detected, consistent with the presence of a high defective graphene-like structure, far from typical graphene in which the signature is a high narrow 2D band, as well as a low D band. For the annealed sample at 500 °C (after 1 h 31 min of thermal annealing), the 2D band was consistent with the formation of few-layer graphene, considering an I_{2D}/I_G ratio of 0.36, an FWHM(2D) of 96 cm^{-1} and an I_D/I_G ratio of 0.12 consistent with a crystallite size of 76 nm. **Figure 3.6b** shows the Raman mappings of the I_{2D}/I_G and I_D/I_G ratios for the graphene film obtained at 500°C. The region related to the spectrum depicted in **Figure 3.6a** is localized by a white mark in the Raman mappings. The average values of the ratios I_{2D}/I_G and I_D/I_G are 0.30 and 0.23 respectively. The I_{2D}/I_G ratio indicates the formation with of few-layer rather homogeneous considering a standard deviation of 0.09 deduced from the 100 Raman spectra of the mapping. However, the defects distribution in the sample over the probed area is more heterogeneous, considering a standard deviation of 0.17 for the I_D/I_G ratio. These results are in agreement with the previous works[4,17] reported on nitrogen-doped graphene synthesis using PLD and CVD methods. Indeed, these authors reported the high temperature (700-900°C) synthesis of nitrogen-doped few-layer graphene with 2 to 6 at % of nitrogen and the I_D/I_G and I_{2D}/I_G values ranging between 0.12-0.34 and of 0.21-0.8 respectively. Comparing our I_D/I_G ratio values to the previously reported values, one can suggest that the relatively high value of our I_D/I_G ratio can be due to the nitrogen doping without excluding the other structural defects such as edges, wrinkles, etc…

The chemistry analysis of carbon and nitrogen diffusing from the a-C:N film across the nickel layer revealed that the graphene growth mechanism can be described using the model of carbon diffusion and interaction with the nickel catalyst, the presence of carbides and subsurface carbon species. Our observation is consistent with the reported study on CVD growth mechanism[5]. To evaluate the kinetics of carbon diffusion across the nickel film during the graphene growth and to consider the changes and interactions between the carbons species highlighted above, time-resolved XPS analysis was performed.

IV. Carbon diffusion kinetics across the nickel catalyst film

Fast acquisition of C1s and $Ni2p_{3/2}$ photoelectron peaks, using the snapshot detector mode of the spectrometer, were performed during *in situ* thermal annealing. Unfortunately, because of the low concentration of nitrogen in the graphene film (4 at. %), we could not record the N1s photoelectron peaks using the snapshot mode due to a too low intensity during the thermal annealing process. Indeed, this type of analysis needs fast acquisition during in-situ heat treatment, which is achievable only above a certain peak intensity threshold that was not reached here for nitrogen. Besides, it should also be mentioned that no particular effect of nitrogen on the diffusion-segregation of carbon is expected here. In the case of the C1s peak, the same function parameters defined previously for analysis of the angle-resolved spectrum were used to fit the four components C_{Gr}, C_B, C_{dis} and $C_{carbide}$. Considering the distribution of the different carbon species presented in **Figure 3.5**, the C_{Gr} and C_B components intensities were converted into monolayers using the following equations (In (Eq.3.2), C_{comp} represents either C_{Gr}, either C_B):

$$C_{comp}(monolayer) = \frac{I_{C1s}^{C_{comp}}}{I_{C1s}^{HOPG} \times \left(1 - \exp\left(\frac{-d}{\lambda_{C1s}^{layer}\cos\theta}\right)\right)} \qquad \text{(Eq.3.2)}$$

where I_{C1s}^{HOPG} is the intensity of the C1s peak measure on a pure HOPG reference sample, d = 0.335 nm is the thickness of a graphene monolayer, λ_{C1s}^{layer} the inelastic mean free path of a photoelectron coming from the core level C1s and traveling through a graphene layer for which we chose a value of 1.2 nm based on the work of Tyagi et al.**[18]** and θ the photoelectron escape angle with respect to the normal of the sample surface. As the C_{dis} and $C_{carbide}$ components were assumed to be only distributed in the catalyst substrate, the intensities were converted into an atomic percentage using the intensity of $Ni2p_{3/2}$ and the following expressions equations (In Eq.3, C_{comp} represents either C_{dis}, either $C_{carbide}$):

$$C_{comp}(\%at) = \frac{I_{C1s}^{C_{comp}} / F_{C1s}}{I_{C1s}^{C_{comp}} / F_{C1s} + I_{Ni2p_{3/2}} / F_{Ni2p_{3/2}}} \qquad \text{(Eq.3.3)}$$

$$F_A = \lambda_A^{sub} \times \sigma_A \times T_A \times \left[\tau \times \left(\exp\left(\frac{-d}{\lambda_A^{layer}\cos\theta}\right) - 1\right) + 1\right] \qquad \text{(Eq.3.4)}$$

where $\lambda_A^{(sub,layer)}$ is the inelastic mean free path of a photoelectron coming from the core level A (A being either C1s, either $Ni2p_{3/2}$) in the substrate “sub” or in the carbon segregated surface film “layer”. σ_A is the Scofield ionization cross-section of core level A. T_A is the transmission function at the kinetic energy of the photoelectron coming from the core level A. The thickness of the carbon-segregated layer is noted d and θ is the photoelectron escape angle with respect to the normal of the sample surface. The values of the inelastic mean free path in the segregated carbon film were chosen based on the work of Tyagi and al.[18], and those in the substrate were estimated with the TPP2M method[19]. The results are presented in **Figure 3.7** which represents the fraction of monolayer or atomic percentage of the four C1s components as a function of the square root of the time since we can consider that the kinetics of the four components are driven by the diffusion of carbon across the nickel catalyst layer.

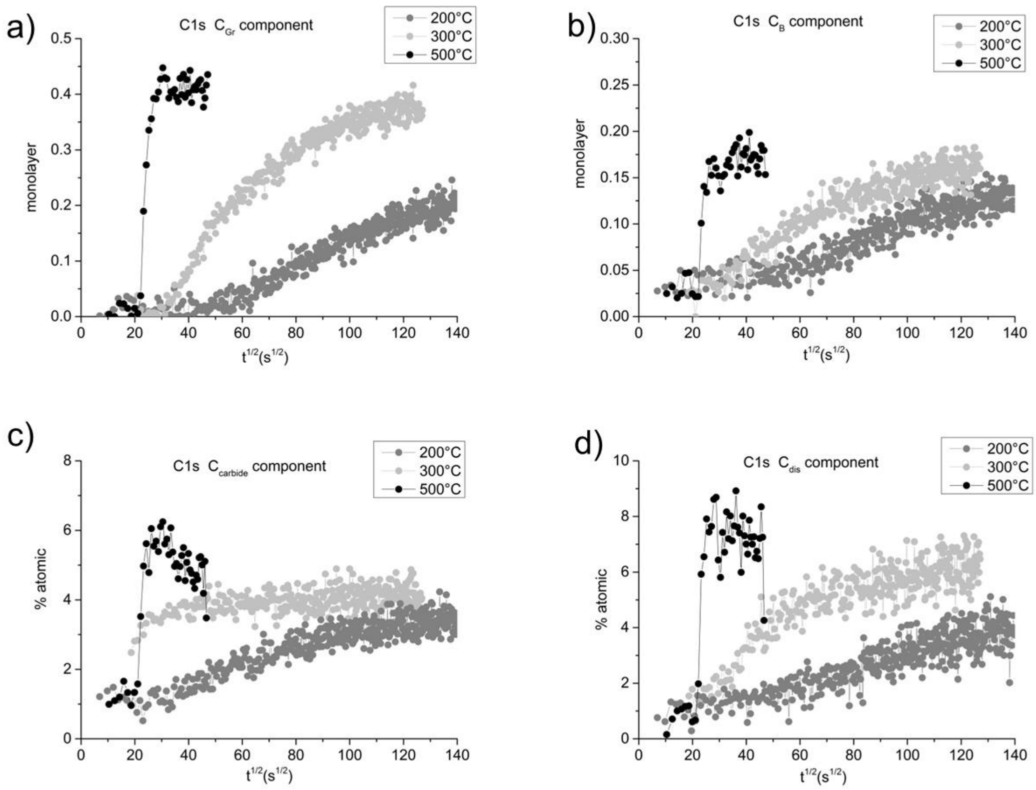

Figure 3. 7 Changes in the function of the square root of the time of surface sensitive components C_{Gr} and C_B of C1s core level expressed as a fraction of the monolayer using Eq.3.2 and bulk sensitive components $C_{carbide}$ and C_{dis} expressed in atomic percent units using Eq.3.3.[2]

Figures 3.7a-b show changes in the fraction of the monolayer of the carbon component that weakly interacts with the nickel catalyst (C_{Gr}) during annealing, and the carbon component, which interacts strongly with the nickel catalyst (C_B). These changes indicate the presence of both types of carbon components even at a temperature as low as 200 °C. It is worth noting that the unambiguous graphene Raman signature was only detected at 500 °C (**Figure 3.2**). This can be explained by the small spatial extent of sp^2 regions at low temperatures and the fact that XPS is more sensitive to local bonding than Raman while the latter is sensitive to the organization, extent, and crystallite size of graphene domains[20]. The changes in C_{Gr} and C_B also suggest that at low temperatures, the diffusion is abnormally fast since the C_B component was detected at the surface after less than one hour ($< t^{1/2} = 60\ s^{1/2}$) at T=200 °C. This point shall be discussed in the following section on the modeling of carbon diffusion and segregation through the nickel film. We also noted that the fraction of monolayer for each component never exceeds a complete monolayer even when both contributions are summed. This can be partly explained by the distribution of the crystallographic orientations of the surface. Among them, some orientations are more favorable for graphene synthesis. In particular, Ni(111) has been reported to be an ideal crystallographic orientation for growing epitaxial graphene[1]. Also, our electron backscattering diffraction orientation map along the sample's *Z*-direction of the sample annealed at 300°C and 500°C indicates a (111) texture for both thermal treatments. Finally, at 500 °C, the presence of a plateau highlights a self-limited reaction that can be described by the diffusion/segregation model. The changes in $C_{carbide}$, shown in **Figure 3.7c**, show the progressive formation of carbides at 200 °C and 300 °C that tends toward a value of 4%. At 500 °C, $C_{carbide}$ first exceeds this value and then starts to decrease due to the decomposition of the metastable carbide. Note that the C_{dis} component appears to be stable when the carbides start to decompose, suggesting that the released carbon does not remain in solid solution but is probably used for graphene growth. Compared to the C_{Gr} component, which clearly shows no change at $t^{1/2} = 30\ s^{1/2}$, C_B appears to increase slightly, suggesting that the released carbon is used for growing graphene strongly interacting with nickel. **Figure 3.7d** shows changes in the C_{dis} component that exhibits atomic concentration in the order of a few percents at the three thermal annealing temperatures (7% at T=500 °C) which represent a large amount of carbon if we consider that this component reflects the presence of dissolved carbon. In particular, the expected equilibrium carbon in a solid solution for the nickel at room temperature is <0.01 at% and in the order of 0.1 at% at 500 °C[21,22]. As we already mentioned, one assumption is to consider that carbon is segregated at nickel grain boundaries.

Analysis of nickel grain size using scanning electron microscopy and electron backscattering diffraction **Figure 3.2 b-e)** showed an average grain size of 200 nm at the end of 300°C and 500°C thermal treatments. Considering the thickness of Ni film with surface equiaxed grains is 150 nm, if the carbon fills all the grain boundaries, this gives an average value of 0.1 atomic percent. This assumption consequently fails to explain the large values associated with the C_{dis} component. Another possible explanation for the high concentration of dissolved carbon is the type of carbon source used in this study, which was amorphous carbon. The measurements of carbon solubility in nickel available in the literature are based on systems in which the carbon source is graphite[21,22], not amorphous carbon. It has been demonstrated that the chemical potential of carbon is significantly higher in amorphous carbon than in graphite[22], which means that the amount of carbon expected to dissolve into nickel is higher when amorphous carbon is used, rather than graphite. This could explain why the concentration of carbon dissolved in nickel is so large in our study.

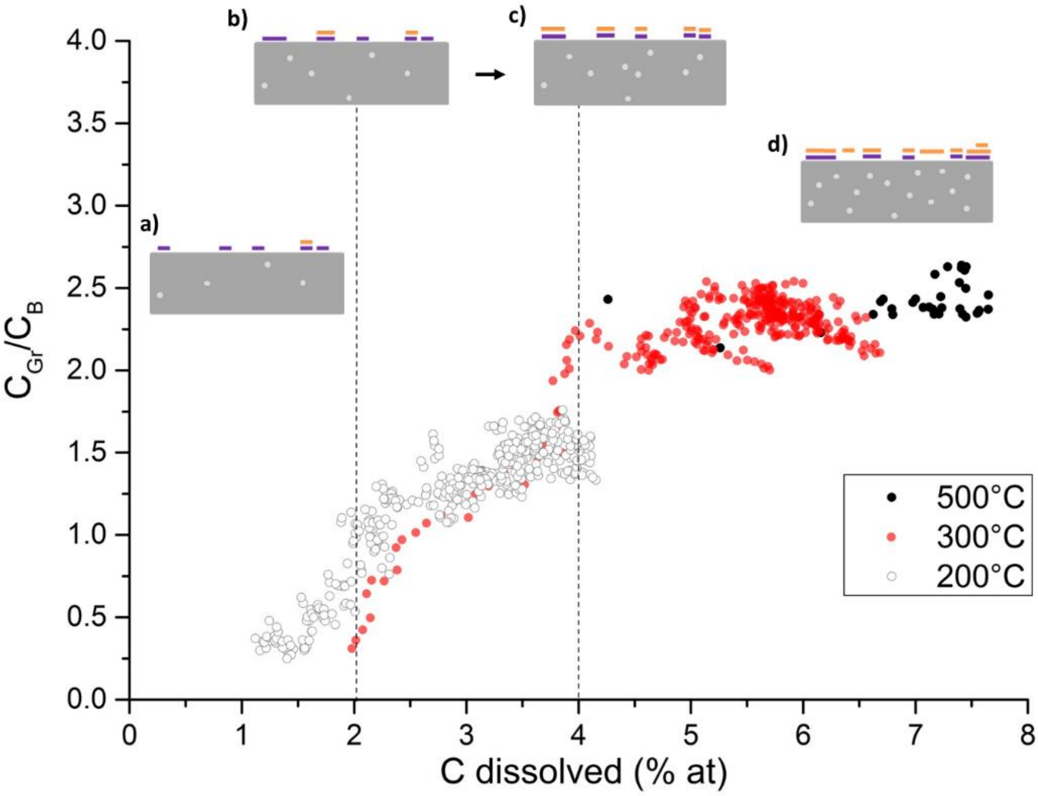

Figure 3. 8 a ratio of the fraction of the C_{Gr} to the C_B component as a function of dissolved carbon based on the kinetics data at 200, 300, and 500 °C (**Figures 3.7 a, b,** and **d**). The sketches a,b,c, and d indicate the effect of C dissolved on the growth of graphene strongly catalyst interacting with nickel (purple) and weakly catalyst interacting graphene layer (purple) for the ranges delimited by dotted lines[2].

The amount of dissolved carbon in the nickel catalyst is of prime importance because it interacts with graphene. In particular, using in-situ XPS measurements and grand canonical Monte Carlo simulation, Weatherup et al.[5] showed that, depending on its amount, the dissolved carbon could weaken the interaction between an epitaxial graphene layer and the catalyst leading to the growth of an additional second layer at the interface between the catalyst and the existing graphene layer. It can also influence the interaction and thus the epitaxy of the graphene as it forms.

Since the work of Weatherup et al.[3] was based on a chemical vapor deposition method, we wanted to investigate whether this behavior will be the same in graphene synthesis via a solid carbon source. **Figure 3.8** shows the influence of the amount of carbon in solid solution on the growth of graphene layers. The figure plots the two graphene components C_{Gr}/C_B ratio of the fraction of the monolayer of weakly interacting carbon with the nickel catalyst, to the one strongly interacting carbon, as a function of the atomic percentage of carbon in solid solution C_{dis} associated with this ratio at each time of the kinetics, at the three annealing temperatures. We observed from this plot three domains:

- A domain with the amount of dissolved carbon < 2 at% where the ratio is weak, and consequently most of the growing graphene is in the form of islands of monolayer epitaxial graphene, with the main contribution coming from C_B (inset (a) in **Figure 3.8**).
- A domain with the amount of dissolved carbon between 2 and 4 at% where the ratio is in the range of 1.3 to 1.5. If we consider a second layer growing between the catalyst and the original islands of graphene monolayers, the ratio of C_{Gr} to C_B should be equal to $\exp(d/\lambda/\cos\theta) = 1.54$. This suggests that in this domain, additional dissolved carbon promotes the progressive growth of bilayer islands (insets (b) and (c) in **Figure 3.8).**
- A domain with the amount of dissolved carbon > 4 at% where the C_{Gr} to C_B ratio is close to 2.5. Such high concentrations of dissolved carbon in nickel additionally favor the formation of weakly interacting graphene (C_{Gr}) (inset (d) in **Figure 3.8**), as observed by Weatherup et al.[7] using CVD synthesis method.

In summary, the analysis of the carbon diffusion kinetics highlights the following points. The carbon diffusion across the nickel catalyst layer is very fast, giving rise to the formation of small graphene islands on the surface of the nickel grains, even at low temperatures. The carbon diffusion triggers the formation of metastable nickel carbides that quickly reach equilibrium at low temperatures but start to decompose at 500 °C, implying that nickel carbides are not the major source involved in the formation of graphene at temperature < 500°C. The behavior of the C_{dis} component reveals that the nickel subsurface is oversaturated with carbon with amounts that can reach 7 at% at 500 °C. Even though it is impossible to unambiguously define the nature of these subsurface carbon atoms (interstitially dissolved or Ni_2C), their presence appears to influence the graphene growth mechanism as already reported in the chemical vapor deposition method[7]. In particular, at low temperatures (T< 500 °C), three domains of subsurface carbon content were identified. For the sake of better understanding the carbon diffusion and segregation through the nickel catalyst film, a model was developed to confront the XPS measurements.

V. Modeling of carbon diffusion and segregation through the nickel thin film

1. Modeling background

The modeling is schematically illustrated in **Figure 3.9**. The solid amorphous carbon located below the nickel film is considered as an infinite source of carbon.

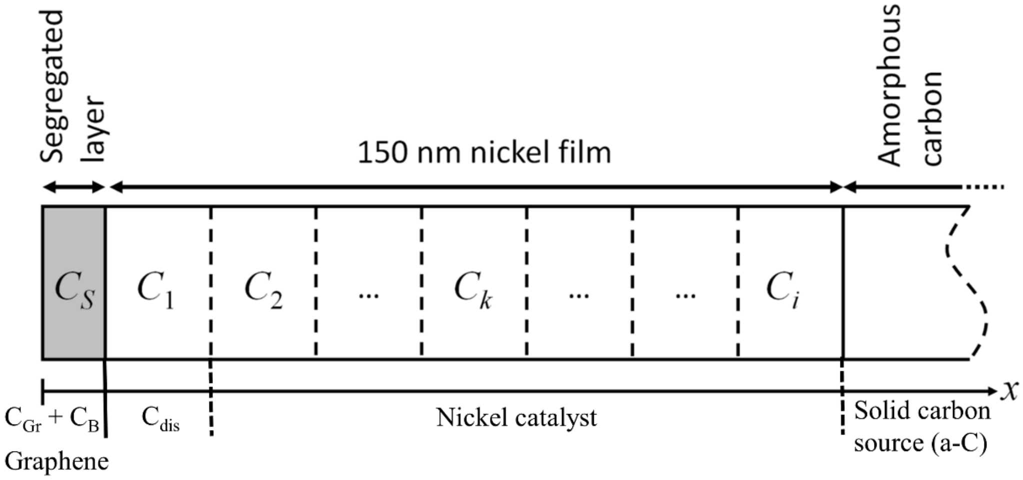

Figure 3. 9 A schematic illustration of the diffusion-segregation model used to fit the experimental kinetics measured using XPS. C_i is considered constant over time at a given temperature (Dirichlet boundary condition). Meshing: one hundred slices in the 150 nm nickel film.

The concentration of dissolved carbon C_i on the underside of the nickel film, i.e. close to the a-C/Ni interface, is fixed (Dirichlet boundary condition). This term is adjusted for each temperature but it is considered constant over time during annealing at a given temperature. Carbon diffusion across the nickel film is calculated using the usual 2nd Fick's law (Eq.3.5):

$$\frac{\partial C}{\partial t} = D\frac{\partial^2 C}{\partial x^2} \qquad \text{(Eq.3.5)}$$

Where C is the carbon concentration (m^{-3}) at depth x and D is the carbon diffusion coefficient in nickel ($m^2\ s^{-1}$). The formation of a carbon-rich film on the nickel surface is treated here as a surface segregation phenomenon. The two types of carbon located at the surface (C_{Gr} and C_B) are considered here as "surface segregated" carbon. The used model to describe carbon surface segregation has been implemented by F. Christien from Ecole des Mines Saint-Etienne. It is based on the Darken-du Plessis approach for interface segregation, which is described in detail in several references[23,24]. This approach has been successfully tested in various complex surface segregation conditions[25–28]. The carbon flux J ($m^{-2}\ s^{-1}$) from the nickel to the segregated layer is given by (Eq.3.6):

$$J = \frac{DC_1}{RT}\frac{\partial \mu}{\partial x} \qquad \text{(Eq.3.6)}$$

where T is the temperature (K), R is the gas constant ($R = 8.314$ J.mol^{-1}.K^{-1}), C_1 is the carbon concentration (m^{-3}) in nickel in contact with the segregated carbon (see **Figure 3.8**) and $\partial\mu/\partial x$ is the gradient of the chemical potential of carbon at the interface between the nickel and the segregated layer. ∂x depends on the mesh size chosen in the calculation. The chemical potential $\partial\mu$ is given by (Eq.3.7):

$$\partial\mu = -\Delta G - RT\ln\frac{\theta}{X_1(1-\theta)}\ , \quad \text{with } X_1 = C_1 / C_{Ni} \text{ and } \theta = C_S / C_{Max} \qquad \text{(Eq.3.7)}$$

where ΔG is the surface segregation free energy of carbon, X_1 and C_1 are respectively the molar fraction and the concentration (m^{-3}) of carbon in nickel in contact with the segregated carbon, C_{Ni} is the number of nickel atoms per unit volume of nickel (m^{-3}), C_S is the carbon concentration in the segregated layer (m^{-2}), C_{Max} is the maximum carbon concentration possible in the segregated layer. The structure of the segregated layer is treated here as a graphene layer so that C_{Max} is the number of carbon atoms per unit surface in a full graphene layer ($3.82\ 10^{19}$ m^{-2}). θ is the coverage ratio. Eq.3.7 is derived from the expressions of the chemical potential of carbon dissolved in nickel and carbon in the segregated layer. Finally, the time-dependence of the carbon concentration in the segregated layer is simply obtained using the following equation (Eq.3.8):

$$\frac{\partial C_S}{\partial t} = J \qquad \text{(Eq.3.8)}$$

The differential equations above were solved using a finite difference method implemented in a bespoke Matlab program. The ode15s solver**[29]** was used and the fitting was performed.

To compare with the XPS measurements, the calculated C_1 concentration (concentration in the bulk just below the segregated layer) and the calculated C_s concentration (carbon concentration in the segregated layer) were compared to C_{dis} and $C_{Gr} + C_B$ values measured by XPS respectively. It worth mentioning that only the carbon diffusion-segregation is addressed by the modeling. Therefore, nitrogen is not taken into account because of its low content measured by XPS. Consequently, no particular effect of nitrogen on the diffusion-segregation behavior of carbon is expected.

	Symbol	Value	Comment
Nickel thickness		150 nm	
Annealing temperature	T	500, 300 and 200 °C	
Number of nickel atoms per unit volume in nickel	C_{Ni}	$9.1\ 10^{28}$ m^{-3}	
Maximum carbon concentration in the segregated layer	C_{Max}	$3.82\ 10^{19}$ m^{-2}	See text
Fixed carbon concentration on the underside of nickel	C_i	7.0%at. at 500 °C 6.2% at. at 300 °C 4.5% at. at 200 °C	Adjusted
The carbon diffusion coefficient in well-crystallized nickel	D	$2.48\ 10^{-4} \exp\left(-\frac{168\ \text{kJ.mol}^{-1}}{RT(K)}\right)\ \text{m}^2\ \text{s}^{-1}$	Lander[30]
Accelerated carbon diffusion coefficient	D	$1.1\ 10^{-18}$ m^2 s^{-1} at 200 °C $3.0\ 10^{-18}$ m^2 s^{-1} at 300 °C	Adjusted
Surface segregation free energy of carbon in nickel	ΔG	-18.8 kJ mol^{-1} at 500 °C -13.6 kJ mol^{-1} at 300 °C -9.8 kJ mol^{-1} at 200 °C	Adjusted

Table 3.3. Modeling inputs.

2. Modeling results

The modeling was performed in two steps. In the first step, bulk diffusion of carbon in nickel was assumed. Lander's temperature-dependent diffusion coefficient was considered (see **Table 3.3**). **Figures 3.9a-b** show the time dependences calculated for segregated carbon and dissolved carbon at 200, 300, and 500 °C respectively, together with the corresponding experimental measurements. The circles represent the experimental carbon surface concentrations ($C_{Gr} + C_B$) measured using XPS. It worth recalling that the used ramping rate to reach the annealing temperature is 1K/s. The arrows in all **Figure 3.10** indicate the time at which the annealing temperature is reached. The temperature dependence of the diffusion coefficient was taken into account in the model. The C_i and ΔG terms were adjusted to 7% at. and -18.8 kJ mol^{-1} respectively to obtain the correct dissolved and segregated carbon concentration at equilibrium at 500 °C. The modeling is in good agreement with the measurements of the annealed sample at 500°C. A sudden rise in the concentration of dissolved and segregated carbon is observed at

$t^{1/2} \approx 20$ s$^{1/2}$, i.e. $t \approx 400$ s, which corresponds to the very end of the temperature ramp ($T \approx 450$ °C).

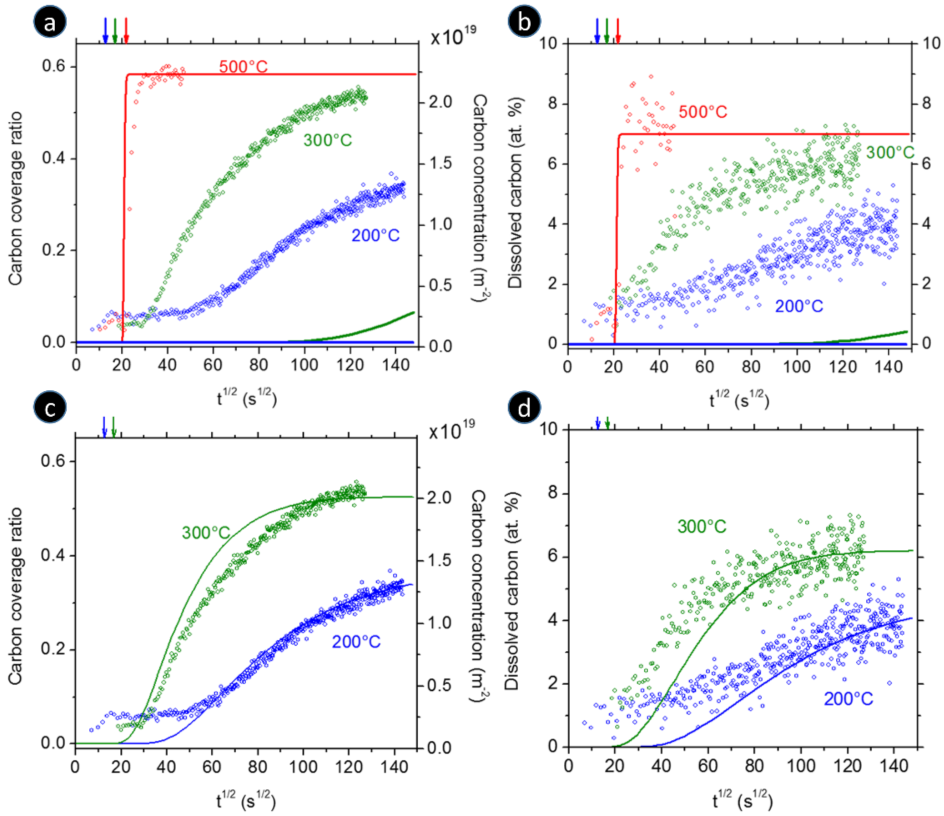

Figure 3. 10 (a) Surface segregation kinetics of carbon during annealing at 200, 300 and 500 °C using the bulk diffusion coefficient of carbon in nickel; (b) Time dependence of dissolved carbon concentration just below the segregated layer during annealing at 200, 300 and 500 °C using the bulk diffusion coefficient of carbon in nickel; (c) Surface segregation kinetics of carbon during annealing at 200 and 300 °C using an accelerated diffusion coefficient of carbon in nickel; (b) Time dependence of dissolved carbon concentration just below the segregated layer during annealing at 200 and 300 °C using an accelerated diffusion coefficient of carbon in nickel.

The good agreement between the modeling and the measurements suggest that the assumption of bulk diffusion of carbon is correct for the annealed sample at 500 °C. However, this is not the case for the two other temperatures. The modeling shows almost no carbon segregated, nor dissolved, even after 20,000 s at 200 °C or 300°C (**Figures 3.10b**). This is in strong disagreement with the experimental data, which shows a significant amount of segregated and dissolved carbon at those temperatures. We can conclude that the effective diffusion coefficient of carbon in the nickel film at 200 °C and 300 °C is certainly far larger than the bulk diffusion coefficient used in the first step of the modeling. The carbon diffusion behavior observed here is related to the nanostructure and defects (vacancies, dislocations, grain boundaries) density of the nickel thin film.

In the annealed sample at 500 °C, the nickel thin film is likely to recover (or even recrystallize) very fast[31,32]. Therefore, carbon diffusion proceeds mainly in a recovered microstructure with a low defect density. However, at 200 °C and 300 °C, the recovery does not take place or at least is much slower than at 500 °C. Consequently, the nickel continues to exhibit a high defect density for longer, which strongly accelerates carbon diffusion[31,33].

In the second step, the accelerated carbon diffusion coefficient was included in the model at 200 °C and 300 °C. Three terms had to be readjusted at each temperature to fit the time dependence of segregated ($C_{Gr} + C_B$) and dissolved (C_{dis}) carbon: the accelerated diffusion coefficient, the segregation free energy, and the carbon concentration on the underside of nickel C_i term. The adjusted values are listed in **Table 3.3** and the plots are shown in **Figure 3.10 c-d**. The diffusion coefficient obtained by fitting at 200 and 300 °C is by one or several orders of magnitude higher than the Lander diffusion coefficient (bulk diffusion). The accelerating factor (ratio of the actual diffusion coefficient to the bulk diffusion coefficient) is 25 at 300 °C and is as high as 16,000 at 200 °C. This shows that the acceleration of diffusion due to the crystal defects in the nickel thin film is more efficient at low temperature, which is consistent with a higher defect density in the nickel thin film.

To conclude this section, one can say that using the modeling based on the Darken-du Plessis approach for interface segregation, we were able to describe carbon diffusion-segregation through the nickel thin film. We found that in the annealed sample at 500 °C, the transport of carbon across the nickel thin film is mainly governed by bulk diffusion. This can be explained by the very fast recovery of the nickel microstructure so that carbon diffusion takes place in a fully recovered microstructure. On the contrary, in the annealed sample at 200 and 300°C, the transport of carbon is faster than bulk diffusion by one or several orders of magnitude. This is consistent with a very slow recovery of the nickel thin film. Consequently, the defect density remains very high, which allows accelerated carbon diffusion.

VI. Summary

This chapter covers the understanding of carbon diffusion and segregation through nickel thin film during graphene synthesis at low temperatures (up to 500°C). To this scope, our samples were investigated by in situ XPS probing during the thermal heating process. Moreover, modeling was performed for a better understanding of the carbon diffusion-segregation mechanism through nickel thin film at different low temperatures. As a result, on one hand, this study shows that up to 500°C, the growth of graphene is driven by the presence and content of subsurface carbon (dissolved carbon in nickel). This subsurface carbon changes the interaction between graphene and catalyst, which results in the growth of epitaxial monolayer to bilayer and rotated graphene domains as the amounts of subsurface carbon increases. Furthermore, from 500°C, the decomposition of metastable Ni_3C is observed and can act as another catalyst phase in graphene growth. On the other hand, the time-resolved XPS measurement and the modeling demonstrated the primary role played by the microstructure and defects density of the catalyst in the case of synthesis from a solid carbon source. Indeed, at low temperatures (200-300°C), the carbon diffusion in nickel catalyst is accelerated due to the high defect density of the nickel film, which is on its turn due to the slow recovery of the nickel microstructure. In contrast, at T=500°C, carbon transport is mainly governed by bulk diffusion due to a fully recovered nickel microstructure. Our findings are in agreement with the reported works on the graphene growth mechanism using the CVD method that uses carbonaceous gases as carbon sources. In summary, this study allows us to describe the graphene synthesis using a solid carbon source at low temperature.

References

1. Natesan, K. & Kassner, T. F. Thermodynamics of carbon in nickel, iron-nickel and iron-chromium-nickel alloys. *MT* **4**, 2557–2566 (1973).
2. Bleu, Y. *et al.* Dynamics of carbon diffusion and segregation through nickel catalyst, investigated by in-situ XPS, during the growth of nitrogen-doped graphene. *Carbon* **155**, 410–420 (2019).
3. Weatherup, R. S. *et al.* Introducing Carbon Diffusion Barriers for Uniform, High-Quality Graphene Growth from Solid Sources. *Nano Lett.* **13**, 4624–4631 (2013).
4. Maddi, C. *et al.* Nano-Architecture of nitrogen-doped graphene films synthesized from a solid CN source. *Scientific Reports* **8**, 3247 (2018).
5. Weatherup, R. S. *et al.* Interdependency of Subsurface Carbon Distribution and Graphene–Catalyst Interaction. *J. Am. Chem. Soc.* **136**, 13698–13708 (2014).
6. Yadav, R. & Dixit, C. K. Synthesis, characterization and prospective applications of nitrogen-doped graphene: A short review. *Journal of Science: Advanced Materials and Devices* **2**, 141–149 (2017).
7. Wang, L., Sofer, Z., Luxa, J. & Pumera, M. Nitrogen doped graphene: influence of precursors and conditions of the synthesis. *J. Mater. Chem. C* **2**, 2887–2893 (2014).
8. Cao, Y. *et al.* Nitrogen-doped graphene: Effect of graphitic-N on the electrochemical sensing properties towards acetaminophen. *FlatChem* **9**, 1–7 (2018).
9. Soo Kang, J. *et al.* Reactively sputtered nickel nitride as electrocatalytic counter electrode for dye- and quantum dot-sensitized solar cells. *Scientific Reports* **5**, 10450 (2015).
10. Patera, L. L. *et al.* In Situ Observations of the Atomistic Mechanisms of Ni Catalyzed Low Temperature Graphene Growth. *ACS Nano* **7**, 7901–7912 (2013).
11. Jiao, M. *et al.* Crystalline Ni_3C as both carbon source and catalyst for graphene nucleation: a QM/MD study. *Scientific Reports* **5**, 12091 (2015).
12. Kovács, Gy. J., Bertóti, I. & Radnóczi, G. X-ray photoelectron spectroscopic study of magnetron sputtered carbon–nickel composite films. *Thin Solid Films* **516**, 7942–7946 (2008).
13. Xiong, W. *et al.* Solid-state graphene formation via a nickel carbide intermediate phase. *RSC Adv.* **5**, 99037–99043 (2015).
14. Malard, L. M., Pimenta, M. A., Dresselhaus, G. & Dresselhaus, M. S. Raman spectroscopy in graphene. *Physics Reports* **473**, 51–87 (2009).

15. Ferrari, A. C. Raman spectroscopy of graphene and graphite: Disorder, electron–phonon coupling, doping and nonadiabatic effects. *Solid State Communications* **143**, 47–57 (2007).
16. Cançado, L. G. *et al.* General equation for the determination of the crystallite size La of nanographite by Raman spectroscopy. *Appl. Phys. Lett.* **88**, 163106 (2006).
17. Wu, J. *et al.* Nitrogen-Doped Graphene with Pyridinic Dominance as a Highly Active and Stable Electrocatalyst for Oxygen Reduction. *ACS Appl. Mater. Interfaces* **7**, 14763–14769 (2015).
18. Tyagi, P. *et al.* Characterization of graphene films grown on CuNi foil substrates. *Surface Science* **634**, 16–24 (2015).
19. Bayer, B. C. *et al.* In Situ Observations of Phase Transitions in Metastable Nickel (Carbide)/Carbon Nanocomposites. *J. Phys. Chem. C* **120**, 22571–22584 (2016).
20. Batzill, M. The surface science of graphene: Metal interfaces, CVD synthesis, nanoribbons, chemical modifications, and defects. *Surface Science Reports* **67**, 83–115 (2012).
21. Singleton, M. & Nash, P. The C-Ni (Carbon-Nickel) system. *Bulletin of Alloy Phase Diagrams* **10**, 121–126 (1989).
22. Jacob, K. T. & Seetharaman, S. Thermodynamic stability of metallurgical coke relative to graphite. *MMTB* **25**, 149–151 (1994).
23. Fournier Dit Chabert, F., Tancret, F., Christien, F., Le Gall, R. & Castagné, J.-F. Finite element simulation of interfacial segregation in dilute alloys. *J Mater Sci* **42**, 9765–9774 (2007).
24. du Plessis, J. & van Wyk, G. N. A model for surface segregation in multicomponent alloys—part III: The kinetics of surface segregation in a binary alloy. *Journal of Physics and Chemistry of Solids* **50**, 237–245 (1989).
25. Tancret, F., Fournier Dit Chabert, F., Christien, F. & Le Gall, R. Finite element simulation of complex interfacial segregation phenomena in dilute alloys. *J Mater Sci* **44**, 4604–4612 (2009).
26. Viljoen, E. C., Jordaan, W. A. & du Plessis, J. On the determination of ternary segregation parameters. *Vacuum* **61**, 141–144 (2001).
27. Wang, J. Y., du Plessis, J., Terblans, J. J. & van Wyk, G. N. Kinetics near the discontinuous surface transition in the Cu(Ag)(111) binary segregating system. *Surface Science* **423**, 12–18 (1999).

28. Christien, F., Le Gall, R. & Saindrenan, G. Application of percolation theory to surface segregation during recovery. *Acta Materialia* **51**, 521–534 (2003).
29. Shampine, L. & Reichelt, M. The MATLAB ODE Suite. *SIAM J. Sci. Comput.* **18**, 1–22 (1997).
30. Lander, J. J., Kern, H. E. & Beach, A. L. Solubility and Diffusion Coefficient of Carbon in Nickel: Reaction Rates of Nickel-Carbon Alloys with Barium Oxide. *Journal of Applied Physics* **23**, 1305–1309 (1952).
31. Humphreys, F. J. & Hatherly, M. *Recrystallization and Related Annealing Phenomena*. (Elsevier, 2012).
32. Darnbrough, J. E. & Flewitt, P. E. J. Growth of abnormal planar faceted grains in nanocrystalline nickel containing impurity sulphur. *Acta Materialia* **79**, 421–433 (2014).
33. Le Gall, R. & Saindrenan, G. Effects of Metastable Diffusion Short-Circuits on Surface Segregation. *Interface Science* **11**, 59–66 (2003).

Chapter 4: Parametric studies for the optimization of graphene synthesis by PLD and RTA

After the study of the mechanism of graphene growth at low temperature in the previous chapter 3, this chapter looks at the synthesis of graphene in a controllable fashion by varying several parameters. The studied parameters to optimize the graphene growth include the substrates, the amorphous carbon thickness, the initial nickel thickness, and the annealing temperature. All together permit to obtain optimized continuous graphene with bilayer predominance using the combination of pulsed laser deposition (PLD) and rapid thermal annealing (RTA) methods.

This chapter comprises three sections as illustrated in **Figure 4.1**. The first part is devoted to the influence of the substrate on the synthesized graphene, the choice of deposition sequence, and the suitable annealing condition for the graphene growth. The second part concerns the effect of the initial thickness of the amorphous carbon and annealing temperature on the graphene synthesis. Finally, the last part investigates the starting thickness of the nickel catalyst effects on the synthesized graphene.

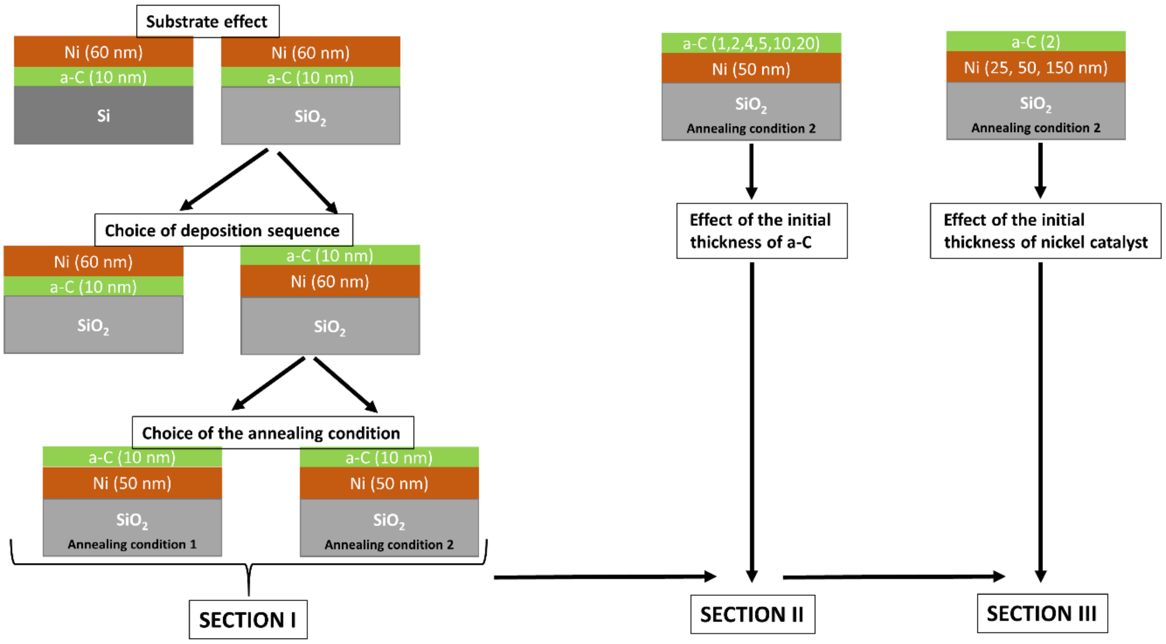

Figure 4. 1 Description of the three parts of this chapter: section I: substrate effect on graphene growth, choice of deposition sequence, and annealing condition. Section II: influence of the thickness of amorphous carbon on the graphene growth. Section III: impact of the nickel catalyst thickness on graphene synthesis.

I. Effect and choice of suitable substrate, deposition sequence and annealing condition for the graphene synthesis

This section highlights first the substrate effect, second the stacking order of the metal / amorphous carbon films effect on the nanostructure of the graphene film, both within an annealing condition range.

1. Substrate effect on the graphene growth

A better understanding of the impact of the substrate on the nature and quality of the resulting graphene is vital for potential applications. One of the objectives of this section I is thus to synthesize graphene on two different typical substrates, crystalline silicon Si(100) and amorphous SiO_2 as illustrated in **figure 4.2**. Indeed, most graphene studies published in the literature report synthesis on those generic substrates more dedicated to electronic applications for Si, and optical applications for SiO_2. We used Raman micro-spectroscopy mapping to examine the influence of modifying the substrate and/or growth temperature (600-1000°C) of graphene synthesis. Several samples were prepared on both substrates at different conditions as shown in **Table 4.1**.

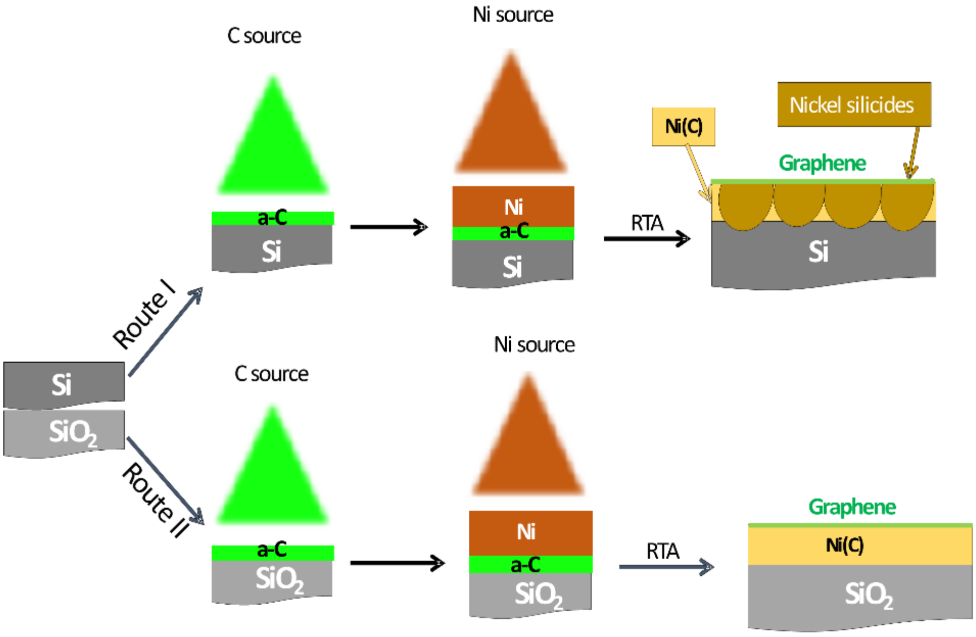

Figure 4. 2 Synthesis route of graphene obtained by combining pulsed laser deposition and rapid thermal annealing on both Si(100) and SiO_2 substrates. The formation of nickel silicides with the Si(100) substrate is detailed in the following paragraphs.

	Graphene precursor & substrate	**RTA temperature**	**Sample label**
Graphene on Si(100)	Ni(60 nm)/a-C(10 nm)/Si(100)	**1000°C**	G-Si-1000
	Ni(60 nm)/a-C(10 nm)/Si(100)	**900°C**	G-Si-900
	Ni(60 nm)/a-C(10 nm)/Si(100)	**800°C**	G-Si-800
	Ni(60 nm)/a-C(10 nm)/Si(100)	**700°C**	G-Si-700
	Ni(60 nm)/a-C(10 nm)/Si(100)	**600°C**	G-Si-600
Graphene on SiO_2	Ni(60 nm)/a-C(10 nm)/SiO_2	**1000°C**	G-SiO_2-1000
	Ni(60 nm)/a-C(10 nm)/SiO_2	**900°C**	G-SiO_2-900
	Ni(60 nm)/a-C(10 nm)/SiO_2	**800°C**	G-SiO_2-800
	Ni(60 nm)/a-C(10 nm)/SiO_2	**700°C**	G-SiO_2-700
	Ni(60 nm)/a-C(10 nm)/SiO_2	**600°C**	G-SiO_2-600

Table 4. 1 The samples and their growth conditions. RTA annealing was performed in a low vacuum at 5×10^{-2} mbar for 600 s, preceded by a +15°C/s heating ramp and followed by cooling limited to -1°C/s.

a. *Influence of substrate on the synthesized graphene as a function of the annealing temperature*

To study the influence of both Si(100) and SiO_2 substrates on the synthesized graphene, Raman mapping of 20 x 20 µm² (each integrating 400 Raman spectra) was carried out on representative areas for each sample. After measurements, we processed the mappings for the following characteristics: I_D/I_G and I_{2D}/I_G intensity ratios, 2D peak FWHM, as well as D, G, and 2D peak positions.

	Graphene on Si(100)					**Graphene on SiO_2**				
RTA temperature	600°C	700°C	800°C	900°C	1000°C	600°C	700°C	800°C	900°C	1000°C
I_D/I_G Std dev	0.297 0.005	0.317 0.008	0.343 0.034	0.459 0.08	0.463 0.031	0.293 0.011	0.269 0.022	0.271 0.016	0.174 0.034	0.140 0.052
La (nm) Std dev	31 0.5	29 0.7	27 6	22 11	20 1	31 1	34 6	34 6	55 11	74 26
I_{2D}/I_G Std dev	0.438 0.012	0.477 0.015	0.409 0.039	0.431 0.085	0.340 0.025	0.412 0.012	0.420 0.042	0.489 0.028	0.721 0.065	0.706 0.118
2D position Std dev	2742 0.8	2739 1	2739 2	2748 3	2754 6	2743 4	2741 3	2737 1	2733 2	2732 3
2D FWHM Std dev	111 1	109 2	110 6	113 14	119 7	108 3	109 6	107 3	87 4	77 6
G position Std dev	1577 0.5	1576 0.6	1575 3	1584 4	1583 2	1580 1	1579 3	1576 2	1574 0.8	1573 1
D position Std dev	1367 0.6	1365 0.7	1365 1	1373 2.5	1373 3	1373 2	1374 3	1367 1	1361 2.5	1360 3

Table 4. 2 Average values and their standard deviations of the Raman characteristics resulting from the 400 Raman spectra performed on representative areas of the synthesized graphene and presented as Raman mappings in the following paragraphs.

Table 4.2 lists the mean values and standard deviation of these characteristics for each sample averaged from each set of 400-recorded spectra. **Figures 4.3a, b** show the Raman mapping of the I_D/I_G intensity ratio and L_a crystallite size for samples grown at all temperatures, on Si and

SiO_2, respectively. On the Si(100) substrate, the mean intensity ratio I_D/I_G increases with the growth temperature from 0.297 to 0.463. This suggests a reduction in the mean crystallite size from 31 to 20 nm as observed in the maps of L_a. This effect is illustrated in **Figure 4.4a** with the plot of I_D/I_G ratio and crystallite size L_a as a function of the growth temperature. On the SiO_2 substrate, the opposite behavior was observed (as shown in **Figure 4.4b**): the mean intensity ratio I_D/I_G decreases from 0.293 to 0.140 with the raise of the growth temperature. This was associated with the increase in the mean crystallite size from 31 to 74 nm. These results suggest that the synthesized graphene using SiO_2 substrate contains lower defects density and larger crystallites compared to the one obtained on Si(100) substrate.

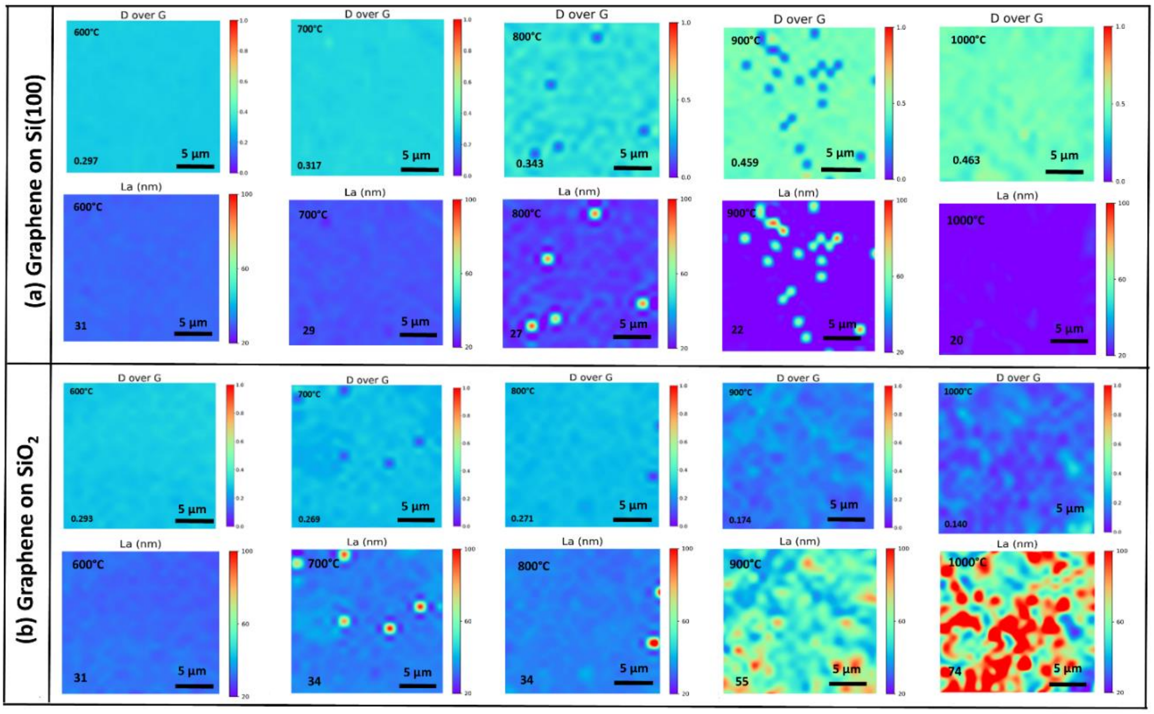

Figure 4. 3 (a) I_D/I_G and L_a Raman mapping of as-grown graphene at temperatures ranging from 600-1000°C on Si(100) with their mean values, (b) I_D/I_G and L_a Raman mapping of as-grown graphene at temperatures ranging from 600-1000°C on SiO_2 with their mean values.

Figure 4.5a, b show Raman mapping of the I_{2D}/I_G intensity ratio and the FWHM of 2D peak for graphene grown at all annealing temperatures, on Si(100) and SiO_2, respectively. On the Si(100) substrate, the mean value of I_{2D}/I_G ratio globally decreases (albeit non-monotonically) with the increase of annealing temperature, from 0.438 to 0.340 (as seen in **Figure 4.4a**), whereas the mean value of FWHM (2D) increases slightly from 111 to 119 cm^{-1}. This suggests that the number of graphene layers increases with increasing the growth temperature. The opposite behavior was observed on the SiO_2 substrate, where the number of graphene layers decreases with an increase in the growth temperature from 600°C to 1000°C. As shown in **Figure 4.4b**, the mean value of the I_{2D}/I_G intensity ratio augments from 0.412 to 0.721, and the

FWHM (2D) mean value diminishes from 108 to 77 cm^{-1} with the increase of the growth temperature. These results suggest that the synthesized graphene on SiO$_2$ substrates presents fewer layers with respect to the synthesized graphene using Si(100) substrate.

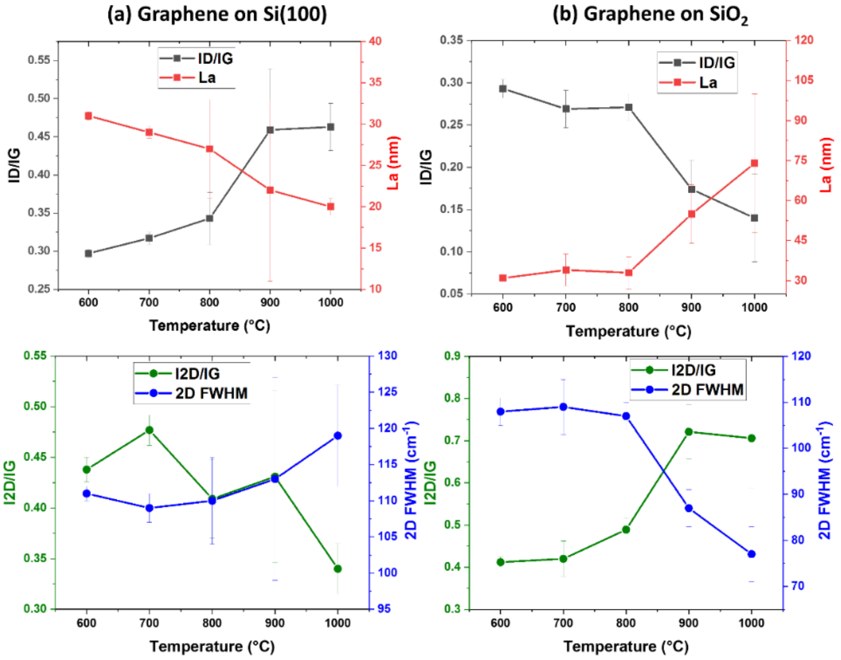

Figure 4. 4 Plots showing dependence on growth temperature as a function of the average value of I$_D$/I$_G$ ratio, crystallite size (La), I$_{2D}$/I$_G$ ratio and the FWHM (2D) for the synthesized graphene: (a) on Si (100); (b) on SiO$_2$.

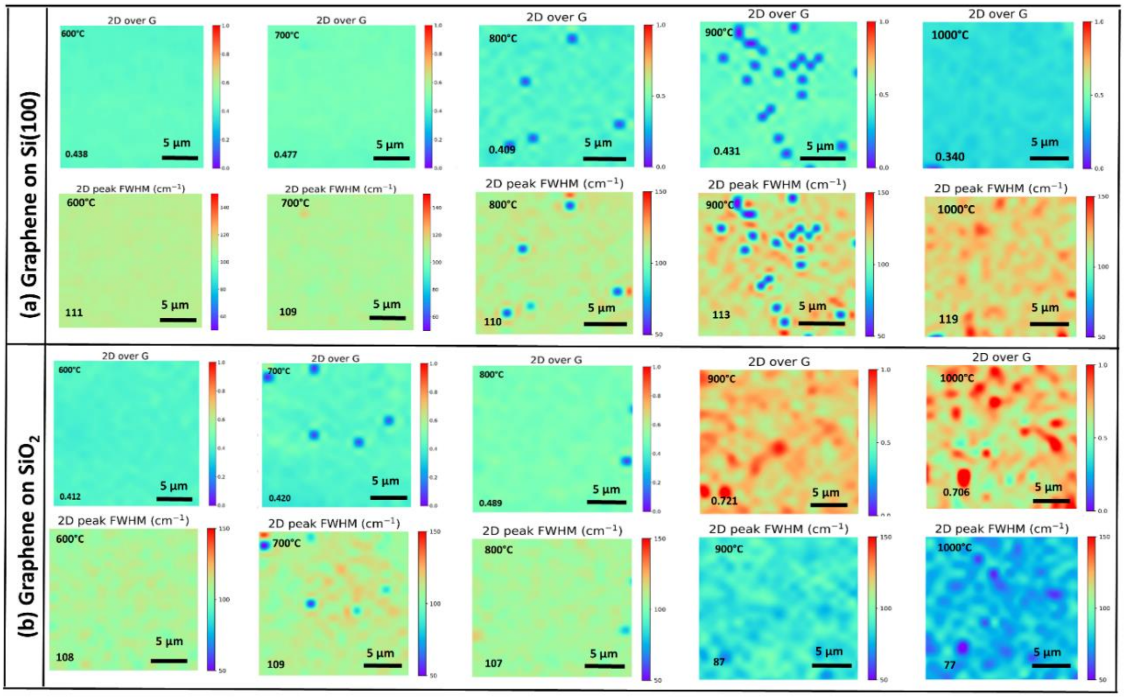

Figure 4. 5 I$_{2D}$/I$_G$ and 2D (FWHM) Raman mapping of as-grown graphene at temperatures ranging from 600-1000°C, with their average values (a) on Si (100), (b) on SiO$_2$.

Figure 4.6 shows typical Raman spectra extracted from the mapping of each of the samples detailed in **Table 4.2**. The major peaks characteristics of graphene D, G, and 2D are visible, with some minor peaks such as D+D'' near 2450 cm^{-1}, D+G near 2950 cm$^{-1,}$ and 2D' near 3250 cm^{-1}, all already observed in some graphene films[1,2]. The red insert in **Figure 4.6b** presents the 2D peak deconvolution of a Raman spectrum from the graphene film obtained at 1000°C on SiO_2. The 2D peak is deconvoluted into four components each with an FWHM of 28 cm^{-1}. According to Malard et al.[3], this is the fingerprint of bilayer graphene. It is worth mentioning that some of the spectra extracted from the mapping of this sample had a substantially larger 2D peak, which was deconvoluted into 6 components (with an FWHM of 28 cm^{-1}), which is consistent with trilayer graphene.

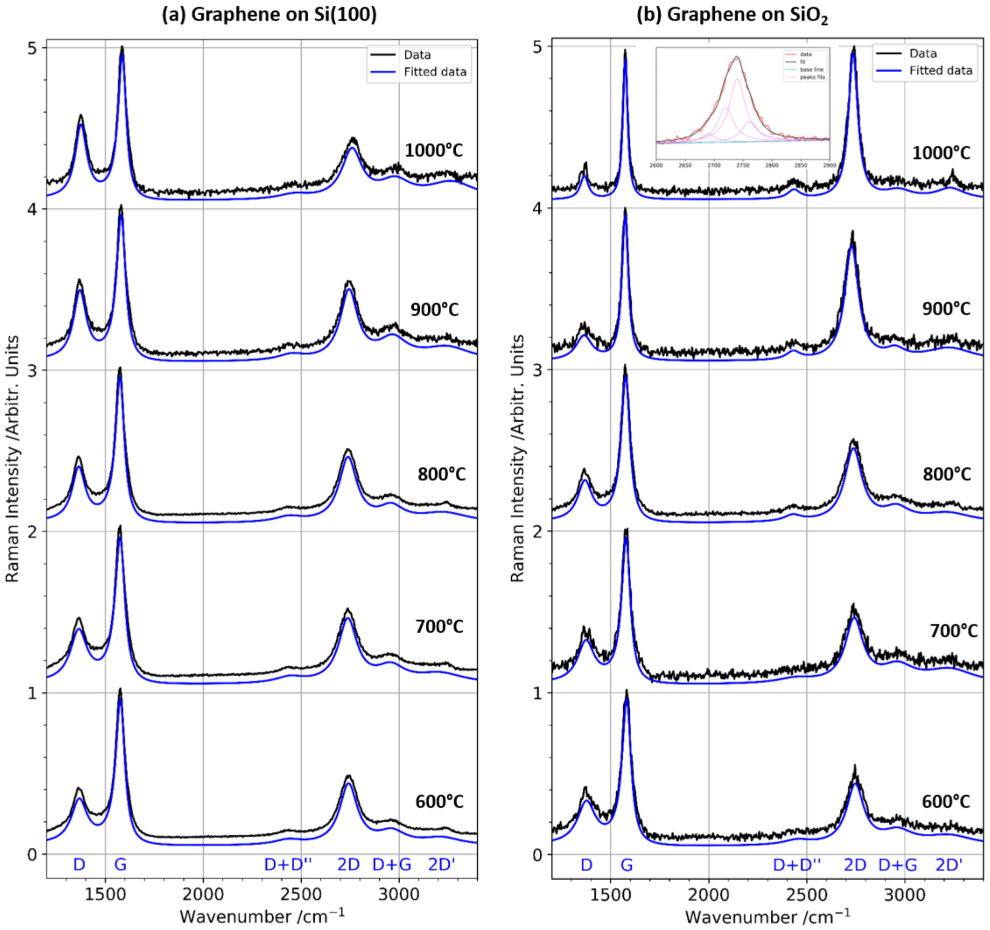

Figure 4. 6 Typical experimental (black) and fitted (blue) Raman spectra of the synthesized graphene films at temperatures ranging from 600-1000°C: (a) on Si (100), (b) on SiO_2 (the red insert corresponds to the deconvolution of the 2D peak of the spectrum of graphene at 1000°C on SiO_2).

Here, we considered that high-quality graphene should exhibit low I_D/I_G and high I_{2D}/I_G ratios. From the Raman mapping of I_D/I_G and I_{2D}/I_G ratios, it appears that, for each substrate, graphene films with the lowest defects content and number of layers were G-Si-600 and G-SiO_2-1000. The G-Si-600 film exhibited I_D/I_G and I_{2D}/I_G ratios of 0.297 and 0.438 respectively, whereas the G-SiO_2-1000 film exhibited I_D/I_G and I_{2D}/I_G ratios of 0.140 and 0.706 respectively. We evaluate the layer number predominance on the surface of both samples based on I_{2D}/I_G ratios values as described in the Raman spectroscopy section of Chapter 2 of this thesis. Therefore, a statistical analysis of the number of graphene layers was performed based on the I_{2D}/I_G values deduced from the 400 spectra recorded on each sample. This analysis quantified the distribution of the I_{2D}/I_G values between their minimum and maximum values for each graphene film. As depicted in **Figure 4.7**, I_{2D}/I_G varied from 0.40 to 0.46 in the Graphene-Si-600 sample, whereas I_{2D}/I_G varied from 0.40 to 1.10 in the Graphene-SiO_2-1000 sample. Based on these statistics, multilayered (>5) graphene is present on 100% of the Graphene-Si-600 sample. Whereas, in the Graphene-SiO_2-1000 sample, 90% of the spectra present an I_{2D}/I_G ranging from 0.65 to 1.10, indicating the formation of predominant 2–3 graphene layers on the SiO_2 substrate. Therefore, we concluded that the Graphene-Si-600 sample has a rather homogeneous architecture comprised of 100% of multilayered graphene, while the Graphene-SiO_2-1000 sample predominantly exhibits a bi- and trilayer architecture.

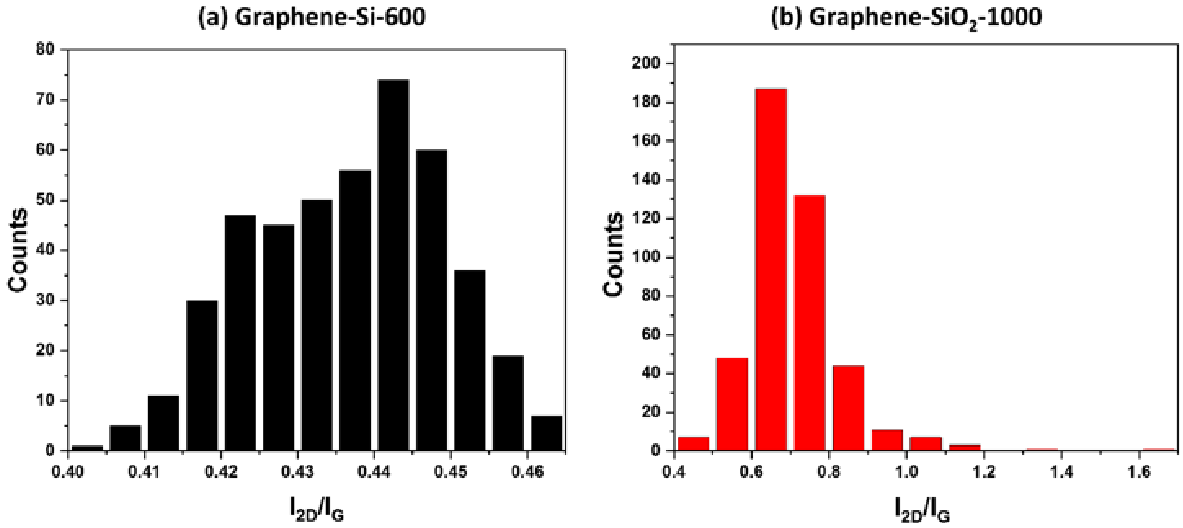

Figure 4. 7 (a) Histogram of the I_{2D}/I_G intensity ratio measured by Raman spectroscopy of 400 graphene films of (a) G-Si-600 sample, (b) G-SiO_2-1000 sample.

b. *Identification of nickel silicide phases when using Si(100) substrate and the related effect with the annealing temperature*

To understand the rather different impacts of the increase of the annealing temperature on the graphene synthesis when using crystalline Si(100) and amorphous SiO_2 substrates, we studied the reactivity of the Ni catalyst layer with the substrate. Indeed, the diffusion of Ni atoms into Si[4] and SiC[5,6] substrates during annealing and the concomitant formation of nickel silicide phases have already been reported. This can affect the diffusion of the carbon through the Ni catalyst as well as nature (number of layers, defects, etc.) of the resulting graphene films. Herein, the nickel silicide formation using Si(100) substrate was studied by Raman spectroscopy in the 100 to 500 cm^{-1} shift range, with laser excitation at 633 nm, as shown in **Figure 4.8a**.

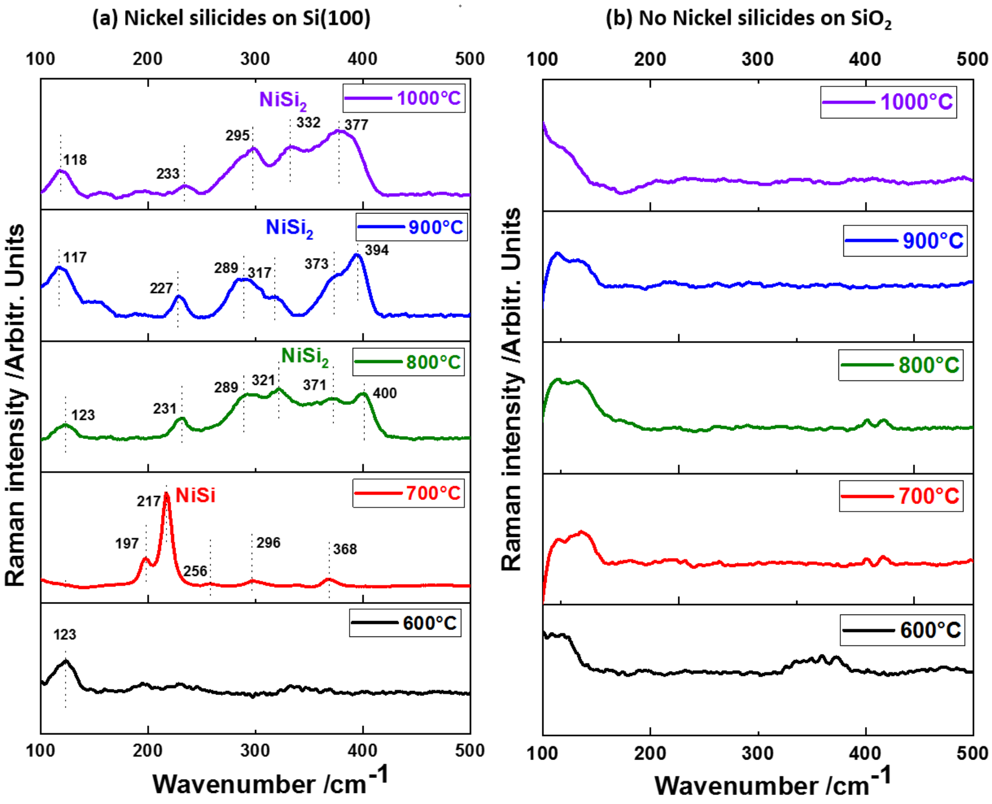

Figure 4. 8 Raman spectra at 633 nm for as-grown graphene with various growth temperatures from 600 to 1000°C (a) On Si(100) substrate, (b) On SiO$_2$ substrate.

The Graphene-Si-600 sample (annealed at 600°C) exhibited no Raman peaks in this spectral region, suggesting that no nickel silicide is formed at this temperature. This could explain the small number of defects in the sample compared with the other samples synthesized at higher temperatures in the similar Si(100) substrate. Besides, the I_D/I_G mean ratio (0.297) of the Graphene-Si-600 sample was quite close to the one (0.293) of Graphene-SiO$_2$-600 (as other Raman characteristics, **Table 4.2**), also annealed at 600°C, meaning that at such low temperature, both synthesized graphene are very similar irrespective of the substrate. At higher growth temperatures, the Raman response evolves very differently in both substrates, which can be correlated with the nickel silicide formation on the Si(100) substrate. According to Raman spectral data in the literature[7–11], Ni_2Si, NiSi, and $NiSi_2$ nickel silicide phases exhibit peaks at 100 and 140 cm^{-1}, 190 and 215 cm^{-1} and 230, 295, 320, and 370 cm^{-1}, respectively. In this study, low wavenumber peaks related to Ni_2Si were never detected irrespective of the annealing temperature. Bhaskaran et al.[11] observed significant background noise in the spectra in this region and concluded that the presence of the Ni_2Si phase, formed by thermal processing of a Ni thin film on a silicon substrate, could not be confirmed. A peak near 120 cm^{-1} (within the 117 and 123 cm^{-1} range) was found at all temperatures, except surprisingly at 700°C. Huong et al.[12] assigned the peak near 120 cm^{-1} to cylindrical graphene walls, but it was not possible to confirm their attribution here. At 700°C, the peaks matching the formation of NiSi were observed, along with weak peaks likely corresponding to $NiSi_2$. Indeed, we cannot exclude the formation of a disilicide nickel phase, which is less Raman sensitive than the NiSi phase. At 800°C and above, only the $NiSi_2$ Raman broad peaks were observed at wavenumbers ranging from 227 to 400 cm^{-1}, while the intensity of the Raman signal of the NiSi phase decreases, which may be consistent with the transformation of the NiSi phase into the $NiSi_2$ phase at the highest temperature. At this point, it is worth noting that all Raman spectra were acquired with the same integration time (30 s). Furthermore, no nickel silicides phases were observed when the graphene was synthesized on the SiO_2 substrate, whatever the temperature, as illustrated in **Figure 4.8b**. The presence of nickel silicide phases is certainly responsible for the differences in the evolution of the Raman responses between the Si(100) and SiO_2 substrates.

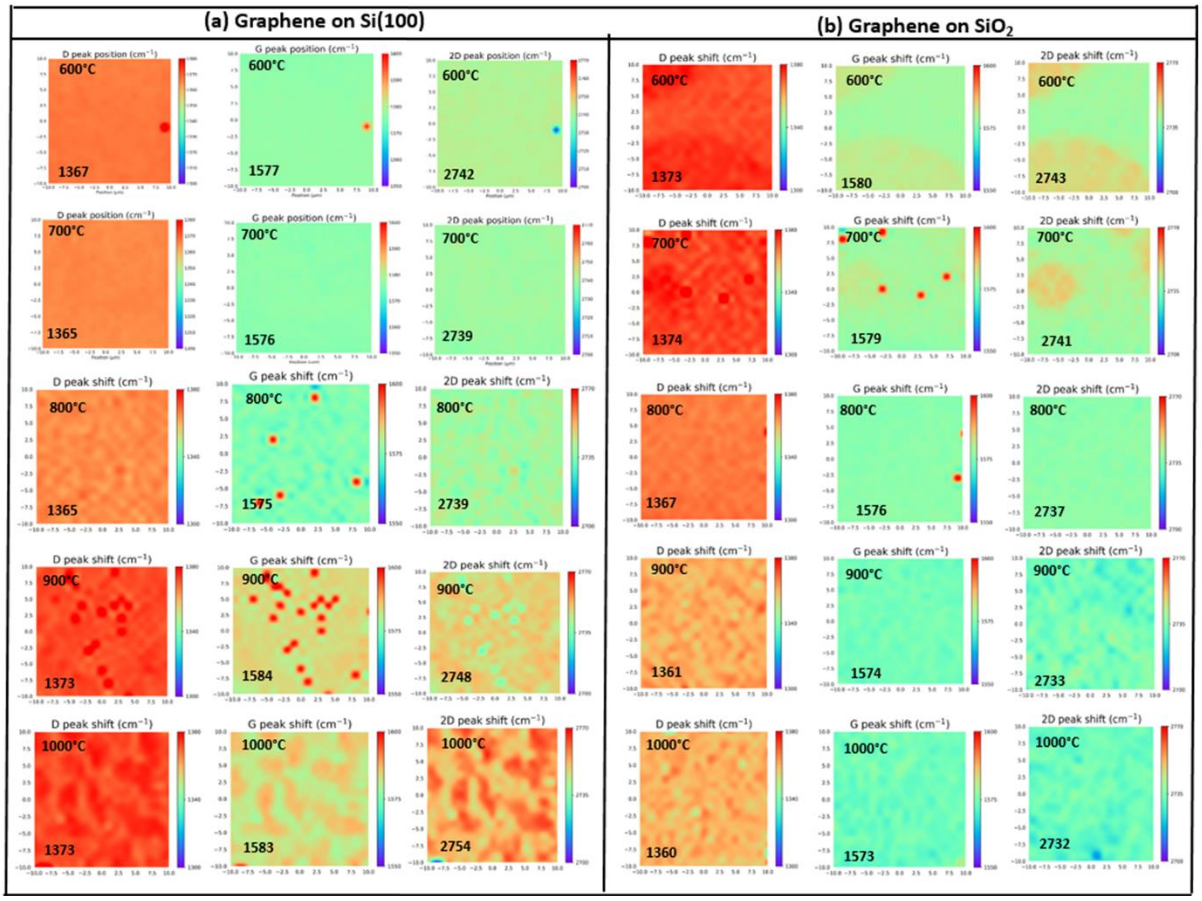

Figure 4. 9 (a) D, G, and 2D positions Raman mapping of as-grown graphene at temperatures ranging from 600-1000°C, with their average values (a) on Si (100), (b) on SiO_2.

In addition to Raman mapping of peak intensity ratios and peaks FWHM, the D, G, and 2D peak positions were also mapped (as shown in **Figure 4.9**). In parallel to the study of I_{2D}/I_G and I_D/I_G, the evolution of those positions as a function of the growth temperature is presented in **Figure 4.10** for each substrate. In general, the G peak position follows the I_D/I_G ratio evolution, in good agreement with what was observed on graphite[13], with both values increasing with the clustering and the reduction in crystallite size. However, one cannot exclude the influence of compressive stress leading to the G peak upshift, as already reported in other studies[14–16]. This can be a concern especially in the case of nickel silicide formation leading to a surface texturing of the substrate during post-annealing cooling of the films. Here, the increase or decrease in the 2D peak position can be correlated with an opposite tendency of the I_{2D}/I_G ratio. This is to be expected when referring to the literature, as the increase in the number of graphene layers upshifts the position of the 2D peak[15–17]. Here, the position of the D peak evolves in the same way as the position of the G peak and the I_D/I_G ratio. Relatively few opinions have been expressed in the literature about the position of the D peak, but we suggest that the increase of clustering leading to the G peak upshift might induce the same effect on the D peak position.

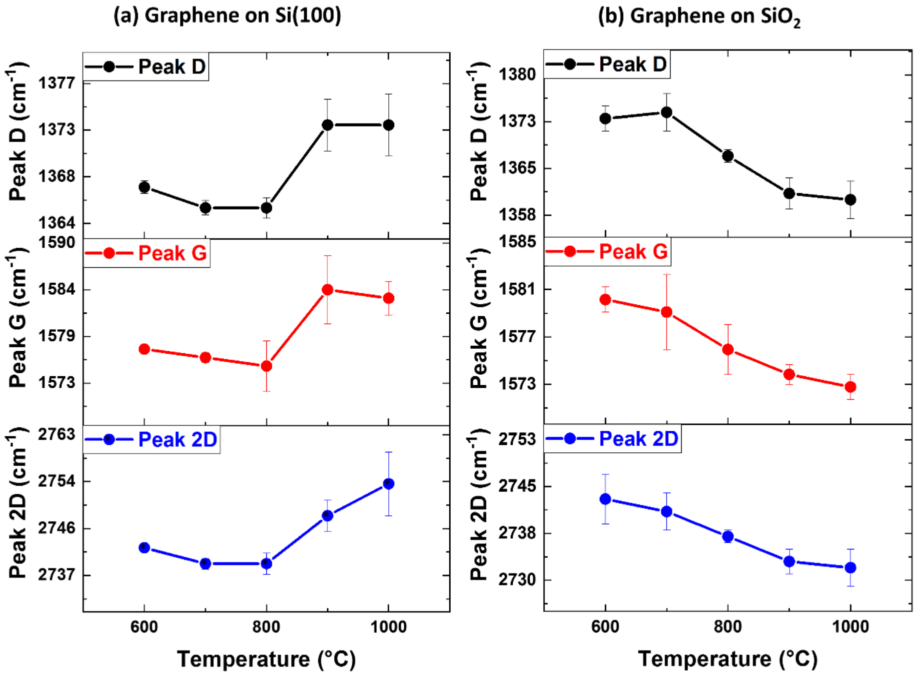

Figure 4. 10 D, G, and 2D peak positions depending on growth temperature for graphene grown (a) on Si(100), (b) on SiO_2.

When considering the SiO_2 substrate, the rise of the annealing temperature has a better influence on graphene quality. An increase in I_{2D}/I_G, a decrease of I_D/I_G, and a decrease in the positions of the D, G, and 2D peaks indicate that the synthesized graphene has fewer layers and lower defects density. Therefore, it appears that high-quality graphene is obtained at higher growth temperatures, which is not the case when graphene is synthesized on the Si(100) substrate. With this last substrate, the impact of temperature appears to be negligible, or at least comparable with what happens on SiO_2 up to 800°C. However, temperatures of 900°C and 1000°C have a detrimental effect on graphene quality, with I_{2D}/I_G decreasing and the other parameters increasing (I_D/I_G, D, G, and 2D positions). This results in multilayered and more defective graphene in the case of Si (100).

Moreover, as can be seen in **Figure 4.10**, these opposite effects arise precisely when the most distinctive features of $NiSi_2$ are present in the Raman signature of the films. Therefore, we concluded that a high annealing temperature is beneficial for the quality of graphene grown using a nickel catalyst, except when the nickel reacts with the substrate. Indeed, it appears that when nickel silicides grow on the surface of Si substrates, less catalyst is available to produce graphene during annealing. If one considers that the Ni is consumed during graphene growth, increasing the temperature optimizes the consumption in the case of SiO_2, but not in the case of Si, as part of the Ni is consumed to form nickel silicide. The formation of such nickel silicide phases reduces the proportion of the metallic nickel phase in which carbon may diffuse towards surface segregation for graphene growth. Thus, with Si (100), a higher proportion of carbon segregates at the surface, compared to what is observed with SiO_2 with no nickel silicide phase formation. Such a difference may explain why, with Si (100), the graphene film is thicker and multilayered, whereas with SiO_2 it is thinner with mostly 2-3 layers.

To conclude the first part of this section in which we have compared the nature of the synthesized graphene on two different substrates (crystalline Si(100) and amorphous SiO_2), from a similar amorphous carbon film, in similar thermal conditions, we can note these following points:

- A quite similar graphene film covers the two different Si(100) and SiO_2 substrates, with an identical a-C/Ni top layer when growth occurs at 600°C. Growth at temperatures ranging from 700 to 1000°C induces very different behavior of the Raman signal, highlighting a significant effect of the substrate on the nanoarchitecture of the graphene film. The nickel silicide formation between 700 and 1000°C, particularly above 900°C, is responsible for such a difference.
- On the Si(100) substrate, rising the growth temperature leads to the synthesis of defective multilayered graphene film, with a decrease in the crystallite size with temperature.

- On the SiO_2 substrate, rising the growth temperature results in less defective graphene films mainly comprised of 2-3 layers with larger crystallites.

These abovementioned results underline the fact that, beyond parameters such as annealing temperature and synthesis conditions, the choice of an appropriate substrate for growth of graphene from a solid source using a nickel catalyst is paramount to control the properties of graphene, including the number of defects and the number of layers. From these results, the following studies in the further section of this chapter will use the SiO_2 substrate for graphene synthesis.

2. Effect of catalyst / amorphous carbon deposition sequence on graphene synthesis

As reported in chapter 2, we used the Ni/a-C stacking order for the study of graphene synthesis mechanism through the carbon diffusion into the nickel catalyst. In the first part of this section, we used the same deposition sequence for the study of the substrate impact on the synthesized graphene. Here, the goal is to analyze the difference between the resulting graphene from both deposition sequences (Ni/a-C/SiO_2 and a-C/Ni/SiO_2), from two different synthesis conditions (condition 1: 900°C, 10 min, 15°C/s and -1°C/s and condition 2: 900°C, 7 min, 15°C/s and -0.5°C/s) and to choose those which are suitable for the rest of our research work.

Figures 4.11a-b show respectively the Raman mapping of I_{2D}/I_G and I_D/I_G for the synthesized graphene using both deposition sequences Ni/a-C and a-C/Ni. From these mapping, we observed that the synthesized graphene using Ni/a-C stacking order present slightly higher I_{2D}/I_G compared to the one produced using the a-C/Ni deposition sequence. The I_D/I_G values are quite similar, suggesting that the defect density in both graphenes are the same. **Figure 4.11c** shows the extracted Raman spectra from the maps related to both deposition order. These spectra present the same characteristics as the mapping with a higher I_{2D}/I_G ratio for the Ni/a-C stacking order and similar defect density for both as indicated by the very close values of I_D/I_G. All these results pointed out on the one hand that graphene always grows irrespective of the deposition sequence. On the other hand, the resulting graphene from the deposition order Ni/a-C is a bit better in terms of the I_{2D}/I_G ratio, meaning that this deposition sequence gives slightly thinner graphene with respect to the other stacking order a-C/Ni.

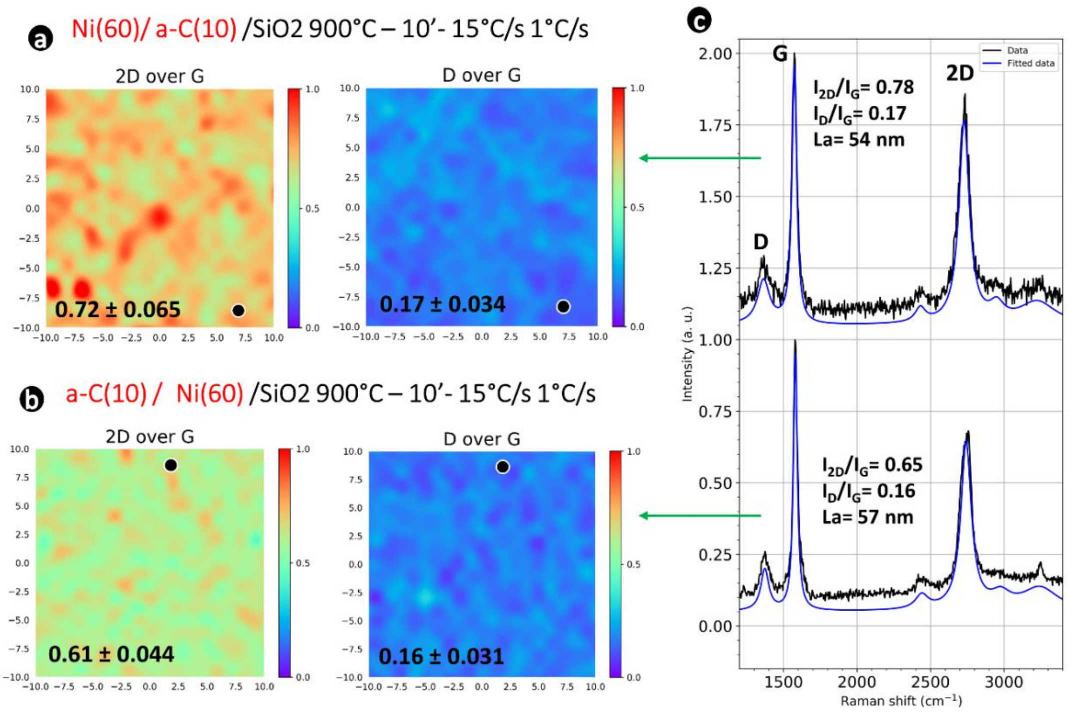

Figure 4. 11 (a) Raman mapping of I_{2D}/I_G and I_D/I_G ratios over 20 × 20 µm² region for the synthesized graphene using Ni/a-C stacking order. (b) Raman mapping of I_{2D}/I_G and I_D/I_G ratios over 20 × 20 µm² region for the synthesized graphene using a-C/Ni stacking order. (c) Extracted Raman spectra of the graphene in both Raman mapping.

Indeed, even though the deposition sequence Ni/a-C gives thinner graphene compared to the a-C/Ni sequence, we have preferred using the a-C/Ni deposition sequence for the next developments of this work, for different reasons. First, because with the a-C/Ni order, one can heat the nickel catalyst to enlarge the nickel grain size and thereby increase the grains of the synthesized graphene as well. Nevertheless, due to the technical problems with our in situ furnace, we could not perform this process. The second reason is that we aimed to study the boron-doped graphene, and it seems that the best deposition sequence is a-C:B/Ni because it might be difficult for the boron to diffuse through the nickel catalyst if using the other deposition order.

Furthermore, when using the deposition sequence a-C/Ni, changing the nickel thickness to 50 nm and adjusting slightly the annealing conditions, we obtained better graphene with higher I_{2D}/I_G and reduced defect density. Indeed, it has been reported**[18,19]** that the cooling rate as well as the annealing time influence also the graphene synthesis, due to the combination of carbon solubility and diffusion in the used metal-catalyzed. Our investigations agree with those observations. **Figures 4.12a-b** show respectively the Raman mapping of I_{2D}/I_G and I_D/I_G for the synthesized graphene using both deposition conditions:

- a-C (10 nm) / Ni(60 nm) with 900°C, 10 min, 15°C/s and -1°C/s (condition 1) ,

- a-C (10 nm) / Ni(50 nm) with 900°C, 7 min, 15°C/s and -0.5°C/s (condition 2).

These two conditions have been selected among the numerous conditions that we have studied to justify the choice of the used growth conditions for the next developments of this work. From these maps, we observed that the synthesized graphene using condition 2 presents slightly higher I_{2D}/I_G compared to the one produced using the condition 1. The I_D/I_G values for the derived graphene from the condition 2 is lower compared to the one derived from the condition 1, suggesting that the defect density is lower in the resulting graphene from the condition 2.

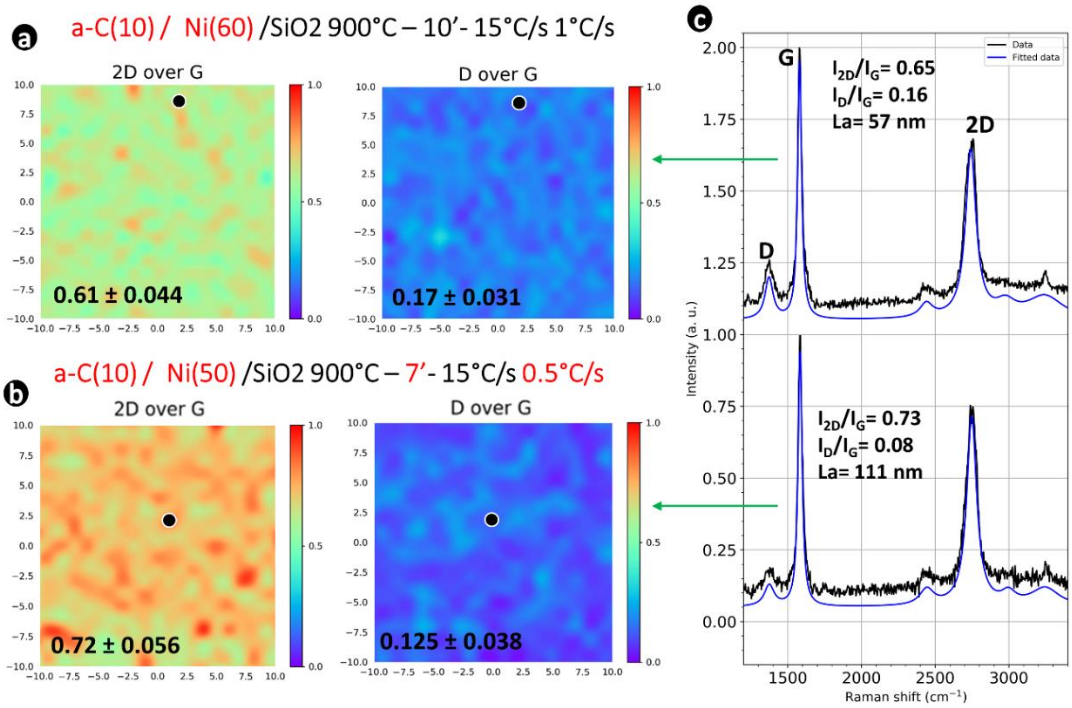

Figure 4. 12 (a) Raman mapping of I_{2D}/I_G and I_D/I_G ratios over 20 × 20 μm² region for the synthesized graphene using a-C/Ni deposition order with 60 nm of Ni and annealing conditions (Condition 1: 900°C, 10 min, 15°C/s and -1°C/s). (b) Raman mapping of I_{2D}/I_G and I_D/I_G ratios over 20 × 20 μm² region for the synthesized graphene using a-C/Ni deposition order with 50 nm of Ni and annealing conditions (Condition 2: 900°C, 7 min, 15°C/s and -0.5°C/s). (c) Extracted typical Raman spectra of the graphene in both Raman mapping (black circle).

Figure 4.12c shows the extracted Raman spectra from the maps of the derived graphene from both synthesis conditions. These spectra present the same characteristics as the maps with a higher I_{2D}/I_G ratio higher and lower defect density for condition 2. All these results demonstrated that the synthesized graphene from the synthesis conditions 2 is better than the one resulting from the condition 1 since it presents thinner graphene (high I_{2D}/I_G value) and lower defect density (low I_D/I_G value). As a consequence, keeping the deposition sequence a-C/Ni, we chose to use the condition 2 (900°C, 7 min, 15°C/s, and -0.5°C/s) for the next developments of this Ph.D. thesis. Moreover, these results pointed out that by changing some parameters, one could tune the characteristics of the synthesized graphene; this point will be detailed in the following sections of this chapter.

II. The effect of the starting thickness of the amorphous carbon on graphene synthesis

As we have shown in chapter 3, graphene synthesis with nickel is due to the diffusion and segregation of carbon through nickel catalyst. Thus, controlling the synthesized graphene thickness is still challenging. Therefore, to optimize our PLD and RTA process for the growth of thin uniform graphene, we studied in section II of this chapter, the influence of the initial amorphous carbon (a-C) thickness and the annealing temperature on the synthesis of graphene by fixing constant the nickel catalyst thickness at 50 nm and using SiO_2 substrate. We used Raman micro-spectroscopy mapping to investigate how these parameters affect the graphene growth. However, further characterizations such as SEM, AFM, XPS, and UV-VIS were performed on the sample with the optimal conditions giving high-quality graphene. The study was realized with a set of 18 graphene growth conditions, crossing 6 initial a-C thicknesses with 3 annealing temperatures as shown in **Table 4.3**.

Ni catalyst thickness (nm)	a-C initial thickness (nm)	Rapid thermal annealing conditions
50	1	Temperature: 800-900-1000 °C Heating ramp: +15 °C/s Time: 420 s Cooling ramp: -0.5 °C/s
	2	
	4	
	5	
	10	
	20	

Table 4. 3 Summary of the conditions of graphene synthesis.

1. Graphene layer number distribution through I_{2D}/I_G ratio mapping, as a function of the initial thickness of a-C and annealing temperature

Table 4.4 (left) depicts the summary of the mean values of the I_{2D}/I_G ratio for all samples. In addition, **Figure 4.13** presents the Raman maps and the average values of the I_{2D}/I_G ratio of all the samples over a region of 20 x 20 µm². These maps demonstrate that the synthesized graphene is heterogeneous, comprising single to multilayered graphene. The difference in the number of graphene layers is remarkable, as detailed in the paragraphs below. With the starting a-C film thickness as low as 1 nm, the I_{2D}/I_G ratio remains low (< 0.6), irrespective of the annealing temperature within the range 800-1000 °C, compared to thicker a-C films. This may be because the initial carbon thickness is too thin to induce the formation of graphene layers over a large area in this temperature range, with domains exhibiting very low I_{2D}/I_G ratios. Among all the conditions for graphene growth, the highest average value of the I_{2D}/I_G ratio was 0.863, corresponding to the resulting graphene from the conditions with a starting a-C film of 2 nm thick and annealed at 900 °C. This suggests the formation of bilayer graphene.

	I_{2D}/I_G		
a-C (nm)	800 °C	900 °C	1000 °C
1	0.548 ± 0.06	0.597 ± 0.16	0.570 ± 0.19
2	0.650 ± 0.10	0.863 ± 0.18	0.767 ± 0.24
4	0.633 ± 0.41	0.809 ± 0.28	0.778 ± 0.25
5	0.710 ± 0.14	0.822 ± 0.24	0.698 ± 0.18
10	0.490 ± 0.39	0.720 ± 0.24	0.662 ± 0.11
20	0.573 ± 0.11	0.675 ± 0.12	0.726 ± 0.07

	I_D/I_G		
a-C (nm)	800 °C	900 °C	1000 °C
1	0.262 ± 0.08	0.320 ± 0.18	0.257 ± 0.15
2	0.248 ± 0.18	0.132 ± 0.05	0.152 ± 0.11
4	0.263 ± 0.22	0.113 ± 0.10	0.088 ± 0.05
5	0.212 ± 0.10	0.081 ± 0.04	0.125 ± 0.09
10	0.455 ± 0.05	0.115 ± 0.09	0.146 ± 0.06
20	0.353 ± 0.06	0.163 ± 0.06	0.069 ± 0.02

Table 4. 4 Summary of the average values of each I_{2D}/I_G and I_D/I_G maps respectively.

The samples a-C (4 nm - 900 °C) and a-C (5 nm - 900 °C) also display high I_{2D}/I_G ratios of 0.809 and 0.822, respectively. However, considering the high standard deviation of their I_{2D}/I_G average values, their maps present more heterogeneous than that of sample a-C (2 nm - 900 °C). **Figure 4.13b** shows the plot of average values of I_{2D}/I_G as a function of the initial a-C thicknesses and synthesis temperatures. At 900 °C, there is a progressive reduction in the I_{2D}/I_G ratio with an increase of from 2 to 20 nm in the thickness of the a-C film. This result is consistent with a previous study in which they observed the decrease of the I_{2D}/I_G ratio when increasing the thickness of a-C film at 1100°C[19]. With the growth temperature of 1000 °C, the I_{2D}/I_G ratio displays a little dependence on the starting a-C film thickness. While at 800 °C, the I_{2D}/I_G intensity ratios values were systematically lower than the I_{2D}/I_G intensity ratios values of the synthesized graphene at 900 and 1000°C. Considering the same growth temperatures for each starting a-C thickness, 900 °C was the temperature at which the average I_{2D}/I_G ratio was higher for all initial a-C thicknesses except 20 nm. Therefore, we conclude that the optimal temperature for high I_{2D}/I_G ratios is 900 °C within our growth conditions.

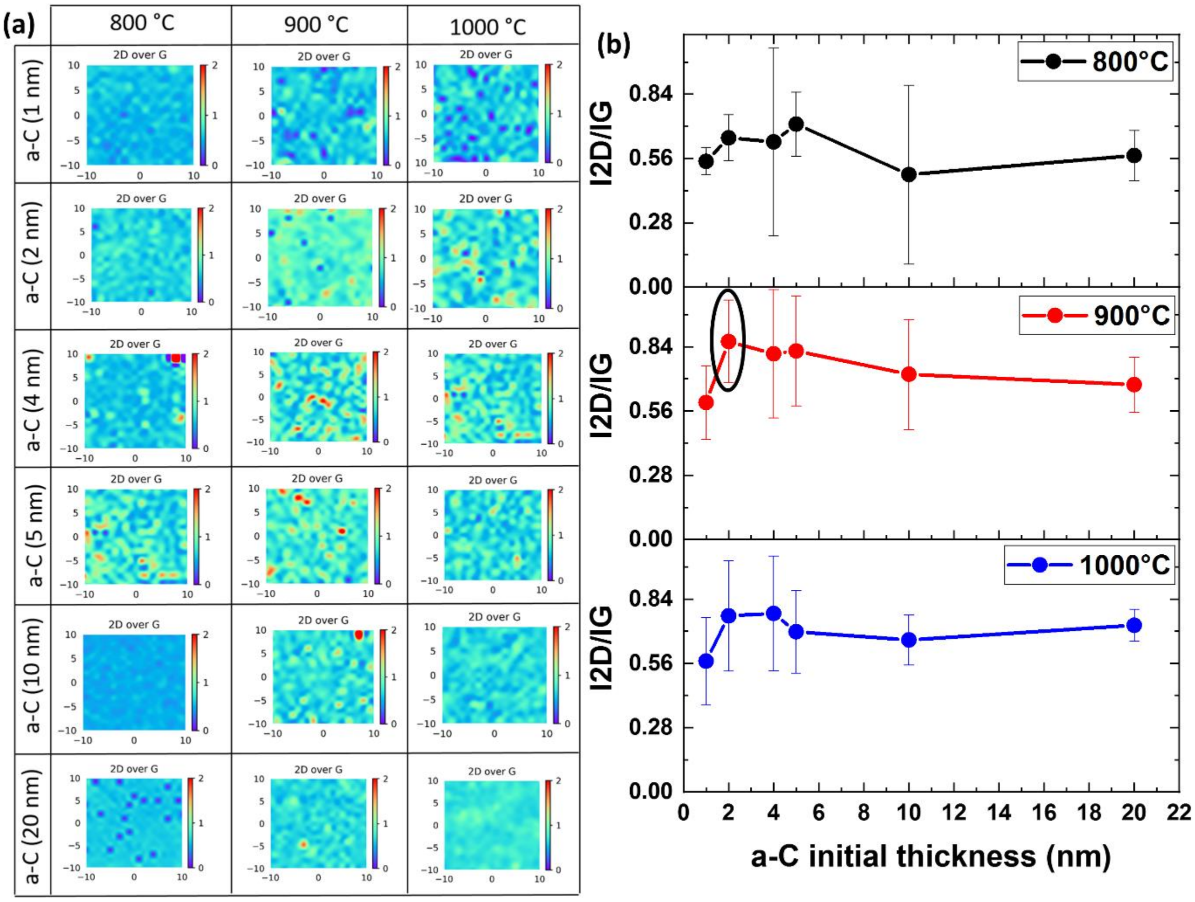

Figure 4. 13 (a) Raman spectroscopy maps of I_{2D}/I_G of all samples; (b) plot of the influence of the initial a-C thickness on the average I_{2D}/I_G values as a function of growth temperature.

2. Defects density distribution through I_D/I_G ratio mapping as a function of the initial thickness of a-C and annealing temperature

Table 4.4 (right) presents the summary of the mean values of the I_D/I_G ratio and **Figure 4.14** shows the Raman maps and the average I_D/I_G ratios of all the samples for a region of 20 x 20 µm². The defect density was rather homogeneous considering the low standard deviation of the I_D/I_G intensity ratio in the most growing conditions. Indeed, the homogeneity was higher at both 900 °C and 1000 °C than at 800 °C in the most a-C thicknesses, except with the 1 nm thick of a-C. Among all, the condition with 20 nm thick of a-C, annealed at 1000°C, gives the lowest average I_D/I_G ratio of about 0.069. **Figure 4.14b** shows the plot of average values of the I_D/I_G ratio deduced from **Figure 4.14a**, as a function of initial a-C thickness at different synthesis temperatures. The samples synthesized at 900 °C and 1000 °C present a lower defect density, with I_D/I_G ratios ranging from 0.069 to 0.163 for a-C of 2 to 20 nm. In the sample synthesized at 800 °C, the defect density was much higher, with the I_D/I_G in between 0.136 and 0.460. From these results, we conclude that, as observed in section I of this chapter, the growth temperature of 800 °C is too low to produce low defect density graphene, whereas those of 900 and 1000 °C are suitable for the graphene formation with a significantly lower defect density. Such obtained defect density is comparable with that found in the resulting graphene from CVD synthesis method**[20]**.

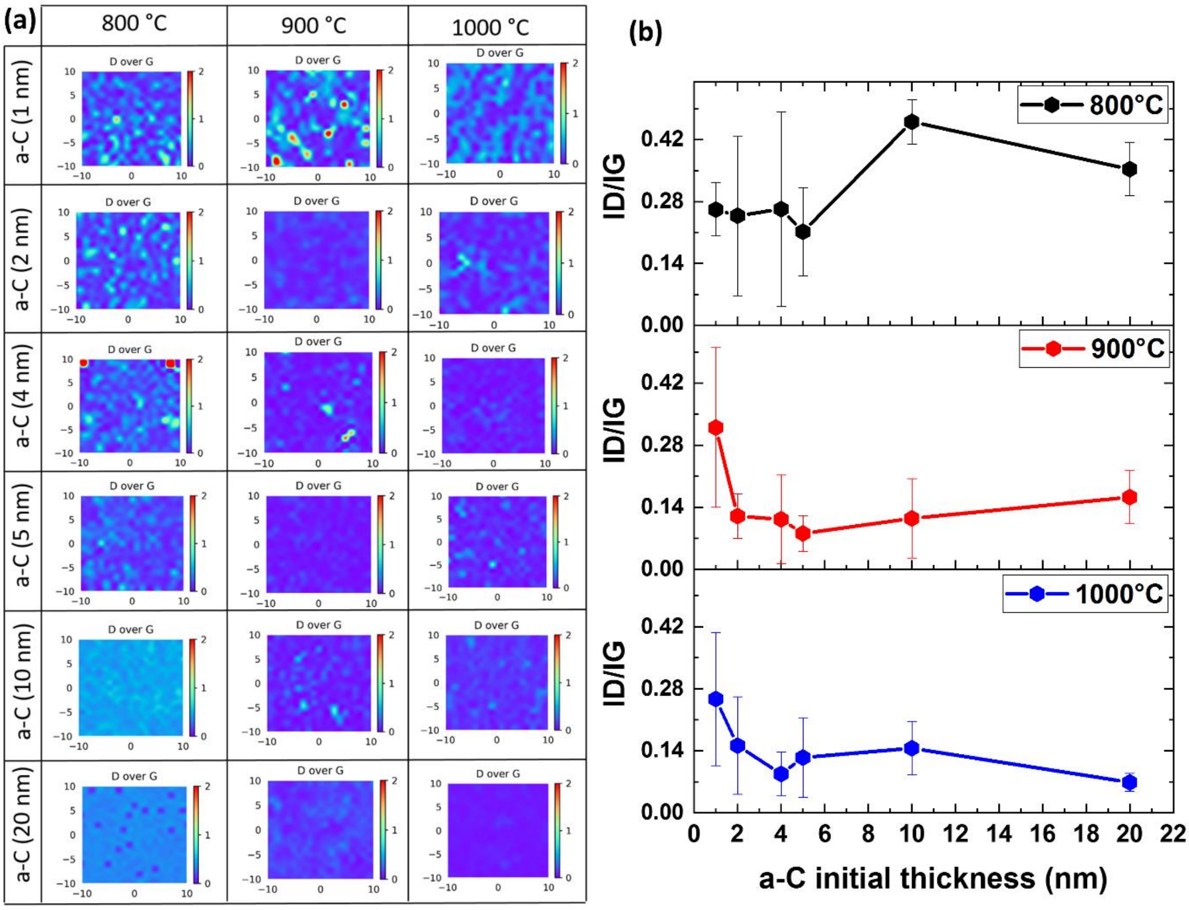

Figure 4. 14 (a) Raman spectroscopy maps of I_D/I_G of all samples; (b) plot of the influence of the initial a-C thickness on the average I_D/I_G values as a function of growth temperature.

3. The optimal synthesis conditions and further analysis

Here, we discussed Raman mapping statistics to quantify the distribution of the graphene layer number as a function of the starting a-C film thickness and annealing temperature. Our statistics procedure is based on the table depicted in the section devoted to Raman analysis in Chapter 2. Indeed, the regions with an I_{2D}/I_G ratio >1.4 are considered to be representative of graphene monolayer, areas with I_{2D}/I_G ratios between 0.75 and 1.4 are associated to graphene bilayer, and domains with I_{2D}/I_G ratios below 0.75 are attributed to thicker graphene comprising three and more layers.

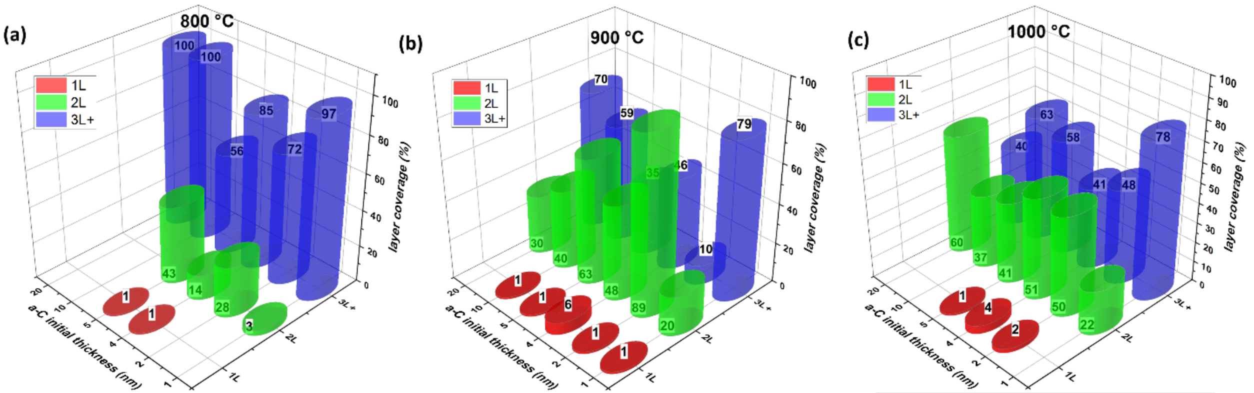

a-C (nm)	800 °C		
	1 L	2 L	3 L+
1	/	3	97
2	/	28	72
4	1	14	85
5	1	43	56
10	/	/	100
20	/	/	100

a-C (nm)	900 °C		
	1 L	2 L	3 L+
1	1	20	79
2	1	89	10
4	6	48	46
5	2	63	35
10	1	40	59
20	/	30	70

a-C (nm)	1000 °C		
	1 L	2 L	3 L+
1	/	22	78
2	2	50	48
4	4	51	41
5	1	41	58
10	/	37	63
20	/	60	40

Figure 4. 15 Raman mapping statistics: 3D plot of percentage graphene layer number distribution as a function of the initial a-C thickness (top) and the coverage percentage values (bottom). (a) 800 °C; (b) 900 °C; (c) 1000 °C.

Figure 4.15a shows the 3D plot, which depicts the distribution of the graphene layer number as a function of the starting a-C thickness at 800 °C. We observed that, at this growth temperature, the synthesized graphene mostly exhibits three and/or more layers. At 900 °C (**Figure 4.15b**), graphene films contained a higher proportion of mono- and bilayers. In particular, the sample a-C (2 nm) comprises 89% of bilayers graphene. At a growth temperature of 1000 °C (**Figure 4.15c**), the heterogeneity of the synthesized graphene was much more pronounced, mostly bilayer, 3-6 layers. Therefore, we conclude that the optimal conditions for bilayer formation are those with a starting a-C thickness of 2 nm and growth temperature of 900 °C when the thickness of the nickel catalyst film is fixed at 50 nm. Such an optimum low thickness of a-C to form a dominant graphene bilayer is explained based on previous works related to graphene synthesis from solid carbon films in the presence of a metal catalyst. It has been already shown[21,22] that graphene growth mainly occurs during the thermal cycle by carbon dissolution and diffusion through the metal catalyst. A lower a-C film of 1 nm thick probably does not supply enough carbon to form homogeneous graphene layers when carbon precipitated on the Ni surface after its dissolution during the steady-state high temperature. Indeed, we observed that the different annealing temperatures have quite no effect on the graphene quality with such a low a-C film thickness. On the other side, an excessive starting a-C film thickness provides more carbon, but the rather high diffusion of carbon in nickel with temperature likely leads to the diffusion of carbon deep into the metal catalyst, and most of this carbon remains trapped upon cooling, limiting the quality of the synthesized graphene. This may be a possible explanation of the optimum a-C film thickness of 2 nm observed with our protocol.

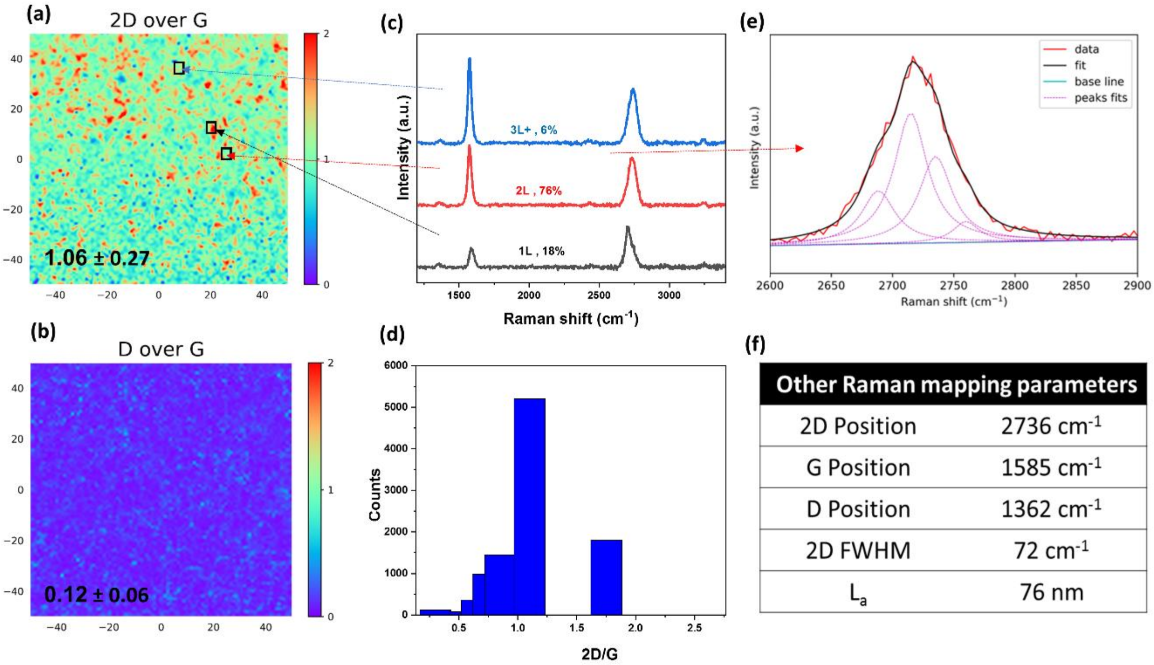

Other Raman mapping parameters	
2D Position	2736 cm^{-1}
G Position	1585 cm^{-1}
D Position	1362 cm^{-1}
2D FWHM	72 cm^{-1}
L_a	76 nm

Figure 4. 16 Raman mapping of a large 100 ×100 µm² region, of sample a-C (2 nm – 900 °C): (a) Mapping of I_{2D}/I_G ratio with an average value of 1.06; (b) Mapping of I_D/I_G ratio with the average value of 0.12; (c) spectra of the graphene with different numbers of layers in Raman mapping of graphene on a SiO_2 substrate; (d) Statistical histogram of the Raman mapping of I_{2D}/I_G ratio showing the predominance of bilayer; (e) Fitting of the 2D band in the Raman spectrum of bilayer graphene showing an asymmetric shape and four Lorentzian peaks corresponding to AB stacking; (f) table showing the other Raman mapping parameters of the sample.

To go further in the investigation of the sample a-C (2 nm – 900 °C) with the optimal synthesis condition, we realized, on the one hand, Raman mapping over a large area (100 ×100 µm²) with the step of 1 µm totaling 10 000 spectra. Such wide Raman mapping is rarely performed but makes it possible to obtain a more representative probed area of the graphene film. On the other hand, we carried out some other analyses such as SEM, AFM, and UV-Vis after acidic treatment.

Figures 4.16a and 4.16b show Raman mapping of I_{2D}/I_G and I_D/I_G ratios with their average values of 1.06 and 0.12, respectively, indicating the predominant formation of the bilayer with low defect density. From the statistical analysis, over the 100 ×100 µm² mapped area, 18% was covered by graphene monolayers, 76% by graphene bilayers, and only 6% by more than three graphene layers (**Figures 4.16c and 4.16d**). This result is in agreement with the results of previous[23] work related to the synthesis of bilayer graphene using a polymer as a solid carbon source. In their work, using Raman mapping, the authors observed that 70% of the 100 × 100 μm² mapped region was covered by bilayer graphene. **Figures 4.16e and 4.16f** show the shape and Lorentzian fitting of the 2D band of the bilayer spectrum and the other Raman parameters extracted from the mapped area. The 2D band shows an asymmetric band and can be decomposed with four Lorentzian peaks, each one with a FWHM of 30 cm^{-1}, corresponding to the AB stacking of the bilayer graphene[24–27].

In addition to Raman characterization, atomic force microscopy (AFM) and scanning electron microscopy (SEM) were performed to get the topological information about our best sample a-C (2 nm – 900 °C). Further XPS characterization was realized to get the chemical composition. Additionally, since the sample was transparent after graphene synthesis, transmittance measurement was carried out for this sample.

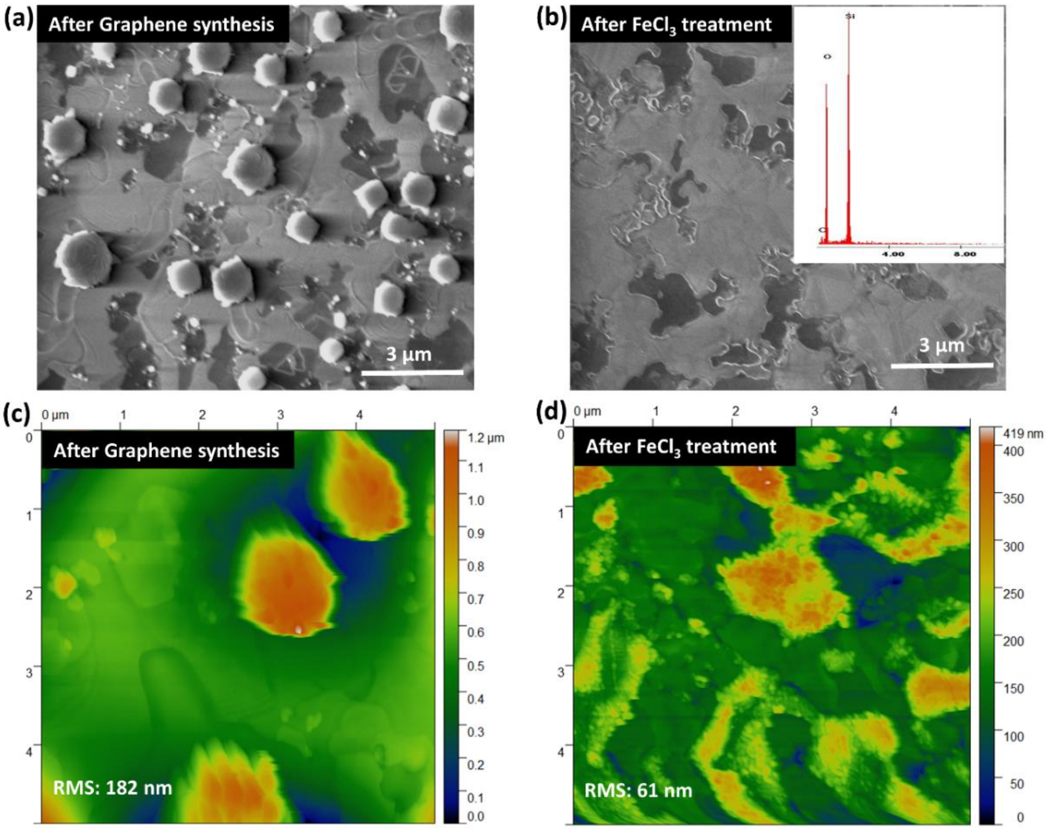

Figure 4. 17 AFM and SEM images of sample a-C (2 nm – 900 °C): (a) SEM image after graphene synthesis showing different contrast and the nickel residual nodules; (b) SEM image after nickel removal with $FeCl_3$ treatment. Inset shows the EDS spectrum indicating the absence of Ni; (c) AFM image after graphene growth showing the surface morphology with a RMS value of 182 nm; (d) AFM image after nickel removal showing the surface morphology with lower roughness RMS value of 61 nm.

Figure 4.17a shows the SEM image, depicting the surface morphology of the sample with the island-shaped metallic nickel nodules. These Ni islands have been also previously reported by others[19,28] when using Ni catalyst for the graphene growth graphene and rapid thermal annealing in the temperature range 900-1100 °C. However, we cannot exclude the presence of a very thin film of nickel on the flat areas surrounding the nickel clusters. Netherveless, after treating the sample with 4M of $FeCl_3$ solution, as presented in **Figure 4.17b**, the nickel particles disappear. This is supported by the EDS spectrum (inset in **Figure 4.17b**), which does not show any detectable presence of nickel. **Figure 4.17c** shows the surface topography of the as-grown graphene with a RMS of 182 nm observed using AFM. This image suggests a relatively high surface roughness probably due to the presence of nickel islands. Indeed, after nickel removal (**Figure 4.17d**), the surface roughness reduces significantly to 61 nm, meaning that the presence of these nickel particles effectively increases the surface roughness of the sample.

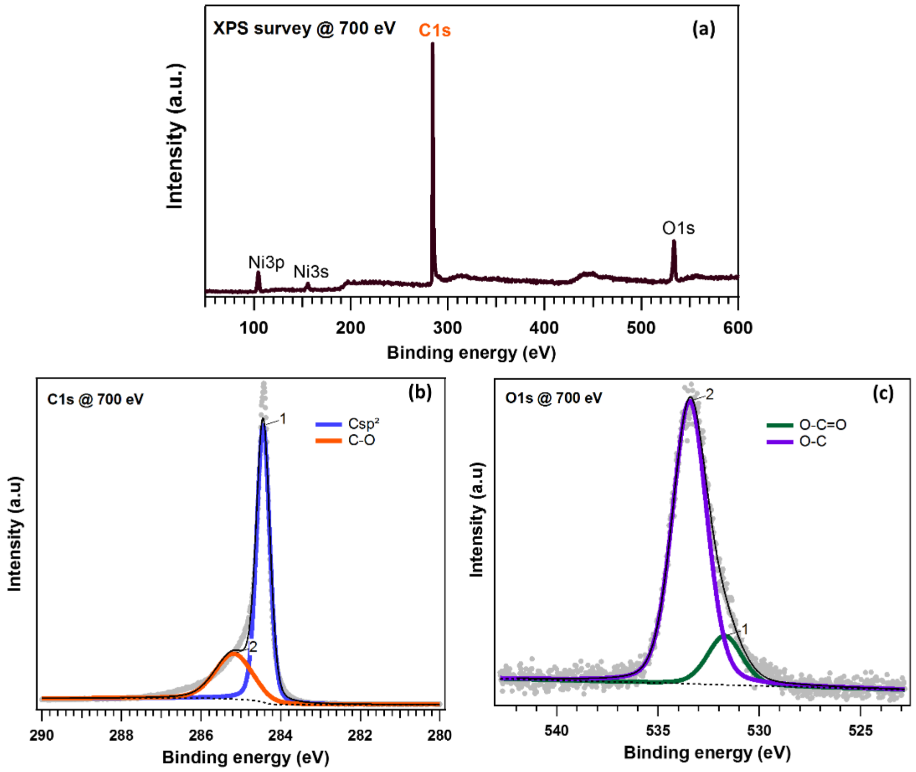

Figure 4. 18 XPS spectra of sample a-C (2 nm – 900 °C) before $FeCl_3$ treatment: (a) XPS survey spectrum; (b) XPS C 1s spectrum; (c) XPS O 1s spectrum[32].

In **Figure 4.18a**, the XPS survey spectrum of the sample a-C (2 nm – 900 °C) before $FeCl_3$ treatment with the optimal growth condition shows carbon located near 284 eV, oxygen located near 533 eV, and some residual of nickel. The presence of the oxygen may be due to the contamination after the a-C film synthesis and/or during thermal annealing at a rather high pressure of 10^{-2} mbar. The nickel traces confirm the observation of SEM and AFM. **Figure**

4.18b shows the C1s deconvolution into two components. The first one is centered at 284.4 eV and attributed to sp^2 hybridized C atoms in graphene. This first component is the most intense and prominent in graphitic carbon demonstrating that most of the amorphous carbon has been transformed into graphene or graphitic carbon[29]. The other less intense component is located at 285.2 eV, related to C-O bonds. **Figure 4.18c** displays the O1s decomposed in two components O-C and O-C=O oxygen group, located at 533.4 and 531.7 eV respectively[30,31].

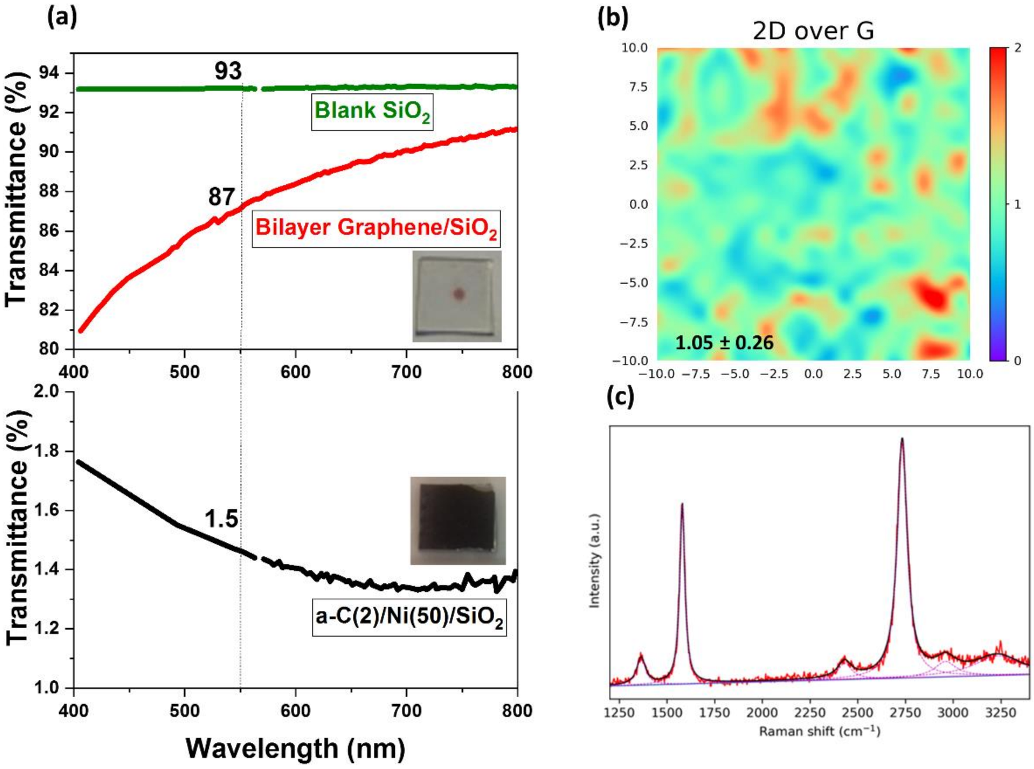

Figure 4. 19 (a) Transmittance curves as a function of wavelength for both: as-deposited sample (bottom) and the synthesized bilayer graphene after thermal annealing and $FeCl_3$ etching and the blank fused silica (top). (b) Raman mapping of I_{2D}/I_G ratio of the bilayer graphene after Ni etching, (c) an extracted spectrum from the mapping depicting the bilayer graphene feature.

Optical transmittance was measured on the sample exhibiting the optimal growth conditions after the nickel etching with 4M of $FeCl_3$ solution. For comparison, the transmittance was also measured on the starting material before annealing (a-C (2nm)/ Ni (50)) on the glass substrate and the blank glass as well (**Figure 4.19a**). The transmittance of the starting material at 550 nm is about 1.5 % (mostly due to the Ni thin film) and 93 % for the blank fused silica alone, while the one for our bilayer graphene is around 87%. Theoretically, each graphene layer absorbs 2-3%[33] of the incident light at 550 nm. Taking into account the difference between the transmittances of the blank glass and the graphene on the glass, we ended up with 6 % of light being absorbed by our graphene, which is in good agreement with the theoretical value of absorption of bilayer graphene and other results reported in previous works[34,35]. **Figure 4.19b** shows the Raman mapping of the I_{2D}/I_G ratio after nickel removal. The average value of the I_{2D}/I_G ratio is about 1.05, practically the same value as for the synthesized graphene before acidic treatment. Besides, the spectrum in **Figure 4.19c** depicts the bilayer graphene characteristics. This result suggests that the $FeCl_3$ treatment does not affect the graphene layer number.

To summarize, we have reported in this section a parametric study in which we adjusted the initial thickness of amorphous carbon (a-C) and the growth temperature of graphene. From the experimental results, we can infer the following conclusions:

- The optimal synthesis conditions to obtain a high proportion of graphene bilayers with lower defect density require a starting a-C thickness of 2 nm and a synthesis temperature of 900°C for 7 min with a heating rate of 15°C/s and cooling rate of 0.5°C/s.
- The sample with the optimal growth conditions a-C (2 nm – 900 °C) presents 76 % of bilayer graphene detected through Raman mapping of 100 ×100 μm^2 area and transmittance at 550 nm corresponding to the one of bilayer graphene.
- The investigated synthesis route allows synthetizing predominantly bilayer graphene films, with a significant low defect density comparable to the graphene sheets obtained by some CVD studies.

These results highlight that the initial thickness of amorphous carbon used for the graphene synthesis is a key parameter. However, we have also observed the reactivity of the nickel thin film catalyst forming the micrometer-sized nodules during the graphene growth. In the following section, we will look at the impact of the starting thickness of the nickel catalyst (another key parameter) on the formation of these particles as well as on the synthesis of graphene.

III. The effect of the starting thickness of the nickel catalyst on graphene synthesis

In the previous section, we observed in one hand the formation of continuous bilayer graphene with nickel particles, and on the other hand, that these nickel islands can be removed using the $FeCl_3$ solution as etching thereby allowing the synthesis of transfer-free graphene. Looking at the literature, it is reported[36,37] that this nickel particle formation is caused by the solid-state dewetting phenomenon at high temperatures. Therefore, in this section, still intending to optimize our PLD and RTA process for graphene growth, in one side, we studied the morphological evolution of the nickel thin film as a function of annealing temperature during the rapid thermal annealing of nickel thin film with various thicknesses. And on the other side, a parametric study on graphene synthesis from an amorphous carbon (a-C) was realized by varying the initial nickel catalyst thickness (25, 50, 150 nm) while fixing the amorphous carbon (a-C) film thickness at 2 nm and annealing temperature at 900°C using SiO_2 substrate. We used Raman micro-spectroscopy mapping to investigate how this parameter affects the graphene growth. Additional characterizations such as SEM-EDS, HRTEM, and UV-vis were performed on the samples. The study was realized with a set of 3 starting nickel thicknesses (25, 50, 150 nm) as shown in **Table 4.5**. The synthesis routes of these two studies are depicted in **Figure 4.20**.

Samples	Nickel thin film thickness	Annealing temperature	Heating rate - Annealing time – Cooling rate
As-deposited	25 nm 50 nm 150 nm	-	+ 15°C/s – 420 s – 0.5°C/s
Ni-500		500 °C	
Ni-700		700 °C	
Ni - 800		800 °C	
Ni - 900		900 °C	
a-C (2nm)/ Ni – 900			

Table 4. 5 Summary of growth conditions.

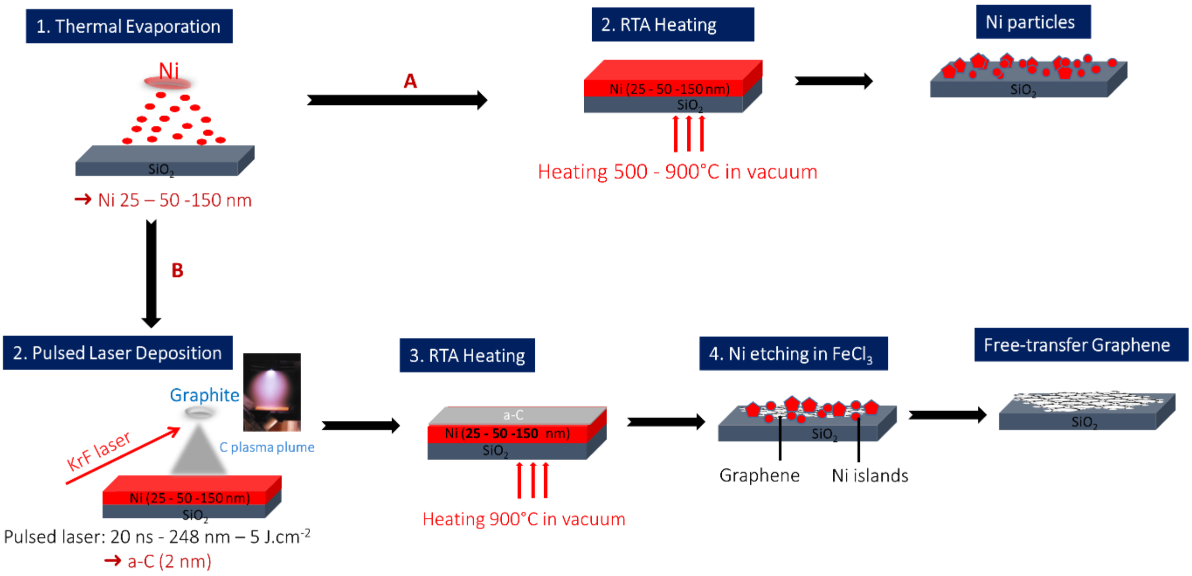

Figure 4. 20 Synthesis route for A) rapid thermal annealing of Ni thin films and B) free-transfer graphene films obtained by pulsed laser deposition of carbon on Ni thin films followed by rapid thermal annealing and Ni etching. The substrate is SiO_2 in both cases.

1. Effect of rapid thermal annealing on the morphology of nickel thin film

a. Nickel thin film dewetting in the absence of carbon

Figures 4.21a, f, and k show that the nickel thin film completely and uniformly covers the SiO_2 substrate before the thermal annealing process. With annealing at different increasing temperatures, a reduction of the covered surface by nickel is observed. This is due to a dewetting process of the nickel film on the SiO_2 surface, as already observed with various metallic thin films annealed in vacuum conditions [38–42]. The dewetting evolution of continuous metal films generally undergoes three successive stages:

1) Hole formation inside the Ni film, due to the initiation of surface diffusion of Ni.
2) Increase of hole density with a transition from the continuous Ni film to a quasi-continuous surface network of stringy Ni.
3) Final transition from the stringy Ni network to a surface distribution of individual Ni (sub-) micrometer-sized particles.

This thermally induced process leads to the gradual formation of nickel particles on the SiO_2 substrate, due to the minimization of the total surface energy of the system.

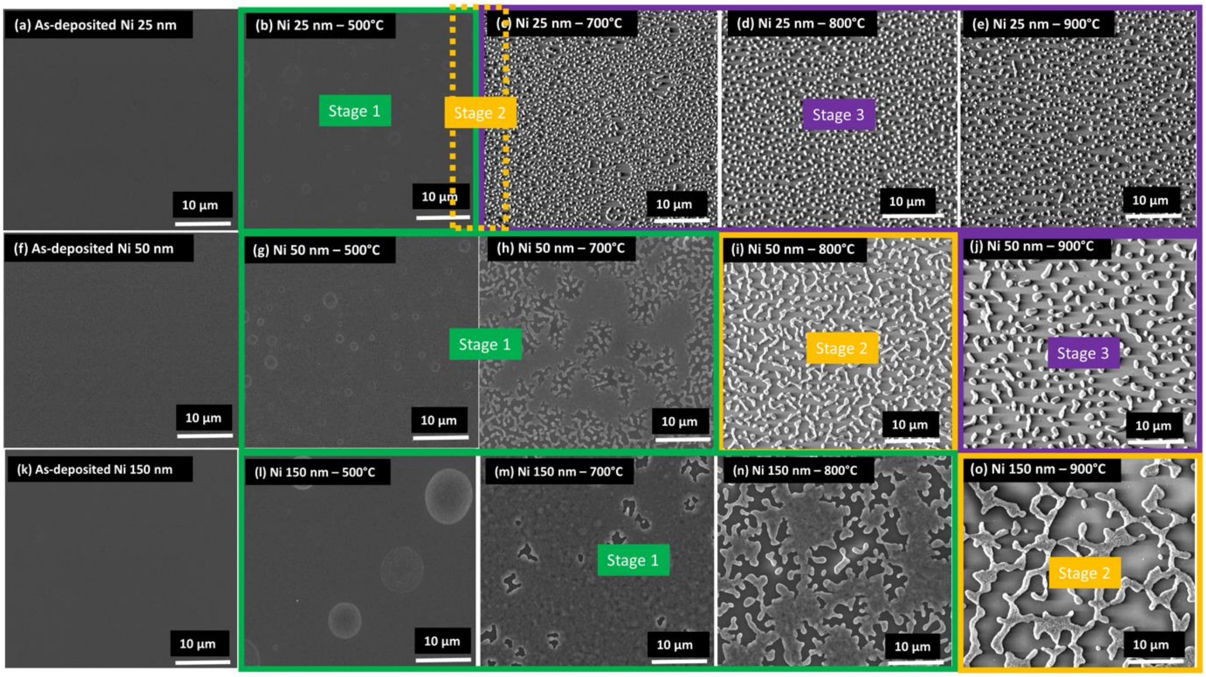

Figure 4. 21 Summary of the solid-state dewetting behavior for nickel thin films deposited on fused silica SiO_2 substrate: SEM images of the dewetting of the nickel thin film of 25 nm (a-e), 50 nm (f-j) and 150 nm (k-o), as a function of annealing temperature (500-900°C range). The three stages related to the Ni dewetting mechanism, described in the text, are superimposed on the SEM images.

Figure 4.21 shows SEM images of the surface of the annealed nickel thin film of various thicknesses (25, 50 and 150 nm) on the fused silica SiO_2 substrates after annealing at 500°C ((b) (g) and (l)), 700°C ((c), (h) and (m)), 800°C ((d), (i) and (n)), 900°C ((e), (j) and (o)). The first line corresponds to the images of nickel thin films dewetting evolution of 25 nm, the second line corresponds to the one of 50 nm and the third line to the nickel thin film of 150 nm. From the first column of **Figure 4.21**, we observe that the as-deposited nickel thin films on SiO_2 samples are quite homogeneous with low roughness, regardless of their thickness. The second column corresponds to the SEM images of the annealed samples at 500°C for the three different nickel film thicknesses. From 500°C, the transition between the three already-mentioned stages can be observed, but at different temperatures depending on the initial thickness of the Ni film, as depicted in **Figure 4.21** and described hereafter.

The 1st stage, corresponding to hole formation with a spherical shape, is observed at 500°C, with various hole sizes and densities depending on the Ni film thickness. The 2nd and 3rd stages are observed with the 50 nm thick Ni within the 700-900°C range. At 800°C (**Figure 4.21i**), we observe the end of the 2nd stage with a quasi-continuous surface network of stringy Ni being transformed into individual Ni particles corresponding to the beginning of the 3rd stage Indeed, at 800°C, the stringy Ni particles are less individualized compared to 900°C (**Figure 4.21j**) corresponding unambiguously to the 3rd stage with a surface distribution of individual Ni (sub-) micrometer-sized particles.

On one side, when the Ni film thickness is lower (25 nm), the 3rd stage is observed as low as 700°C (**Figure 4.21c**), and higher temperatures induce only a slight size increase of the Ni individual particles. On the other side, when the Ni film is thicker (150 nm), the 2nd stage occurs within 700 and 900°C, producing at the highest temperature (**Figure 4.21o**) the quasi-continuous surface network of stringy Ni islands whose size is significantly larger compared to the 50 nm thick Ni at 800°C (**Figure 4.21i**). We do not observe the 3rd stage with the 150 nm thick Ni. Probably higher temperatures are required to form individual Ni particles.

We noticed clearly that the dewetting three-stage process depends on the initial nickel film thickness and annealing temperature. Also, the dewetting rate and driving force increase with decreasing the film thickness, and the temperature at which dewetting occurs decreases when film thickness decreases, in agreement with the previous work[38]. This could explain why the 25 nm thick Ni film starts coalescing at a lower temperature than the thicker Ni films, and why the 150 nm thickest film starts to coalesce into nickel islands lately at the highest temperatures. In other words, the transition between the three already-mentioned stages occurs at higher temperatures when the Ni film thickness increases.

Samples	Processing temperature (°C)	Average perimeter (µm)	Surface coverage (%)	Particles interspacing (µm)
Ni 25 nm	700	1.47 ± 0.5	21	0.62
	800	1.88 ± 0.5	19	0.80
	900	1.70 ± 0.8	16	0.84
Ni 25 nm with Graphene	900	1.04 ± 0.6	11	0.70
Ni 50 nm	800	N/A	24	N/A
	900	3.90 ± 2.3	16	1.50
Ni 50 nm with Graphene	900	2.34 ± 1.18	15	1.10
Ni 150 nm	800	N/A	58	N/A
	900	N/A	35	N/A
Ni 150 nm with Graphene	900	N/A	14	N/A

Table 4. 6 Summary of the statistical values of the average perimeter, surface coverage, and interspacing of nickel particles extracted from the SEM images in Figure 4.21 and Figure 4.23.

SEM images in **Figure 4.21** were used to extract, using ImageJ software, the information about the surface coverage by the Ni islands or particles, the particle perimeter, and the interparticle spacings (i.e. the distance between the nearest neighbor particles). Values are reported in **Table 4.6**. Whatever the film thickness, the surface coverage by the stringy Ni islands (2nd stage) or particles (3rd stage) decreases when the temperature increases, from 21% to 16% with the 25 nm film, from 24% to 16% with the 50 nm film, and from 58% to 35 % for the 150 nm film. This is consistent with the dewetting and coalescence mechanism described above. Moreover, at the highest temperature of 900°C, the surface coverage is even higher when the initial Ni film is thick. With respect to the particle perimeter and interparticle distance, only their values can be extracted and compared for the 3rd stage, which is to say for the 25 nm thick film annealed at 700, 800, and 900°C, and for the 50 nm film annealed at 900°C.

Figure 4.22 shows the size distribution of the perimeter of the Ni particles related to the dewetting process of the 25 nm nickel film. The average particle perimeters are 1.47 ± 0.5, 1.88 ± 0.5 and 1.70 ± 0.8 µm, and the interparticle spacings are 0.62, 0.80, 0.84 µm, for the annealing temperatures of 700, 800, 900°C respectively. At the highest temperature of 900°C, the perimeter of the particles related to the thicker 50 nm film is a little more than a factor two compared to the 25 nm thick film (3.9 µm compared to 1.7 µm) at the same temperature, and the interparticle spacing is a little less than a factor two (1.50 µm compared to 0.84 µm), with a similar surface coverage of 16%. This analysis suggests that with the 25 nm thick Ni film, the increase of annealing temperature during stage 3 leads to a substantial increase in particle sizes and interparticle spacing, accompanied by a decrease in their surface coverage. Moreover, when keeping constant the annealing temperature, the particles derived from the dewetting of the 25 nm thick film are smaller, cover a lower surface, and have lower interparticle spacing with respect to those derived from the 50 nm thicker Ni films. These results are in perfect agreement with previously reported results on the high-temperature annealing effect on metallic thin film, including Ni [36,37,43] relating in particular that the reduction of surface coverage is due to the specific thermo-kinetic conditions during the rapid thermal annealing process. Finally, one cannot exclude that residual Ni remains present within Ni particles, meaning that the Ni dewetting would be not complete, even at 900°C. This assumption will be studied in the next section related to the behavior of the Ni film at high temperature, in the presence of a carbon film to achieve graphene synthesis.

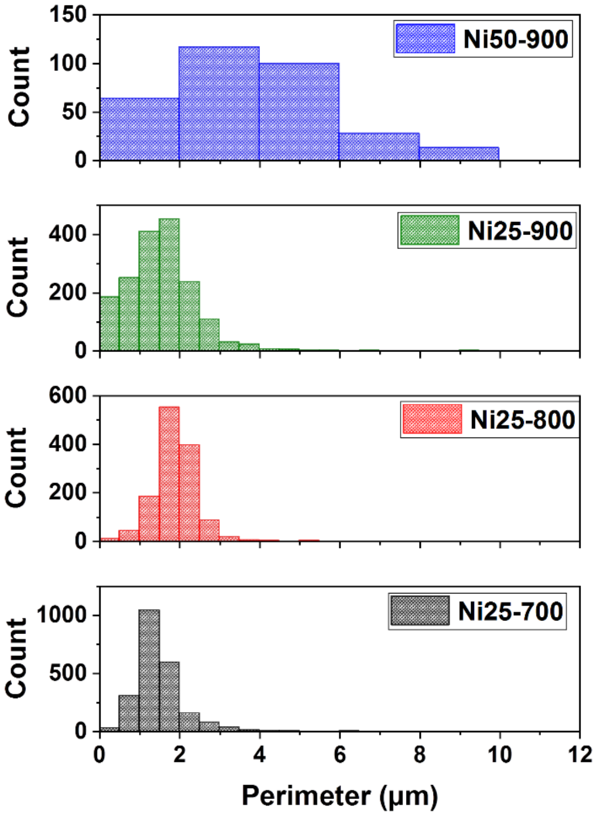

Figure 4. 22 Particle size distribution corresponding to the 3rd stage of the Ni dewetting process, obtained by using ImageJ software on the SEM images in Fig.2, and related to the 25 nm thick Ni film after thermal annealing at 700, 800 and 900°C, and the 50 nm thick Ni film after thermal annealing at 900°C.

b. Nickel thin film dewetting with the presence of carbon

Figure 4.23d shows the SEM image of the as-grown graphene using 25 nm of a nickel catalyst after thermal annealing at 900°C. A similar nickel island distribution than with the 25 nm thick Ni film annealed the same temperature (**Figure 4.23a**) is observed. By comparing the statistic values of the pure Ni film with the same film covered by graphene, the perimeter of nickel particles is reduced from 1.70 µm without graphene to 1.04 µm with graphene. The surface coverage diminished from 16 to 11 % and the distance between the particles goes down slightly as well from 0.80 to 0.70 µm. This difference may due to the presence of dissolved carbon in nickel, which modifies the surface energy of the nickel during the dewetting process.

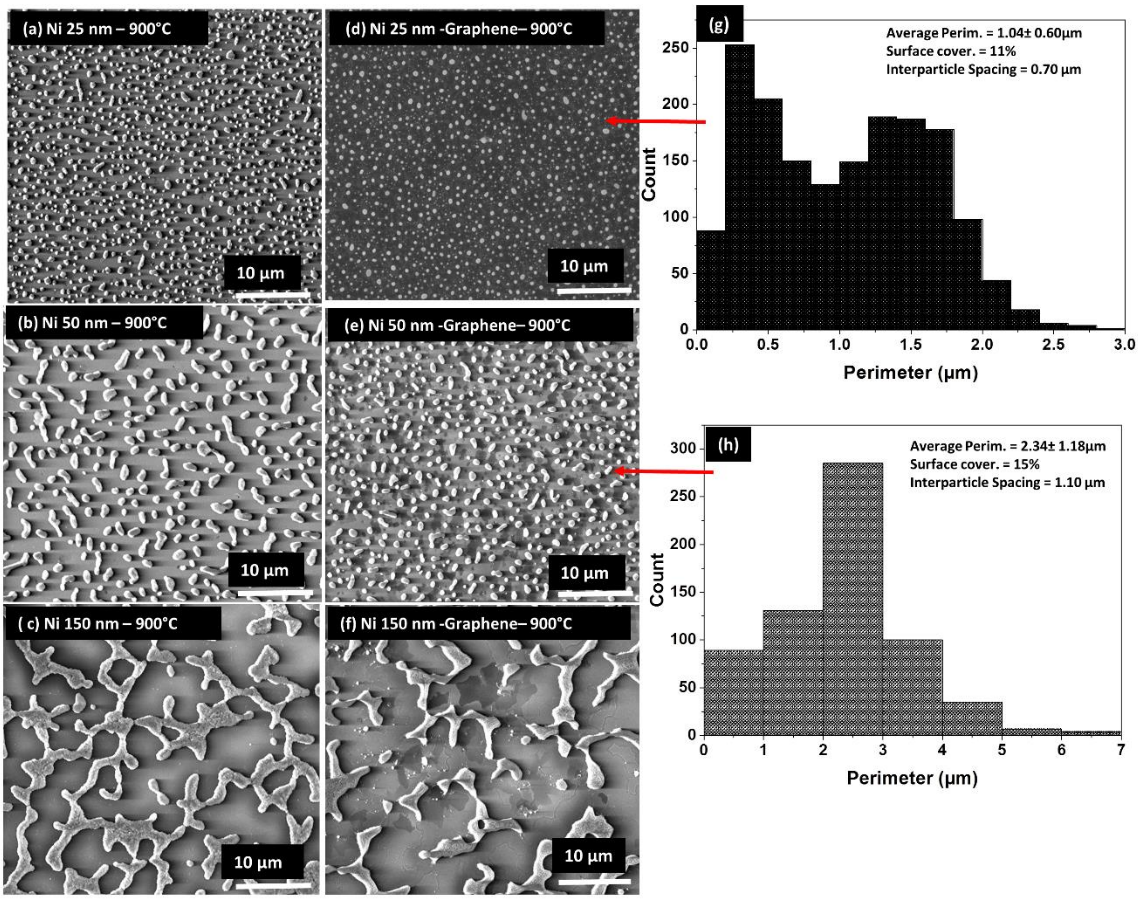

Figure 4. 23 Comparison of the solid-state dewetting behavior for nickel thin films deposited on fused silica SiO_2 substrate in the presence and absence of graphene at 900°C. (a-c) SEM images of the dewetting of nickel thin film of 25, 50, and 150 nm at 900°C in absence of carbon. (d-f) SEM images of the dewetting of nickel thin film of 25, 50, and 150 nm at 900°C in presence of carbon. (g) Histogram of particle size distribution extracted from the SEM image in **Figure 4.23d**. (h) Histogram of particle size distribution extracted from the SEM image in **Figure 4.23e**. The insets in both figures are the values of the mean perimeter, surface coverage, and interparticle spacing of the nickel particles.

Figure 4.23e shows the SEM image of the as-grown graphene using 50 nm of the nickel catalyst. As for the annealed 50 nm thick of nickel, this sample presents many island-shaped nickel particles. By comparing the statistic values, the perimeter of nickel particle decreases from 3.9 µm in the absence of graphene to 2.34 µm with the presence of graphene. The surface coverage slightly decreases from 16 to 15 % and the distance between the particles diminishes from 1.50 to 1.10 µm. This observation shows the same trend as using 25 nm of nickel film.

Figure 4.23f shows the SEM image of the as-grown graphene using 150 nm of the nickel catalyst. Here, we extracted only the surface coverage, which is about 14 %, suggesting that the same trend as for the other cases. **Table 4.6** summarizes the statistical values extracted from the SEM images in **Figure 4.21** and **4.23**.

From all these results, we observed a huge effect of temperature on the shape, size, surface coverage, and interspacing of the particle. Indeed, whatever the initial nickel thickness, the considered statistical parameters evolved by changing the annealing temperature. This effect shows that the process of the formation of these nickel particles is thermally activated. Moreover, the temperature at which dewetting occurs is lower for thinner films, and the island size scales with the film thickness[44]. Furthermore, considering the initial nickel thickness, the particle size increases with the increase of temperature for Ni 25 nm, while it decreases for Ni 50 nm with the increase of temperature. This opposite trend between both nickel thicknesses may be due to the shape change of the nickel particles derived from Ni 50 nm. It has been also reported[45] that the surface coverage decreases with the increase of the annealing temperature. This is the same case here in our study, whatever the starting nickel thickness, the surface coverage decreases with the rising of temperature. Moreover, with the presence of carbon, the size, spacing, and surface coverage of the Ni islands diminish. This suggests that the carbon favors the dewetting of nickel particles, which is in agreement with the work of Diarra et al.[46]. Furthermore, the dewetting of nickel is much more pronounced with the decrease of the initial nickel film thickness. From all these results, we conclude that the most important aspects that affect the nickel islands derived from the dewetting of nickel thin film are the annealing temperature, the starting nickel film thickness and the presence of carbon deposited before the rapid thermal annealing.

2. Nickel thickness influence on the transformation of PLD amorphous carbon into graphene after thermal annealing at 900°C

At the highest RTA temperature of 900°C and pressure of 10^{-2} mbar used in our study, nickel is well below its melting point (1455°C). Therefore, it remains in solid-state, but it dewets progressively, as evidenced in the previous section, by the three-stage mechanism process with temperature thresholds depending on the initial Ni film thicknesses (25, 50, 150 nm). Along with that, the annealing process caused the dissolution of carbon into nickel films and its further surface segregation results in the formation of graphene. Besides, the objective of this section is to elucidate how nickel dewetting remains compatible with the synthesis of graphene and to highlight the quality of the graphene obtained in such conditions. Ideally, such a process may avoid the transfer of graphene on another substrate, if the residual Ni particles can be removed from the surface, for example via an acidic treatment.

a. Graphene growth using 25 nm thick of nickel thin film catalyst

Figure 4.24 shows the Raman analysis of the synthesized graphene using 25 nm thick of nickel catalyst film, after thermal annealing at 900°C. **Figure 4.24a** is the Raman mapping of the I_D/I_G ratio, where the average value is about 0.25 with a very low standard deviation of 0.05 suggesting the good uniformity of the synthesized graphene with low defect density. **Figure 4.24b** shows the Raman mapping of the I_{2D}/I_G ratio with a mean value of 0.62 and a low standard deviation of 0.05. This result demonstrates the formation of a uniform few-layer (3-6 layers) graphene using 25 nm thick of nickel catalyst. **Figure 4.24c** shows a representative spectrum of the Raman mapping. In this spectrum, the different D, G, and 2D are located at 1372, 1587, 2746 cm^{-1} respectively. Besides, the intensity ratio values are 0.67 for I_{2D}/I_G and 0.21 for I_D/I_G. Moreover, the crystallite size L_a is about 44 nm. This value is derived from the I_D/I_G ratio by the mean of the Tuinstra–Koenig equation evoked in the Raman section of Chapter 2. **Fig. 4.24d** illustrates the predominance of a few-layer (3-6 layers) graphene with the statistical histogram of the Raman mapping of the I_{2D}/I_G ratio showing the distribution of graphene layer number. Indeed, with the 25 nm thick of Ni film only 5% of the mapped area is a bilayer, whereas, three-layer and more graphene layers cover 95%. This suggests that the synthesized graphene is uniform and of good quality, even with the presence of the nickel particles derived from the dewetting of nickel catalyst film. It is worth noticing that all these maps comprise the graphene at the top surface of the nickel particles as well as the one at the interface between the nickel nodules and the SiO_2 substrate.

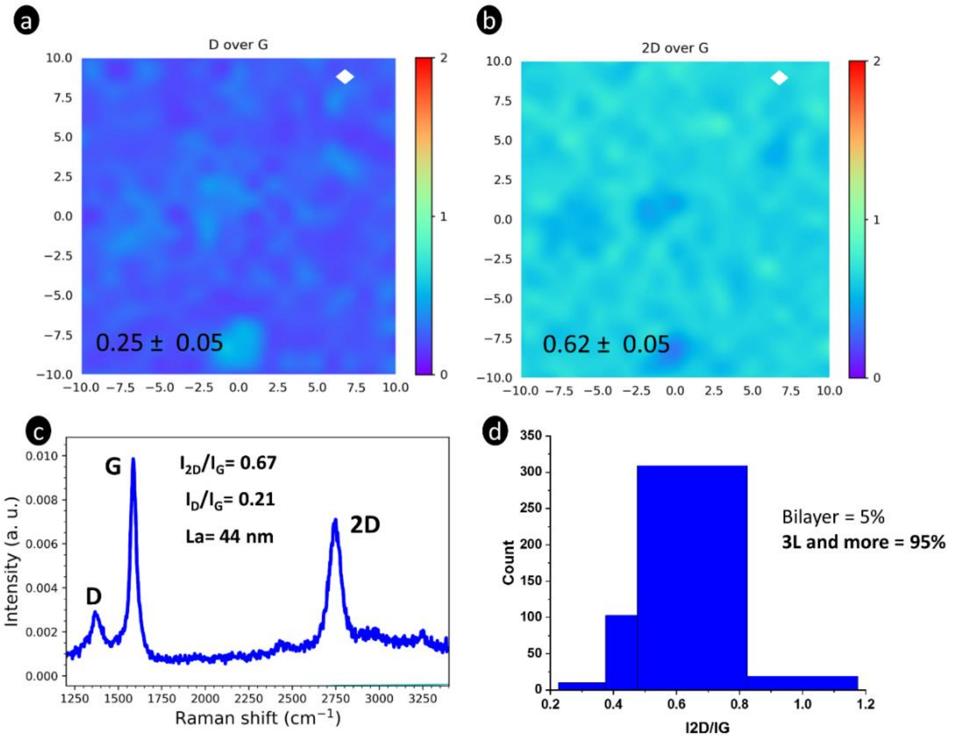

Figure 4. 24 Raman analysis of the synthesized graphene using 25 nm thick of nickel catalyst : (a) Raman mapping of ID/IG ratio in a 20 ×20 µm² region with the average value of 0.25 ; (b) Raman mapping of I2D/IG ratio in a 20 ×20 µm² region with the average value of 0.62; (c) A representative spectrum from the mapping of the synthesized graphene, its position corresponds to the white mark in the Raman mappings ; (d) Statistical histogram of the Raman mapping of I2D/IG ratio showing the few-layer predominance.

Figure 4.25a shows the SEM image of the as-grown graphene using the 25 nm thick nickel film catalyst after thermal annealing at 900°C. **Figure 4.25c** shows the SEM image of the treated graphene with $FeCl_3$ acidic solution and this graphene can be called interfacial graphene because the other graphene at the top surface of the nickel nodules probably disappeared with the removal of nickel residuals. It can be observed the disappearing of the nickel nodules leaving some spherical white traces. **Figure 4.25 b, d** show EDS spectra for the as-grown graphene and the treated graphene. For the as-grown graphene (**Figure 4.25b**), the spectra were taken by focusing the electron-beam spot either on the nickel particle (lower spectrum), either on the graphene layer (upper spectrum). The results revealed that these two areas contain nickel and other expected elements such as C, O, and Si. However, the area corresponding to the Ni particles contains a bit more amount of nickel with respect to the other region. This means that the dewetting of Ni is not fully achieved on the initial surface, even at 900°C. However, after $FeCl_3$ treatment, the EDS spectra recorded both inside and outside the footprints left by the Ni removed particles (**Figure 4.25d**) do not exhibit any Ni signals. This result is consistent with the previously reported studies[28,47] on acidic etching to obtain transfer-free graphene.

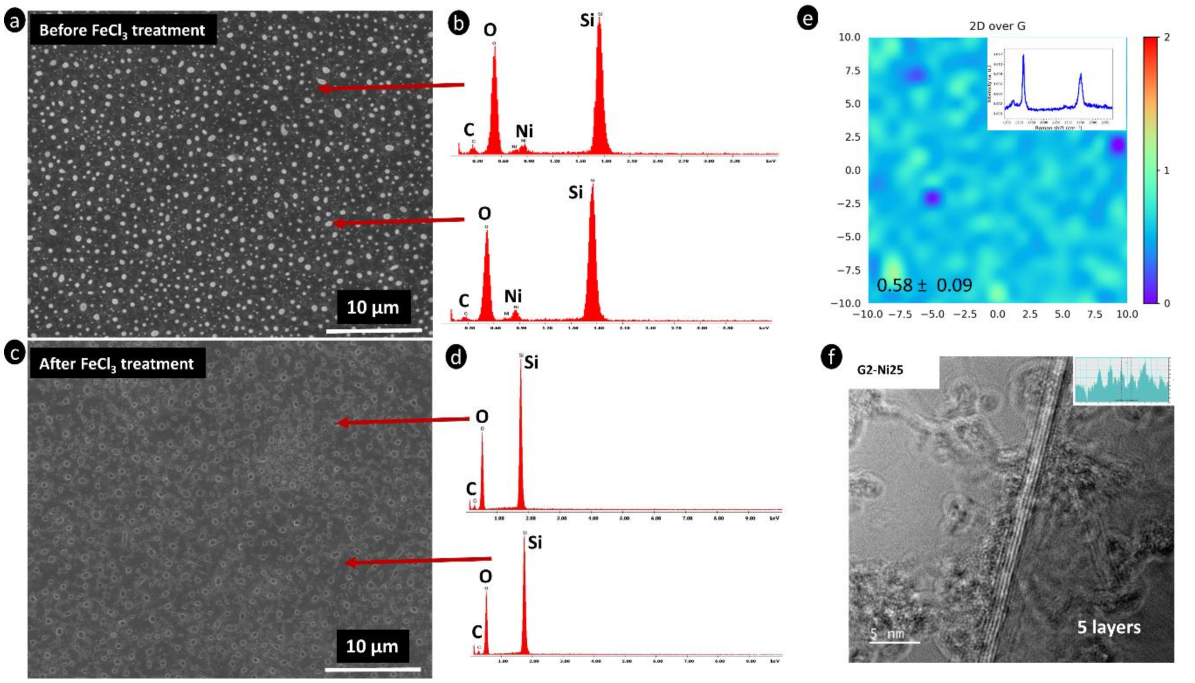

Figure 4. 25 (a) SEM image of the as-synthesized graphene using the 25 nm thick of nickel catalyst, after annealing at 900°C; (b) EDS spectra of two different regions of the samples, the grey-black zone (on the top) and the white islands zone (below); (c) SEM image of the treated graphene with $FeCl_3$ for nickel particles removal leading to the appearing of the interfacial graphene; (d) EDS spectra of two different regions of the samples, the zone with traces of islands (on the top) and the grey-black zone (below), both showing the absence of nickel; (e) Raman mapping of I_{2D}/I_G ratio in a 20 ×20 µm² region with an average value of 0.58 of the interfacial graphene after $FeCl_3$ treatment. The inset shows a representative spectrum from the Raman mapping; (f) HRTEM image of resulting graphene edges showing five layers, after $FeCl_3$ treatment. The inset is the intensity profile image.

Figure 4.25e shows the Raman mapping of the I_{2D}/I_G ratio in a 20 ×20 µm² region related to the interfacial graphene after $FeCl_3$ treatment, with an average value of 0.58. The inset shows a representative spectrum extracted from the Raman mapping. Both exhibit the same characteristics as for the one of as-synthesized graphene showed in **Figure 4.24b-c**. An uniform surface graphene distribution is observed, as for the as-grown graphene. This suggests that the $FeCl_3$ treatment appears to be a transfer-free process allowing the removal of the Ni catalyst without any significant alteration of the graphene nature and characteristics consistent with a dominant few-layer architecture. **Figure 4.25f** shows the HRTEM images of the graphene after $FeCl_3$ treatment. The observation, typical of the graphene edges, provides an accurate way to measure the number of graphene layers at different locations. Here, the synthetized graphene from 25 nm Ni exhibits five lines, consisting of five layers graphene as reported through Raman analysis.

b. Graphene growth using 50 nm thick of nickel thin film catalyst

As for the synthesized graphene using 25 nm of nickel film, Raman analysis, SEM-EDS were performed for the as-grown graphene using 50 nm thick of nickel after thermal annealing at 900°C.

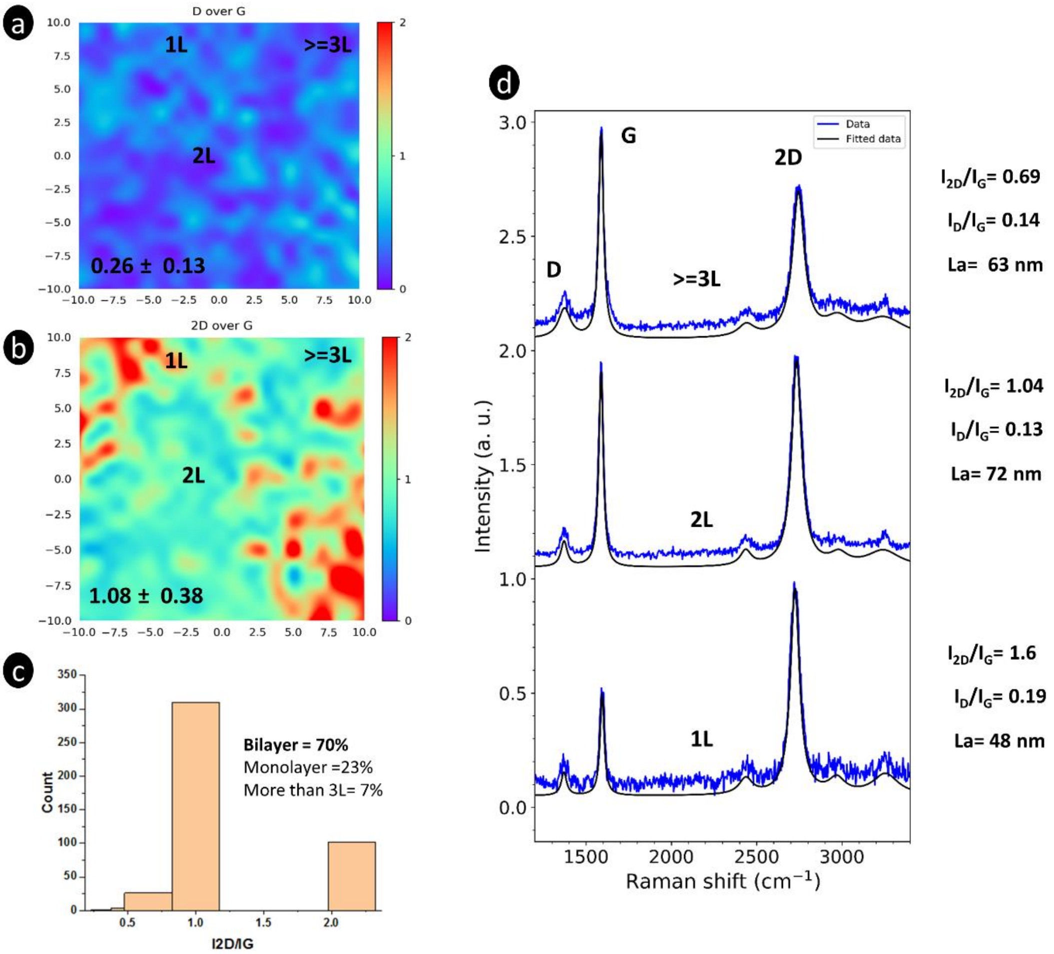

Figure 4. 26 Raman analysis of the as-synthesized graphene using 50 nm of nickel catalyst film: (a) Raman mapping of I_D/I_G ratio in a 20 ×20 μm² region with the average value of 0.26; (b) Raman mapping of I_{2D}/I_G ratio in a 20 ×20 μm² region with the average value of 1.08; (c) Statistical histogram of the Raman mapping of I_{2D}/I_G ratio showing the bilayer graphene predominance. (d) Representative spectra from the mapping of the as-grown graphene, their positions are highlighted with the corresponding number of the layer in the Raman mappings.

Figure 4.26a is the Raman mapping of the I_D/I_G ratio, where the average value is about 0.26 with a low standard deviation of 0.13 suggesting the reasonable uniformity of defect density in the synthesized graphene. **Figure 4.26b** shows the Raman mapping of the I_{2D}/I_G ratio with a mean value of 1.08 and a high standard deviation of 0.38. This result demonstrates the formation of continuous, but non-uniform graphene using 50 nm thick of nickel catalyst. Indeed, the derived graphene from the utilization of 50 nm of nickel is heterogeneous, containing monolayer, bilayer, and few-layer graphene. This observation is supported by the statistical histogram of the Raman mapping of the I_{2D}/I_G ratio showing the distribution of the graphene layer number (**Figure 4.26c)**. From this statistical data, 7% of the mapped area is a few-layer (3 and more layers), 70% is bilayer and 23% is monolayer, suggesting the bilayer predominance in the mapped area. **Figure 4.26d** exhibits the different types of Raman spectra being representative of the monolayer, bilayer, and few-layer graphene with their values characteristics. This finding was also reported in our previous section II meaning that our method is quite reproducible. Again, all these maps encompass the graphene at the top surface of the nickel particles as well as the one at the interface between the nickel nodules and the SiO_2 substrate.

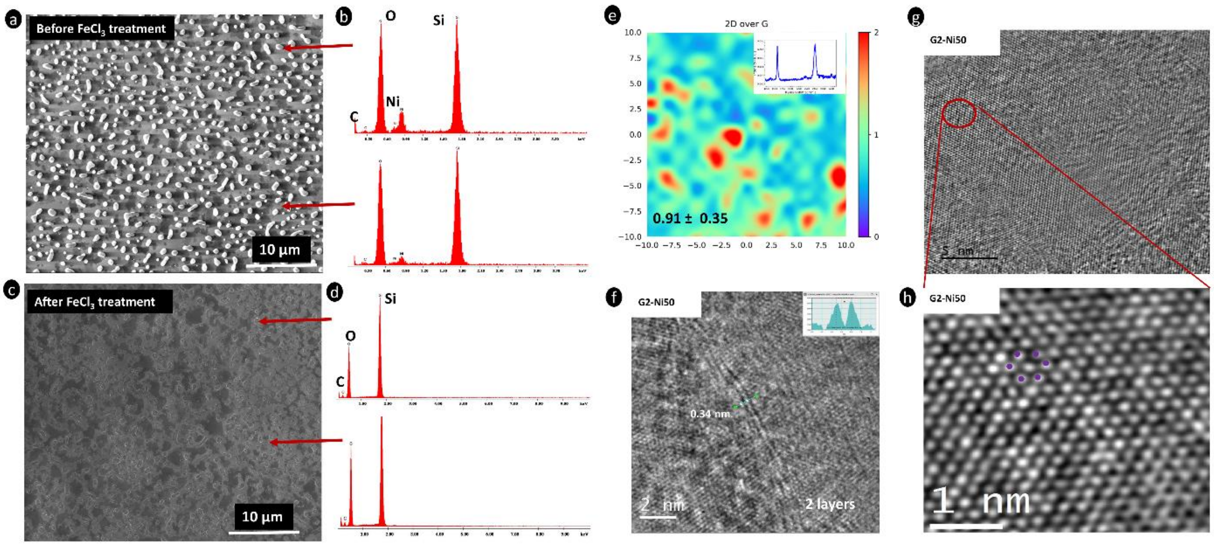

Figure 4. 27 (a) SEM image of the as-synthesized graphene using the 50 nm of nickel catalyst film. (b) EDS spectra of two different regions of the samples, the white islands zone (on the top) and the grey-black zone (below). (c) SEM image of the treated graphene with $FeCl_3$ for nickel particles removal leading to the appearing of the interfacial graphene (d) EDS spectra of two different regions of the samples, the zone with traces of islands (on the top), and the grey-black zone (below), both showed the absence of nickel. (e) Raman mapping of I_{2D}/I_G ratio in a 20 ×20 µm² region with the average value of 0.91 of the treated graphene with $FeCl_3$. The inset shows a bilayer graphene spectrum from the Raman mapping of the $Fecl_3$ treated graphene. (f) HRTEM of resulting graphene edges from 50 nm of nickel, showing two layers after $FeCl_3$ treatment. The inset is the intensity profile image. (g – h) HRTEM of resulting graphene from 50 nm of nickel, showing a "one monolayer" area (red circle) and the hexagonal atomic resolution of the monolayer graphene. The purple dots in the inset of Figure. 4.27h highlights the hexagonal structure of graphene.

Figure 4.27a shows the SEM image of the as-grown graphene using 50 nm of the nickel catalyst. SEM image (**Figure 4.27c)** of the treated graphene with $FeCl_3$ shows that the round-shaped nickel particles are not present anymore. Elemental analysis with EDS was performed for the as-grown graphene and the treated graphene. The results show the presence of nickel for the as-synthesized graphene sample (**Figure 4.27b**), while in the treated graphene spectrum (**Figure 4.27d**) the removal of nickel is confirmed. **Figure 4.27e** shows the Raman mapping of the I_{2D}/I_G ratio in a 20 ×20 µm² region with an average value of 0.91, related to the treated graphene with $FeCl_3$ leading to the interfacial graphene. The inset spectrum represents the one of bilayer graphene. This mapping shows that the interfacial graphene has the same characteristics as the as-grown graphene. This means that the interfacial graphene is also continuous but non-uniform, containing monolayer, (mainly) bilayer, and some few-layer graphene. **Figure 4.27f** shows the HRTEM images depicting the edges in the bilayer graphene region showing a double line. The estimated interplanar spacing from the intensity profile images, as shown in the insets of **Figure 4.25f** and **4.27f**, is about 0.345 nm, which in agreement with previously reported works[48,49]. **Figure 4.27g** shows a typical graphene monolayer region indicated by the red circle, and **Figure 4.27h** displays the hexagonal structure of such a typical monolayer illustrated with the purple dots. This HRTEM examination confirms also that the initial thickness of nickel affects strongly the final synthesized graphene layers, in agreement with our Raman results.

c. Graphene growth using 150 nm thick of nickel thin film catalyst

Here, the graphene is formed using 150 nm of nickel film as the catalyst, after thermal annealing at 900°C. As the annealing response on 150 nm is different from 25 and 50 nm nickel film, the derived graphene is also different. The first striking point is that the synthesized graphene is not continuous as shown in **Figure 4.28**.

Indeed, **Figure 4.28a** shows the SEM image of the as-grown graphene using 150 nm thick of nickel film. This image presents the same features as for the annealed 150 nm thick of nickel film at 900°C, with the agglomeration of nickel islands. In addition, the graphene formation occurred at the top surface of nickel islands and in the interface between the nickel and the SiO_2 substrate like in the case of 25 and 50 nm of nickel thick. The difference here is the presence of graphene with a different contrast: dark contrast for high layer number and bright contrast for low layer number, as it has been reported by previous works[50–52]. The layer numbers in the SEM image mark the locations of thin and thick graphene layers. **Figure 4.28b** exhibits the EDS spectra, showing clearly that the synthesized graphene is not continuous. In **Figure 4.28c,** the representative Raman spectra of the synthesized graphene using 150 nm of nickel film is shown. Even though the obtained graphene is not continuous, it contains monolayer, bilayer, and few-layer as for the derived graphene from 50 nm of nickel film. It is then heterogeneous, with rather very low defect density and larger crystallite size compared to the derived graphene from 25 and 50 nm nickel film.

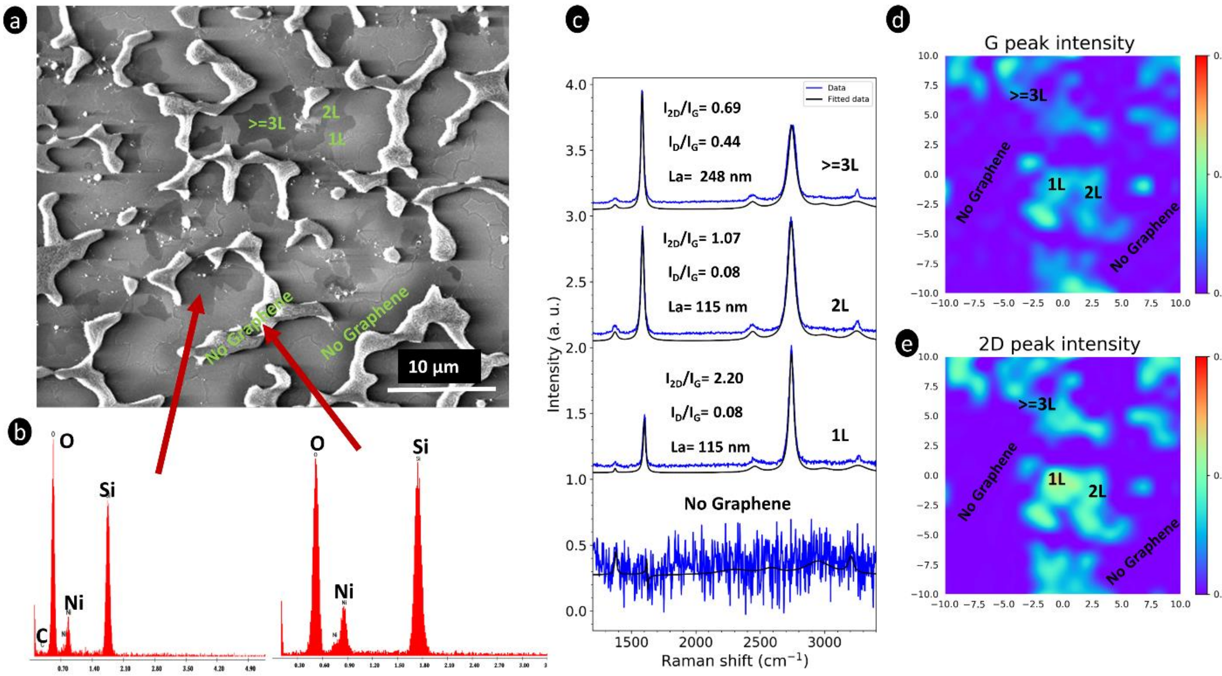

Figure 4. 28 (a) SEM image of the as-synthesized graphene using the 150 nm of nickel catalyst film, showing a dark and bright contrast for thicker and thinner graphene respectively. (b) EDS spectra of two different regions of the samples, the grey-black zone (on the left) and the white islands zone (right). (c) Representative spectra from the sample of the as-grown graphene, their positions are illustrated with the corresponding number of the layer in the Raman mapping. (d) Raman mapping results of G peak intensity with the sample area of 20 ×20 µm². (e) Raman mapping results of 2D peak intensity with the sample area of 20 ×20 µm².

Moreover, at the bottom of **Figure 4.28c**, the Raman spectrum of the area without graphene is presented, showing no signal. This result is consistent with the synthesis graphene using nickel catalyst film with the initial thickness below 170 nm[23]. Furthermore, to argue more on the discontinuity and the non-uniformity of the synthesized graphene, Raman mapping was performed. **Figures 4.28d-e** show the Raman mapping of the G and 2D peaks intensities respectively, where the low-intensity areas are regions without graphene. From all these analyses, we conclude that 150 nm thick of nickel catalyst is not suitable for obtaining continuous graphene when using 2 nm of amorphous carbon as a carbon source and 900°C as processing temperature.

3. The optimal synthesis condition and further characterizations

Table 4.7 summarizes the different characteristics of the resulting graphene from the synthesis process using 25, 50, and 150 nm thick of nickel film. The reported results in **Table 4.7** show that by increasing the nickel thickness from 25 to 50 nm, the layer number of the resulting graphene decreases. This is consistent with the previously reported works[28,53,54], showing that the graphene films derived from thicker metal films have better structural qualities with lower layer numbers. Indeed, by increasing the nickel thickness from 25 to 50 nm, the graphene layer number switches from few-layer (3-6 layers) to bilayer predominance. Moreover, using both nickel thicknesses (25 and 50 nm), the synthesized graphene is well continuous with low defect density. In fact, on metals with significant carbon solubility such as nickel, the formation of heterogeneous graphene constituted with monolayer, bilayer, and few-layer is very common because of the additional graphene growth from the carbon reservoir in the catalyst bulk. Nevertheless, this segregation effect seems to be limited when using 50 nm thick of nickel compared to 25 nm of nickel thin film, probably because a thicker Ni film of 50 nm constitutes a “deeper” reservoir of carbon, compared to a thinner Ni film of 25 nm when similar heating treatment is performed on both films. This may explain why the synthesized graphene is thicker with the 25 nm nickel film and thinner with the 50 nm nickel film.

Nickel thickness (nm)	Processing conditions	a-C thickness (nm)	Synthesized Graphene
25	900°C with a heating rate of 15°C/s, during 420 s and a cooling rate of 0.5°C/s	2	Continuous and uniform few-layer graphene
50			Continuous and heterogeneous graphene with bilayer predominance
150			Non-continuous and heterogeneous graphene

Table 4. 7 Summary of the different characteristics of the resulting graphene from the synthesis process using 25, 50, and 150 nm thick of nickel film.

Consequently, the synthesized graphene at the investigated temperature (900°C) is thicker for the 25 nm nickel and thinner for the 50 nm nickel. However, further increase of nickel thickness up to 150 nm affects considerably the resulting graphene, being non-continuous graphene, even if monolayer, bilayer, and few-layer graphene with very low defect density are observed. This surface discontinuity may be due in one hand to the large attached nickel islands derived from the dewetting process of the 150 nm thick nickel film, and on the other hand, to the low concentration of dissolved carbon which has diffused far in the thick nickel film. Because of this strong surface heterogeneity, it was not possible to make the Raman statistical analysis to get an overview of the graphene layer distribution.

From these results, we conclude that the larger amount of graphene is precipitated out from the thinner nickel films whereas a smaller amount of graphene is precipitated out from the thicker nickel films. Furthermore, as for the quality of graphene films, it can be speculated that the increase in the layer number caused the structural disorder of graphene films. This indicates that the layer number and film quality (in terms of defects) can be controlled by choosing the appropriate nickel thickness for a given annealing temperature.

Besides, let us remind that using 25, 50 and 150 nm Ni thick, the graphene is not only formed on the top surface of the nickel but also at the interface between the nickel and the SiO_2 substrate, except that with 150 nm thick, the formed graphene is non- continuous. Indeed, this occurs because, during the thermal annealing, carbon diffuses through the nickel film and segregates out of both sides of the Ni film, as illustrated in **Figure 4.29a**.

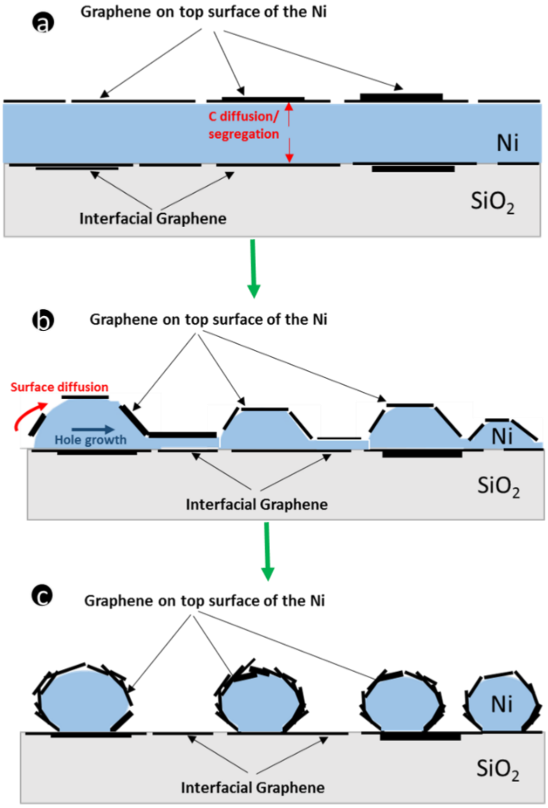

Figure 4. 29 A schematic illustration of graphene growth at the top surface of nickel film and in the interface between the Ni and SiO_2 substrate along with the nickel dewetting process. (a) The stage with carbon diffusion and segregation through nickel for the initial graphene formation before the start of the nickel dewetting (low temperature, e.g. 500°C) (b) The stage related to the beginning of the nickel dewetting (c) The stage with the end of nickel dewetting process. During stages (b) and (c), the initially formed graphene undergoes certainly further evolution in terms of nanostructures.

In chapter 3, we have demonstrated using *in situ* XPS analysis that the graphene already forms at 500°C through the carbon diffusion and segregation in the nickel catalyst during the annealing process. Such a mechanism also occurs with thermal annealing up to 900°C, but the highest temperatures induce also nickel dewetting, as we observed. More precisely, during the annealing process, three main phenomena take place when the temperature increases up to 900°C:

- The carbon diffusion and segregation out of both sides of the nickel catalyst, leading to the graphene formation at the same time on the top surface of the nickel and the interface between the Ni and the substrate, depicted in Figure 4.29a. This is consistent with our results in chapter 3, showing graphene formation after annealing at 500°C without any Ni dewetting at this temperature.
- The starting of nickel dewetting with the hole growth and the surface carbon diffusion on the nickel leading to the graphene formation on the nickel surface, illustrated in Figure 4.29b.
- The final stage of the nickel dewetting with the formation of nickel particles with the synthesized graphene on its surface and at the interface between the nickel particles and the SiO_2 substrate, as shown in Figure 4.29c.

All these phenomena cover the graphene synthesis with the nickel dewetting during the thermal annealing. However, they depend considerably on the initial nickel film thickness and the annealing temperature. Indeed, using a nickel of 25 and 50 nm, we observed the continuous surface and interfacial graphene growth with the formation of rounded nickel particles. While using the 150 nm nickel thick, we observed non-continuous surface and interfacial graphene growth with stringy nickel particles. Further investigation is needed to understand why using 150 nm thick of nickel, there is the formation of non-continuous graphene.

Furthermore, after nickel island removal with $FeCl_3$ treatment, we performed the UV-Vis analysis on the continuous interfacial graphene from 25 and 50 nm of nickel. The objective of this investigation was to correlate the graphene architecture with its optical transmission property as known from the literature. **Figure 4.30** shows the measurement of the transmittance of both derived graphene from 25 and 50 nm nickel after nickel particles etching. The transmittance value of the derived graphene from 25 nm nickel at 550 nm is about ~84 %, which is consistent with the reported values[53–55] for few-layer graphene of (~3-6 layers). For the resulting graphene from 50 nm nickel, the transmittance value is much higher about 88% consistent with our previous reported values for bilayer graphene in section II. Indeed, the transmittance of the synthetized graphene from 25 nm nickel is lower than the transparency of the resulting graphene from 50 nm nickel because it has a higher layer number as indicated by Raman data. These results are consistent with the idea that the optical transmittance is strongly correlated to the layer number of graphene. The graphene transmittance decreases with the increase of layer number[58–60].

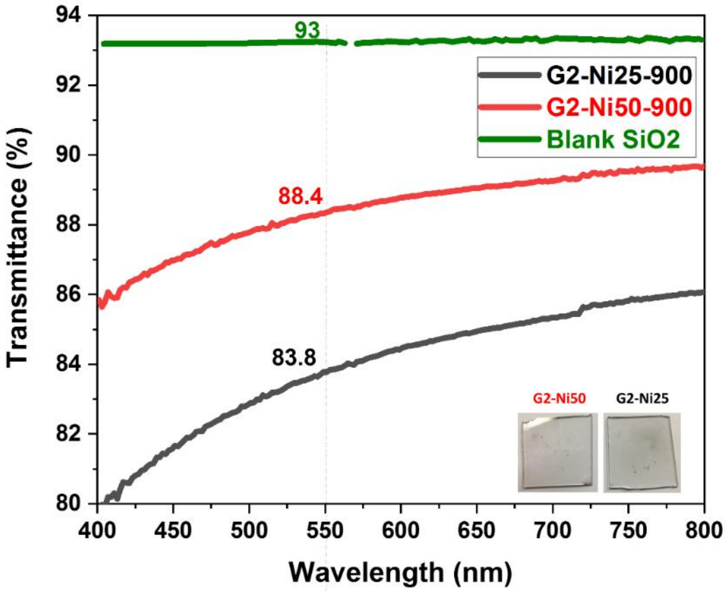

Figure 4. 30 Transmittance curve as a function of wavelength for both: derived graphene from 25 nm nickel (bottom) and the synthesized graphene derived from 50 nm nickel (top) (middle) after thermal annealing and $FeCl_3$ etching and the blank fused silica (top). The inset at the bottom figure shows the appearance of both samples after graphene growth and Ni etching.

In summary, we investigated the transformation of PLD amorphous carbon into transfer-free graphene utilizing nickel catalyst dewetting phenomena. We performed a systematic study of nickel dewetting, as well as of the effect of nickel thickness on graphene growth and we can conclude the following points:

- The most crucial parameters for the formation of nickel particles during the thermal annealing through the dewetting phenomenon are the annealing temperature, the initial nickel film thickness, and the thin carbon layer deposited on Ni before the rapid thermal annealing, and partially dissolved into Ni at high temperature.
- Microscopic Raman mapping, SEM and HRTEM study indicated that graphene films were preferentially continuous for 25 and 50 nm of nickel, whereas the synthetized graphene from 150 nm of nickel was discontinuous. It was also confirmed that the graphene layer thickness, as well as the nickel particle size, is dependent on the starting nickel thickness.

- We observed also that graphene films were formed on the top surface of the nickel particles and at the interface between the nickel particles and the SiO_2 substrate.
- With acidic etching of the residual nickel, the substrate with graphene regained high transparency corresponding to the bilayer interfacial graphene for the derived graphene from 50 nm of nickel as reported in the previous section. This confirms the reproducibility of our process.

These results corroborate that the initial thickness of the nickel catalyst used for the graphene synthesis is a key parameter and that with our method the interfacial graphene can be obtained directly onto the desired area of the substrate, thereby avoiding the relatively complicated, costly, and not always defect-free transfer process.

IV. Summary of the parametric study for graphene synthesis by PLD and RTA

In this chapter, a multi-parametric study has been performed to optimize the growth of continuous free-transfer graphene using the solid carbon source and a nickel catalyst, by combining PLD and RTA. The studied parameters include the substrates, the initial thickness of amorphous carbon, the initial thickness of the nickel catalyst, and the growth temperature, as depicted in **Figure 4.31**. To the scope of optimizing the synthesis process of our graphene, this parametric study was performed along with various nanomaterials characterization techniques: Raman micro-spectroscopy, SEM, AFM, XPS, HRTEM, and UV-Vis, which offer a strong complementarity to investigate few layers of defective graphene synthetized at high temperature from the interaction between a thin amorphous carbon film and a nickel catalyst film.

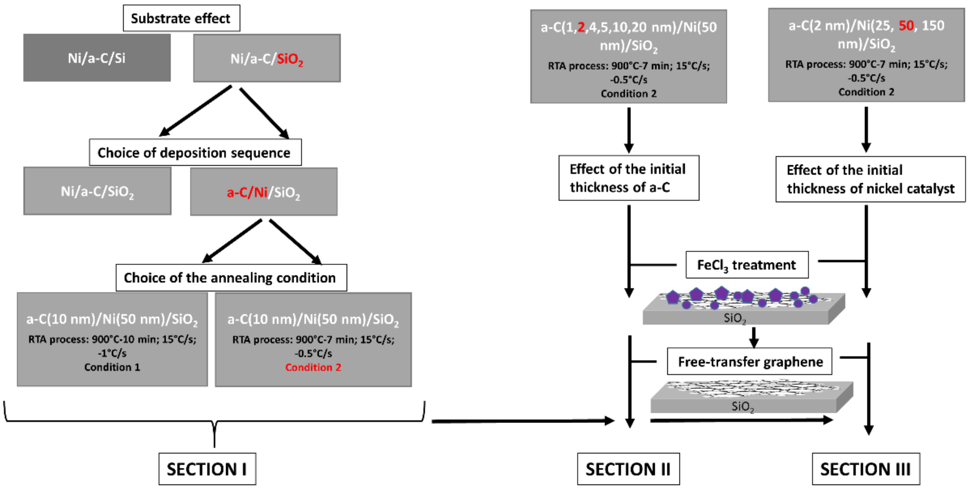

Figure 4. 31 Description of the different sections of this chapter, the conditions colored in red are those used for obtaining our best free transfer continuous graphene.

As illustrated in **Figure 4.31**, we can conclude the following points:

- The growth of graphene on a Si (100) substrate leads to the synthesis of defective multilayered graphene, due to the concomitant nickel silicide formation during the annealing process. Whereas, on the SiO_2 substrate, the graphene growth gives rise to less defective few-layer (2-3 layers) graphene films.
- Using the SiO_2 substrate, the resulting graphene from the deposition sequence Ni/a-C gives slightly thinner graphene with respect to the other deposition order a-C/Ni. We kept the a-C/Ni deposition sequence mainly in the perspective to investigate boron-doped graphene (Chapter 5) from an a-C:B film, without any consideration of boron diffusion through the nickel catalyst.
- Using the SiO_2 substrate and the a-C/Ni deposition sequence, the synthesized graphene from the synthesis conditions 2 (**see Figure 4.31**) presents thinner graphene and lower defect density compared to the graphene resulting to the synthesis conditions 1. This is certainly due to both carbon solubility and diffusion processes in nickel at high temperatures.
- Using the SiO_2 substrate, the a-C/Ni deposition sequence with a fixed Ni thickness and performing the synthesis condition 2, the optimal synthesis conditions to obtain a high proportion of graphene bilayers with lower defect density require a starting a-C thickness of 2 nm and a synthesis temperature of 900°C during 7 min, with a heating rate of 15°C/s and cooling rate of 0.5°C/s.
- The solid-state dewetting phenomenon of the Ni catalyst film, observed at high temperature, does not inhibit the graphene growth mechanism which starts with carbon diffusion into nickel at temperatures well below the dewetting process (in agreement with Chapter 3). Nickel dewetting is controlled by the initial nickel film thickness, temperature, and presence of carbon dissolved in nickel.
- Using the SiO_2 substrate, the a-C/Ni deposition sequence, the synthesis condition 2 and varying the starting nickel catalyst thickness while keeping constant the amorphous carbon thickness, graphene films are preferentially continuous surface and interfacial for 25 and 50 nm of nickel, whereas the synthesized graphene from 150 nm of nickel was discontinuous surface and interfacial. It was also confirmed that the graphene layer number is dependent on the starting nickel thickness. The thinnest graphene films with the lowest defect densities are obtained with a 50 nm thick nickel film, as an ideal "carbon reservoir" to promote surface carbon segregation into graphene.

- After nickel residual removal by $FeCl_3$ solution, free transfer continuous graphene, the so-called "interfacial graphene" was obtained with 76 % of bilayer graphene detected through Raman mapping of 100 ×100 μm^2 area and high transmittance of 88% at 550 nm for the resulting graphene from 50 nm of nickel, in agreement with literature data related to the optical transmission of bilayer graphene.

All these results demonstrate that we have developed an alternative synthesis route allowing the growth of predominantly continuous bilayer graphene films, with a significant low defect density comparable to the graphene sheets obtained by some CVD and PVD studies. Our method thus widens the range of substrate materials on which graphene can be directly synthesized, eliminating the need for an extra graphene-transfer process step. Based on these results, the following chapter will deal with the boron doping of our graphene and its electrochemistry responses, highlighting the effect of boron on the nanoarchitecture of graphene and a typical property widely investigated in graphene studies.

References

1. Iqbal, M. W., Singh, A. K., Iqbal, M. Z. & Eom, J. Raman fingerprint of doping due to metal adsorbates on graphene. *Journal of Physics: Condensed Matter* **24**, 335301 (2012).
2. Bourquard, F. *et al.* Electroanalytical Performance of Nitrogen-Doped Graphene Films Processed in One Step by Pulsed Laser Deposition Directly Coupled with Thermal Annealing. *Materials* **12**, 666 (2019).
3. Malard, L. M., Pimenta, M. A., Dresselhaus, G. & Dresselhaus, M. S. Raman spectroscopy in graphene. *Physics Reports* **473**, 51–87 (2009).
4. Tite, T. *et al.* Surface enhanced Raman spectroscopy platform based on graphene with one-year stability. *Thin Solid Films* **604**, 74–80 (2016).
5. Escobedo-Cousin, E. *et al.* Local solid phase growth of few-layer graphene on silicon carbide from nickel silicide supersaturated with carbon. *Journal of Applied Physics* **113**, 114309 (2013).
6. Juang, Z.-Y. *et al.* Synthesis of graphene on silicon carbide substrates at low temperature. *Carbon* **47**, 2026–2031 (2009).
7. Cichoň, S., Macháč, P., Barda, B., Machovič, V. & Slepička, P. Raman study of Ni and Ni silicide contacts on 4H– and 6H–SiC. *Thin Solid Films* **520**, 4378–4388 (2012).
8. Zhao, F. F. *et al.* Thermal stability study of NiSi and NiSi2 thin films. *Microelectronic Engineering* **71**, 104–111 (2004).
9. Lee, P. S. Micro-Raman Spectroscopy Investigation of Nickel Silicides and Nickel (Platinum) Silicides. *Electrochemical and Solid-State Letters* **3**, 153 (1999).
10. Donthu, S. K., Chi, D. Z., Tripathy, S., Wong, A. S. W. & Chua, S. J. Micro-Raman spectroscopic investigation of NiSi films formed on BF2+-, B+- and non-implanted (100)Si substrates. *Appl. Phys. A* **79**, 637–642 (2004).
11. Bhaskaran, M. *et al.* In situ micro-Raman analysis and X-ray diffraction of nickel silicide thin films on silicon. *Micron* **40**, 89–93 (2009).
12. Huong, P. V., Cavagnat, R., Ajayan, P. M. & Stephan, O. Temperature-dependent vibrational spectra of carbon nanotubes. *Phys. Rev. B* **51**, 10048–10051 (1995).
13. Ferrari, A. C. & Robertson, J. Raman spectroscopy of amorphous, nanostructured, diamond–like carbon, and nanodiamond. *Philosophical Transactions of the Royal Society of London. Series A: Mathematical, Physical and Engineering Sciences* **362**, 2477–2512 (2004).

14. Röhrl, J. *et al.* Raman spectra of epitaxial graphene on SiC(0001). *Appl. Phys. Lett.* **92**, 201918 (2008).
15. Lee, D. S. *et al.* Raman Spectra of Epitaxial Graphene on SiC and of Epitaxial Graphene Transferred to SiO2. *Nano Lett.* **8**, 4320–4325 (2008).
16. Ni, Z. H. *et al.* Tunable Stress and Controlled Thickness Modification in Graphene by Annealing. *ACS Nano* **2**, 1033–1039 (2008).
17. Nguyen, T. A., Lee, J.-U., Yoon, D. & Cheong, H. Excitation energy dependent Raman signatures of ABA- and ABC-stacked few-layer graphene. *Sci Rep* **4**, 4630 (2014).
18. Koh, A. T. T., Foong, Y. M. & Chua, D. H. C. Cooling rate and energy dependence of pulsed laser fabricated graphene on nickel at reduced temperature. *Appl. Phys. Lett.* **97**, 114102 (2010).
19. Xiong, W. *et al.* Single-Step Formation of Graphene on Dielectric Surfaces. *Advanced Materials* **25**, 630–634 (2013).
20. Umair, A. & Raza, H. Controlled synthesis of bilayer graphene on nickel. *Nanoscale Research Letters* **7**, (2012).
21. Koh, A. T. T., Foong, Y. M. & Chua, D. H. C. Comparison of the mechanism of low defect few-layer graphene fabricated on different metals by pulsed laser deposition. *Diamond and Related Materials* **25**, 98–102 (2012).
22. Weatherup, R. S. *et al.* Introducing Carbon Diffusion Barriers for Uniform, High-Quality Graphene Growth from Solid Sources. *Nano Lett.* **13**, 4624–4631 (2013).
23. Peng, Z., Yan, Z., Sun, Z. & Tour, J. M. Direct Growth of Bilayer Graphene on SiO2 Substrates by Carbon Diffusion through Nickel. *ACS Nano* **5**, 8241–8247 (2011).
24. Gong, Y. *et al.* Layer-Controlled and Wafer-Scale Synthesis of Uniform and High-Quality Graphene Films on a Polycrystalline Nickel Catalyst. *Advanced Functional Materials* **22**, 3153–3159 (2012).
25. Yang, N., Choi, K., Robertson, J. & Park, H. G. Layer-selective synthesis of bilayer graphene via chemical vapor deposition. *2D Mater.* **4**, 035023 (2017).
26. Fang, W. *et al.* Rapid Identification of Stacking Orientation in Isotopically Labeled Chemical-Vapor Grown Bilayer Graphene by Raman Spectroscopy. *Nano Lett.* **13**, 1541–1548 (2013).
27. Madito, M. J. *et al.* Raman analysis of bilayer graphene film prepared on commercial Cu(0.5 at% Ni) foil. *Journal of Raman Spectroscopy* **47**, 553–559 (2016).
28. Banno, K. *et al.* Transfer-free graphene synthesis on insulating substrates via agglomeration phenomena of catalytic nickel films. *Appl. Phys. Lett.* **103**, 082112 (2013).

29. Blume, R. *et al.* Characterizing Graphitic Carbon with X-ray Photoelectron Spectroscopy: A Step-by-Step Approach. *ChemCatChem* **7**, 2871–2881 (2015).
30. Wang, Y., Shao, Y., Matson, D. W., Li, J. & Lin, Y. Nitrogen-Doped Graphene and Its Application in Electrochemical Biosensing. *ACS Nano* **4**, 1790–1798 (2010).
31. Malitesta, C., Losito, I., Sabbatini, L. & Zambonin, P. G. New findings on polypyrrole chemical structure by XPS coupled to chemical derivatization labelling. *Journal of Electron Spectroscopy and Related Phenomena* **76**, 629–634 (1995).
32. Bleu, Y. *et al.* Graphene synthesis on SiO2 using pulsed laser deposition with bilayer predominance. *Materials Chemistry and Physics* **238**, 121905 (2019).
33. Nair, R. R. *et al.* Fine Structure Constant Defines Visual Transparency of Graphene. *Science* **320**, 1308–1308 (2008).
34. Liu, Q., Gong, Y., Wilt, J. S., Sakidja, R. & Wu, J. Synchronous growth of AB-stacked bilayer graphene on Cu by simply controlling hydrogen pressure in CVD process. *Carbon* **93**, 199–206 (2015).
35. Sun, Z. *et al.* Growth of graphene from solid carbon sources. *Nature* **468**, 549–552 (2010).
36. Chhowalla, M. *et al.* Growth process conditions of vertically aligned carbon nanotubes using plasma enhanced chemical vapor deposition. *Journal of Applied Physics* **90**, 5308–5317 (2001).
37. Geissler, A., He, M., Benoit, J.-M. & Petit, P. Effect of Hydrogen Pressure on the Size of Nickel Nanoparticles Formed during Dewetting and Reduction of Thin Nickel Films. *J. Phys. Chem. C* **114**, 89–92 (2010).
38. Thompson, C. V. Solid-State Dewetting of Thin Films. *Annu. Rev. Mater. Res.* **42**, 399–434 (2012).
39. Henley, S. J., Carey, J. D. & Silva, S. R. P. Pulsed-laser-induced nanoscale island formation in thin metal-on-oxide films. *Phys. Rev. B* **72**, 195408 (2005).
40. Kwon, J.-Y., Yoon, T.-S., Kim, K.-B. & Min, S.-H. Comparison of the agglomeration behavior of Au and Cu films sputter deposited on silicon dioxide. *Journal of Applied Physics* **93**, 3270–3278 (2003).
41. Ruffino, F., Censabella, M. & Grimaldi, M. G. Dewetted Pt nanostructures on Silicon Carbide surface. *Journal of Physics and Chemistry of Solids* **140**, 109403 (2020).
42. Krishna, H., Shirato, N., Favazza, C. & Kalyanaraman, R. Energy driven self-organization in nanoscale metallic liquid films. *Phys. Chem. Chem. Phys.* **11**, 8136–8143 (2009).
43. Bhattacharyya, S. R. *et al.* Growth and melting of silicon supported silver nanocluster films. *J. Phys. D: Appl. Phys.* **42**, 035306 (2008).

44. Nuryadi, R., Ishikawa, Y., Ono, Y. & Tabe, M. Thermal agglomeration of single-crystalline Si layer on buried SiO2 in ultrahigh vacuum. *Journal of Vacuum Science & Technology B: Microelectronics and Nanometer Structures Processing, Measurement, and Phenomena* **20**, 167–172 (2002).
45. Sudheer, Mondal, P., Rai, V. N. & Srivastava, A. K. A study of growth and thermal dewetting behavior of ultra-thin gold films using transmission electron microscopy. *AIP Advances* **7**, 075303 (2017).
46. Diarra, M., Zappelli, A., Amara, H., Ducastelle, F. & Bichara, C. Importance of Carbon Solubility and Wetting Properties of Nickel Nanoparticles for Single Wall Nanotube Growth. *Phys. Rev. Lett.* **109**, 185501 (2012).
47. Nakagawa, K., Takahashi, H., Shimura, Y. & Maki, H. A light emitter based on practicable and mass-producible polycrystalline graphene patterned directly on silicon substrates from a solid-state carbon source. *RSC Adv.* **9**, 37906–37910 (2019).
48. Sharma, S., Kalita, G., Hirano, R., Hayashi, Y. & Tanemura, M. Influence of gas composition on the formation of graphene domain synthesized from camphor. *Materials Letters* **93**, 258–262 (2013).
49. Kalita, G., Wakita, K. & Umeno, M. Monolayer graphene from a green solid precursor. *Physica E: Low-dimensional Systems and Nanostructures* **43**, 1490–1493 (2011).
50. Zhou, Y. *et al.* Quantitative secondary electron imaging for work function extraction at atomic level and layer identification of graphene. *Sci Rep* **6**, 1–8 (2016).
51. Park, M.-H., Kim, T.-H. & Yang, C.-W. Thickness contrast of few-layered graphene in SEM. *Surface and Interface Analysis* **44**, 1538–1541 (2012).
52. Hiura, H., Miyazaki, H. & Tsukagoshi, K. Determination of the Number of Graphene Layers: Discrete Distribution of the Secondary Electron Intensity Stemming from Individual Graphene Layers. *Appl. Phys. Express* **3**, 095101 (2010).
53. Miyoshi, M. *et al.* Study on transfer-free graphene synthesis process utilizing spontaneous agglomeration of catalytic Ni and Co metals. *Mater. Res. Express* **2**, 015602 (2015).
54. Kim, E., Lee, W.-G. & Jung, J. Agglomeration effects of thin metal catalyst on graphene film synthesized by chemical vapor deposition. *Electron. Mater. Lett.* **7**, 261–264 (2011).
55. Park, H. J., Meyer, J., Roth, S. & Skákalová, V. Growth and properties of few-layer graphene prepared by chemical vapor deposition. *Carbon* **48**, 1088–1094 (2010).
56. Chen, Y.-Z. *et al.* Large-scale and patternable graphene: direct transformation of amorphous carbon film into graphene/graphite on insulators via Cu mediation engineering and its application to all-carbon based devices. *Nanoscale* **7**, 1678–1687 (2015).

57. Fan, X., Chen, T. & Dai, L. Graphene networks for high-performance flexible and transparent supercapacitors. *RSC Adv.* **4**, 36996–37002 (2014).
58. Tu, Z. *et al.* Controllable growth of 1–7 layers of graphene by chemical vapour deposition. *Carbon* **73**, 252–258 (2014).
59. Peng, K.-J. *et al.* Hydrogen-free PECVD growth of few-layer graphene on an ultra-thin nickel film at the threshold dissolution temperature. *J. Mater. Chem. C* **1**, 3862–3870 (2013).
60. Lin, T. *et al.* Self-regulating homogenous growth of high-quality graphene on Co–Cu composite substrate for layer control. *Nanoscale* **5**, 5847–5853 (2013).

Chapter 5: Boron doped graphene synthesis and electrochemical characterization

I. Introduction: why boron doping?

After the study of the influence of the substrates, the amorphous carbon thickness, and the initial nickel thickness on the synthesis of our PLD graphene in the last chapter, here, we focus on the synthesis of boron-doped graphene and its electrochemistry response. Indeed, the incorporation of boron in the graphene structure, which is less investigated than nitrogen doping, increases the concentration of holes, inducing a p-doping effect, with a downshift of the Fermi level towards the Dirac point[1]. Besides, boron atoms form sp^2 hybridization in the carbon lattice, thus the planar structure of graphene is retained. Since B-C bonds are slightly longer than C-C bonds in graphene, lower strain energy is induced by substitutional boron doping. Due to the strong B-C bond energy, the mechanical properties of graphene are preserved but the thermal conductivity of boron-doped graphene (BG) is dramatically reduced compared to pristine graphene[2]. Furthermore, the B-C bond introduces defects in the nearby sites because boron atom possesses three valence electrons, and thereby induces uneven charge distribution, which can facilitate charge transfer between neighboring carbon atoms and therefore enhance their electrochemical performance[3].

In this chapter, we study, for the best of our knowledge, the first attempt of using the PLD method to synthesize boron-doped graphene by co-ablation of carbon and boron solid precursors. In the past, our group has demonstrated the ability of PLD to obtain boron-doped diamond-like carbon films (a-C:B)[4], which provides a considerable baseline to develop the synthesis of boron-doped graphene (BG) films.

This chapter is organized in three parts consecutive to the description of the experimental protocol. In the first section, we analyzed the results of the structural and chemical features of the undoped and boron-doped graphene through Raman and XPS characterization techniques. In the second part, we examined the electrochemical response through cyclic voltammetry curves of the electrodes made up of the undoped and boron-doped graphene. Lastly, we discussed the relation between the defects density in the synthesized undoped and boron-doped graphene with their corresponding electrochemistry responses.

II. Experimental protocol to synthetize BG layers from a-C:B films

Based on Chapter 2 (paragraph 2b), let us remind that the BG growth involves three main steps, as depicted in **Figure 5.1** already presented as **Figure 2.7**: the deposition of a nickel thin film catalyst 50 nm thick by thermal evaporation, the deposition of a-C:B film on the SiO_2(300nm)/Si substrates by co-ablation of carbon and boron targets, and the RTA process, detailed hereafter, responsible for the synthesis of boron-doped graphene. In the present chapter, we have selected thickness of the a-C:B film precursor equal to about 4 nm, compared to 2 nm for the optimized pure graphene films in Chapter 4. Indeed, the goal in this chapter 5 is not to reach the graphene exhibiting the highest bilayer proportion and quality in terms of low defect concentration, as demonstrated in section III of the previous chapter 4. The objective is to provide doped graphene films with enough incorporated boron through a controlled and reproducible procedure, which becomes more difficult when the matter quantity is too low. Moreover, it is worth noticing that SiO_2(300nm)/Si was chosen in this chapter as the selected substrate for two reasons. Firstly, the electrochemistry experiment requires a conductor or semiconductor substrate; secondly, to avoid the formation of nickel silicide as demonstrated in **section I of Chapter 4**.

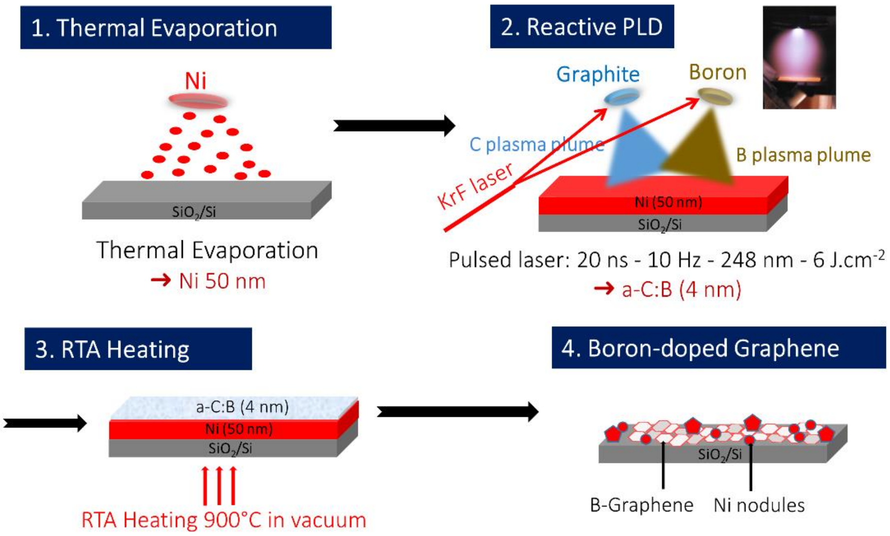

Figure 5. 1 The synthesis process of B-doped graphene films, by PLD and thermal heating of an a-C:B/Ni SiO_2(300nm)/Si.

In chapter 2, we have shown how to synthetize the a-C:B films (4 nm thick) used in the present chapter as the solid precursor for obtaining the BG films. From XPS analysis, we obtained 4 nm thick a-C:B films, containing 2, 4.5, and 9 at% of boron.

Thus, the main problem is now focused on the ability of the RTA process to convert that a-C:B film into boron-doped graphene, taking care of the boron content and nature of chemical bonds incorporated in the graphene network, as well as the defects induced by boron doping. Indeed, one of the challenges of boron-doped graphene is to control accurately the boron concentration in graphene whatever the synthesis method and investigate if the boron concentration in the a-C:B films remains or not similar in the BG film. Ideally, a congruent concentration would be of great interest in the perspective of BG production.

Boron-doped graphene was obtained by heating the a-C:B/Ni/ SiO_2(300nm)/Si film to 900 °C for 7 min at a vacuum pressure of 10^{-2} mbar by RTA with a heating ramp rate of 15 °C/s and a cooling rate of about 1 °C/s, which are our optimal conditions discussed in **Chapter 4**. After annealing, the graphene and boron-doped graphene form on the substrate and will be the subject of the investigations described in the next sections.

III. Structural and chemical analysis of the synthesized films

By using Raman spectroscopy and XPS, we investigated the nanostructure and chemical composition of the synthesized graphene and boron-doped graphene. Great attention will be paid on the difference in features between the undoped and boron-doped graphene films, as well on the boron content both in the a-C:B precursors and the BG films. For this reason, prior BG films, we included in this section the detailed XPS analysis of the a-C:B precursors, whose boron contents were mentioned in Table 2.2. of Chapter 2.

1. X-rays photoelectron spectroscopy (XPS) analysis of a-C:B and BG films

As reported in Chapter 2, X-ray photoelectron spectroscopy (XPS) is a powerful tool to characterize the doping levels of heteroatoms. In the overview spectra (not shown) of the a-C:B films, we observed the presence of carbon, boron, and oxygen. Besides, the nickel was not detected probably because of the 4 nm thick of a-C:B which screens the nickel peaks. On the contrary, in the overview spectra of the BG films, we observed not only C1s, B1s, and O1s, but also Ni2p and Si2s and Si2p. This means that after the annealing process, we still have some nickel residuals as explained in chapter 4. Furthermore, the presence of oxygen in the a-C:B precursor sample can be attributed to adventitious contamination and oxygen incorporation in the films due to residual water vapor in the PLD chamber (maintained near 10^{-7} mbar during deposition) or during air storage after deposition. After quantification, we obtained that the a-C:B of 4.5 at.% of boron leads to the BG film containing 1at.% of boron, and the a-C:B precursor of 9at.% of boron conducts to the BG film with 2.5at.%. Note that those percentages are related to the ratio B/(B+C). Therefore, we observe a loss of boron after the annealing process, when comparing the boron content of the BG films with their precursors, for both boron concentrations. This may be due to the thermal annealing process, which provokes the evaporation/desorption of a part of boron during the synthesis of BG films, with a mechanism, which remains to be clarified.

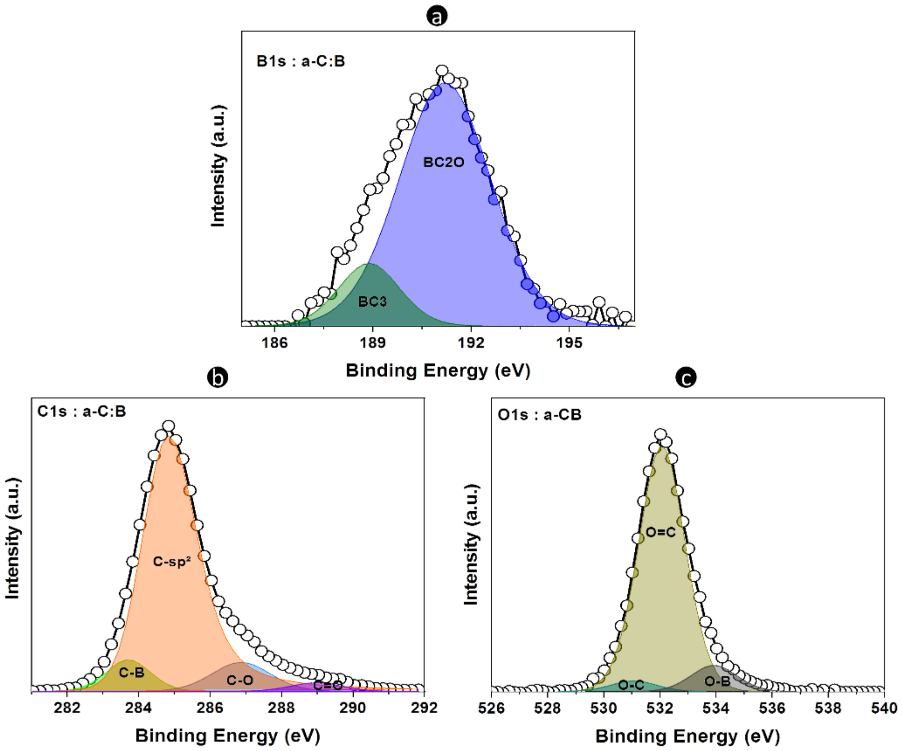

Figure 5. 2 (a) XPS-B1s, (b) XPS-C1s spectrum, (c) XPS-O1s spectrum. All of a-C:B (9 at.%).

Using the high-resolution core-level spectra, we performed the peak deconvolution to reveal the detailed configurations of the boron dopant, carbon, and oxygen. Moreover, the peak deconvolutions and their exact interpretation are rather controversial, due to the proximity of electronic configuration of carbon and boron with a slight difference in their electronegativity, and due to the many chemical functions combining B, C and O species. Our interpretation of XPS is based on a compilation of previously published data related to boron-doped graphene[5–11]. XPS spectra depicted in **Figure 5.2a-c** show the B1s, C1s, and O1s core levels of the a-C:B film containing 9 at.% of boron, as deposited by the co-ablation process of carbon and boron (i.e. before annealing allows its conversion into boron-doped graphene). In the a-C:B film, the B1s contributions (**Figure 5.2a**), centered at 188.8 and 191.2 eV, are assigned to BC3 and BC2O respectively. The C1s contributions (**Figure 5.2b**), centered at 283.7, 284.7, 286.8 and 288.9 eV, are respectively assigned to C-B (peak related to B-doped structure, indicating the successful doping of B), sp^2 carbon (typically observed in diamond-like carbon films), C-O and

C = O species. The O1s core level spectrum (**Figure 5.2c**) shows the deconvoluted peaks at about 531, 532, and 533.9 eV are associated respectively with O-C, O=C, and O-B bonds.

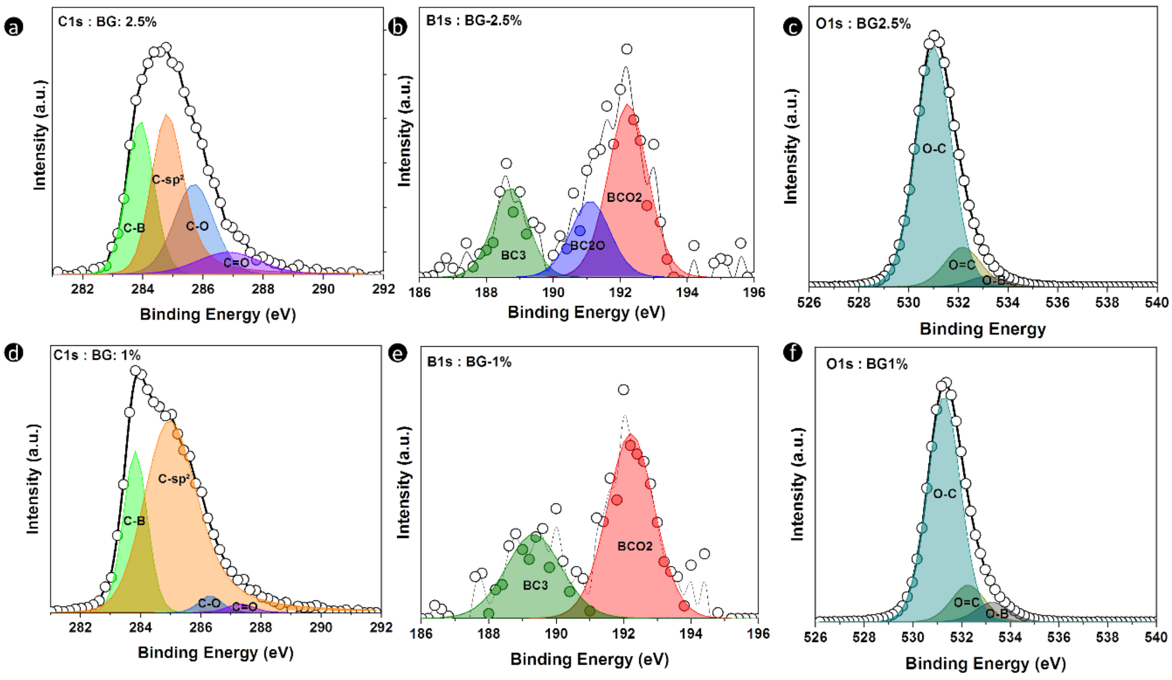

Figure 5. 3 High resolution XPS spectra of BG (2.5 at.%): (a) C1s, (b) B1s, (c) O1s. High-resolution XPS spectra of BG (1 at. %): (d) C1s, (e) B1s, (f) O1s.

The high-resolution XPS spectra of C1s, B1s, and O1s for BG2.5% and BG1% are reported in **Figure 5.3**. Indeed, after the conversion of the a-C:B films into the BG films using thermal rapid annealing, the position of the C1 contributions is not significantly modified. A relative increase in the C-B contribution is observed, which may be due to the good incorporation of boron atom into the carbon network upon the annealing process. Moreover, an increase in the C-O and C=O contributions is observed in BG2.5%, in agreement with the higher O1s contribution. Concerning the boron signal, in BG2.5%, the B1s contribution was fitted in three peaks centered at 188.8, 191.1, and 192.2, assigned to BC3, BC2O, and BCO2 respectively. In BG1%, the B1s deconvolution gives rather two boron species BC3 (189.3 eV) and BCO2 (192.2). In any case, the presence of BC3, BC2O and BCO2 bonds suggests the replacement of carbon atoms by boron atoms within the graphene network and the boron atom doped at the defect sites as reported in most of the references related to BG films cited above. The O1s core level spectra (**Figure 5.3c, f**) show the same oxygen species O-C, O=C, and O-B as observed in a-C:B films. The relative abundance of oxygen in boron- and carbon-containing chemical groups is typical of top-surface compositions.

2. Raman spectroscopy analysis

To study the boron doping effect on the synthesized graphene, Raman mapping of 20 x 20 µm² (each integrating 400 Raman spectra) was performed on representative areas for the undoped and boron-doped graphene with 1 and 2.5 at.%.

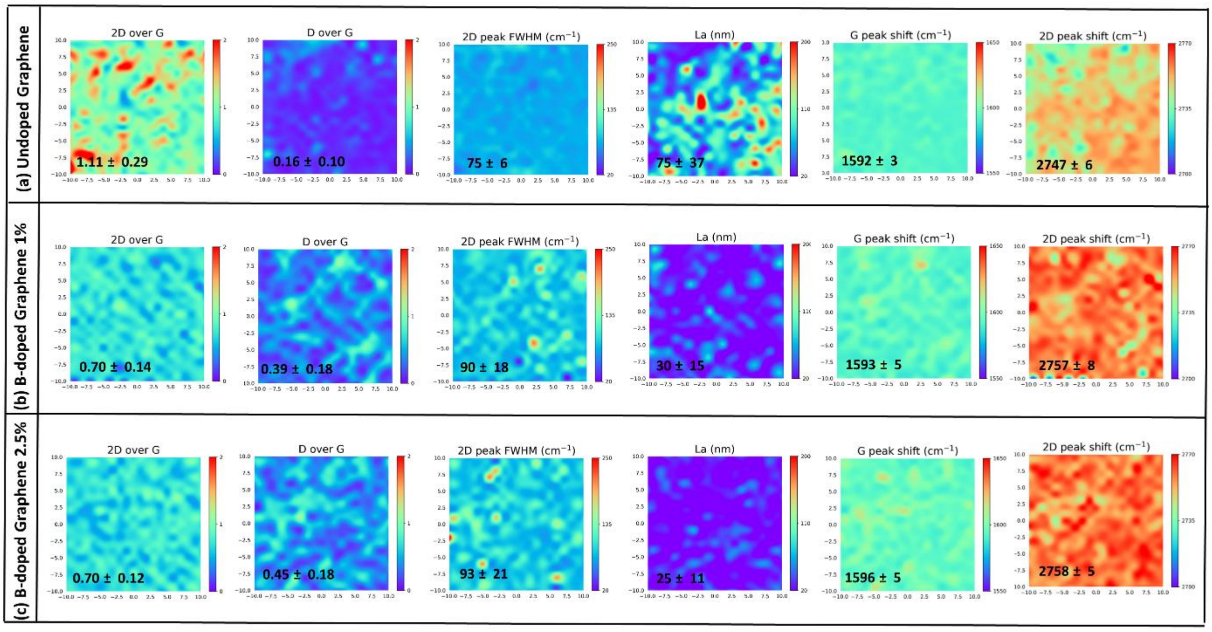

Figure 5. 4 I_D/I_G, I_{2D}/I_G, 2D (FWHM), L_a, G, and 2D positions Raman mappings of (a) undoped graphene, (b) boron-doped graphene 1%, (c) boron-doped graphene 2.5%, with their average values.

After measurements, we processed the mappings for the following characteristics: I_D/I_G and I_{2D}/I_G intensity ratios, 2D peak FWHM, and crystallite size La, as well as G, and 2D peak positions as shown in **Figure 5.4**.

	I_D/I_G	L_a (nm)	I_{2D}/I_G	2D (FWHM) (cm^{-1})	2D position (cm^{-1})	G position (cm^{-1})
G	0.16 ± 0.10	75 ± 37	1.11 ± 0.29	75 ± 6	2747 ± 6	1592 ± 3
BG1	0.39 ± 0.18	30 ± 15	0.70 ± 0.14	90 ± 18	2757 ± 8	1593 ± 5
BG2.5	0.45 ± 0.18	25 ± 11	0.70 ± 0.12	93 ± 21	2758 ± 5	1596 ± 5

Table 5. 1 Average values and their standard deviations of the Raman characteristics resulting from the 400 Raman spectra performed on representative areas of the synthesized undoped and boron graphene.

Table 5.1 lists the average values and standard deviation of the I_D/I_G, I_{2D}/I_G, 2D (FWHM), L_a, G, and 2D positions taken from Raman mappings of each sample. We observed that the average value of the I_D/I_G intensity ratio increases with the boron doping from 0.16 to 0.45. In addition, a decrease in the average value of the crystallite size (L_a) from 75 to 25 nm is observed when the boron doping level increases. These results suggest that the boron doping induces higher defects density in graphene structure and lowered the crystallites size of graphene. Besides, the average value of the I_{2D}/I_G ratio diminishes with the boron doping, from 1.11 to 0.70, whereas the average value of FWHM (2D) raises from 75 to 93 cm^{-1}. This suggests that the number of graphene layers decreases with the boron doping. Furthermore, we observed a little change in the position of G and 2D peaks as a function of the boron doping level. Indeed, the G peak slightly upshifts when raising the boron doping level. It is worth noting that this upshift of the G peak can be due either to the reduction of the graphene crystallite size**[12]** or to the doping effect**[13]** or the influence of compressive stress**[14–16]**. Therefore, it is not straightforward to conclude to this upshift of the G peak is only due to the boron doping effect. However, we observed clearly that the boron doping influences considerably the graphene structure.

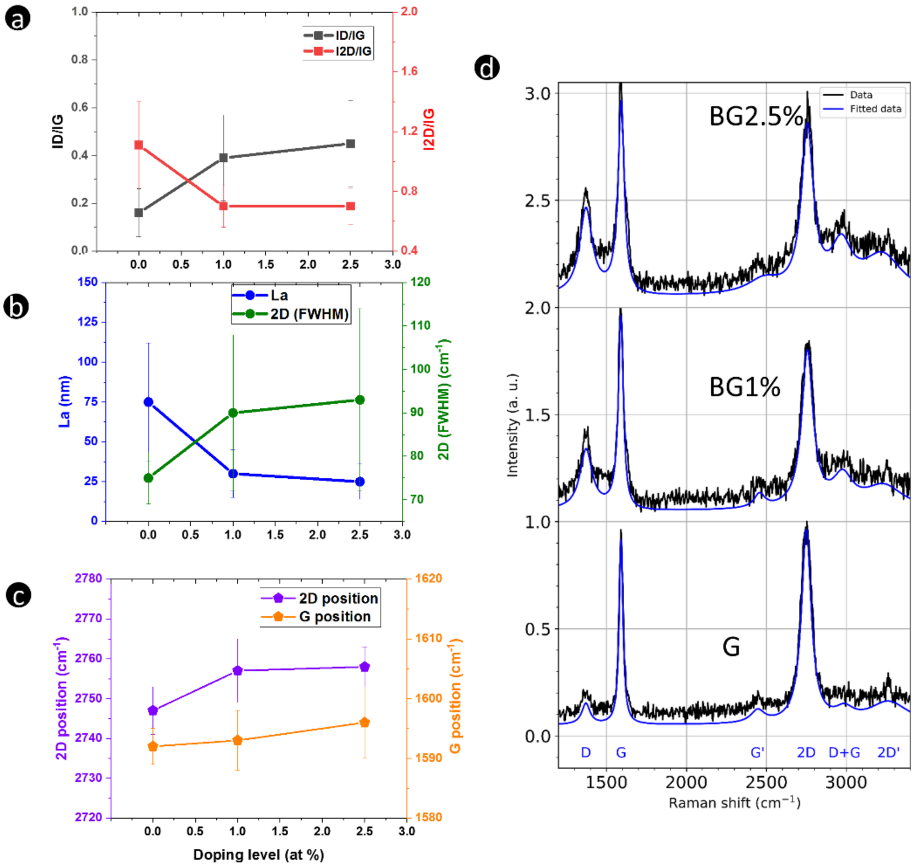

Figure 5. 5 Plots showing the dependence on boron doping level as a function of the average value of (a) I_D/I_G ratio, I_{2D}/I_G ratio, (b) crystallite size (La), the FWHM (2D), and (c) G and 2D peaks positions for the synthesized undoped and boron-doped graphene (1, 2.5 at%). (d) Typical experimental (black) and fitted (blue) Raman spectra of the synthesized undoped and boron-doped graphene films (1, 2.5 at.%).

Concerning the 2D peak, we observed also an upshift from 2747 to 2758 cm^{-1} with boron doping. Again, the upshift can be due either to the increase in the number of graphene layers[15–17] or to the doping effect[13]. All these effects are illustrated in **Figure 5.5a-c** with the plot of I_D/I_G and I_{2D}/I_G ratios and crystallite size L_a and FWHM (2D) as well as G and 2D peaks positions as a function of boron doping level. As noticed in the average value of the different mappings, the ratio intensity I_D/I_G and I_{2D}/I_G display an opposite evolution when the boron doping level augments. The crystallite size L_a and the FWHM (2D) present also the opposite trend with the boron doping, while the G and 2D peaks positions rather follow the same trend. Furthermore, it is worthwhile to highlight the high values of the standard deviations for all the mapping demonstrates that the synthesized undoped and boron-doped graphene are heterogeneous in terms of the number of layers, defects density, and crystallite size. **Figure 5.5d** shows typical Raman spectra extracted from the mapping of each of the samples detailed in **Table 5.1**. The major peaks characteristics of graphene D, G, and 2D are visible. We observed that the D peak becomes more intense with the boron doping suggesting the existence of high defects density in the BG films.

Taking into consideration the results of XPS and Raman analysis and interpretations, we have demonstrated that an amorphous a-C:B film obtained by co-ablation of carbon and boron can be thermally converted into a boron-doped graphene film containing a lower boron content that in the precursor film. In the next section, we are going to highlight the electrochemistry performance of these BG films.

IV. Electrochemistry response of our synthesized G and BG films

The cyclic voltammetry (CV) was performed on the synthesized graphene and boron-doped graphene containing different boron doping levels 0, 1, and 2.5 at. %. Samples are labeled G, BG1%, and BG2.5%, respectively. At this stage, it is worth mentioning that all the cyclic voltammetry measurements were performed on the as-grown undoped and boron-doped graphene without further acidic treatments. This means that the samples contain some nickel residuals. However, during the CV measurements, the signal of these nickel nodules was not observed by the CV analysis, suggesting that the presence of these nickel residuals does not influence the electrochemical results.

1. Cyclic voltammetry measurements of the as-grown graphene and boron-doped graphene

Cyclic voltammetry (CV) measurements obtained with ferrocene dimethanol on undoped graphene (G) and B-doped graphene (BG) at the scan rate of 50 mV s^{-1} are presented in **Figure 5.6**, and the comparative electrochemical parameters are listed in **Table 5.2**.

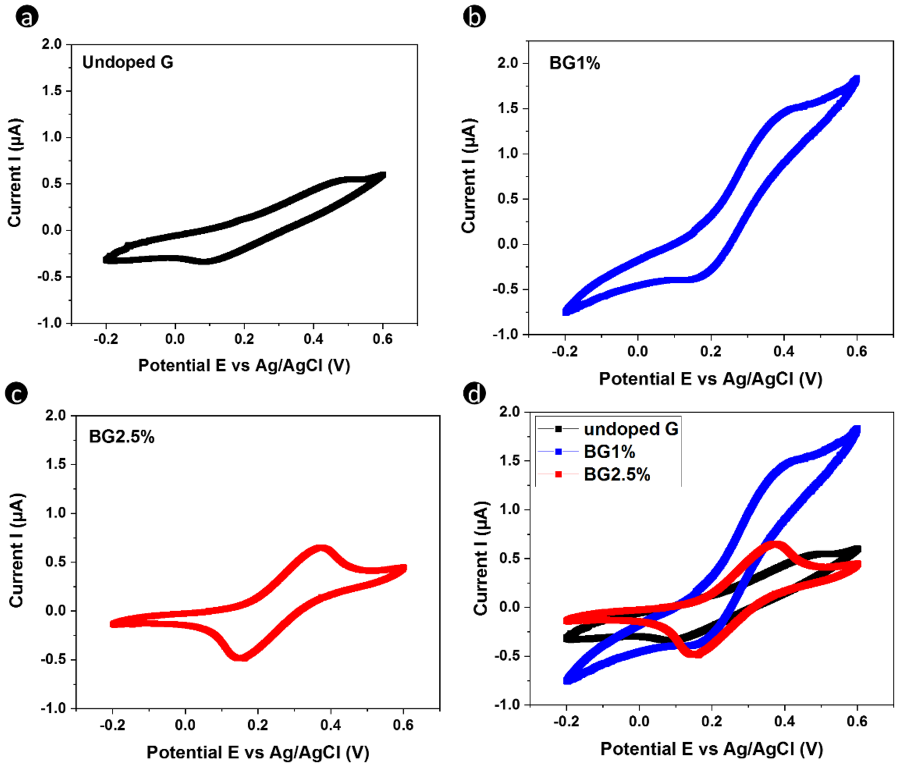

Figure 5. 6 Cyclic voltammetry curves measured in a 0.5 M 1, 1' ferrocene-dimethanol solution of 0.1 M NaClO$_4$ with the scan rate of 50 mV/s. (a) CV of undoped graphene. (b) CV of BG1%. (c) CV of BG2.5%. (d) All the CV curves together.

Samples	B (at.%	E_{ox} (V)	E_{red} (V)	I_{ox} (μA)	I_{red} (μA)	ΔE (V)
G	0	0.46	0.11	0.09	0.15	0.35
BG	1	0.36	0.19	0.38	0.44	0.17
BG	2.5	0.36	0.16	0.40	0.47	0.20

Table 5. 2 Results of electrochemical measurements on BG and undoped graphene films.

The values of ΔE for G, BG1%, and BG2.5% are respectively 0.35, 0.17, and 0.20 V, which demonstrate that the two boron-doped graphene electrodes exhibit better kinetic electronic transfer compared to the undoped graphene electrode. These measurements show that electronic transfers are quasi-reversible and not Nernstian (ΔE ~ 59 mV). Besides, we observed the increase of both oxidation and reduction currents with the rise of the boron concentration, which is in agreement with previous work reported[3] on BG film. Looking at the shape of the CV curves, the capacitive current appears to be higher with undoped graphene film compared to the boron-doped graphene films. This can be due to the formation of more edge in the graphene structure**[18]**. Comparing the two boron-doped graphene films, the one with 2.5 at. % of boron presents lower capacitive current and essentially faradaic current due to the redox molecule. This suggests that the electrode with BG with 2.5 at. % boron exhibits superior electrochemical properties over that of 1 at. % boron.

To estimate the value of the kinetic rate of interfacial electron transfer constant k_0, the dimensionless kinetic parameter Ψ was first determined using the method developed by Lavagnini**[19]** for a quasi-reversible system with ΔE values higher than 200 mV using the following equation:

$$\Psi = 2.18 \left[{}^{\beta}/_{\pi}\right]^{1/2} \exp\left[-\left(\beta^{2}\, {}^{F}/_{R\,T}\right) n\, \Delta E\right]$$

where Ψ is a kinetic parameter, n is the number of electrons involved in the process (n = 1), F is the Faraday constant (F = 96485 $C.mol^{-1}$), R the gas constant (R = 8.314 $J.mol^{-1}K^{-1}$), T the temperature (T= 298 K), β the transfer coefficient generally assumed to be 0.5**[20,21]** and ΔE is the peak-to-peak separation. From this, a plot of Ψ against $\nu^{-1/2}$ (ν being the experimental CV scan rate) allows the electron transfer rate constants k_o to be determined through the slope value of the linear fit. Indeed, to calculate the kinetic parameter Ψ, the voltammetry curves were recorded for each sample at different scan rates from 2 to 200 mV/s. Afterward, we plot the calculated kinetic parameter (Ψ) versus the reverse of the square root of the scan rate ($\nu^{-1/2}$), as shown in **Figure 5.7.**

Consequently, k_o is found to be equal to 2.3×10^{-3}, $2.5 \times 10^{-3,}$ and 4.9×10^{-3} $cm.s^{-1}$ for undoped graphene G, BG1%, and BG2.5% respectively. From these results, the undoped graphene possesses the smallest k_o indicating unfavorable electrochemical properties. If the increase due to a boron doping level of 1% appears very limited, it appears that increasing the boron doping level up to 2.5% increases the k_o value almost twice times. All these results demonstrate that BG2.5% exhibits better electrochemical performance with respect to BG1% probably due to the higher boron content of BG2.5%, which can facilitate charge transfer between the neighboring carbon atoms in graphene lattice**[9,21]**. For further analysis, BG2.5% was used for the stability study presented next.

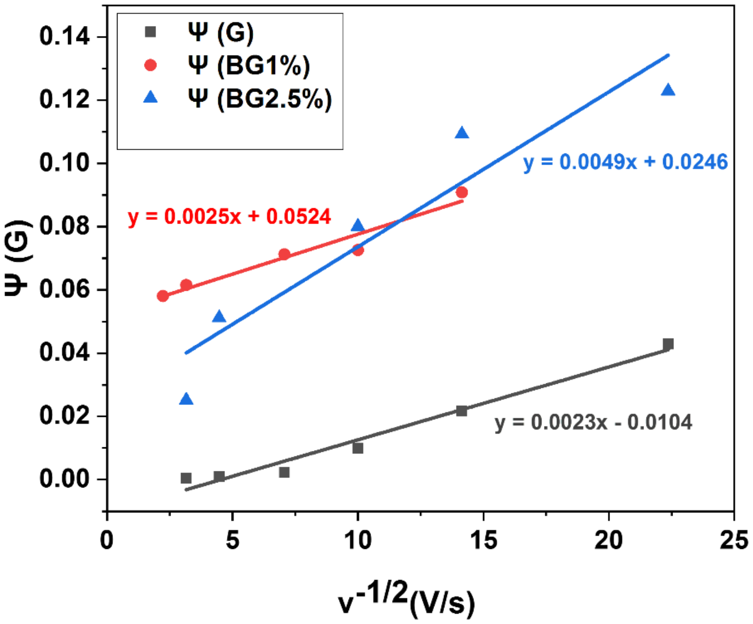

Figure 5. 7 Plot of Ψ against $v^{-1/2}$ enabling the estimation of the kinetic rate of interfacial electron transfer constant k_o.

2. Evaluation of the stability of the Boron doped graphene with 2.5 at. %

Figures 5.8a-b show the CV curves of BG2.5% for the different time during in ferrocene dimethanol. Several cycles have been realized at 50 mV/s. We observed from **Figure 5.8a** that the intensity of oxidation and reduction current signal decreases with time and number of cycles, from 0 to 30 minutes of cycling. Indeed, initially, the fresh BG2.5% electrode presents a redox behavior with the fastest kinetics and highest peak currents (red curve). By increasing its time duration in the ferrocene dimethanol electrolyte, the peaks currents decrease, especially for 10, 30 min, and ΔE values slightly increases except for 10 min duration. This can be due to the number of cycles, which can also alter the sensitivity of the BG film.

It is worth mentioning that the values of potential and currents of BG2.5% in **Table 5.3** are slightly different from those in **Table 5.2** because the measurements were not done in the same areas, which evidenced the heterogeneity observed in Raman mapping.

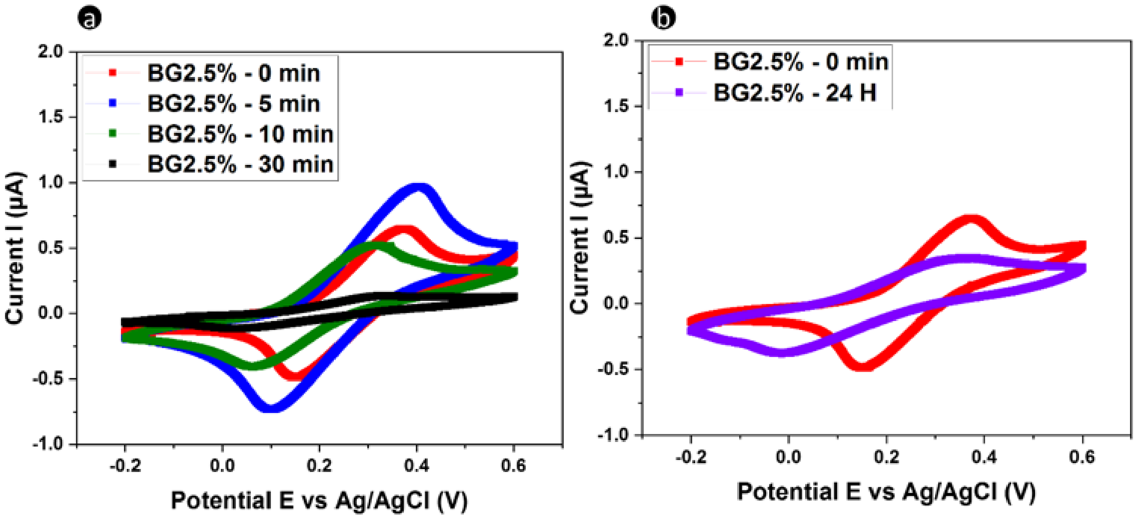

Figure 5. 8 Cyclic voltammetry on BG20 in a 0.5 M 1, 1'ferrocene-dimethanol solution of 0.1 M $NaClO_4$ (a) for 0 min (red), 5 min (blue), 10 min (green), and 30 min (black); (b) for 0 min (red) and 24 hours (purple). The scan rate is 50 mV/s.

Time (min)	E_{ox} (V)	E_{red} (V)	I_{ox} (µA)	I_{red} (µA)	ΔE (V)
0	0.37	0.15	0.43	0.56	0.22
5	0.39	0.11	0.63	0.68	0.28
10	0.30	0.15	0.34	0.56	0.15
30	0.32	0.03	0.08	0.09	0.29
1440	0.315	0.00536	0.168	0.198	0.310

Table 5. 3 Results of electrochemical measurements on BG2.5% for a different time duration in ferrocene dimethanol with the scan rate of 50 mV/s.

Figure 5.8b shows a complementary stability study in which the sample was left in the cell in contact with the solution overnight at 4°C to compare from day to day in the same area. In this case, the curve (red curve) that was initially very reversible tends to widen and more resemble the signal of undoped graphene. Indeed, the current peaks significantly decrease while the ΔE value increases close to the one of undoped graphene. The cumulative effect of cycling (~ 20th cycle on the same area) and incubation in the solution for 24 hours (1440 min) seem to affect the electrochemical response. However, even though the peaks currents decreased, the peak potential of the BG2.5% electrode with 5, 10, 30, and 1440 min duration shifts a little. That means the kinetic rate does not change too much, and the decrease of the peak current can be due to the decrease in the apparent geometric area of the BG2.5% electrode. Consequently, these results demonstrate that the time and number of cycles affect the preservation stability of BG2.5%.

V. The relation between graphene nanostructures and their electrochemistry response

To correlate the nanostructure of the undoped and boron-doped graphene with the kinetic rate of interfacial electron transfer (k_o), Raman mappings were performed and the average intensity ratios of the D peak over the G peak (I_D/I_G) were calculated from the imaging data as shown in **Figure 5.4**. **Figure 5.9** shows the correlation between the k_o and the average I_D/I_G value. We observed that the I_D/I_G ratios of the graphene and the BG1% are very similar, but k_o augments for BG2.5% for which both values of I_D/I_G and k_o are much higher compared to the other G and BG1% electrodes. Therefore, it can be concluded that the interfacial electron transfer capability is dependent on the defects in the graphene materials, which is in agreement with the previous work on CVD graphene[22]. It is well known that the pristine graphene does not present good interfacial electron transfer kinetics. Even though the defects in graphene reduce its electrical conductivity, an appropriate defect density can improve its electrochemical activity, i.e., the interfacial electron transfer capability as previously reported by other groups[22,23].

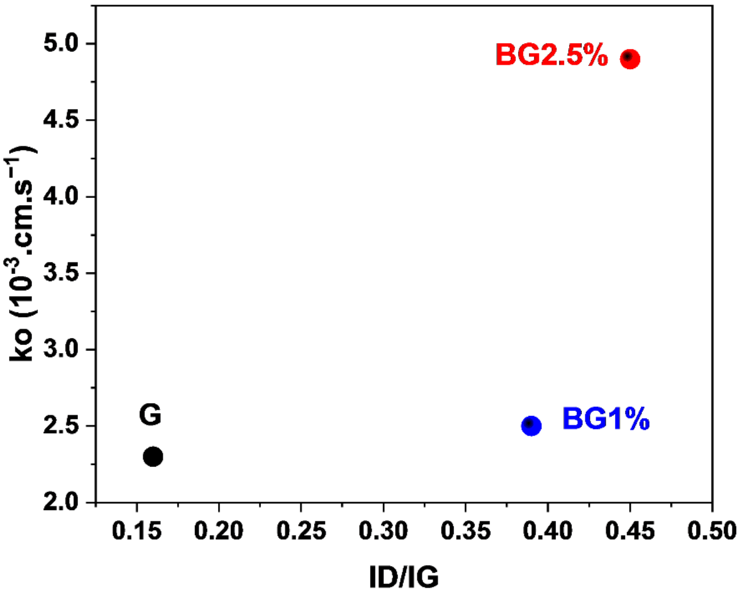

Figure 5. 9 The correlation between the kinetic rate of interfacial electron transfer (k_o) and the average intensity ratio of the D-peak over the G-peak (I_D/I_G) of the G, BG1% and BG2.5%.

VI. Summary

This chapter covers the demonstration of the synthesis of boron-doped graphene films using pulsed laser co-ablation of carbon and boron in high vacuum conditions. The structural and chemical characteristics of the films were investigated by combining Raman, and XPS. The novelty of the results consists of the possibility of using the PLD method to grow boron-doped graphene. The synthesized boron-doped graphene films are constituted of few layers contains 1 to 2.5 at. % of boron predominantly bonded to carbon in both BC3 and BCO2 configurations and high defect density associated with a decrease of cluster size. We observe a systematic “loss” of boron during the RTA process, when comparing the boron content of the BG films with their precursors, for both boron concentration. Furthermore, the electrochemistry measurements show that the boron-doped graphene films possess higher performance compared to the undoped graphene. In addition, by increasing the doping level from 1 to 2.5 at.%, the electron transfer is much higher. However, the preservation of the stability of the BG2.5% electrode is time-dependent. Therefore, further studies can be done to achieve much higher stability over time. Another perspective is to investigate the electronic properties of these BG films to highlight the shift of the Fermi level as already reported by some works.

References

1. Rani, P. & Jindal, V. K. Designing band gap of graphene by B and N dopant atoms. *RSC Adv.* **3**, 802–812 (2012).
2. Agnoli, S. & Favaro, M. Doping graphene with boron: a review of synthesis methods, physicochemical characterization, and emerging applications. *J. Mater. Chem. A* **4**, 5002–5025 (2016).
3. Sheng, Z.-H., Gao, H.-L., Bao, W.-J., Wang, F.-B. & Xia, X.-H. Synthesis of boron doped graphene for oxygen reduction reaction in fuel cells. *J. Mater. Chem.* **22**, 390–395 (2011).
4. Sikora, A. *et al.* Effect of boron incorporation on the structure and electrical properties of diamond-like carbon films deposited by femtosecond and nanosecond pulsed laser ablation. *Thin Solid Films* **518**, 1470–1474 (2009).
5. Cheng, W. *et al.* Boron-doped graphene as a metal-free catalyst for gas-phase oxidation of benzyl alcohol to benzaldehyde. *RSC Advances* **8**, 11222–11229 (2018).
6. Chowdhury, S., Jiang, Y., Muthukaruppan, S. & Balasubramanian, R. Effect of boron doping level on the photocatalytic activity of graphene aerogels. *Carbon* **128**, 237–248 (2018).
7. Fang, H., Yu, C., Ma, T. & Qiu, J. Boron-doped graphene as a high-efficiency counter electrode for dye-sensitized solar cells. *Chem. Commun.* **50**, 3328 (2014).
8. Sun, Y. *et al.* Boron-doped graphene as promising support for platinum catalyst with superior activity towards the methanol electrooxidation reaction. *Journal of Power Sources* **300**, 245–253 (2015).
9. Xu, X. *et al.* Facile synthesis of boron and nitrogen-doped graphene as efficient electrocatalyst for the oxygen reduction reaction in alkaline media. *International Journal of Hydrogen Energy* **39**, 16043–16052 (2014).
10. Yu, X. *et al.* Boron-Doped Graphene for Electrocatalytic N2 Reduction. *Joule* **2**, 1610–1622 (2018).
11. Sahoo, M., Sreena, K. P., Vinayan, B. P. & Ramaprabhu, S. Green synthesis of boron doped graphene and its application as high performance anode material in Li ion battery. *Materials Research Bulletin* **61**, 383–390 (2015).
12. Ferrari, A. C. & Robertson, J. Interpretation of Raman spectra of disordered amorphous carbon. *Physical Review B* **61**, 14095–14107 (2000).
13. Tongay, S. *et al.* Stable hole doping of graphene for low electrical resistance and high optical transparency. *Nanotechnology* **22**, 425701 (2011).

14. Röhrl, J. *et al.* Raman spectra of epitaxial graphene on SiC(0001). *Appl. Phys. Lett.* **92**, 201918 (2008).
15. Lee, D. S. *et al.* Raman Spectra of Epitaxial Graphene on SiC and of Epitaxial Graphene Transferred to SiO2. *Nano Lett.* **8**, 4320–4325 (2008).
16. Ni, Z. H. *et al.* Tunable Stress and Controlled Thickness Modification in Graphene by Annealing. *ACS Nano* **2**, 1033–1039 (2008).
17. Nguyen, T. A., Lee, J.-U., Yoon, D. & Cheong, H. Excitation energy dependent Raman signatures of ABA- and ABC-stacked few-layer graphene. *Sci Rep* **4**, 4630 (2014).
18. Zribi, B. *et al.* Large area graphene nanomesh: an artificial platform for edge-electrochemical biosensing at the sub-attomolar level. *Nanoscale* **8**, 15479–15485 (2016).
19. Lavagnini, I., Antiochia, R. & Magno, F. An Extended Method for the Practical Evaluation of the Standard Rate Constant from Cyclic Voltammetric Data. *Electroanalysis* **16**, 505–506 (2004).
20. Brownson, D. A. C., Kampouris, D. K. & Banks, C. E. Graphene electrochemistry: fundamental concepts through to prominent applications. *Chem. Soc. Rev.* **41**, 6944 (2012).
21. Niu, L. *et al.* Pyrolytic synthesis of boron-doped graphene and its application as electrode material for supercapacitors. *Electrochimica Acta* **108**, 666–673 (2013).
22. Liu, X., Sartin, M. M., Liu, Y., Tian, Z.-Q. & Zhan, D. Optimizing the interfacial electron transfer capability of single layer graphene by thermal annealing. *Chem. Commun.* **56**, 253–256 (2020).
23. Xiao, Y., Su, Y., Liu, X. & Xu, W. Defect-Driven Heterogeneous Electron Transfer between an Individual Graphene Sheet and Electrode. *J. Phys. Chem. Lett.* **10**, 5402–5407 (2019).

General conclusions and perspectives

The synthesis of graphene-based material is widely studied for the past decade because of its attractive properties. Today, the main challenge remains to achieve graphene synthesis homogenously on wide surfaces in a controlled and reproducible way, to target applications in various technological sectors, including materials, energy, optoelectronics, and biomedical. In recent years, attempts have been made to broaden and consolidate the graphene growth methods and procedures using solid carbon source, as an alternative way of using the well-known Chemical Vapor Deposition (CVD) technique, which uses carbonaceous gas and rather high temperatures for graphene synthesis. Physical Vapor Deposition (PVD) techniques offer an interesting alternative in this way, based on solid carbon precursors instead of gaseous precursors, in particular, to incorporate dopants in the graphene layers.

The present work investigated the synthesis of graphene and doped graphene using a particular PVD process, Pulsed Laser deposition (PLD), combined with a Rapid Thermal Annealing (RTA) process. The aim was to explore the capability of such a combined procedure for graphene and doped graphene growth.

Indeed, this thesis was in the framework of the collaboration between different laboratories. The synthesis of graphene and doped graphene was realized in the Hubert Curien Laboratory by using the PLD platform and a RTA furnace. More than 200 samples have been produced to study the growth mechanism of PLD graphene through the carbon diffusion and segregation by interaction with a nickel catalyst film obtained by thermal evaporation, the influences of growth parameters, such as time, annealing temperature and temperature ramp during RTA, the nature of the substrate, the thickness of both the carbon precursor and the nickel catalyst, on the obtained graphene films. Complementary multi-scale characterization techniques, such as Raman spectroscopy, Transmission electron microscope (TEM), Scanning Electron Microscopy coupled with Energy Dispersive Spectroscopy (SEM/EDS), Atomic Force Microscopy (AFM), X-rays photoelectron spectroscopy (XPS) and UV-Visible, aiming for graphene and doped graphene structural, morphological, topographical, chemical and transmittance investigation were performed at the Hubert Curien laboratory and in the laboratory of our partnership.

The main scientific conclusions of this work are the following:

i. The mechanism of graphene growth by coupling PLD with RTA using nickel catalyst is rather similar compared to other PVD methods coupled with thermal treatments (which is not surprising since one starts from a comparable carbon-based thin film), as well as the CVD method: the graphene growth is driven by high-temperature dissolution of carbon atoms (or phases, such as carbides) in the nickel catalyst, followed by diffusion and interfacial/surface segregation.

ii. During the graphene growth, the carbon diffusion is dependent on both the annealing temperature and the nickel catalyst microstructure. More fundamentally, we observed a significant difference with most published papers which indicate that graphene growth does occur mainly (sometimes only) during the cooling process, due to a lower carbon solubility in the metal catalyst when temperature decreases down to room temperature. We have demonstrated that carbon diffusion and surface segregation start at rather low temperatures, during the heating ramp, with an unambiguous presence of Csp^2 based few-layers graphene at 500°C. Using *in situ* XPS analysis during thermal heating, we observed that at low temperatures (200-300°C), the carbon diffusion in the nickel catalyst is accelerated due to the high defect density of the nickel film. This may explain the rapid formation of carbon-based layers acting as a "proto-graphene" film within 200-500°C. While, at 500°C, the carbon diffusion in the nickel catalyst is governed by a bulk diffusion due to a fully recovered nickel microstructure.

iii. We observed that the selected substrates for graphene growth highly influence the quality and layer number of the resulting graphene, whether it is silicon or fused silica. We have shown that silicon chemically interacts with nickel to form nickel silicide between 700 and 1000°C, inducing a defective multilayered graphene film, with a decrease in the crystallite size with temperature. On the contrary, silicon oxide does not react with the Ni catalyst, and less defective graphene films mainly comprised of 2-3 layers with larger crystallites are produced. Thus, the choice of the substrate for graphene growth cannot be disconnected to the choice of the metallic catalyst.

iv. The starting thickness of the amorphous carbon and the nickel catalyst as well as annealing temperature affect considerably the synthesized graphene. Using thinner starting a-C thicknesses such, as 2 nm, and fixing the growth temperature at 900°C and the nickel catalyst thickness equal to 50 nm, we observed the formation of a high proportion of graphene bilayers with lower defect density, whereas thicker starting a-C thicknesses led to the growth of few-layer graphene. In addition, when varying the starting nickel catalyst thickness while keeping constant the a-C thickness and the growth temperature, graphene films are preferentially continuous for 25 and 50 nm of nickel, whereas the synthesized graphene from 150 nm of nickel was significantly more discontinuous.

v. During the growth of graphene at high temperatures, we observed a solid-state dewetting phenomenon of the Ni catalyst film. We have shown that this phenomenon does not inhibit the graphene growth mechanism, and it appears compatible with graphene formation despite nickel residuals nodules. The graphene formation occurs on the top surface of the nickel nodules and at the interface between the nickel and the substrate. The nickel nodules can be further removed using an acidic solution such as iron chloride ($FeCl_3$) to obtain only interfacial graphene, also called “free transfer graphene”. We have also put in evidence that such a nickel dewetting is controlled by the initial nickel film thickness, temperature, and presence of carbon dissolved in nickel.

vi. Considering the previous results and conclusions, by appropriately tuning the growth parameters, a reproducible and controlled bilayer graphene growth with lower defect density and high transparency was obtained. This requires a SiO_2 substrate, a starting a-C thickness of 2 nm, an initial nickel thickness of 50 nm, and a growth temperature of 900°C during 7 min, with a heating rate of 15°C/s and cooling rate of 0.5°C/s.

vii. The synthesis of boron-doped graphene using the PLD method was successfully achieved for the first time. The synthesized boron-doped graphene films are constituted of few layers contains 1 to 2.5 at. % of boron predominantly bonded to carbon in both BC_3 and BCO_2 configurations. We observed a systematic “loss” of boron during the RTA process, when comparing the boron content of the BG films with their precursors, for both boron concentrations. We have shown that the electrochemical performances of the boron-doped graphene films are significantly higher than the ones of the pristine graphene. Moreover, these electrochemical performances increase with the rise of the boron doping level. More precisely, we observed that the cyclic voltammetry curves for the boron-doped graphene with higher boron content exhibit better reversibility compared to the other boron-doped graphene with a lower boron content and with the undoped graphene. In addition, the interfacial electron transfer value increases with rising boron content. This value for the highest boron-containing doped graphene is around twice the one of the boron-doped graphene with the lower boron content.

These findings enrich our understanding of the graphene growth using a nickel catalyst and a solid carbon (and boron-doped carbon) source obtained by pulsed laser deposition. Indeed, all the results position the PLD method as one of the alternative routes for graphene and doped graphene synthesis.

Our results and conclusions open some interesting directions for further researches in this field:

i. Even though the combination of the PLD and *ex-situ* RTA process allows obtaining graphene with the good quality compared to the literature, there is un-negligible oxygen contamination due to the sample transportation in ambient air after PLD and the low vacuum in the RTA furnace. Therefore, it would be interesting to investigate the one-step graphene synthesis using PLD and the *in-situ* annealing. This will permit us to avoid some oxygen contamination, including during the heating of the nickel catalyst before the carbon deposition to enlarge the nickel grain size for better graphene growth surface.

ii. As we observed the nickel thin film dewetting during the graphene growth at high temperature, one perspective is to perform an *in situ* XPS experiment as well as a model of carbon diffusion-segregation at high temperature to better understand the influence of this dewetting phenomenon on the graphene growth mechanism. Moreover, we highlighted that the presence of carbon favors the nickel dewetting process. Therefore, further studies may allow deeper investigations to understand how the presence of carbon accelerates the nickel dewetting process.

iii. We demonstrated the capability of PLD to grow boron-doped graphene with promising electrochemical properties. However, the preservation of the stability of these films is time-dependent and should be improved. Further studies on the synthesis can be done to improve the stability over time of these films, for example by playing with the growth temperature, the boron doping level, and so on. Furthermore, boron doping in graphene tunes its energy gap. So it is needed to study the electrical properties of boron-doped graphene to know its band gap as it is a promising material for electronic applications.

iv. Besides the nitrogen and boron doping, graphene can also be doped with these two elements at the same time, forming a boron-nitrogen doped graphene film. This could modify more significantly the electronic structure due to the synergistic coupling effects of these two elements. Therefore, B and N co-doping can improve the overall electrochemical performance of carbon materials by adjusting chemical reactivity, electronic conductivity, and surface compatibility. Another perspective is to use the PLD method to explore the synthesis of this dual graphene doping and compare its characteristics to the other growth methods.

List of publications and conferences

A. Publications

1. Y. Bleu, F. Bourquard, T. Tite, A.-S. Loir, C. Maddi, C. Donnet, F. Garrelie, Review of graphene growth from a solid carbon source by Pulsed Laser Deposition (PLD), **Frontier in chemistry** 6 (2018) 572-1 to 18.
2. Y. Bleu, V. Barnier, F. Christien, F. Bourquard, A.-S. Loir, F. Garrelie, C. Donnet, "Dynamics of carbon diffusion and segregation through nickel catalyst, investigated by in situ XPS, during the growth of nitrogen-doped graphene", **Carbon** 155 (2019) 410-420.
3. Y. Bleu, F. Bourquard, A.-S. Loir, V. Barnier, F. Garrelie, C. Donnet, "Raman study of the substrate influence on graphene synthesis using a solid carbon source via rapid thermal annealing" published in early view in **J. Raman Spectroscopy** 50 (2019) 1630-1641.
4. Y. Bleu, F. Bourquard, V. Gartiser, A.-S. Loir, B. Caja-Munoz, J. Avila, V. Barnier, F. Garrelie, C. Donnet, Graphene synthesis on SiO_2 using pulsed laser deposition with bilayer predominance, **Materials Chemistry and Physics** 238 (2019) 121905.
5. F. Bourquard, Y. Bleu, A.-S. Loir, B. Caja-Munoz, J. Avila, M.-C. Asensio, G. Raimondi, M. Shokouhi, I. Rassas, C. Farre, C. Chaix, V. Barnier, N. Jaffrezic-Renault, F. Garrelie, C. Donnet, Electroanalytical performance of nitrogen-doped graphene films processed in one step by pulsed laser deposition directly coupled with thermal annealing, **Materials**, 12(4) (2019) 00666-1 to -14.
6. Y. Bleu, F. Bourquard, V. Barnier, A.-S. Loir, F. Garrelie, C. Donnet, Boron-doped Graphene Synthesis by Pulsed Laser Co-Deposition of Carbon and Boron, **Applied Surface Science** 513 (2020) 145843.

B. International conferences

B.1. Invited talks

Y. Bleu

26th Advanced Materials Congress – "7th Edition of Graphene and 2D Materials Conference" Stockholm (Sweden) 10 – 13 June 2019 **-** Elaboration of graphene and doped-graphene by pulsed laser deposition

B.2. Contributed talks

(ORAL) Y. Bleu, V. Barnier, F. Bourquard, J. Avila, A.-S. Loir, F. Garrelie, M.C. Asensio, C. Donnet, Dynamics of nitrogen-doped graphene growth through nickel catalyst, investigated by in situ XPS, "**European Material Research Society, E-MRS 2018**", Strasbourg (France), 18 – 22 June 2018.

(POSTER) F. Bourquard, Y. Bleu, V. Barnier, A.-S. Loir, G. Raimondi, F. Lagarde, C. Chaix, N. Jaffrezic-Renault, F. Garrelie, C. Donnet, Electrochemical properties of nitrogen-doped graphene for environmental sensors, "**European Material Research Society, E-MRS 2018**", Strasbourg (France), 18 – 22 June 2018.

(ORAL) Y. Bleu, V. Barnier, F. Christien, J. Avila, F. Garrelie, M.C. Asensio, C. Donnet, Mechanism of formation of nitrogenated doped graphene films, investigated by in situ XPS during thermal annealing in vacuum, "**International Conference on Metallurgical Coatings and Thin Films, ICMCTF 2019**", San Diego (USA), 19-24 May 2019

(ORAL) Y. Bleu, F. Bourquard, V. Barnier, A.-S. Loir, F. Garrelie, C. Donnet, Pulsed laser co-deposition of carbon and boron for boron-doped graphene synthesis, "**European Material Research Society, E-MRS 2019**", Nice (France), 27– 31 May 2019.

(POSTER) Y. Bleu, F. Bourquard, A.-S. Loir, C. Donnet, F. Garrelie, Comparative Raman study of graphene growth from solid carbon source on Si(100) and SiO_2 substrates by combining pulsed laser deposition and rapid thermal annealing, "**European Material Research Society, E-MRS 2019**", Nice (France), 27– 31 May 2019.